

**UNIVERSITÀ DEGLI STUDI DI  
MODENA E REGGIO EMILIA**

---

***PhD Course in “Models and Methods for  
Material and Environmental Sciences”***

***XXXIII Cycle***

***Synthesis, characterisation and application of  
silicon-based materials in different areas***

**Tutor:**

**Prof.ssa Gigliola Lusvardi**

**Student:**

**Maria Laura Ligabue**

---

Director of the PhD Course: Prof. Alfonso Pedone

<b>Index</b>	<b>page</b>
<b>- Summary</b>	<b>5</b>
<b>- Introduction</b>	<b>13</b>
1.1. Silicon characteristics, history and most abundant compounds	13
1.2. Application of silicon and its compound	14
1.3. Alkaline-earth silicate phosphors	15
1.4. Sol-gel and its application in chemistry	16
1.5. KRY·AS: thermally treated cement asbestos used as secondary raw material	18
1.6. References	19
<b>- Purpose of the study</b>	<b>27</b>
<b>- Chapter 1: Preparation and luminescence properties of Ba<sub>5</sub>Si<sub>8</sub>O<sub>21</sub> long persistent phosphors doped with rare-earth elements (Paper)</b>	<b>30</b>
<b>- Chapter 2: One-pot sonocatalyzed synthesis of sol–gel graphite electrodes containing gold nanoparticles for application in amperometric sensing (Paper)</b>	<b>43</b>
<b>- Chapter 3: Silica-based pellets containing copper nanoparticles as disposable systems for electrocatalytic glycerol oxidation</b>	<b>56</b>
3.1. Introduction	57
3.2. Materials and methods	58
3.2.1. Chemicals	58
3.2.2. Composite material synthesis	58
3.2.3. Electrode preparation	59
3.2.4. Electrochemical investigations	59
3.2.5. Characterisation of the pellets	60
3.3. Results and Discussion	61
3.3.1. Voltammetric behaviour of the pellets	61
3.3.2. Experimental design	62
3.3.3. Characterisation	65
3.4. Conclusion	68
3.5. References	68
<b>- Chapter 4: Recycling of thermally treated cement-asbestos for the production of porcelain stoneware slabs (Paper)</b>	<b>73</b>

<b>- Chapter 5: Synthesis of blue and black ceramic pigments from KRY·AS</b>	<b>85</b>
5.1. Introduction	86
5.1.1. Ceramic pigments	86
5.1.2. Blue ceramic pigments	86
5.1.3. Black ceramic pigments	87
5.1.4. Production of ceramic pigments with recycled raw materials	87
5.1.5. Mineralogical, chemical and morphological characteristics of KRY·AS	88
5.2. Experimental	89
5.2.1. Synthesis and preparation of the samples	89
5.2.2. Characterisation	91
5.2.3. Application in mass coloration of ceramic tiles	92
5.3. Blue pigments: Results and discussion	92
5.4. Black pigments: Results and discussion	98
5.5. Ceramic tiles	103
5.6. Conclusion	104
5.7. References	105
<b>- Chapter 6: Innovative use of thermally treated cement-asbestos in the production of foaming materials: effects of composition, reducing agent, temperature, and reaction time</b>	<b>110</b>
6.1. Introduction	111
6.2. Materials and methods	112
6.2.1. Materials	112
6.2.2. Characterisation of the raw materials	114
6.2.3. Foam glass mixtures preparation	114
6.2.4. Characterisation of the mixtures	115
6.3. Results and discussion	116
6.3.1. Firing behaviour of raw materials	116
6.3.2. Phase 1: KRY·AS: RG wt. % ratio	119
6.3.3. Phase 2: flux agents	120
6.3.4. Phase 3: effect of foaming agent	124

6.3.5.	Phase 4: synthetic variables	125
6.3.5.1.	External and internal structure	125
6.3.5.2.	Apparent density	128
6.3.6.	Study of the foaming mechanism	131
6.4.	Conclusion	142
6.5.	References	143
-	<b>Appendix A: Supporting Information, Chapter 1</b>	<b>148</b>
-	<b>Appendix B: Supporting Information, Chapter 2</b>	<b>151</b>
-	<b>Appendix C: Supporting Information, Chapter 4</b>	<b>156</b>

## Summary

Silicon (Si) is the 14<sup>th</sup> element of the periodic table, as well as a tetravalent metalloid and a semiconductor. It possesses a high affinity for oxygen; therefore, it is extremely common to use it in the form of natural minerals, which compose the 90% of the earth's crust. Silicon, silica (SiO<sub>2</sub>) and silicates are the principal components of numerous building materials such as concrete, bricks, ceramic materials, and refractory materials (enamels and pottery); SiO<sub>2</sub> is also used to produce glass and glassware. Finally, synthetic polymers containing Si in addition to C, O and H are yet another different application, among which we can find silicones or silicon-based sol-gel.

This thesis reports different applications of silicon-based materials: i) Ba-silicate doped with rare earth elements used as phosphorescent pigment, ii) sol-gel electrodes prepared with the polysiloxane methyltrimethoxysilane (MTMOS), and metal nanoparticles (MeNPs), with different applications in electrochemistry, iii) thermally treated cement-asbestos, named KRY·AS, recycled in frits for porcelain stoneware slabs, blue and black ceramic pigments and foam glass.

The photoluminescent pigment, called also phosphor, of formula Ba<sub>5</sub>Si<sub>8</sub>O<sub>21</sub>:Eu<sup>2+</sup>,Dy<sup>3+</sup> was synthesized and the effect of precursors, crucible composition, flux agents, dopants, atmosphere and temperatures was also evaluated. The samples were characterised by means of a systematic investigation through elemental, mineralogical (both qualitative and quantitative), and morphological analysis. As for the synthesis conditions, the use of Na<sub>2</sub>SiO<sub>3</sub>, BaCO<sub>3</sub> and NH<sub>4</sub>Cl as precursors was very important to reduce the temperature and time of synthesis. The reducing atmosphere was produced with purified coal, cheaper and similar in results than the more traditional gas mixture H<sub>2</sub>/N<sub>2</sub>. At the end of this study, a phosphor with improved long persistent phosphorescence (LPP) characteristics was obtained with Ba/Si = 0.7, Eu/Si = 2.8 × 10<sup>-3</sup> and Dy/Si = 3.6 × 10<sup>-3</sup>, following a 6 h-synthesis in a quartz crucible at 1100°C.

Regarding the sol-gel electrodes, the first study is a one-pot synthetic approach to prepare sol-gel graphite electrodes containing gold nanoparticles (AuNPs). At variance with the traditional synthesis, in which AuNPs are prepared in advance with respect to the silica matrix, they were here obtained directly inside the sol-gel, during its formation. Two reduction methods, namely chemical and thermal reduction, were used to achieve AuNPs starting from a suitable gold precursor, either consisting of NaAuCl<sub>4</sub> or HAuCl<sub>4</sub>. In order to direct the synthesis of the material to the sought characteristics, different experimental parameters were tested: Si/Au molar ratio; graphite (g) :

silane precursor (mL) ratio; chemical nature of the gold precursor and of the reductant; duration and temperature of thermal treatment. Sol-gel was prepared by means of sonocatalysis, in order to reduce the amount of solvent and required time for the hydrolysis step. The composition of the material, as well as shape, size and distribution of AuNPs inside the silica matrix, were evaluated by spectroscopic and microscopic techniques. Furthermore, electrochemical tests allowed us to ascertain the good conductivity of the composite material and the electrocatalytic activity of AuNPs with respect to glucose and ascorbic acid oxidation. These tests demonstrated that the best performance has been obtained by the thermal reduction performed for 24 h at 150 °C, starting from the NaAuCl<sub>4</sub> precursor, with a 24:1 Si/Au molar ratio and a 1:1 graphite (g) : MTMOS (mL) ratio.

As for the second type of sol-gel electrodes, silica-based pellets containing copper nanoparticles (CuNPs), graphite and polystyrene used as binder, were proposed as disposable devices for the electrochemical oxidation of polyalcohols, namely glycerol. Graphite flakes provided both an adequate electrical conductivity for the use of the device in the electrochemical field and the right support to CuNPs, which are responsible for the electrocatalytic oxidation of glycerol. Si-based sol-gel was added to the formulation to enhance the performance of the composite material. The chemical composition of the material was optimized on the basis of the current intensity due to glycerol oxidation, taking advantage of a proper experimental design. The best performant composite had been prepared with 63 g of C<sub>gr</sub>+CuNPs (60:40% w/w), 27 mL of MTMOS and 10 g of PS, and it was characterized by spectroscopic and morphologic techniques, with the objective to define the structure-property relationship.

The last part of the research focused on different uses for KRY-AS, a secondary raw material obtained through the thermal transformation of cement-asbestos, and already applied in the production of concrete, clay bricks, ceramics, and plastic materials.

In the first of three applications discussed here, KRY-AS was used in the production of glass-ceramic frits intended for the manufacturing of porcelain stoneware slabs. Two novel frits were obtained by vitrifying KRY-AS together with minor amounts of natural raw materials as well as glass waste. The resulting frits were added to a standard ceramic body formulation (SCB) with the subsequent SCB: frits ratios (wt. %): 100:0, 99:1, 97:3 and 95:5. Phases composition, microstructure, technological and mechanical properties (water absorption (WA), linear firing shrinkage (LFS), modulus of rupture (MOR), stain resistance, colour parameters (CIELab)) were evaluated, and the results compared to

those of standard commercial frit and SCB. According to WA tests, the new products can be classified as Bla-type, which corresponds to porcelain ceramic tiles. Comparable or even improved technological properties were found between the SCB sample and the frit-bearing ones. More precisely, the addition of 5 wt. % of the novel frits led to better stain resistance as well as higher productivity due to the reduction of the LFS. Improved MOR (ca. 75 MPa compared to ca. 60 MPa for the standard) was also obtained.

Nowadays, inorganic natural and synthetic pigments are widely applied in decorations and coatings, and they are preferred to organic pigments because of their higher stability under chemical attacks, high temperatures and UV radiations. The second application of KRY·AS consisted in the synthesis of blue and black ceramic pigments; the amount of KRY·AS per sample was between 50 and 90 wt. %. Each pigment was synthesised considering the interaction of different variables: type and ratio of raw materials, temperature and time of the thermal treatment. For the blue pigments (A series) the aim was to synthesise Co-doped åkermanite ( $\text{Ca}_2\text{Co}_x\text{Mg}_{1-x}\text{Si}_2\text{O}_7$ ), mixing KRY·AS, MgO, SiO<sub>2</sub> and Co<sub>3</sub>O<sub>4</sub> (the latter used as chromophore) at different ratio treating the samples at 1200 or 1250 °C for 6 h. Two different types of black pigments have been prepared with Co<sub>3</sub>O<sub>4</sub> and MnO<sub>2</sub> as chromophores. In the first (B series) the stoichiometry was Co<sub>1.0</sub>Fe<sub>1.0</sub>Mn<sub>1.0</sub>O<sub>4</sub>, while in the second (C series) Cr<sub>2</sub>O<sub>3</sub> have been also added, with stoichiometry Co<sub>1.0</sub>Fe<sub>1.0</sub>Mn<sub>1.0</sub>Cr<sub>1.0</sub>, Co<sub>4.0</sub>Fe<sub>4.0</sub>Mn<sub>4.0</sub>Cr<sub>3.0</sub>, Co<sub>6.0</sub>Fe<sub>6.0</sub>Mn<sub>6.0</sub>Cr<sub>1.0</sub>, Co<sub>3.0</sub>Fe<sub>3.0</sub>Mn<sub>3.0</sub>Cr<sub>1.0</sub>. Different temperatures (1250 or 1300°C) and times (2, 4, 6, 12 h) were tested. All the samples have been characterised through UV-vis spectroscopy, colorimetry, mineralogical analysis and scanning electron microscopy. The best samples, regarding their colour, were obtained: i) in A series with Mg/Co molar ratio = 1, treated at 1250°C for 6 h, ii) in B series with stoichiometry Co<sub>1.0</sub>Fe<sub>1.0</sub>Mn<sub>1.0</sub>O<sub>4</sub> treated at 1250°C for 12 h, iii) C series, because of the use of Cr, possessed a green shade therefore the results have been discharged. To evaluate the stability and performance of the best pigments of A and B series, they have been tested as mass colorant for ceramic tiles, with successful results.

Lastly, KRY·AS was used in the preparation of foam glass, a multi-phase material with extremely low density, containing gaseous, amorphous and crystalline phases. In general, foam glass is prepared from silica sand or soda-lime glass and a foaming agent (coke, graphite or SiC) through a high temperature foaming process. Foam glass does not need highly pure raw materials. This study was focused on the manufacturing of foam glass from KRY·AS and glass waste (obtained from the processing of soda-lime glass (RG) in domestic recycling processes). This study consisted of four

phases. The first step was the investigation, in the preparation of the base mixture, of the effect of different ratios (wt. %) RG: KRY·AS (70:30, 60:40, 50:50) at different firing temperatures (950, 1000, 1050, 1100°C) with a soaking time of 6 min. The mixture with RG: KRY·AS at 60:40 (wt. %) was chosen as the best and successively optimised. Secondly, a flux agent ( $\text{Na}_2\text{CO}_3$  or  $\text{Li}_2\text{CO}_3$ ) was added, as partial substitute for RG, at the aforementioned mixture in order to obtain a sample with a higher amorphous content at a lower temperature and, consequently, a value of water absorption and open porosity near to zero. In the third step, we studied the addition of the foaming agent SiC, at different grits and amounts, to the defined composition (wt. %) RG: KRY·AS 55:40 with 5 wt. % of  $\text{Li}_2\text{CO}_3$ . Finally, twenty-seven samples have been prepared using the following conditions: composition RG: KRY·AS 55:40 (wt. %) with  $\text{Li}_2\text{CO}_3$  5 wt. %, differing in the amount of foaming agent, namely SiC-1500 (1, 2.5, 5 wt. %), firing temperature (1000, 1050, 1100°C) and soaking time (1, 6, 30 min). The final samples have been characterised and confronted to define the best conditions that lead to an AD near  $0.5 \text{ g/cm}^3$  (characteristic value for commercial foam glass), and to study the foaming process. The best samples were obtained with RG: KRY·AS 55:40, 5  $\text{Li}_2\text{CO}_3$  and SiC-1500 2.5 (wt. %), at 1100°C for 1 min.



## Riassunto

Il silicio (Si) è il 14° elemento della tavola periodica, è un metalloide tetravalente e un semiconduttore. Possiede un'alta affinità per l'ossigeno ed è quindi molto frequente che esso sia utilizzato in forma di minerali naturali, poiché essi compongono il 90% della crosta terrestre. Il silicio, la silice (SiO<sub>2</sub>) e i silicati sono frequentemente utilizzati come materiali da costruzione come il cemento, i mattoni, i materiali ceramici e i materiali refrattari (smalti e ceramiche); SiO<sub>2</sub> è inoltre utilizzato per produrre vetro e cristalleria. Infine, un'altra applicazione sono i polimeri sintetici contenenti Si, C, O, e H, tra i quali troviamo i siliconi o il sol-gel a base siliconica.

Questa tesi riporta diverse applicazioni di materiali a base di silicio: i) un Ba-silicato dopato con elementi di terre rare, usato come pigmento fosforescente ii) elettrodi a base sol-gel preparati con il polisilossano metiltrimetossilano (MTMOS), e nanoparticelle metalliche (MeNPs) con diverse applicazioni elettrochimiche, iii) cemento-amianto inertizzato tramite trattamento termico, chiamato KRY-AS, riciclato in fritte per la produzione di gres porcellanato per grandi formati, pigmenti ceramici blu e neri, e vetro schiuma.

Il pigmento fotoluminescente di formula Ba<sub>5</sub>Si<sub>8</sub>O<sub>21</sub>:Eu<sup>2+</sup>,Dy<sup>3+</sup> è stato sintetizzato, valutando gli effetti di: diversi precursori, la composizione del crogiolo, gli agenti fondenti, i dopanti e la temperatura di sintesi. I campioni sono stati caratterizzati tramite analisi elementare, cinetica, mineralogica (qualitative e quantitative) e morfologica. Le osservazioni effettuate riportano l'importanza di Na<sub>2</sub>SiO<sub>3</sub>, BaCO<sub>3</sub> e NH<sub>4</sub>Cl come precursori per ridurre la temperatura e il tempo della sintesi. L'atmosfera riducente è stata prodotta con carbone purificato, il quale è più economico e dà risultati simili rispetto alla tradizionale miscela gassosa H<sub>2</sub>/N<sub>2</sub>. In conclusione, è stato ottenuto un pigmento fosforescente con maggiore durata della luminosità (long persistent phosphorescence) dopo una sintesi di 6h in un crogiolo di quarzo a 1100°C con rapporti Ba/Si = 0.7, Eu/Si = 2.8 × 10<sup>-3</sup> e Dy/Si = 3.6 × 10<sup>-3</sup>.

Per quanto riguarda gli elettrodi sol-gel, il primo lavoro si basa su di una sintesi one-pot (contemporanea) di elettrodi contenenti sol-gel, grafite e nanoparticelle di oro (AuNPs). In alternativa alla sintesi tradizionale, che prevede, rispetto alla matrice silicatica, la preparazione a parte di AuNPs, qui le nanoparticelle sono state ottenute direttamente all'interno del sol-gel, durante la sua formazione. Per poterle sintetizzare sono stati applicati due diversi metodi di riduzione (chimico e termico) di altrettanti precursori dell'oro (NaAuCl<sub>4</sub> or HAuCl<sub>4</sub>). Per raggiungere

le caratteristiche ricercate per il materiale sono stati valutati diversi parametri sperimentali: il rapporto molare Si/Au, il rapporto grafite (g) : polisilossano (mL), la natura chimica del precursore dell'oro e del riducente, la durata e la temperatura del trattamento termico. Il sol-gel è preparato tramite sono-catalisi, utilizzata per ridurre la quantità di solvente e tempo necessari per lo step di idrolisi. Le caratterizzazioni, con tecniche di spettroscopia e microscopia, sono effettuate per valutare la composizione del materiale e la forma, dimensione e distribuzione delle AuNPs nella matrice silicatica. Inoltre, i test elettrochimici hanno permesso di accertarsi della buona conduttività del materiale e dell'attività elettrocatalitica delle AuNPs rispetto all'ossidazione di glucosio, acido ascorbico e dopamina. Questi test hanno dimostrato che le performance migliori sono state ottenute tramite riduzione termica attuata per 24 h a 150°C, a partire dal precursore NaAuCl<sub>4</sub>, con un rapporto molare Si/Au di 24:1 e un rapporto grafite (g) : MTMOS (mL) di 1:1.

Il secondo tipo di elettrodi sono pastiglie a base sol-gel contenenti nanoparticelle di rame (CuNPs), grafite e polistirene, utilizzato come legante. La proposta di utilizzo è rivolta all'applicazione nell'ambito dei device monouso per l'ossidazione elettrochimica di polialcoli, nello specifico il glicerolo. La polvere di grafite ha permesso di ottenere conduttività elettrica adeguata, oltre che a dare il giusto supporto alle CuNPs, che sono le effettive responsabili dell'ossidazione elettrocatalitica del glicerolo. Il sol-gel a base Si è stato aggiunto alla formulazione per migliorare le performance del materiale composito. La composizione chimica del materiale è stata ottimizzata sulla base dell'intensità di corrente del picco di ossidazione del glicerolo, utilizzando un appropriato disegno sperimentale. Il composto che ha mostrato la migliore performance è stato preparato con 63 g di C<sub>gr</sub>+CuNPs (60:40% w/w), 27 mL di MTMOS e 10 g di PS, ed è successivamente stato caratterizzato tramite tecniche spettroscopiche e microscopiche, con l'obiettivo di definire la relazione tra la struttura dell'elettrodo e le sue proprietà.

L'ultima parte della ricerca è basata su diversi utilizzi del KRY·AS, una materia prima seconda ottenuta tramite trasformazione termica del cemento-amianto, già utilizzata nella produzione di cemento, mattoni d'argilla, ceramiche e materie plastiche.

Nella prima di tre applicazioni, il KRY·AS è stato utilizzato per la produzione di fritte ceramiche con l'obiettivo di preparare gres porcellanato per grandi formati. Due nuove fritte sono state ottenute tramite vetrificazione di KRY·AS, scarti di vetro e minore quantità di materie prime naturali. Le fritte risultanti sono state aggiunte ad un atomizzato (SCB) in rapporto in peso SCB: fritta pari a 100:0,

99:1, 97:3 and 95:5. Sono state valutate le proprietà tecnologiche e meccaniche (assorbimento di acqua (WA), ritiro (LFS), modulo di rottura (MOR), resistenza alla macchia e parametri di colore (CIELab)), la composizione delle fasi e la microstruttura dei provini ottenuti, e i risultati sono stati confrontati con quelli ottenuti a partire dai campioni ottenuti con una fritta commerciale o solo SCB. Tramite i risultati di WA è stato possibile classificare il prodotto come tipo Bla, cioè gres porcellanato. Le proprietà tecnologiche risultano comparabili o in alcuni casi migliori nei confronti effettuati con campioni preparati con una fritta commerciale e con solo SCB. Più precisamente è risultato che le nuove fritte contenenti KRY·AS apportano una migliore resistenza alla macchia e ad un minore LFS, dando quindi la possibilità di avere una maggiore produttività. Inoltre, anche i valori di MOR sono stati migliorati passando da 60 MPa con solo atomizzato a 75 MPa per quelli contenenti le fritte.

Al giorno d'oggi i pigmenti inorganici naturali e sintetici sono ampiamente applicati per decorazioni e ricoprimenti, e il loro utilizzo è preferito a quello dei pigmenti organici per la loro maggiore stabilità agli attacchi chimici, alte temperature e radiazioni UV. La seconda applicazione del KRY·AS è stata quindi quella di sintetizzare dei pigmenti di colore blu e nero, contenenti una quantità di KRY·AS variabile tra 50 e 90 wt. %. Ciascun pigmento è stato sintetizzato considerando l'interazione di diverse variabili: la tipologia di materie prime, il loro rapporto, la temperatura e il tempo del trattamento termico. Per quanto riguarda il pigmento blu (serie A) lo scopo era di sintetizzare åkermanite dopata con Co ( $\text{Ca}_2\text{Co}_x\text{Mg}_{1-x}\text{Si}_2\text{O}_7$ ), miscelando KRY·AS, MgO, SiO<sub>2</sub> e Co<sub>3</sub>O<sub>4</sub> (quest'ultimo usato come cromoforo) in diversi rapporti, trattando i campioni a 1200 o 1250°C per 6 h. Sono stati sviluppati due diversi tipi di pigmenti neri, utilizzando Co<sub>3</sub>O<sub>4</sub> and MnO<sub>2</sub> come cromofori. Nei primi (serie B) la stechiometria del composto era Co<sub>1.0</sub>Fe<sub>1.0</sub>Mn<sub>1.0</sub>O<sub>4</sub>, mentre nei secondi (serie C) è stato aggiunto anche Cr<sub>2</sub>O<sub>3</sub> e le stechiometrie valutate sono state Co<sub>1.0</sub>Fe<sub>1.0</sub>Mn<sub>1.0</sub>Cr<sub>1.0</sub>, Co<sub>4.0</sub>Fe<sub>4.0</sub>Mn<sub>4.0</sub>Cr<sub>3.0</sub>, Co<sub>6.0</sub>Fe<sub>6.0</sub>Mn<sub>6.0</sub>Cr<sub>1.0</sub>, Co<sub>3.0</sub>Fe<sub>3.0</sub>Mn<sub>3.0</sub>Cr<sub>1.0</sub>. I campioni sono stati testati a diverse temperature (1250 e 1300°C) e tempi (2, 4, 5, 12 h). I campioni sono stati tutti analizzati tramite spettroscopia UV-vis, colorimetria, analisi mineralogia e microscopia elettronica a scansione. I campioni migliori, per quanto riguarda il colore, sono stati ottenuti: i) nella serie A con un rapporto molare Mg/Co pari a 1, trattandolo a 1250°C per 6 h, ii) nella serie B con stechiometria Co<sub>1.0</sub>Fe<sub>1.0</sub>Mn<sub>1.0</sub>O<sub>4</sub>, trattandolo a 1250°C per 12 h, iii) la serie C, a causa dell'utilizzo del Cr, possedeva una colorazione verde, di conseguenza i risultati sono stati scartati. Per valutare la stabilità e le performance dei pigmenti migliori delle serie A e B, questi sono stati testati nella colorazione a tutta massa di provini ceramici, con ottimi risultati.

Per ultimo il KRY·AS è stato utilizzato per la preparazione di vetro schiuma, una materiale multifase a bassissima densità, contenete una fase gassosa, una fase amorfa e una fase cristallina. Generalmente, il vetro schiuma è formato da sabbia silicea o vetro soda-lime e da un agente schiumante (carbone, grafite o SiC), che vengono fatti reagire tramite un processo ad alta temperatura. I vetri schiuma non necessitano di materie prime pure per la loro sintesi. Lo studio in oggetto si concentra sulla sintesi di vetro schiuma a partire da KRY·AS e scarti di vetro provenienti dal riciclo di vetro soda-lime domestico (RG). La ricerca presenta quattro step. Il primo step è stato lo studio degli effetti, nella preparazione della miscela di base, di diversi rapporti in peso tra RG e KRY·AS (70:30, 60:40, 50:50) a diverse temperature di cottura (950, 1000, 1050, 1100°C) con un'isoterma di 6 min. La miscela RG: KRY·AS con rapporti 60:40 (wt. %) è stata scelta come base per essere poi successivamente ottimizzata. Secondariamente, è stato aggiunto un agente fondente in diverse quantità ( $\text{Na}_2\text{CO}_3$  or  $\text{Li}_2\text{CO}_3$ ), come sostituto parziale di RG, alla miscela precedentemente nominata, con l'obiettivo di ottenere un campione con un quantitativo maggiore di fase amorfa ad una temperatura inferiore, quindi avere valori di assorbimento di acqua e porosità aperte prossimi allo zero. Il terso step è stato lo studio della grana e della quantità dell'agente schiumante, in questo caso SiC, aggiunto alla miscela scelta con rapporti RG: KRY·AS 55:40 e 5  $\text{Li}_2\text{CO}_3$  (wt. %). Per concludere sono stati preparati ventisette campioni con composizione RG: KRY·AS 55:40 e 5  $\text{Li}_2\text{CO}_3$  (wt. %), nei quali sono stati variati la quantità di agente schiumante, SiC-1500 (1, 2.5, 5 wt. %), la temperatura di lavoro (1000, 1050, 1100°C) and il tempo alla massima T (1, 6, 30 min) del processo di cottura. I campioni finali sono stati caratterizzati e confrontati per definire le condizioni migliori che portano ad una densità apparente (AD) vicina a  $0.5 \text{ g/cm}^3$  (valore AD per un vetro schiuma commerciale), e per studiare il processo di foaming. I campioni migliori sono stati preparati con RG: KRY·AS 55:40, 5  $\text{Li}_2\text{CO}_3$  e SiC-1500 2.5 (wt. %), a 1100°C per 1 min.

## Introduction

### 1.1. Silicon characteristics, history and most abundant compounds

Silicon (Si) is the second most abundant element in the earth's crust after oxygen, and, due to its diffusion and properties, it is extensively used in numerous application areas. It is so prominent that an entire valley, the Silicon Valley in California (USA), is named after it. In the periodic table, Si is the 14<sup>th</sup> element, and its name derives from the Latin *silicis* or *silex*, which means "hard stone", "flint" or "pebble-stone". It is classified as a metalloid and it has a diamond-like octahedral crystalline structure, it is very brittle, and it has a remarkable metallic lustre, as can be seen from **Figure 1**. Aside from some cases of bivalent compounds, silicon is mostly tetravalent, and in general it is purely electropositive [1].



**Figure 1.** Piece of pure silicon. [2]

The most common Si-compound is silica ( $\text{SiO}_2$ ), which has been known and employed as tool by humans since ancient times. Earlier than 1500 BCE, Egyptians and Phoenicians were already turning sand into glass, in addition to using other forms of silica, such as rock crystal. It was only in 1824 that the chemists were able to isolate pure silicon, after numerous attempts. Jöns Jacob Berzelius, a Swedish chemist, worked on heating potassium fluorosilicate with potassium, obtaining silicon powder contaminated with potassium silicide, which was removed with water. Crystalline elemental silicon was finally produced through electrolysis in 1854 [3].

Because of its extreme reactivity, pure silicon cannot be found in nature, although it is found in silicates, mostly combined with oxygen and in minor part with other elements (such as aluminium, magnesium, calcium, sodium, potassium, or iron). As previously reported, silica and silicates are regular components of the earth's crust and mantle, but they can be also found in the atmosphere, waters, plants and even in animal bones and tissues [1].

The tetrahedral structure of the orthosilicate anion helps to create different types of crystalline silicate of pure silica, such as quartz and cristobalite. With the addition of other elements, it produces other types of mineral, such as clays, feldspar, olivine, pyroxene, amphiboles, micas, and zeolites. Silicon dioxide is also the main structure of amorphous or seemingly amorphous minerals as agate and opal. The natural silicates are characterized by their abundance, wide distribution, and structural and compositional complexity [4, 5].

## **1.2. Application of silicon and its compound**

The fact that Si is a semiconductor is among the most important characteristics of this element, and because of that it is widely applied in the electronics and technology sectors. Specifically, it can be used in the form of silicon wafers, created with the addition of other elements such as boron, arsenic or phosphorous; they are the basic material for diodes, liquid crystal displays, transistors, computer chips and other devices.

Silica and various silicate are the principal components of numerous building materials such as concrete, bricks, ceramic materials, and refractory materials as enamels and pottery. SiO<sub>2</sub> is also the raw material of glass and glassware, as well as ceramic bodies [3, 6].

Synthetic organosilicon compounds are one last application of silicon, they are also composed of carbon, oxygen and hydrogen. These molecules are crosslinkers in the preparation of silicones or polysiloxane polymers [7,8]. They are characterised by chemical inertia and stability at high temperature, which has led to their frequent applications in lubrication, waterproof compounds and varnishes [9].

This thesis is a collection of different applications of silicon-based material: a Ba-silicate doped with rare earth elements used as phosphorescent pigment; sol-gel electrodes prepared with a specific organosilicon compound, namely methyltrimethoxysilane (MTMOS), and metal nanoparticles (MeNPs), with different electrochemical application; thermally treated cement-asbestos, named KRY-AS, recycled in frits for porcelain stoneware slabs, blue and black ceramic pigments and foam glass. The following paragraphs are a general introduction to these applications, which will be presented in more detail in further chapters.

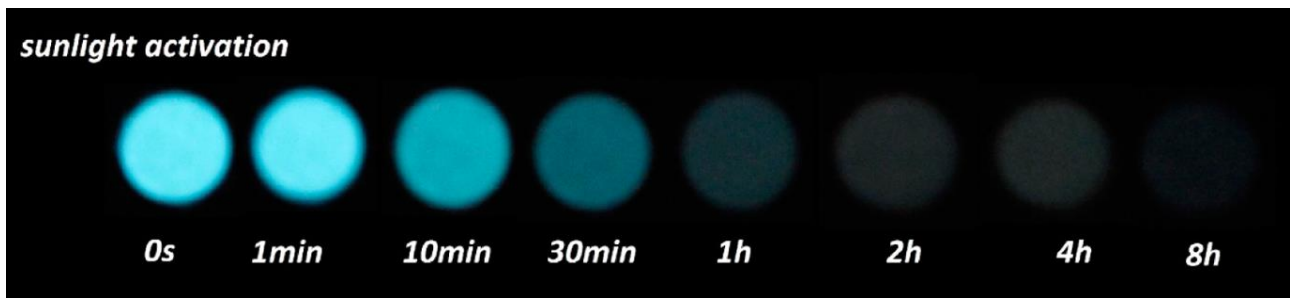
### 1.3. Alkaline-earth silicate phosphors

Photoluminescence consists in the emission of light from a material through the excitation of its electronic states with electromagnetic radiation [10, 11]. The emitted light, or afterglow, is caused by the electrons decay from excited states or the formation of holes caused by the energy transfer from the radiation source [10, 12-17]. The absorption of energy can occur in the UV or visible regions of the electromagnetic spectrum, while the emission occurs in the visible region. These types of materials are generally inorganic and are called photoluminescent pigments or phosphors [11, 18, 19]. Some of the afterglow phosphors emit using the mechanism of phosphorescence, consequently their light emission persists after the removal of the excitation source. Phosphors with a very long afterglow emission (in some cases even a whole day) are defined long persistent phosphor (LPP).

ZnS:Cu,Co is one of the most studied LPP and the first commercial application of phosphors, specifically in watch dials [20]. In the last thirty years, different types of photoluminescent pigments have been discovered, each with better stability and efficiency compared to ZnS:Cu,Co [21-23]. Among them, the best compounds are alkaline-earth metal (Ca, Sr, Ba) aluminates or silicates doped with rare earth ions [22-25]. Silicate phosphors have gathered more attention in the last few years because of their better synthesis conditions and physical-chemical properties in regard to the aluminate LPP [26-32]. Moreover, they have a wider range of colours, for example green [33], red [34], white [35], and yellow [26], though the duration of the emission is lower than the aluminate phosphors.

During the years, the use of LPP has widely increased, mostly because they are photoelectric conversion materials, which can be applied to night vision, optical storage media, solar energy utilization, and in vivo-imaging. [36-42].

Ba-silicates phosphors doped with  $\text{Eu}^{2+}$  and other rare earth ions have attracted considerable interest as well, due to their luminescent properties. Some examples are  $\text{Eu}^{2+}$  doped  $\text{BaSi}_2\text{O}_5$  [43],  $\text{Ba}_2\text{Si}_3\text{O}_8$  [44],  $\text{Ba}_2\text{SiO}_4$  [45], and  $\text{Ba}_3\text{SiO}_5$  [26], which have a green emission, or  $\text{Eu}^{2+}$  and Dy  $3+$  doped  $\text{Ba}_4(\text{Si}_3\text{O}_8)_2$  [27] and  $\text{Ba}_5\text{Si}_8\text{O}_{21}$  (**Figure 2**) [28], which are stable luminophores even in water and can be activated by sunlight.

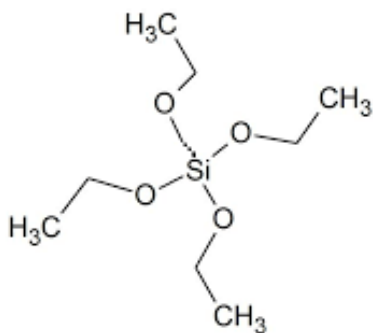


**Figure 2.** Emission of  $Ba_5Si_8O_{21}:Eu^{2+}, Dy^{3+}$  phosphor after sunlight activation for 10 min, from Wang et al, 2015 [28]

The research developed for this thesis is an improvement of  $Ba_5Si_8O_{21}, Eu^{2+}, Dy^{3+}$  [28] and it is reported in Chapter 1 [46].

#### 1.4. Sol-gel and its application in chemistry

Interest in the sol-gel process began in the middle of the XIX century, when the hydrolysis of tetraethyl orthosilicate (TEOS, **Figure 3**) under acidic conditions was observed [47-49].



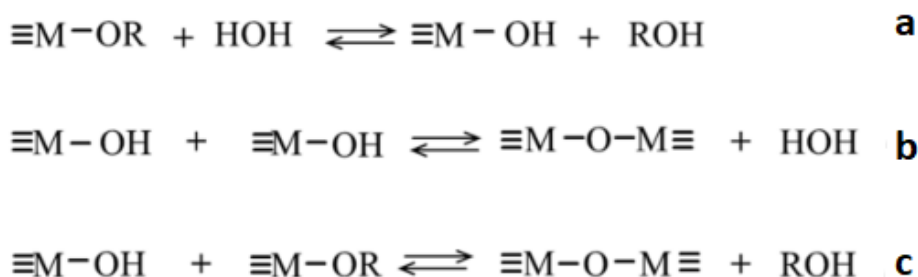
**Figure 3.** TEOS chemical structure.

During the years, the sol-gel process has become a standard production technique used to transform an alkoxide in different types of three-dimensional materials; these possess the reactivity of its organic components and a glass-like aspect. [50-54] This process allows to create homogeneous porous materials using lower processing temperatures compared with traditional glass melting techniques or ceramic powder methods. [55-60] The traditional sol-gel process consists of a sequence of reactions between the organometallic precursor and alcohol, activated with an acid or basic catalyst. It is divided into three main phases:

1. *Hydrolysis and polycondensation:* the hydrolysis reaction occurs through a nucleophilic substitution mechanism, which results in the replacement of an alkoxy group with a hydroxyl one (**Figure 4 a**). The following polycondensation takes place when the partially hydrolysed



- alkoxide reacts with another OH-bearing species (**Figure 4 b**) or with alkoxy group (**Figure 4 c**). At the end of this phase, numerous clusters can be found inside the solution, which create a colloidal suspension of solid particles ( $\varnothing = 1-100$  nm) called sol. [61-64]
2. *Gelation*: the interaction between these cluster creates a three-dimensional polymeric network called gel. [62]
  3. *Aging and drying*: to obtain the final product it is necessary to remove the liquid retained in the pores formed inside the gel. This occurs through thermal evaporation, leaving the sample at ambient temperature or drying it between 100 and 180°C. [8]

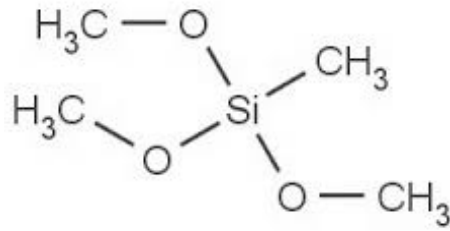


**Figure 4.** The three main reaction steps occurring in the sol-gel process of an alkoxide  $\text{M}(\text{OR})_4$ , (a) hydrolysis of an alkoxy group (b) condensation of two OH-bearing species; (c) mixed condensation of a -OH group and an alkoxy group bearing species. [65]

By controlling the parameters affecting the various steps of the sol-gel process, the physico-chemical properties of the resulting material can be changed, obtaining powder, film and low-density silica monoliths (aerogel and xerogel). [62, 66-68]

Among the possible different applications, our attention focused on the field of electrochemistry, specifically in the creation of sol-gel electrodes applied as amperometric sensors. The characteristic porosity and chemical properties of sol-gel make it a perfect support for different sensing agents, for example enzymes or metal nanoparticles. [69-72] Moreover, in order to ensure an electrical conduction through the electrode, it is necessary to mix an appropriate amount of graphite inside the silica-based matrix.

Chapter 2 [73] and Chapter 3 describe the application of a sol-gel matrix prepared with methyltrimethoxysilane (MTMOS) (**Figure 5**) in manufacturing amperometric sensors. One case illustrates the addition of graphite and gold nanoparticles (AuNPs), whereas a second case shows the use of copper nanoparticle (CuNPs).



**Figure 5.** MTMOS structure.

### 1.5. KRY-AS: thermally treated cement asbestos used as secondary raw material

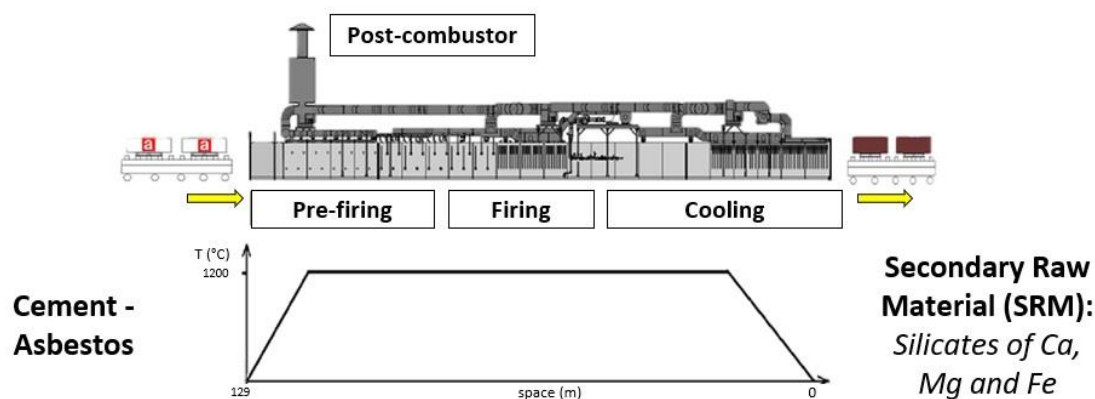
Driven by the necessity to find alternative solutions to landfill in order to dispose of hazardous and non-hazardous waste, the European Commission issued the European Directive 2008/98/EC of 19-11-2008, stressing the necessity to recycle said wastes as secondary raw materials.

In Italy, this further developed into the Italian D.Lgs 152, 03-04-2006 “Codice ambientale” (Environmental Code).

Among the hazardous waste, asbestos-containing materials (ACM) are one of the most diffused and, although asbestos have been banned in Italy since 1992, they can still be easily found in the environment. Approximately 2 billion m<sup>2</sup> of cement asbestos (CA), a specific type of ACM, still covers private and public buildings and industrial sites. [74]

A conclusive solution to dispose of these wastes can be found in the inertization of the ACM via thermal transformation, a procedure made possible through the Italian Decree no. 248 (D.M. 19/07/2004). [75-79] This solution relies upon the scientific evidence that all asbestos minerals transform into stable crystalline silicates in the inertization process. [78, 80-83]

Recently, an industrial process for the thermal destruction of ACM, and CA in particular, has been developed and patented (**Figure 6**). [78,84] Sealed packages of CA slates undergo prolonged annealing in the temperature range 1200–1300°C, during which asbestos minerals (both serpentine and amphibolite) are transformed and crystallised into newly formed cement phases such as larnite (Ca<sub>2</sub>SiO<sub>4</sub>), ferrite (ideally Ca<sub>4</sub>Al<sub>2</sub>Fe<sub>2</sub>O<sub>10</sub>) and Al-, Ca-, Mg-rich silicates for example åkermanite (Ca<sub>2</sub>MgSi<sub>2</sub>O<sub>7</sub>), and merwinite (ideally Ca<sub>3</sub>MgSi<sub>2</sub>O<sub>8</sub>). [85-87]



**Figure 6.** KRY·AS industrial process

This newly formed secondary raw material has been named KRY·AS (from Greek, *krústallos* and *ásbeston*, crystal from asbestos), and it is mainly composed of  $\text{SiO}_2$  and  $\text{CaO}$  (about 40 wt. % each) with a chemical nature comparable to Mg-rich clinker. [78] Different investigations have confirmed that this is a non-hazardous product, safe from any toxic phases present in the original CA. [88-91]

KRY·AS can be successfully recycled in medium-high percentage (10-40 wt. %) in different products: clay bricks, glasses, glass–ceramics, stoneware ceramics, ceramic pigments, plastic materials, and cement for commercial concrete. [78]

The applications of KRY·AS studied during my PhD years will be fully described in the last three chapters of the thesis and they are: frits of stoneware ceramic slabs (Chapter 4, paper Ligabue et al, 2019 [91]); blue and black ceramic pigments (Chapter 5); and foam glass (Chapter 6, this work have been carried out at the Instituto de Tecnología Cerámica, Universitat Jaume I, Castellón de la Plana, Spain).

## 1.6. References

- [1] P. Jutzi, U. Schubert, *Silicon chemistry: from the atom to extended systems*, eds. Wiley-VCH, Weinheim, Germany (2003).
- [2] <https://www.britannica.com/science/silicon/Uses>. Accessed 3<sup>rd</sup> December 2020.
- [3] N. Spomer, S. Holl, L. Zherlitsyna, F. Maysamy, A. Frost, N. Auner, *Amorphous Silicon: New Insights into an Old Material*, *Chem. Eur. J.* 21 (2015) 5600–5616.
- [4] A.F. Holleman, E. Wiberg, N. Wiberg, *Inorganic Chemistry (1<sup>st</sup> edition)*, eds. M. Eagleson, W. Brewer, San Diego/Berlin: Academic Press/De Gruyter (2001).

- [5] H. Bock, Fundamentals of silicon chemistry: molecular states of silicon-containing compounds. *Angew. Chem. Int. Ed.* 28 (1989) 1627–1650.
- [6] M.I. Ojovan, Glass formation in amorphous SiO<sub>2</sub> as a percolation phase transition in a system of network defects, *JETP Lett.* 79 (2004) 632–634.
- [7] J.Y. Corey, in *The Chemistry of Organic Silicon Compounds, Part 1*, eds. S. Patai, Z. Rappoport, Chichester: Wiley (1989) 1-57.
- [8] L.L. Hench, J.K. West, *The Sol-Gel Process*, *Chem. Rev* 90 (1990) 33-72.
- [9] M. Tolinski, Additives for Polyolefins, Chapter 15 in *Crosslinking*, eds. M. Tolinski, William Andrew Publishing (2009) 215-220.
- [10] G. Blasse, B.C. Grabmaier, *Luminescent Materials*; eds. Springer, Berlin/Heidelberg, Germany, (1994).
- [11] P.E.A. Lenard, F. Schmidt, R.Tomaschek, Phosphoreszenz und fluoreszenz, Chapter 23 in: *Handbuch der Experimentalphysik*, Akademie Verlagsgesellschaft, Leipzig, Germany, (1928).
- [12] F. Clabau, X. Rocquefelte, S. Jobi, P. Deniard, M.-H. Whangbo, A. Garcia, T. Le Mercier, Mechanism of Phosphorescence Appropriate for the Long-Lasting Phosphors Eu<sup>2+</sup>-Doped SrAl<sub>2</sub>O<sub>4</sub> with Codopants Dy<sup>3+</sup> and B<sup>3+</sup>, *Chem. Mater.* 17 (2005) 3904–3912.
- [13] M.W. Yen, S. Shionoya, H. Yamamoto, *Fundamentals of Phosphors*, eds. Taylor& Francis Group, CRC Pres (2007).
- [14] E.L. Wehry, B.W. Rossiter, R.C. Baetzold, *Physical Methods of Chemistry, Vol. 8*, eds. Wiley, New York (1993) 109.
- [15] Q. Guanming, C. Yongjie, C. Jingqiang, G. Xiujuan, W. Hui, S. Bo, Synthesis of Long Afterglow Phosphors Doped B SrAl<sub>2</sub>O<sub>4</sub>:Eu<sup>2+</sup>, Dy<sup>3+</sup> and Its Luminescent Properties, *J. Rare Earths* 25 (2007) 86-89.
- [16] C. Zhang, C. Lin, C. Li, Z. Quan, X. Liu, J. Lin, Enhanced Luminescence of BPO<sub>4</sub> by Mixing with SiO<sub>2</sub> and Al<sub>2</sub>O<sub>3</sub> *J. Phys. Chem.* 112 (2008) 2183-2192.
- [17] H.W. Leverenz, *An Introduction to Luminescence of Solids*, eds. John Wiley & Sons, New York, (1949).
- [18] W. Lehmann, Activators and co-activators in calcium sulfide phosphors, *J. Lumin.* 5 (1972) 87–107.
- [19] G.F.J. Garlick, D.E. Mason, Electron Traps and Infrared Stimulation of Phosphors, *J. Electrochem. Soc.* 96 (1949) 90–103.

- [20] W. Hoogenstraaten, H.A. Klasens, Some properties of zinc sulfide activated with copper and cobalt, *J. Electrochem. Soc.* 100 (1953) 366–375.
- [21] Y. Lin, Z. Tang, Z. Zhang, C.W. Nan, Anomalous luminescence in  $\text{Sr}_4\text{Al}_{14}\text{O}_{25}:\text{Eu},\text{Dy}$  phosphors, *Appl. Phys. Lett.* 81 (2002) 996–998.
- [22] L.C.V. Rodrigues, H.F. Brito, J. Hölsä, R. Stefani, M.C.F.C. Felinto, M. Lastusaari, T. Laamanen, L.A.O.J. Nunes, Discovery of the Persistent Luminescence Mechanism of  $\text{CdSiO}_3:\text{Tb}^{3+}$ , *Phys. Chem. C* 116 (2012) 11232–11240.
- [23] T. Lin, Z. Tang, Z. Zhang, X. Wang, J. Zhang, Preparation of a new long afterglow blue-emitting  $\text{Sr}_2\text{MgSi}_2\text{O}_7$ -based photoluminescent phosphor, *J. Mater. Sci. Lett.* 20(16) (2001) 1505–1506.
- [24] T. Matsuzawa, Y. Aoki, N. Takeuchi, Y.J. Murayama, A New Long Phosphorescent Phosphor with High Brightness,  $\text{SrAl}_2\text{O}_4:\text{Eu}^{2+},\text{Dy}^{3+}$  *Electrochem. Soc.* 143 (1996) 2670–2673.
- [25] X. Yang, T.S. Tiam, X. Yu, H.V. Demir, X.W. Sun, Europium (II)-Doped Microporous Zeolite Derivatives with Enhanced Photoluminescence by Isolating Active Luminescence Centers, *ACS Appl. Mater. Interfaces* 3 (2011) 4431–4436.
- [26] K.P. Joung, A.L. Mi, J.C. Kyoung, H.K. Chang, Luminescence characteristics of yellow emitting  $\text{Ba}_3\text{SiO}_5:\text{Eu}^{2+}$  phosphor, *J. Mater. Sci.* 40 (2005) 2069–2071.
- [27] Y. Gong, Y. Wang, Y. Li, X. Xu, W. Zeng, Fluorescence and phosphorescence properties of new long-lasting phosphor  $\text{Ba}_4(\text{Si}_3\text{O}_8)_2:\text{Eu}^{2+},\text{Dy}^{3+}$ , *Opt. Express* 19 (2011) 4310–4315.
- [28] P. Wang, X. Xu, D. Zhou, X. Yu, J. Qiu, Sunlight Activated Long-Lasting Luminescence from  $\text{Ba}_5\text{Si}_8\text{O}_{21}:\text{Eu}^{2+},\text{Dy}^{3+}$  Phosphor, *Inorg. Chem.* 54 (2015) 1690–1697.
- [29] Z. Xia, Y. Zhang, M.S. Molokeev, V.V. Atuchin, Y. Luo, Linear structural evolution induced tunable photoluminescence in clinopyroxene solid-solution phosphors, *Sci. Rep.* 3 (2013) 3310–3317.
- [30] W. Yi, L.C. Che, Q. Zewei, M. Maxim, S. Atuchin, V. Victor, C. Ting-Shan, L. Yujun, L. Jun, L. Guogang, Structural evolution induced preferential occupancy of designated cation sites by  $\text{Eu}^{2+}$  in  $\text{M}_5(\text{Si}_3\text{O}_9)_2$  (M = Sr, Ba, Y, Mn) phosphors, *RSC Adv.* 6 (2016) 57261–57265.
- [31] Y. Eagleman, E. Bourret-Courchesne, S.E. Derenzo, Fellow, Investigation of  $\text{Eu}^{2+}$  Doped Barium Silicates as Scintillators, *IEEE Trans. Nuclear Sci.* 59 (2012) 479–486.
- [32] M. Yamaga, Y. Masui, S. Sakuta, N. Kodama, K. Kaminaga, Radiative and nonradiative decay processes responsible for long-lasting phosphorescence of  $\text{Eu}^{2+}$ -doped barium silicates, *Phys. Rev. B* 71 (2005) 205102 (1-7).
- [33] X. Zhang, X. Tang, J. Zhang, M. Gong, An efficient and stable green phosphor  $\text{SrBaSiO}_4:\text{Eu}^{2+}$  for light-emitting diodes, *J. Lumin.* 130 (2010) 2288–2292.

- [34] M. Nazarov, Luminescent materials and applications, *Mater. Sci. Chem.* 6 (2016) 41–74.
- [35] Y. Li, M. Geceviciusa, J. Qiu, Long persistent phosphors—from fundamentals to applications, *Chem. Soc. Rev.* 45 (2016) 2090–2136.
- [36] F. Liu, W. Yan, Y. J. Chuang, Z. Zhen, J. Xie, Z. Pan, Photostimulated near-infrared persistent luminescence as a new optical read-out from Cr<sup>3+</sup>-doped LiGa<sub>5</sub>O<sub>8</sub>, *Sci. Rep.* 3 (2013) 1554–1563.
- [37] B. Wang, H. Lin, Y. Yu, D. Chen, R. Zhang, J. Xu, Y. J. Wang, Ce<sup>3+</sup>/Pr<sup>3+</sup>: YAGG: A Long Persistent Phosphor Activated by Blue-Light, *Am. Ceram. Soc.* 97 (2014) 2539–2545.
- [38] T. Maldiney, A. Lecointre, B. Viana, A.I. Bessière, M. Bessodes, D. Gourier, C. Richard, D.J. Scherman, Controlling Electron Trap Depth To Enhance Optical Properties of Persistent Luminescence Nanoparticles for In Vivo Imaging, *Am. Chem. Soc.* 133 (2011) 11810–11815.
- [39] T. Maldiney, A. Bessière, J. Seguin, E. Teston, S.K. Sharma, B. Viana, A. J. J. Bos, P. Dorenbos, M. Bessodes, D. Gourier, D. Scherman, C. Richard, The in vivo activation of persistent nanophosphors for optical imaging of vascularization, tumours and grafted cells, *Nat. Mater.* 13 (2014) 418–426.
- [40] X. Jian, T. Setsuhisa, Persistent luminescence instead of phosphorescence: History, mechanism, and perspective, *J. Lumin.* 205 (2019) 581–620.
- [41] S. Kamei, Y. Kojima, N. Nishimiya, Preparation and fluorescence properties of novel red-emitting Eu<sup>3+</sup>-activated amorphous alkaline earth silicate phosphors, *J. Lumin.* 130 (2010) 2288–2292.
- [42] L. Mishra, A. Sharma, A.K. Vishwakarma, K. Jha, M. Jayasimhadri, B.V. Ratnam, K. Jang, A.S. Rao, R.K. Sinha, White light emission and color tunability of dysprosium doped barium silicate glasses, *J. Lumin.* 169 (2016) 121–127.
- [43] J.H. Park, J.S. Kim, J.T. Kim, Luminescent properties of BaSi<sub>2</sub>O<sub>5</sub>:Eu<sup>2+</sup> phosphor film fabricated by spin-coating of Ba-Eu precursor on SiO<sub>2</sub> glass, *J. Opt. Soc. Korea* 18 (2014) 45–49.
- [44] F. Xiao, Y. Xue, Q. Zhang, Bluish-green color emitting Ba<sub>2</sub>Si<sub>3</sub>O<sub>8</sub>:Eu<sup>2+</sup> ceramic phosphors for white light-emitting diodes, *Spectrochim. Acta A: Mol. Biomol. Spectrosc.* 74 (2009) 758–760.
- [45] M. Zhang, J. Wang, Q. Zhang, W. Ding, Q. Su, Optical properties of Ba<sub>2</sub>SiO<sub>4</sub>:Eu<sup>2+</sup> phosphor for green light-emitting diode (LED), *Mater. Res. Bull.* 42 (2007) 33–39.
- [46] A. Silvestri, M.L. Ligabue, G. Malavasi, G. Lusvardi, Preparation and Luminescence Properties of Ba<sub>5</sub>Si<sub>8</sub>O<sub>21</sub> Long Persistent Phosphors Doped with Rare-Earth Elements, *Materials* 12 (2019) 183–195.
- [47] M. Ebelmen, *Ann. Chimie. Phys.* 16 (1846) 129.
- [48] M. Ebelmen, *C. R. Acad. Sci.* 25 (1847) 854.

- [49] T. Graham, XXXV-On the properties of silicic acid and other analogous colloidal substances, *J. Chem. Soc.* 17 (1864) 318-327.
- [50] A. Walcarius, D. Mandler, J.A. Cox, M. Collinson, O. Lev, Exciting new directions in the intersection of functionalized sol-gel materials with electrochemistry, *J. Mater. Chem.* 15 (2005) 3663-3689.
- [51] R. Sui, P. Charpentier, Synthesis of metal oxide nanostructure by direct sol-gel chemistry in supercritical fluids, *Chem. Rev.* 112 (2011) 3057-3082.
- [52] D.A. Ward, E.I. Ko, Preparing catalytic materials by the sol-gel method, *Ind. Eng. Res.* 34 (1995) 421-433.
- [53] M.A. Cauqui, J.M. Rodriguez-Izquierdo, Application of the sol-gel methods to catalyst preparation, *J. Non-Cryst. Solids.* 147-148 (1992) 724-738.
- [54] A.E. Danks, S.R. Hall, Z. Schnepf, The evolution of "sol-gel" chemistry as a technique for material synthesis, *Mater. Horiz.* 3 (2016) 91-112.
- [55] H. Schroeder, Properties and Applications of Oxide Layers Deposited on Glass from Organic Solutions, *Opt. Acta* 9 (1962) 249-254.
- [56] J.D. Mackenzie, State of the art and prospects of glass science, *J. Non-Cryst. Solids* 41 (1982) 1-8.
- [57] J.D. Mackenzie, In *Ultrasonic Processing of Ceramics, Glasses and Composites*; eds. L.L. Hench, D.R. Ulrich, Wiley, New York (1984) 15.
- [58] L.L. Hench, S.H. Wang, J.L. Noguez, In *Multifunctional Materials*, Vol. 878, eds. R.L. Gunshor, SPIE: Bellingham, WA, (1988) 76.
- [59] L.L. Hench, M.J.R. Wilson, C. Balaban, J.L. Noguez, *Sol-Gel Processing of Large Silica Optics. Proceedings of 4<sup>th</sup> International Conference on Ultrastructure Processing of Ceramics, Glasses and Composites*, Tucson, AZ, (1989).
- [60] S.H. Wang, C. Campbell, L.L. Hench, In *Ultrastructure Processing of Advanced Ceramics*; eds. J.D. Mackenzie, D.R. Ulrich, Wiley: New York (1988) 145.
- [61] J.T. Davis, E.K. Rideal, In *Interfacial Phenomena*; eds. Academic Press, New York, (1963).
- [62] C.J. Brinker, G. Scherer, *Sol-Gel Science: The Physics and Chemistry of Sol-Gel Processing*. (1<sup>st</sup> edition), eds. Academic Press Inc, New York, NY, USA (1990).
- [63] D. Levy, M. Zayat, *The Sol-Gel Handbook: Synthesis, Characterization and Applications*. Eds. Wiley-VCH; Weinheim, Germany (2015).

- [64] L.L. Hench, J.K. West, The sol-gel process, *Chem. Rev.* 90 (1990) 33–72.
- [65] S. Esposito, "Traditional" Sol-Gel Chemistry as a Powerful Tool for the Preparation of Supported Metal and Metal Oxide Catalysts, *Materials (Basel)*. 12(4) (2019) 668-693.
- [66] J.P. Vareda, A. Lamy-Mendes, L. Durães, A reconsideration on the definition of the term aerogel based on current drying trends, *Microporous Mesoporous Mater.* 258 (2018) 211–216.
- [67] B.E. Yoldas, Alumina sol preparation from alkoxide, *Bull. Am. Ceram. Soc.* 54 (1975) 286.
- [68] J. Fricke, Capo, in *Ultrastructure Processing of Advanced Ceramics*; eds. J.D. Mackenzie, D.R. Ulrich, Wiley, New York, 1988.
- [69] J. Lin, C.W. Brown, Sol-gel glass as a matrix for chemical and biochemical sensing, *trends in analytical chemistry*, 16 (1997) 200-211.
- [70] B. Ballarin, C. Zanardi, L. Schenetti, R. Seeber, J.L. Hidalgo-Hidalgo de Cisneros, Synthesis and electrochemical characterisation of novel sonogel-carbon-polythiophene microstructured electrodes, *Synth Metals* 139 (2003) 29–33.
- [71] M.Y.M. Abdelrahim, S.R. Benjamin, L.M. Cubillana-Aguilera, I. Naranjo-Rodríguez, J.L. Hidalgo-Hidalgo de Cisneros, J.J. Delgado, J.M. Palacios-Santander, Study of electrocatalytic activity of cerium oxide and gold-studded cerium oxide nanoparticles using a sono-gel-carbon material as supporting electrode: electroanalytical study in apple juice for babies. *Sensors* 13 (2013) 4979–5007.
- [72] J.R. Crespo-Rosa, C. Zanardi, M. ElKaoutit, F. Terzi, R. Seeber, I. Naranjo-Rodríguez, Electroanalytical applications of a graphite-Au nanoparticles composite included in a sonogel matrix, *Electrochim Acta* 122 (2014) 310–315.
- [73] M.L. Ligabue, F. Terzi, C. Zanardi, G. Lusvardi, One-pot sonocatalyzed synthesis of sol-gel graphite electrodes containing gold nanoparticles for application in amperometric sensing, *J Mater Sci* 54 (2019) 9553–9564.
- [74] A.F. Gualtieri, G. Elmi, 2006. Understanding the high temperature reaction sequence during the thermal treatment of cement-asbestos slates. In: *Proceedings of the European Conference on Asbestos Risks and Management*. December 4-6, 2006. ARAM, Rome.
- [75] C. Abruzzese, A.M. Marabini, F. Paglietti, P. Plescia, CORDIAM process: A new treatment for asbestos wastes. In: eds. B. Mishra, *EPD Congress, DSan Antonio TX USA*, TMS Springer, Boston (1998) 563–577.
- [76] A. Borderes, Vitrification of the incineration residues, *Revue Verre* 6 (2000) 1–2.



- [77] A. Downey, D.M. Timmons, Study into the applicability of thermochemical conversion technology to legacy asbestos wastes in the UK. In: WM'05, Abstract Conference Book, February 27–March 3, Tucson, AZ, USA (2005).
- [78] A.F. Gualtieri, C. Cavenati, I. Zanatto, M. Meloni, G. Elmi, Lassinantti, M. Gualtieri, The transformation sequence of cement–asbestos slates up to 1200 °C and safe recycling of the reaction product in stoneware tile mixtures, *Journal of Hazardous Materials* 152 (2008) 563–570.
- [79] C. Leonelli, P. Veronesi, D.N. Boccaccini, M.R. Rivasi, L. Barbieri, F. Andreola, I. Lancellotti, D. Rabitti, G.C. Pellacani, Microwave thermal inertisation of asbestos containing waste and its recycling in traditional ceramics, *Journal of Hazardous Materials* B135 (2006) 149–155.
- [80] K.J.D. Mackenzie, R.H. Meinhold, Thermal reactions of chrysotile revisited: A  $^{29}\text{Si}$  and  $^{25}\text{Mg}$  MAS NMR study. *American Mineralogist*, 79 (1994) 43-50.
- [81] C.J. Martin, The thermal decomposition of chrysotile, *Mineralogical Magazine*, 35 (1977) 189-195.
- [82] A.F. Gualtieri, A. Tartaglia, Thermal decomposition of asbestos and recycling in traditional ceramics, *Journal of the European Ceramic Society*, 20, 9, (2000) 1409-1418.
- [83] A.F. Gualtieri, Recycling asbestos-containing material (ACM) from construction and demolition waste (CDW). in: *Handbook of recycled concrete and demolition waste*, eds. F. Pacheco-Torgal, V.W.Y. Tam, J.A. Labrincha, Y. Ding and J. De Brito, Woodhead Publishing series in Civil and Structural Engineering, Cambridge, UK (2013) 500-525.
- [84] A.F. Gualtieri, I. Zanatto, Industrial process for the direct temperature induced recrystallization of asbestos and/or mineral fibres containing waste products using a tunnel kiln and recycling, European Patent No. EP07425495 (2007).
- [85] A. Croce, M. Allegrina, P. Trivero, C. Rinaudo, A. Viani, S. Pollastri, A.F. Gualtieri, The concept of 'end of waste' and recycling of hazardous materials: in depth characterization of the product of thermal transformation of cement-asbestos, *Mineralogical Magazine*, 78 (2014) 1177–1191.
- [86] A. Cattaneo, A.F. Gualtieri, G. Artioli, Kinetic study of the dehydroxylation of chrysotile asbestos with temperature by in situ XRPD, *Phys. Chem. Miner.* 30 (2001) 177–183.
- [87] A.F. Gualtieri, D. Levy, E. Belluso, M. Dapiaggi, Kinetics of the decomposition of crocidolite asbestos: a preliminary real-time X-ray powder diffraction study, *Mater. Sci. Forum.* 443–444 (2004) 291–294.
- [88] A. Pugnali, F. Giantomassi, R. Di Primio, A.F. Gualtieri, C. Giacobbe, In vitro study of the cytotoxic potential of the product of thermal transformation of cement-asbestos, in: VII FIST Conference – Geoitalia 2009, Rimini, Italy, 9–11<sup>th</sup> September 2009.

[89] F. Giantomassi, A.F. Gualtieri, L. Santarelli, M. Tomasetti, G. Lusvardi, G. Lucarini, M. Governa, A. Pugnali, Biological effects and comparative cytotoxicity of thermal transformed asbestos-containing materials in a human alveolar epithelial cell line, *Toxicol. In Vitro* 24 (6) (2010) 1521–1531.

[90] A.F. Gualtieri, A. Viani, G. Sgarbi, G. Lusvardi, In vitro biodurability of the product of thermal transformation of cement-asbestos, *J. Hazard. Mater.* 205–206 (2012) 63–71.

[91] M.L. Ligabue, A.F. Gualtieri, M. Lassinantti Gualtieri, D. Malferrari, G. Lusvardi, Recycling of thermally treated cement-asbestos for the production of porcelain stoneware slabs, *Journal of Cleaner Production*, 247 (2020) 119084

## Purpose of the study

The purpose of this study concerns different applications of silicon-based materials: i) Ba-silicate doped with rare earth elements used as phosphorescent pigment, ii) sol-gel electrodes prepared with a specific silane precursor, namely methyltrimethoxysilane (MTMOS), and metal nanoparticles (MeNPs), with different electrochemical applications, iii); thermally treated cement-asbestos, named KRY-AS, recycled in frits for porcelain stoneware slabs, blue and black ceramic pigments and foam glass.

i) Alkali or alkaline-earth metal aluminates doped with rare earth ions or transition metals ions, with the property of long persistent phosphors (LPP), are extremely remarkable materials. They have a strong phosphorescent emission that lasts overnight, but they possess a partial solubility in water, and, consequently, they need a protective coating. Therefore, the possible applications of these phosphors for night vision and solar energy utilisation are limited to an indoor environment. Consequently, it is mandatory to find a different type of phosphor with the same LPP properties, but exploitable for outdoor applications. Alkaline-earth silicate phosphors can be a proper solution, since, in comparison to the aluminates, they have better physico-chemical properties, stability over time and lower synthesis temperature, yet they have a shorter emission time. This research aimed to improve this property and to create a pigment with near-white emission. The starting point was a literature work based on the phosphor  $\text{Ba}_5\text{Si}_8\text{O}_{21}:\text{Eu}^{2+},\text{Dy}^{3+}$ . We carried out a careful evaluation of the effects of precursors, crucible composition, flux agents, dopants, time and temperatures used in the synthesis. The characterization through elemental, kinetic, mineralogical (both qualitative and quantitative) and morphological analysis helped to establish the best experimental conditions to obtain this kind of phosphors with improved properties.

ii) The sol-gel technique has received increasing interest in the recent years in many fields, including the preparation of amperometric sensors. The resulting material combines the properties of a rigid three-dimensional structure, typical of inorganic materials, with the reactivity of organic functionalities. These sensors are extremely performing and cheap, thanks to the characteristics of the sol-gel and to the possibility to incorporate different electroactive materials in this structure. Furthermore, it is possible to find a faster and simpler approach compared to the formation of a new electrode coating, which is the most used method. An example is the preparation of electrodes

with a renewable electroactive surface, by means of routine mechanical cleaning procedures, or the use of a sol-gel powder to create a disposable disk electrode (or pellet). The sol-gel also permits to activate the synergic effects between the different components, for example by means of the Strong Metal Support Interaction (SMSI), which typically leads to an increase in the electrocatalytic activity of MeNPs in contact with an oxide, in this case, SiO<sub>2</sub>. Sol-gel graphite electrodes containing AuNPs and CuNPs have been studied as potential amperometric sensors.

Differently from the traditional synthesis, in which AuNPs are prepared in advance with respect to the silica matrix, they were here obtained directly inside the sol-gel, during its formation. Moreover, sol-gel was prepared by means of sonocatalysis, to reduce the amount of solvent and time needed for the hydrolysis step. Electrochemical tests allowed us to ascertain the good conductivity of the composite material, which was enabled by the graphite, and the electrocatalytic activity of AuNPs with respect to glucose and ascorbic acid oxidation.

For the sensor with CuNPs, we reported the application of multicomponent disk electrodes as disposable devices for electrocatalytic glycerol oxidation. These pellets sensors were constituted of silica-based sol-gel, copper nanoparticles, graphite and polystyrene. Copper nanoparticles were responsible for the oxidation step, the silica-based sol-gel improved the electrocatalytic performances of the pellets, polystyrene reinforced the mechanical stability of the structure and graphite conferred electrical conductivity.

iii) KRY·AS process represents a successful and economically practicable solution that realize the crystal-chemical transformation of CA slates in safe products. It is an actual possibility to solve the asbestos problem and remove it from the environment. Once obtained the new secondary raw material, the challenge is to create new ways to employ it. A secondary effect of the recycling of thermally treated cement asbestos is the possibility to substitute natural raw materials in the preparation of final products; this leads to a cost reduction and to avoid the consuming of non-renewable natural resources. KRY·AS has already been successfully recycled in different products: clay bricks, glasses, glass-ceramics, stoneware ceramics, pink and green ceramic pigments, plastic materials, and cement for commercial concrete. The present research showed three additional applications with a medium-high amount of KRY·AS:

a) preparation of ceramic frits adding a minor amount of natural raw materials as well as glass waste. The chemical composition and glass properties (e.g. viscosity, surface tension, crystallization

behaviour) of the frits made them an interesting sintering modifier in the production of porcelain stoneware slabs.

b) synthesis of blue and black ceramic pigments, with the addition of a low amount of natural raw materials such as  $\text{SiO}_2$  and  $\text{MgO}$ , as well as  $\text{Co}_3\text{O}_4$ ,  $\text{MnO}_2$  and  $\text{Cr}_2\text{O}_3$  as chromophores. The attention in the pigment synthesis was devoted to lower the production costs, using waste instead of raw materials and to develop environmentally friendly products.

c) preparation of foam glasses, with the addition of glass waste, a flux agent and a foaming agent. The attention was focused on the main property of this material, which was the extremely low density ( $< 0.5 \text{ g/cm}^3$  for commercial foam glass) and high porosity (up to 90% vol) that permits its application as insulating material in buildings and structures.

# **Chapter 1**

**Preparation and luminescence properties of  $\text{Ba}_5\text{Si}_8\text{O}_{21}$  long persistent phosphors doped with rare-earth elements**

Article

# Preparation and Luminescence Properties of Ba<sub>5</sub>Si<sub>8</sub>O<sub>21</sub> Long Persistent Phosphors Doped with Rare-Earth Elements

Andrea Silvestri, Maria Laura Ligabue , Gianluca Malavasi and Gigliola Lusvardi \*

Department of Chemical and Geological Sciences, University of Modena and Reggio Emilia, Via G. Campi 103, 41125 Modena, Italy; 191646@studenti.unimore.it (A.S.); mlauraligabue@gmail.com (M.L.L.); gianluca.malavasi@unimore.it (G.M.)

\* Correspondence: gigliola.lusvardi@unimore.it; Tel.: +39-05-9205-8549

Received: 13 December 2018; Accepted: 29 December 2018; Published: 7 January 2019



**Abstract:** The phosphors of formula Ba<sub>5</sub>Si<sub>8</sub>O<sub>21</sub>:Eu<sup>2+</sup>,Dy<sup>3+</sup> were synthesized and studied in order to improve their properties. Their synthesis conditions were evaluated as a function of precursors, crucible composition, flux agents, dopants and temperatures. The samples were characterised by means of a systematic investigation through elemental, kinetic, mineralogical (both qualitative and quantitative), and morphological analysis. This study allows for a careful evaluation of the parameters that influence the formation and properties of Ba<sub>5</sub>Si<sub>8</sub>O<sub>21</sub>:Eu<sup>2+</sup>,Dy<sup>3+</sup> phosphors. As for the synthesis conditions, the use of Na<sub>2</sub>SiO<sub>3</sub>, BaCO<sub>3</sub> and NH<sub>4</sub>Cl as precursors was very important to reduce the temperature and time of synthesis. The reducing atmosphere produced with purified coal was cheaper and gave results similar to the more traditional gas mixture (H<sub>2</sub>/N<sub>2</sub>). At the end of this study, a phosphor with improved long persistent phosphorescence (LPP) characteristics was obtained with Ba/Si = 0.7, Eu/Si = 2.8 × 10<sup>-3</sup> and Dy/Si = 3.6 × 10<sup>-3</sup> following a 6 h-synthesis in a quartz crucible.

**Keywords:** barium silicates; phosphors; kinetic analysis; quantitative phase analysis; luminescence

## 1. Introduction

The term luminescence indicates the phenomenon of light emission from a material after the excitation of its electronic states by an external source [1,2]. Photoluminescence is the most widely occurring phenomenon, and it involves excitation by electromagnetic radiation. Depending on the material, photons can be emitted using the mechanism of fluorescence (light emission for less than 10<sup>-8</sup> s) or phosphorescence (light emission for minutes or hours).

The materials which possess these characteristics are mostly inorganic compounds and are generally called phosphors [2–4].

In the last 30 years, other types of long persistent phosphorescence (LPP) [1–7] phosphors based on either alkali or alkaline-earth metal aluminates doped with rare earth ions or transition metals ions attracted much attention and were actively investigated [8]. In particular, special attention was given to strontium aluminates doped with Eu<sup>2+</sup> and Dy<sup>3+</sup>, SrAl<sub>2</sub>O<sub>4</sub>:Eu<sup>2+</sup>/Dy<sup>3+</sup> [9] and Sr<sub>4</sub>Al<sub>14</sub>O<sub>25</sub>:Eu<sup>2+</sup>/Dy<sup>3+</sup> [10,11], which are characterised by a strong emission, centred in the range of green-blue at 520 and 495 nm, respectively, and a phosphorescence that lasts overnight. These compounds possess partial solubility in water [12] and, consequently, require a protective coating [13–15]. Therefore, their limited outdoor applications, possible increase in production costs and the challenging employment of their emission colour led to a further search for different phosphors.

Alkaline-earth silicate phosphors, synthesized in the last few years [16–20], have garnered much attention for their better physico-chemical properties [21,22], their stability over time and their

lower synthesis temperature compared to those of aluminate-derived phosphors [18]. Moreover, these phosphors emit a wider range of light colours, like green [23], red [24], yellow [16] and white [25]. Unfortunately, the duration of their emission is lower compared to that of aluminate-derived phosphors; consequently, a lot of studies are aimed at improving this property. Yu Gong et al. [17] reported the synthesis of  $\text{Ba}_4(\text{Si}_3\text{O}_8)_2:\text{Eu}^{2+},\text{Dy}^{3+}$  as an LPP phosphor, with high chemical stability and an emission of more than 24 h after light excitation at  $\lambda = 500\text{--}550$  nm. Later, Pengjiu Wang et al. [18] reported the preparation of  $\text{Ba}_5\text{Si}_8\text{O}_{21}:\text{Eu}^{2+},\text{Dy}^{3+}$ , that got a better luminescence characteristic due to its crystalline structure. This phosphor possesses sustained phosphorescence when activated by sunlight ( $\lambda = 473$  nm), with a lasting time beyond 16 h.

The LPP phosphors are studied by different researchers and their applications have increased from the civil uses (i.e., traditional displays, lighting, medicine, security) to a wide range of scientific fields, such as life sciences, biomedicine, clinical medicine, energy and environmental engineering [26–28].

In the present study, we aimed to further improve the synthesis of  $\text{Ba}_5\text{Si}_8\text{O}_{21}:\text{Eu}^{2+},\text{Dy}^{3+}$  phosphors and their LPP characteristics.

On the basis of our previous experience [29], we carried out a careful evaluation of the effect of precursors, crucible composition, flux agents, dopants, time and temperatures used in the synthesis. The characterization through elemental, kinetic, mineralogical and morphological analysis will help establish the best experimental conditions to obtain this kind of phosphors with improved properties.

## 2. Materials and Methods

### 2.1. Synthesis

Barium silicate phosphors doped with  $\text{Eu}^{2+}$  and  $\text{Dy}^{3+}$  ( $\text{Ba}_5\text{Si}_8\text{O}_{21}:\text{Eu}^{2+}/\text{Dy}^{3+}$ ) were prepared through a solid-state reaction. The raw materials used consisted of barium carbonate ( $\text{BaCO}_3$ ; Riedel-de Haën, Hannover, Germany, 99.0%) or barium chloride ( $\text{BaCl}_2$ ; Carlo Erba, Cornaredo (MI), Italy, 99%), sodium metasilicate pentahydrate ( $\text{Na}_2\text{SiO}_3 \cdot 5\text{H}_2\text{O}$ ; Aldrich, St. Louis, MO, USA, 95.0%) or silicon oxide ( $\text{SiO}_2$ ; Aldrich, purum), dysprosium oxide ( $\text{Dy}_2\text{O}_3$ ; Aldrich, 99.9%), europium oxide ( $\text{Eu}_2\text{O}_3$ ; Aldrich, 99.9%), ammonium chloride ( $\text{NH}_4\text{Cl}$ ; Riedel-de Haën, 99.5%) and boric acid ( $\text{H}_3\text{BO}_3$ ; Aldrich 99.8%). Some phosphors ( $\text{Ba}_5\text{Si}_8\text{O}_{21}:\text{Eu}^{2+}/\text{Er}^{3+}$ ) were also doped with  $\text{Er}^{3+}$  ( $\text{Er}_2\text{O}_3$ ; Aldrich, 99.9%).

The reagents were weighed with an analytical balance ( $\pm 0.01$  mg) according to the stoichiometric composition of  $\text{Ba}_5\text{Si}_8\text{O}_{21}$  and then mixed in an agate mortar; the mixture was dried at  $100$  °C for 2 h and successively put into a crucible. The reducing atmosphere was created with purified coal, which produces  $\text{CO}_2$  and  $\text{CO}$  on burning; it is, in fact, well-known that this kind of atmosphere is cheaper and more efficient for the sintering process than the one obtained with a more traditional gas mixture ( $\text{H}_2/\text{N}_2$ ) [30]. The crucible with the mixture surrounded by coal was inserted inside a large alumina crucible, which was closed with a lid. The synthesis was carried out at  $1100\text{--}1250$  °C for 3–12 h, and the obtained material was then grounded in an agate mortar to obtain a fine powder used for the characterisation.

### 2.2. Characterisation

Mineralogical studies (phase identification and quantification) performed by XRPD (X-Ray Powder Diffraction) were carried out with a PANalytical X'Pert Pro Bragg-Brentano diffractometer (Panalytical, Malvern, UK), using Ni-filtered  $\text{Cu K}\alpha$  radiation ( $\lambda = 1.54060$  Å) with an X'Celerator detector. The patterns were taken over the diffraction angle range of  $2\theta = 5\text{--}55^\circ$ , with a time step of 50 s and a step size of  $0.03^\circ$  (angular step). In the case of quantitative phase analysis (QPA), the patterns were collected in the range of  $2\theta = 3\text{--}100^\circ$ , with a time step of 100 s and a step size of  $0.03^\circ$ . The QPA results were elaborated by means of the combined Rietveld-reference intensity ratio (RIR) method [31]. QPA refinements of the powder spectra were performed using the GSAS software [32], and its graphical interface EXPGUI [33]. The structural models for all phases were taken from the ICSD database [34]. The refined instrumental parameters were the Chebyshev polynomial background function and the



zero-shift. For each phase, the refined parameters consisted of the scale factor, unit-cell parameters, Gaussian and Lorentzian coefficients of the pseudo-Voigt peak-profile function, offset function for the correction of the peak asymmetry and sample-displacement correction.

Surface morphology and its composition were examined with a Scanning Electron Microscope (FEI Quanta 200, FeiCo., Abingdon, UK), equipped with an energy dispersive spectroscopy (EDS) instrument (INCA 350, Oxford Instrument, Abingdon, UK). EDS analyses were performed in quadruplicate for each examined agglomerate onto the surface; the result was a mean of the replicates and a standard deviation of 0.5%.

A quantification of Si and Ba was performed with an ICP spectrometer (Perkin Elmer Optima 4200 DV, Waltham, MA, USA), while for Eu, Dy and Er, an ICP-MS spectrometer was applied (X Series, Thermo Fisher Scientific, Waltham, MA, USA). The standard deviation for ICP results was lower than 1%, and the detection limit for ICP-MS shows was 0.05 pg/mL.

The afterglow decay was used to measure the luminous intensity with a luminance meter (Minolta CS-100A, Ramsey, NJ, USA). Following the procedure of P. Wang et al. [18], we excited each sample for 10 min with a Wood lamp (366 nm), after which the luminance was measured in a dark room (1 m was the distance between the sample and the Luminance Meter). The reproducibility determined was 0.005 cd/m<sup>2</sup>. The instrument works in the range of 0.002–49.900 cd/m<sup>2</sup> with a sampling time of 0.4 s. The obtained decay curves were elaborated by means of a kinetic analysis with first, second and third-order functions.

The best fitting was evaluated by the calculation of deviation (D%), which is defined as the root mean square offset between the experimental and computed data through the use of first, second, or third-order decay equations [35]. In other words, these results were compared since the conditions used in the tests are always the same.

In our samples, the afterglow decay can be fitted with a second-order function:

$$y(t) = y_0 + A_1e^{-t/\tau_1} + A_2e^{-t/\tau_2}$$

where  $y(t)$  is the luminance emission intensity at time  $t$  after switching off the excitation source,  $y_0$  is the luminance emission at time zero,  $A_i$  is a time-invariant constant that represents the amplitude of luminescence intensity corresponding to the  $i$  decay component, while  $t_i$  is the corresponding decay time-constant. We used the values of  $\tau_1$  and  $\tau_2$  to compare the behaviour of the differently synthesized phosphor; it was possible to use  $\tau_m$  for this purpose.

### 3. Results

We started from a reference phosphor Ba<sub>5</sub>Si<sub>8</sub>O<sub>21</sub>:Eu<sup>2+</sup>,Dy<sup>3+</sup> [18], with these molar ratios: Ba/Si = 0.625, Eu/Si = 2.5 × 10<sup>-3</sup> and Dy/Si = 11.25 × 10<sup>-3</sup>. These were obtained from BaCO<sub>3</sub>, SiO<sub>2</sub>, Dy<sub>2</sub>O<sub>3</sub>, Eu<sub>2</sub>O<sub>3</sub> and H<sub>3</sub>BO<sub>3</sub> (2.5 wt.%) by treatment at 1250 °C for 10 h in a platinum crucible.

In order to perform an accurate comparison, we reproduced the synthesis of this phosphor in our laboratory and the product was named sample 1.

The sample synthesized with the same molar ratios and reagents and at the same annealing conditions but in a quartz crucible instead of platinum was named sample 2. Mineralogical studies confirm that in both cases, it is possible to obtain Ba<sub>5</sub>Si<sub>8</sub>O<sub>21</sub> as the dominant crystalline phase and the sample 1 maintains their long-persistent phosphorescence characteristics. Then, the synthesis of this phosphor was evaluated by varying the types and amounts of precursors, dopants, flux agents, crucibles type, temperature and time of annealing. For all samples, the reducing atmosphere was created with purified coal.

Each sample was obtained by changing the variables step by step; this will be discussed in the following paragraphs.

In Table 1, the compositions and synthesis conditions of the samples (A–H) are reported with respect to those of sample 1.

**Table 1.** Theoretical molar ratios and synthesis conditions of phosphors.

Sample	Ba/Si	Eu/Si	Dy/Si	Er/Si	Flux Agent	Temperature (°C)	Time (h)
1	0.625	$2.5 \times 10^{-3}$	$11.25 \times 10^{-3}$	/	H <sub>3</sub> BO <sub>3</sub>	1250	10
2	0.625	$2.5 \times 10^{-3}$	$11.25 \times 10^{-3}$	/	H <sub>3</sub> BO <sub>3</sub>	1250	10
A	0.700	$2.5 \times 10^{-3}$	$11.25 \times 10^{-3}$	/	H <sub>3</sub> BO <sub>3</sub>	1100	6
B	0.700	$2.5 \times 10^{-3}$	$11.25 \times 10^{-3}$	/	NaCl	1100	6
C	0.700	$2.8 \times 10^{-3}$	$3.6 \times 10^{-3}$	/	NaCl	1100	6
D	0.700	$2.8 \times 10^{-3}$	$3.6 \times 10^{-3}$	/	H <sub>3</sub> BO <sub>3</sub>	1100	6
E	0.700	$2.8 \times 10^{-3}$	/	$3.6 \times 10^{-3}$	NaCl	1100	6
F	0.700	$2.8 \times 10^{-3}$	$3.6 \times 10^{-3}$	/	NaCl	1100	12
G	0.700	$2.8 \times 10^{-3}$	$3.6 \times 10^{-3}$	/	NaCl	1100	4
H	0.700	$2.8 \times 10^{-3}$	$3.6 \times 10^{-3}$	/	NaCl	1100	3

### 3.1. Effect of the Precursors

Our first aim was to find precursors of silicon and barium that could react faster and at lower temperatures in contrast to those used for sample 1. The combined use of Na<sub>2</sub>SiO<sub>3</sub> and BaCO<sub>3</sub> as sources of silicon and barium produces a glassy compound instead of a crystalline one, probably due to the low fusion temperature of Na<sub>2</sub>SiO<sub>3</sub> (T = 1088 °C). To avoid this problem and help the formation of a crystalline phase, we decided to use H<sub>2</sub>SiO<sub>3</sub> instead of Na<sub>2</sub>SiO<sub>3</sub> [17]. H<sub>2</sub>SiO<sub>3</sub> was obtained by reaction between NH<sub>4</sub>Cl and Na<sub>2</sub>SiO<sub>3</sub>:

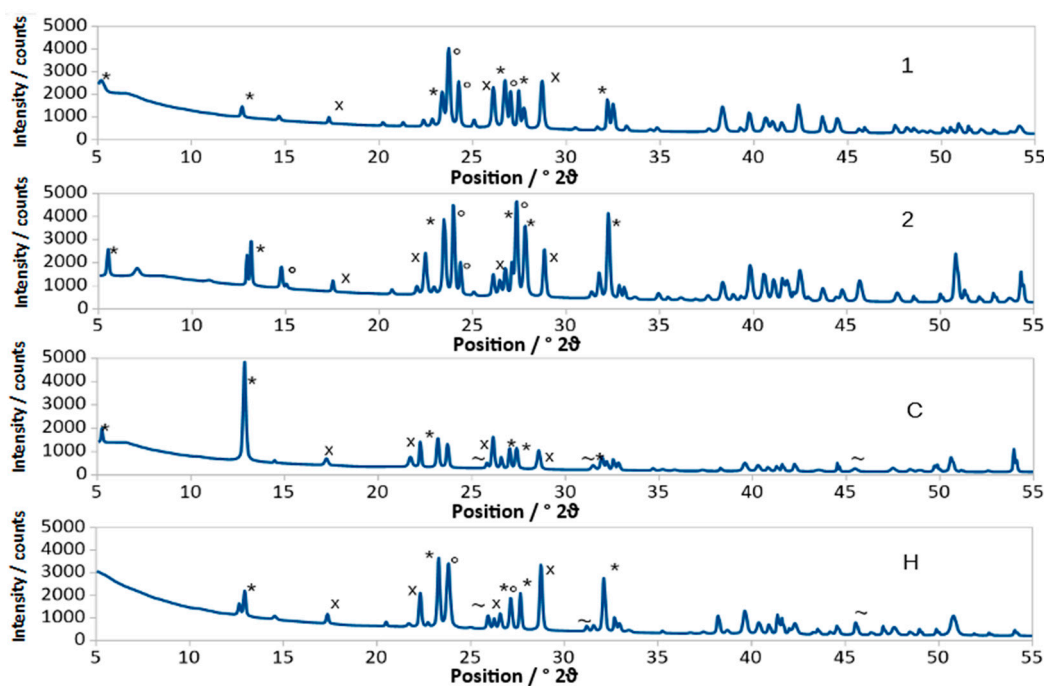


To confirm the correctness of this procedure, we carried out a mineralogical study [36] on the mixture with all precursors (BaCO<sub>3</sub>, Na<sub>2</sub>SiO<sub>3</sub>, NH<sub>4</sub>Cl, Eu<sub>2</sub>O<sub>3</sub> and Dy<sub>2</sub>O<sub>3</sub>) before the heat treatment, and the results (Table S1, Supplementary Materials) indicated the presence of NaCl, BaCO<sub>3</sub> and the absence of any foreign crystalline phase. Furthermore, the presence of NaCl is also useful as a flux agent for the synthesis.

We have tried other reagents with the following aims:

- to reduce reagents number: using BaCl<sub>2</sub> instead of NH<sub>4</sub>Cl and BaCO<sub>3</sub>. The mineralogical results indicate that even at high temperature (1200 °C) and for a long time (12 h), the final product showed the presence of some residual reagents. The reaction was not complete in terms of the formation of Ba<sub>5</sub>Si<sub>8</sub>O<sub>21</sub> and displayed a weak afterglow luminescence with respect to the reference (Figure S1, Supplementary Materials).
- to use a low expensive reagent: using SiO<sub>2</sub> instead of Na<sub>2</sub>SiO<sub>3</sub>, and H<sub>3</sub>BO<sub>3</sub> as a flux agent instead of NaCl. The afterglow was good, but the reaction required a high temperature (1250 °C) and a long synthesis time (10 h) (Figure 1, sample 2).

Consequently, we decided to always use H<sub>2</sub>SiO<sub>3</sub> (from NH<sub>4</sub>Cl and Na<sub>2</sub>SiO<sub>3</sub>) and BaCO<sub>3</sub> as sources of silicon and barium, respectively.



**Figure 1.** XRPD of samples 1, 2, C, H;  $\text{Ba}_5\text{Si}_8\text{O}_{21}$  [36, PDF350766] (\*),  $\text{Ba}_4\text{Si}_6\text{O}_{16}$  [36, PDF831482] (°)  $\text{BaSi}_2\text{O}_5$  [36, PDF260176] (x), NaCl [36, PDF882300] (~).

### 3.2. Effect of Crucible and Ba/Si Molar Ratio

In this case, our aim was to find cheaper and more versatile crucible materials and replace platinum. We tried crucibles constituting of different materials: platinum, alumina, boron nitride and quartz. We decided to discard platinum because of the lack of reproducibility of the photoluminescent properties, which is probably due to chemical interactions between the crucible and its reagents. Similarly, for the alumina crucible, the precursors interacted with the crucible and, in fact, from mineralogical analysis, the presence of a barium aluminate phase ( $\text{Ba}_2\text{Al}_2\text{O}_5$ ) was identified (Figure S2, Supplementary Materials). Boron nitride also interacts with the reagents, making it difficult to remove the mixture from the crucible.

Generally, in the case of the quartz crucible, the mineralogical analysis indicates the formation of competitive crystalline phases for the formation of  $\text{Ba}_5\text{Si}_8\text{O}_{21}$ ; these phases,  $\text{BaSi}_2\text{O}_5$  and  $\text{Ba}_4\text{Si}_6\text{O}_{16}$ , are in agreement with the earlier reported phase diagrams of the system BaO-SiO<sub>2</sub> [37]. In particular, the presence of  $\text{BaSi}_2\text{O}_5$  and its Ba/Si molar ratio of 0.5, indicate a probable interaction with the quartz crucible and a consequent increase of the amount of Si inside the phosphor. To obtain the optimal Ba/Si molar ratio required for the formation of  $\text{Ba}_5\text{Si}_8\text{O}_{21}$ , we increased the amount of  $\text{BaCO}_3$ . Different Ba/Si molar ratios were tested (0.65, 0.66, 0.7, 0.75 and 1), and the most promising results was 0.7.

Consequently, we decided to use the crucible of quartz in all the samples.

### 3.3. Effect of Flux Agents and of Eu/Si, Dy/Si Molar Ratios

On the basis of the previous considerations, the interesting results were obtained with a molar ratio Ba/Si = 0.7 with  $\text{H}_2\text{SiO}_3$  and  $\text{BaCO}_3$  as precursors, synthesized in a quartz crucible. Starting from these parameters, we prepared a sample with the same type and amount of flux agent as in sample 1 (sample A), and sample B was prepared with NaCl (10 wt.%) instead of  $\text{H}_3\text{BO}_3$  (2.5 wt.%). NaCl was obtained by the reaction of  $\text{NH}_4\text{Cl}$  and  $\text{Na}_2\text{SiO}_3$  (see Section 3.1).

In sample B, the principal phase was  $\text{Ba}_5\text{Si}_8\text{O}_{21}$  (45 wt.%) and the secondary phases were  $\text{Ba}_4\text{Si}_6\text{O}_{16}$  (15 wt.%) and  $\text{BaSi}_2\text{O}_5$  (10 wt.%). Contrary to that, in sample A, the principal phase was  $\text{Ba}_4\text{Si}_6\text{O}_{16}$  (44 wt.%), while  $\text{Ba}_5\text{Si}_8\text{O}_{21}$  (20 wt.%) and  $\text{BaSi}_2\text{O}_5$  (15 wt.%) were the secondary ones. The  $\text{H}_3\text{BO}_3$  use (sample A) lead to the dominant formation of  $\text{Ba}_4\text{Si}_6\text{O}_{16}$ , which reduced the afterglow

luminescence. In fact, the initial emission of sample B ( $A_1 = 109 \text{ mcd/m}^2$ ) was higher than that of A ( $A_1 = 93 \text{ mcd/m}^2$ ) (Table 2).

**Table 2.** Luminescence kinetic analysis results.

Sample	$A_1$ (mcd/m <sup>2</sup> )	$t_1$ (s)	$A_1 \times t_1$ (%)	$A_2$ (mcd/m <sup>2</sup> )	$t_2$ (s)	$A_2 \times t_2$ (%)	$t_m$ (s)
1	133	85	8	35	3759	92	1922
2	94	233	14	20	7056	86	3645
A	94	206	13	13	9602	87	4904
B	109	223	19	23	4431	81	2327
C	180	134	16	20	6358	84	3248
D	18	176	19	3	4393	81	2285
E	213	45	66	10	494	34	269
F	40	225	12	14	4847	88	2536
G	57	186	16	19	3004	84	1595
H	57	151	21	17	1895	79	1023

To improve the reaction yield, different amounts of  $\text{H}_3\text{BO}_3$  and dopant molar ratios were tested (samples C, D). Samples C and D have the same molar ratios and were synthesized at the same conditions, but they differ by flux agents and contain, respectively, NaCl and  $\text{H}_3\text{BO}_3$  (10 wt.%).

Mineralogical analysis (Table S2, Supplementary Materials) allowed us to identify different crystalline phases. Due to pattern complexity (Figure 1), a qualitative study that refers to the diffraction peaks intensity is not sufficient to quantify the amount of each phase even from a semi-quantitative point of view. In fact, sometimes, there are peaks positioned very close to each other or overlapped (e.g.,  $d = 3.73 \text{ \AA}$  and  $d = 3.74 \text{ \AA}$  respectively for  $\text{Ba}_5\text{Si}_8\text{O}_{21}$  and  $\text{Ba}_4\text{Si}_6\text{O}_{16}$ ) and, also, preferential orientation can appear ( $d = 6.88 \text{ \AA}$  for  $\text{Ba}_5\text{Si}_8\text{O}_{21}$ ).

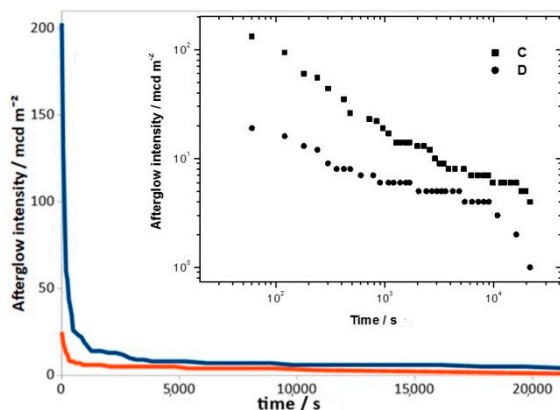
Consequently, using the Rietveld method in order to perform a quantitative phase analysis (QPA) gives us more accurate results (Table 3); it indicated whether  $\text{Ba}_5\text{Si}_8\text{O}_{21}$  is the principal crystalline phase and also demonstrated other competitive crystalline phases besides the amorphous phase.

**Table 3.** QPA (wt.%  $\pm$  1) obtained from XRPD analysis.

Phase	A	B	C	D	E	F	G	H
$\text{Ba}_5\text{Si}_8\text{O}_{21}$	20	45	59	76	58	57	66	56
$\text{Ba}_4\text{Si}_6\text{O}_{16}$	44	15	8	/	7	12	4	10
$\text{BaSi}_2\text{O}_5$	15	10	13	7	11	11	11	7
Amorphous	21	30	20	17	24	20	19	27

$\text{Ba}_5\text{Si}_8\text{O}_{21}$  is the principal crystalline phase in both cases, with 59 wt.% for sample C and 76 wt.% for sample D.  $\text{BaSi}_2\text{O}_5$  is a secondary phase presented at 13 and 7 wt.%, respectively, for samples C and D. Sample C also contains  $\text{Ba}_4\text{Si}_6\text{O}_{16}$  (8 wt.%).

The lower number of competitive phases in sample D makes it possible to suppose that  $\text{H}_3\text{BO}_3$  could be the best flux agent. However, the luminescence decay curves (Figure 2) and the initial emission ( $A_1$ ) (Table 2) demonstrates that sample C has a better performance than sample D. Comparing with samples 1 and 2, we observe a higher value of  $A_1$  for C:  $180 \text{ mcd/m}^2$  for C, compared with 133 and  $94 \text{ mcd/m}^2$ , respectively, for 1 and 2.



**Figure 2.** Decay curves of samples C (blue) and D (red). The upper inset showed the log-log plot.

Therefore, we can suppose that  $\text{H}_3\text{BO}_3$  (used in the sample D, 1 and 2) somehow inhibits the emission intensity in the samples.

We also prepared a sample with both flux agents, but the final result was an amorphous compound that did not show any phosphorescence.

These results indicate that, in our conditions, NaCl is the best flux agent.

For all studied samples, similarly to Y. Gong et al. [17] and P. Wang et al. [18], we used  $\text{Eu}^{2+}$  as emission source and  $\text{Dy}^{3+}$  to enhance the afterglow emission; different molar ratios (Eu/Si, Dy/Si) were tested, and the most promising ones are reported in Table 1.

Furthermore, as seen from P. Wang et al. [38], we tried using  $\text{Er}^{3+}$  instead of  $\text{Dy}^{3+}$ .

We compared the luminescence emission and kinetic analysis of sample C (doped with  $\text{Eu}^{2+}$ ,  $\text{Dy}^{3+}$ ) and sample E (doped with  $\text{Eu}^{2+}$ ,  $\text{Er}^{3+}$ ) (Table 2). The initial emission  $A_1$  is higher for sample E: 213 against 180  $\text{mcd}/\text{m}^2$ . Unfortunately though, it has got a very short afterglow decay:  $\tau_2 = 494$  s compared to  $\tau_2 = 6358$  s of sample C.

We synthesised the samples with both  $\text{Er}^{3+}$  and  $\text{Dy}^{3+}$ ; the elements were added in the same molar ratios  $X/\text{Si}$  ( $X = \text{Er}$  or  $\text{Dy}$ ) =  $2 \times 10^{-3}$ ,  $3.5 \times 10^{-3}$  and  $3.6 \times 10^{-3}$ . In all cases, the initial emission was not comparable with sample E, while  $\tau_2$  remained similar to one of the samples with only  $\text{Eu}^{2+}$  and  $\text{Dy}^{3+}$ . Consequently, we decided to use only  $\text{Eu}^{2+}$  and  $\text{Dy}^{3+}$  as dopants.

The parameters reported in Table 2 indicated that the contribution to the total photon emission of the fast decay  $A_1 \times \tau_1$  (%) is lower, as compared to the slow decay component  $A_2 \times \tau_2$  (%). The fast and slow decay components correspond to 10 and 90%, respectively. This suggests that, for the major part of the phosphors, the afterglow decay process is the same, except for sample E (doped with  $\text{Er}^{3+}$ ), which has the brightest initial emission, but with the shortest afterglow time.

### 3.4. Effect of Heat Treatment

The synthesis conditions, in addition to raw material selection, play a crucial role in the process. Higher temperatures or longer thermal treatment times improved both the solid-state reaction and the formation of the desired crystalline phase responsible for photoluminescence.

The most promising synthesis was carried out at 1100 °C, instead of 1250 °C used for the reference sample 1.

We tested different synthesis times: 12 h for sample F, 6 h for sample C, 4 h for sample G and 3 h for sample H.

From QPA (Table 3), we can see that the principal phase is  $\text{Ba}_5\text{Si}_8\text{O}_{21}$  in all the samples.

Sample G got the higher amount (66 wt.%) of  $\text{Ba}_5\text{Si}_8\text{O}_{21}$ , but sample C (59 wt.%) possesses better phosphorescence, as one can see from the luminescence emission and kinetic analysis results (Table 2).

The secondary phases amounts are similar in samples F, G and H. Sample H presents the greatest quantity of amorphous phase (27 wt.%), and this could explain the worst values in the luminescence decay curves and kinetic parameters (Figure 3, Table 2).

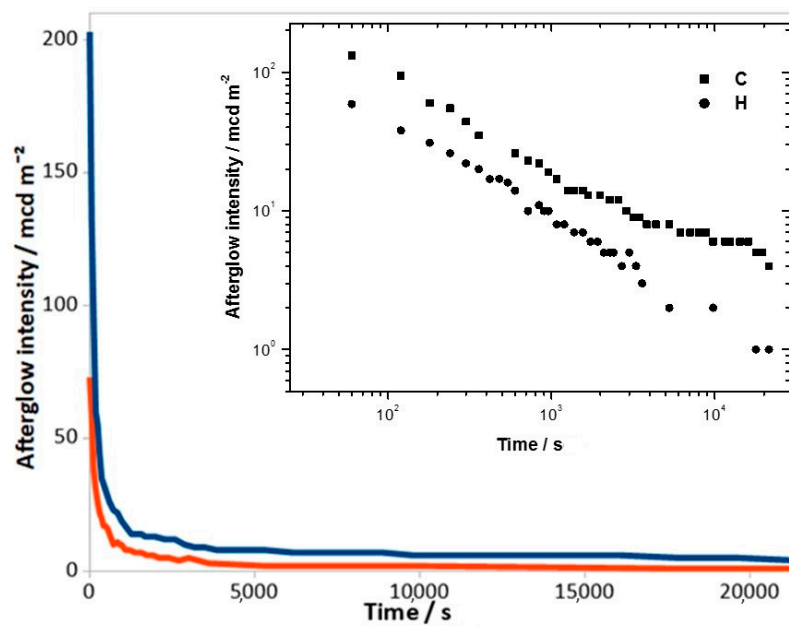


Figure 3. Decay curves of samples C (blue) and H (red). The upper inset showed the log-log plot.

For all samples, we also performed a morphological/compositional evaluation. The morphology was similar in all cases, the agglomerates are well-defined and they are in agreement with the amorphous phase amount. Mapping performed by EDS analysis reveals the presence of the constituent elements Ba, Si, O, Eu and Dy homogeneously distributed over the grain surface. An element mapping was performed as well for the surface and, in the case of sample C (Figure 4), the regular element distributions are evidently compatible with the formation of a doped barium silicate compound.

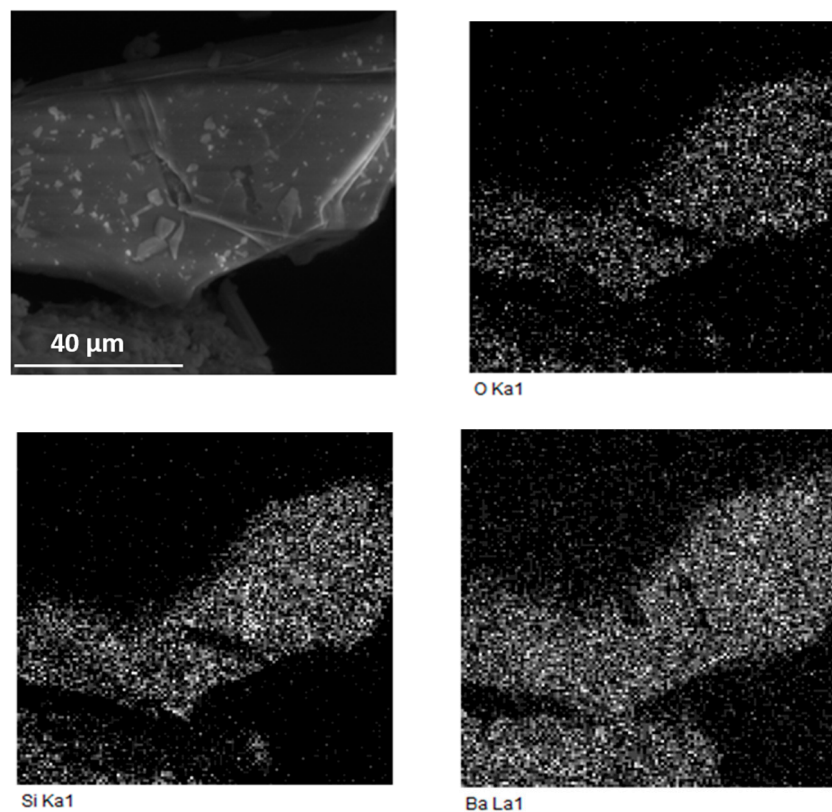
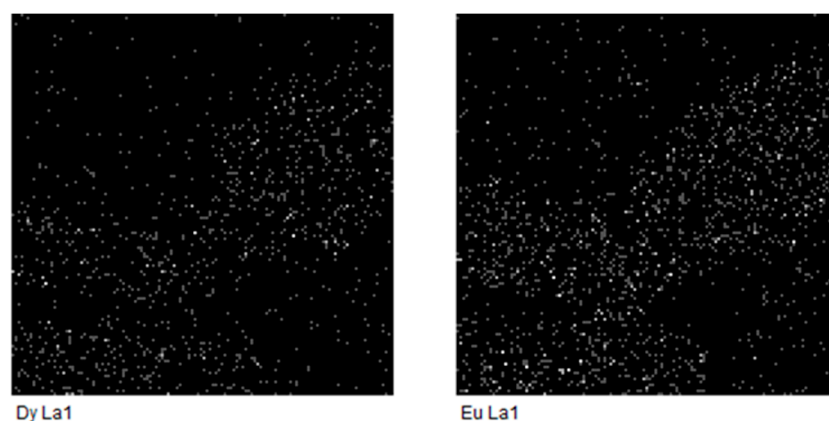


Figure 4. Cont.



**Figure 4.** SEM micrographs and relative maps of elements performed by EDS analysis for sample C.

#### 4. Discussion

The purpose of this paper is to improve the properties of  $\text{Ba}_5\text{Si}_8\text{O}_{21}:\text{Eu}^{2+},\text{Dy}^{3+}$  and to make them comparable to those of other well-studied phosphors, such as strontium aluminates doped with  $\text{Eu}^{2+}$  and  $\text{Dy}^{3+}$ .

It is well known that  $\text{Ba}_5\text{Si}_8\text{O}_{21}:\text{Eu}^{2+},\text{Dy}^{3+}$  is an LPP material that can emit sustainable phosphorescence activated by sunlight with a lasting time longer than 16 h.

Initially, we wanted to improve its LPP characteristics and, for this reason, it was necessary to evaluate the effect of precursors, crucible composition, flux agents, dopants, time and temperatures used for synthesis.

The results derived from elemental, kinetic, mineralogical and morphological analyses indicate that the variation of these parameters strongly affects the phosphorescence.

The reference phosphor (sample 1) possesses the following characteristics:  $\text{Ba}/\text{Si} = 0.625$ ,  $\text{Eu}/\text{Si} = 2.5 \times 10^{-3}$  and  $\text{Dy}/\text{Si} = 11.25 \times 10^{-3}$ , and it was obtained using  $\text{BaCO}_3$ ,  $\text{SiO}_2$ ,  $\text{Dy}_2\text{O}_3$ ,  $\text{Eu}_2\text{O}_3$  and  $\text{H}_3\text{BO}_3$  at  $1250\text{ }^\circ\text{C}$  for 10 h in a platinum crucible. The principal phase is  $\text{Ba}_5\text{Si}_8\text{O}_{21}$  and the phosphor is characterized by  $A_1$  133 mcd/m<sup>2</sup>.

Table 4 shows that the experimental molar ratios match well with the theoretical values.

**Table 4.** Theoretical (theo) and experimental (exp) molar ratios for phosphors from elemental analysis.

Sample	Ba/Si (theo)	Ba/Si (exp)	Eu/Si (theo)	Eu/Si (exp)	Dy/Si (theo)	Dy/Si (exp)	Er/Si (theo)	Er/Si (exp)
1	0.625	0.60	$2.5 \times 10^{-3}$	$2.3 \times 10^{-3}$	$11.25 \times 10^{-3}$	$10.75 \times 10^{-3}$	/	/
2	0.625	0.59	$2.5 \times 10^{-3}$	$2.4 \times 10^{-3}$	$11.25 \times 10^{-3}$	$10.75 \times 10^{-3}$	/	/
A	0.700	0.62	$2.5 \times 10^{-3}$	$2.6 \times 10^{-3}$	$11.25 \times 10^{-3}$	$10.45 \times 10^{-3}$	/	/
B	0.700	0.64	$2.8 \times 10^{-3}$	$2.6 \times 10^{-3}$	$11.25 \times 10^{-3}$	$11.05 \times 10^{-3}$	/	/
C	0.700	0.63	$2.8 \times 10^{-3}$	$2.7 \times 10^{-3}$	$3.6 \times 10^{-3}$	$3.7 \times 10^{-3}$	/	/
D	0.700	0.65	$2.8 \times 10^{-3}$	$2.7 \times 10^{-3}$	$3.6 \times 10^{-3}$	$3.5 \times 10^{-3}$	/	/
E	0.700	0.65	$2.8 \times 10^{-3}$	$2.5 \times 10^{-3}$	/	/	$3.6 \times 10^{-3}$	$3.4 \times 10^{-3}$
F	0.700	0.66	$2.8 \times 10^{-3}$	$2.9 \times 10^{-3}$	$3.6 \times 10^{-3}$	$3.8 \times 10^{-3}$	/	/
G	0.700	0.65	$2.8 \times 10^{-3}$	$2.7 \times 10^{-3}$	$3.6 \times 10^{-3}$	$3.5 \times 10^{-3}$	/	/
H	0.700	0.63	$2.8 \times 10^{-3}$	$2.6 \times 10^{-3}$	$3.6 \times 10^{-3}$	$3.7 \times 10^{-3}$	/	/

Our studies indicate that the best precursors are  $\text{H}_2\text{SiO}_3$  and  $\text{BaCO}_3$  in the molar ratio  $\text{Ba}/\text{Si} = 0.7$ . The suitable dopants are  $\text{Eu}^{2+}$  and  $\text{Dy}^{3+}$ , and they must be taken in ratio of  $\text{Eu}/\text{Si} = 2.8 \times 10^{-3}$  and  $\text{Dy}/\text{Si} = 3.6 \times 10^{-3}$ . The best flux agent is NaCl, obtained directly from the reaction reported in Section 3.1 between  $\text{NH}_4\text{Cl}$  and  $\text{Na}_2\text{SiO}_3$ . Finally, the optimal thermal treatment conditions are 6 h at  $1100\text{ }^\circ\text{C}$  and the quartz crucible is the most appropriate.

Using these synthesis variables, we fabricated the best phosphor (sample C).

The reason for this choice comes from the combination of two factors: (i)  $\text{Ba}_5\text{Si}_8\text{O}_{21}$  as the main crystalline phase and (ii) the best characteristics in terms of luminescence. In fact, compared to sample D (76 wt.% of  $\text{Ba}_5\text{Si}_8\text{O}_{21}$ ), even if sample C has a lower amount of  $\text{Ba}_5\text{Si}_8\text{O}_{21}$  (59% wt.% due to its incomplete crystallization and the preferred orientation of some peaks), its luminescence characteristics are better. Table 2 and Figure 2 indicate a significant difference for the value of the initial emission:  $A_1$  of 180  $\text{mcd}/\text{m}^2$  and 18  $\text{mcd}/\text{m}^2$  for C and D, respectively. Furthermore, its luminescence characteristics are also higher than those of the reference sample (samples 1):  $A_1$  of 180  $\text{mcd}/\text{m}^2$  and 133  $\text{mcd}/\text{m}^2$  for C and 1, respectively (Table 2 and Figure 5). Sample C is better than sample E, which is comparable for the amount of  $\text{Ba}_5\text{Si}_8\text{O}_{21}$  and for  $A_1$ , but the  $\tau_2$  value of which is much lower (Table 2). Finally, if we compare sample C with samples F, G, and H, even if we have a similar amount of  $\text{Ba}_5\text{Si}_8\text{O}_{21}$ , they have a lower  $A_1$  value (Table 2).

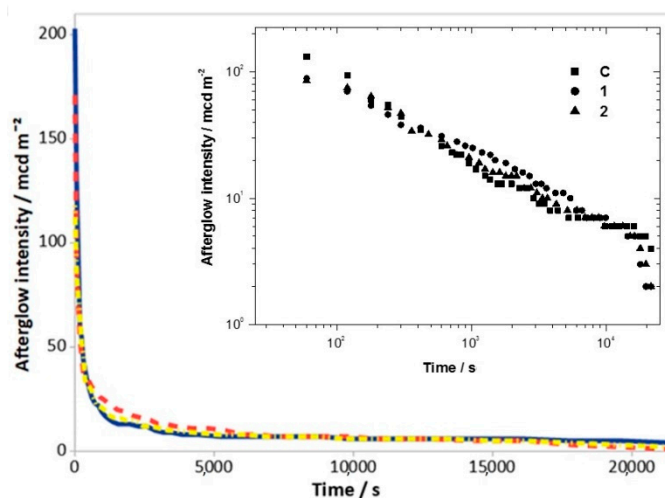


Figure 5. Decay curves of samples C (blue), 1 (red) and 2 (yellow). The upper inset showed the log-log plot.

## 5. Conclusions

In this study, we revealed the possibility to improve the characteristics of known phosphor  $\text{Ba}_5\text{Si}_8\text{O}_{21}:\text{Eu}^{2+},\text{Dy}^{3+}$ . To optimize the process and identify the correct parameters, it was necessary to select an appropriate procedure, as derived by experimental analysis. The variations of precursors, crucible composition, flux agents, dopants, time and temperatures of the treatment strongly influence the LPP characteristics.

Our best synthesis procedure must consider the following parameters:

- quartz crucible that is cheaper and more easily available than the platinum one.
- use of purified coal instead of  $\text{N}_2/\text{H}_2$  as a source of reducing atmosphere, which permits much more disposable and cheaper facilities.
- precursors such as  $\text{BaCO}_3$ ,  $\text{Na}_2\text{SiO}_3$ ,  $\text{NH}_4\text{Cl}$  and an economic flux agent such as  $\text{NaCl}$  (directly obtained during the synthesis).

Therefore, the data obtained in this study indicate that it is possible to prepare a  $\text{Ba}_5\text{Si}_8\text{O}_{21}:\text{Eu}^{2+},\text{Dy}^{3+}$  phosphor with improved LPP characteristics:  $A_1$  of 180  $\text{mcd}/\text{m}^2$  respect to 133  $\text{mcd}/\text{m}^2$ , which is the reference.

This phosphor was obtained from  $\text{Ba}/\text{Si} = 0.7$ ,  $\text{Eu}/\text{Si} = 2.8 \times 10^{-3}$ , and  $\text{Dy}/\text{Si} = 3.6 \times 10^{-3}$ , from  $\text{BaCO}_3$ ,  $\text{Na}_2\text{SiO}_3$ ,  $\text{NH}_4\text{Cl}$ ,  $\text{Dy}_2\text{O}_3$ , and  $\text{Eu}_2\text{O}_3$  at 1100 °C after 6 h of synthesis in a quartz crucible.

**Supplementary Materials:** The following are available online at <http://www.mdpi.com/1996-1944/12/1/183/s1>, Table S1: Most important peaks of  $\text{NaCl}$ ,  $\text{BaCO}_3$  in the sample C before the heat treatment compared with the reference data; Table S2: Most important peaks of  $\text{Ba}_5\text{Si}_8\text{O}_{21}$ ,  $\text{Ba}_4\text{Si}_6\text{O}_{16}$ ,  $\text{BaSi}_2\text{O}_5$  compared with the reference data; Figure S1: XRD of sample synthesised with  $\text{SiO}_2$ ,  $\text{BaCl}_2$  as precursor with molar ratio  $\text{Ba}/\text{Si} = 0.625$ ;  $\text{H}_3\text{BO}_3$



as flux agent;  $\text{Eu}_2\text{O}_3$ ,  $\text{Dy}_2\text{O}_3$  as dopants with molar ratios  $\text{Eu}/\text{Si} = 2.8 \times 10^{-3}$  and  $\text{Dy}/\text{Si} = 3.6 \times 10^{-3}$ . Thermal treatment conditions are 1200 °C for 12 h; Figure S2. XRD of sample synthesised with  $\text{Na}_2\text{SiO}_3$ ,  $\text{BaCO}_3$  and  $\text{NH}_4\text{Cl}$  as precursor with molar ratio  $\text{Ba}/\text{Si} = 0.7$ ;  $\text{Eu}_2\text{O}_3$ ,  $\text{Dy}_2\text{O}_3$  as dopants with molar ratios  $\text{Eu}/\text{Si} = 2.8 \times 10^{-3}$  and  $\text{Dy}/\text{Si} = 3.6 \times 10^{-3}$ . Thermal treatment conditions are 1100 °C for 12 h.

**Author Contributions:** Methodology: M.L.L., G.M., G.L., Investigation: A.S., M.L.L., G.M., G.L., Data Curation: M.L.L., G.M., G.L., Supervision: G.L.

**Funding:** This research received no external funding.

**Conflicts of Interest:** The authors declare no conflict of interest.

## References

1. Blasse, G.; Grabmaier, B.C. *Luminescent Materials*; Springer: Berlin/Heidelberg, Germany, 1994.
2. Lenard, P.E.A.; Schmidt, F.; Tomaschek, R. *Phosphoreszenz und fluoreszenz*, in: *Handbuch der Experimentalphysik*, 23; Akademie Verlagsgesellschaft: Leipzig, Germany, 1928.
3. Lehmann, W. Activators and co-activators in calcium sulfide phosphors. *J. Lumin.* **1972**, *5*, 87–107. [[CrossRef](#)]
4. Garlick, G.F.J.; Mason, D.E. Electron Traps and Infrared Stimulation of Phosphors. *J. Electrochem. Soc.* **1949**, *96*, 90–103. [[CrossRef](#)]
5. Yen, W.M.; Shionoya, S.; Yamamoto, H. *Phosphor Handbook*, 2nd ed.; CRC Press: New York, NY, USA, 1998.
6. Sonoda, M.; Takano, M.; Miyahara, J.; Kato, H. Computed radiography utilizing scanning laser stimulated luminescence. *Radiology* **1983**, *148*, 833–838. [[CrossRef](#)] [[PubMed](#)]
7. Chen, R.; McKeever, S.W.S. *Theory of Thermoluminescence and Related Phenomena*; World Scientific: Singapore, 1997.
8. Katsumata, T.; Sasajima, K.; Nabae, T. Characteristics of Strontium Aluminate Crystals Used for Long-Duration Phosphors. *J. Am. Chem. Soc.* **1998**, *81*, 413–416. [[CrossRef](#)]
9. Yamamoto, H.; Matsuzawa, T. Mechanism of long phosphorescence of  $\text{SrAl}_2\text{O}_4$ :  $\text{Eu}^{2+}$ ,  $\text{Dy}^{3+}$  and  $\text{CaAl}_2\text{O}_4$ :  $\text{Eu}^{2+}$ ,  $\text{Nd}^{3+}$ . *J. Lumin.* **1997**, *72*, 287–289. [[CrossRef](#)]
10. Matsuzawa, T.; Aoki, Y.; Takeuchi, N.; Murayama, Y.J. A New Long Phosphorescent Phosphor with High Brightness,  $\text{SrAl}_2\text{O}_4$ :  $\text{Eu}^{2+}$ ,  $\text{Dy}^{3+}$ . *Electrochem. Soc.* **1996**, *143*, 2670–2673. [[CrossRef](#)]
11. Lin, Y.; Tang, Z.; Zhang, Z.; Nan, C.W. Anomalous luminescence in  $\text{Sr}_4\text{Al}_{14}\text{O}_{25}$ :Eu, Dy phosphors. *Appl. Phys. Lett.* **2002**, *81*, 996–998. [[CrossRef](#)]
12. Guo, C.; Luan, L.; Huang, D.; Su, Q.; Lv, Y. Study on the stability of phosphor  $\text{SrAl}_2\text{O}_4$ :  $\text{Eu}^{2+}$ ,  $\text{Dy}^{3+}$  in water and method to improve its moisture resistance. *Mater. Chem. Phys.* **2007**, *106*, 268–272. [[CrossRef](#)]
13. Luitel, H.N.; Watari, T.; Torikai, T.; Yada, M.; Chand, R.; Xu, C.N.; Nanoka, K. Highly water resistant surface coating by fluoride on long persistent  $\text{Sr}_4\text{Al}_{14}\text{O}_{25}$ :  $\text{Eu}^{2+}/\text{Dy}^{3+}$  phosphor. *Appl. Surf. Sci.* **2010**, *256*, 2347–2352. [[CrossRef](#)]
14. Lü, X. Silica encapsulation study on  $\text{SrAl}_2\text{O}_4$ : $\text{Eu}^{2+}$ ,  $\text{Dy}^{3+}$  phosphors. *Mater. Chem. Phys.* **2005**, *93*, 526–530. [[CrossRef](#)]
15. Yu, S.; Pi, P.; Wen, X.; Cheng, J.; Yang, Z. Preparation and Luminescence of  $\text{SrAl}_2\text{O}_4$ :  $\text{Eu}^{2+}$ ,  $\text{Dy}^{3+}$  Phosphors Coated with Maleic Anhydride. *Can. J. Chem. Eng.* **2008**, *86*, 30–34. [[CrossRef](#)]
16. Joung, K.P.; Mi, A.L.; Kyoung, J.C.; Chang, H.K. Luminescence characteristics of yellow emitting  $\text{Ba}_3\text{SiO}_5$ : $\text{Eu}^{2+}$  phosphor. *J. Mater. Sci.* **2005**, *40*, 2069–2071.
17. Gong, Y.; Wang, Y.; Li, Y.; Xu, X.; Zeng, W. Fluorescence and phosphorescence properties of new long-lasting phosphor  $\text{Ba}_4(\text{Si}_3\text{O}_8)_2$ : $\text{Eu}^{2+}$ ,  $\text{Dy}^{3+}$ . *Opt. Express* **2011**, *19*, 4310–4315. [[CrossRef](#)] [[PubMed](#)]
18. Wang, P.; Xu, X.; Zhou, D.; Yu, X.; Qiu, J. Sunlight Activated Long-Lasting Luminescence from  $\text{Ba}_5\text{Si}_8\text{O}_{21}$ :  $\text{Eu}^{2+}$ ,  $\text{Dy}^{3+}$  Phosphor. *Inorg. Chem.* **2015**, *54*, 1690–1697. [[CrossRef](#)] [[PubMed](#)]
19. Xia, Z.; Zhang, Y.; Molocheev, M.S.; Atuchin, V.V.; Luo, Y. Linear structural evolution induced tunable photoluminescence in clinopyroxene solid-solution phosphors. *Sci. Rep.* **2013**, *3*, 3310. [[CrossRef](#)] [[PubMed](#)]
20. Yi, W.; Che, L.C.; Zewei, Q.; Maxim, M.; Atuchin, S.; Victor, V.; Ting-Shan, C.; Yujun, L.; Jun, L.; Guogang, L. Structural evolution induced preferential occupancy of designated cation sites by  $\text{Eu}^{2+}$  in  $\text{M}_5(\text{Si}_3\text{O}_9)_2$  (M = Sr, Ba, Y, Mn) phosphors. *RSC Adv.* **2016**, *6*, 57261–57265.
21. Eagleman, Y.; Bourret-Courchesne, E.; Derenzo, S.E. Fellow, Investigation of  $\text{Eu}^{2+}$  Doped Barium Silicates as Scintillators. *IEEE Trans. Nuclear Sci.* **2012**, *59*, 479–486. [[CrossRef](#)]

22. Yamaga, M.; Masui, Y.; Sakuta, S.; Kodama, N.; Kaminaga, K. Radiative and nonradiative decay processes responsible for long-lasting phosphorescence of  $\text{Eu}^{2+}$ -doped barium silicates. *Phys. Rev. B* **2005**, *71*, 205102/1–205102/7. [CrossRef]
23. Zhang, X.; Tang, X.; Zhang, J.; Gong, M. An efficient and stable green phosphor  $\text{SrBaSiO}_4:\text{Eu}^{2+}$  for light-emitting diodes. *J. Lumin.* **2010**, *130*, 2288. [CrossRef]
24. Nazarov, M. Luminescent materials and applications. *Mater. Sci. Chem.* **2016**, *6*, 41–74.
25. Li, Y.; Gecevicius, M.; Qiu, J. Long persistent phosphors—from fundamentals to applications. *Chem. Soc. Rev.* **2016**, *45*, 2090. [CrossRef] [PubMed]
26. Jian, X.; Setsuhisa, T. Persistent luminescence instead of phosphorescence: History, mechanism, and perspective. *J. Lumin.* **2019**, *205*, 581–620. [CrossRef]
27. Kamei, S.; Kojima, Y.; Nishimiya, N. Preparation and fluorescence properties of novel red-emitting  $\text{Eu}^{3+}$ -activated amorphous alkaline earth silicate phosphors. *J. Lumin.* **2010**, *130*, 2288–2292. [CrossRef]
28. Mishra, L.; Sharma, A.; Vishwakarma, A.K.; Jha, K.; Jayasimhadri, M.; Ratnam, B.V.; Jang, K.; Rao, A.S.; Sinha, R.K. White light emission and color tunability of dysprosium doped barium silicate glasses. *J. Lumin.* **2016**, *169*, 121–127. [CrossRef]
29. Lusvardi, G.; Malavasi, G.; Menabue, L.; Smargiassi, M. Systematic investigation of the parameters that influence the luminescence properties of photoluminescent pigments. *J. Lumin.* **2016**, *175*, 141–148. [CrossRef]
30. El-Khalik, M.A.; Hanafi, S.; Selim, S.A. Effect of various atmospheres and of autoclaving on the surface texture of thermally treated strontium oxalate. *Surf. Technol.* **1985**, *25*, 349–362. [CrossRef]
31. Rietveld, H.M. Line profiles of neutron powder-diffraction peaks for structure refinement. *Acta Crystallogr.* **1967**, *22*, 151–152. [CrossRef]
32. Toby, B.H.; Von Dreele, R.B. “GSAS-II: the genesis of a modern open-source all purpose crystallography software package”. *J. Appl. Crystallogr.* **2013**, *46*, 544–549. [CrossRef]
33. Toby, B.H. EXPGUI, a graphical user interface for GSAS. *J. Appl. Crystallogr.* **2001**, *34*, 210–213. [CrossRef]
34. Inorganic Crystal Structure Database (ICSD), Version 4.0.0. Available online: [http://www.fiz-karlsruhe.de/icsd\\_home.html](http://www.fiz-karlsruhe.de/icsd_home.html) (accessed on 13 December 2018).
35. Tsai, C.Y.; Lin, J.W.; Huang, Y.P.; Huang, Y.C. Modeling and Assessment of Long Afterglow Decay Curves. *Sci. World J.* **2014**, *104*, 1–8. [CrossRef]
36. Centre for Diffraction Data, A Windows Retrieval/display Program for Accessing the ICDD PDF-2 Database, PCPDFWIN version 2.3. Available online: <http://www.icdd.com/International> (accessed on 13 December 2018).
37. Huntelaar, M.E.; Cordfunke, E.H.P. The ternary system  $\text{BaSiO}_3\text{-SrSiO}_3\text{-SiO}_2$ . *J. Nucl. Mater.* **1993**, *201*, 250–253. [CrossRef]
38. Wang, P.; Xu, X.; Qiu, J.; Yu, X.; Wang, Q. Effects of  $\text{Er}^{3+}$  doping on the long-persistent luminescence properties of  $\text{Ba}_4(\text{Si}_3\text{O}_8)_2:\text{Eu}^{2+}$  phosphor. *Opt. Mater.* **2014**, *36*, 1826–1829. [CrossRef]



## **Chapter 2**

**One-pot sonocatalyzed synthesis of sol–gel graphite electrodes containing gold nanoparticles for application in amperometric sensing**



# One-pot sonocatalyzed synthesis of sol–gel graphite electrodes containing gold nanoparticles for application in amperometric sensing

Maria Laura Ligabue<sup>1</sup>, Fabio Terzi<sup>1</sup>, Chiara Zanardi<sup>1,\*</sup> , and Gigliola Lusvardi<sup>1,\*</sup>

<sup>1</sup>Department of Chemical and Geological Sciences, University of Modena e Reggio Emilia, Via G. Campi 103, 41125 Modena, Italy

**Received:** 21 January 2019

**Accepted:** 28 March 2019

**Published online:**

5 April 2019

© Springer Science+Business Media, LLC, part of Springer Nature 2019

## ABSTRACT

We propose here a one-pot synthetic approach to prepare sol–gel graphite electrodes containing gold nanoparticles (AuNPs). At variance with the traditional synthesis, in which AuNPs are prepared in advance with respect to the silica matrix, they were here obtained directly inside the sol–gel, during its formation. Two reduction methods, namely chemical and thermal reduction, were used to achieve AuNPs starting from a suitable gold precursor, either consisting of NaAuCl<sub>4</sub> or HAuCl<sub>4</sub>. Different experimental parameters were tested in order to direct the synthesis of the material to the characteristics sought, namely Si/Au molar ratio, graphite (g): silane precursor (mL) ratio, chemical nature of the gold precursor and of the reductant, duration and temperature of thermal treatment. Sol–gel was prepared by means of sonocatalysis, in order to reduce the amount of solvent and time necessary for the hydrolysis step. Composition of the material, as well as shape, size and distribution of AuNPs inside the silica matrix was evaluated by spectroscopic and microscopic techniques. Furthermore, electrochemical tests allowed us to ascertain the good conductivity of the composite material and the electrocatalytic activity of AuNPs with respect to glucose and ascorbic acid oxidation. These tests demonstrated that the electrodes obtained by thermal reduction show the best performance in terms of sensitivity for the detection of these analytes, suggesting the possible application of this composite in the field of amperometric sensing.

Address correspondence to E-mail: chiara.zanardi@unimore.it; gigliola.lusvardi@unimore.it

## Introduction

Sol–gel technique has received increasing interest in the recent years in many fields, including the preparation of amperometric sensors [1–7]. The resulting material combines the properties of a rigid three-dimensional structure, typical of inorganic materials, with the reactivity of organic functionalities. These sensors are extremely performing and cheap, thanks to the characteristics of the sol–gel structure and to the possibility to incorporate different electroactive materials in this structure. Furthermore, the renewal of the electroactive surface after each measurement, by means of routine mechanical cleaning procedures, is more rapid and simple in respect to the formation of a new electrode coating, that is the approach more frequently adopted [8].

A traditional sol–gel synthesis is generally carried out at relatively low temperatures and with the use of few reagents: an alkoxy silane, an acid or an alkaline catalyst and ethanol as solvent. In particular, tetraethoxysilane (TEOS) or methyltrimethoxysilane (MTMOS), possessing hydrophilic or hydrophobic properties, respectively, are among the alkoxy silane most widely used [9]. The material finally obtained is homogeneous, porous and possesses a low density [10].

An alternative sol–gel synthesis, based on the application of high-energy ultrasounds directly to the sol–gel precursors, was developed in the last 20 years [11]; the resulting material is generally called “sonogel”. Compared to the traditional synthesis, the advantages are the possibility to carry out the process without both adding the solvent and heating, with consequent reduction in the synthesis time.

An appropriate quantity of graphite has to be added to the silica-based matrix, aiming at obtaining a material with a conductivity suitable to be used in the electroanalytical field. Defined electroactive species can be also incorporated during the synthesis, aiming at modulating the properties of the material towards a specific application [12–14], e.g. the activation of electrocatalytic processes is useful for the detection of the target analyte. In particular, gold nanoparticles (AuNPs) were added to a sol–gel matrix, aiming at obtaining an electrode possessing quite interesting electrocatalytic properties to be exploited in the electroanalytical frame [14–18]. AuNPs are generally prepared in advance with

respect to the sol–gel synthesis, by following the synthetic method proposed by Turkevich et al. [19, 20], exploiting citrate ions as the chemical reductant. This approach allows the control of size and shape of AuNPs metal cores, constituting the two main factors affecting the electrocatalytic properties of the electrode materials.

As an alternative approach to embed AuNPs in the silica matrix, we recently proposed a method to obtain AuNPs during a sol–gel synthesis, by thermal reduction in a suitable gold precursor introduced in the silica matrix [21]. Shape, size and distribution of AuNPs, as well as the evolution of nano- and microstructure of the material, were tested as a function of the thermal treatment adopted. Moreover, physicochemical characterization of the material was carried out in order to single out the best conditions to obtain a sol–gel material containing AuNPs. These results enabled us to obtain materials for potential application in the field of bioactive systems.

Based on these interesting results, we decided to attempt the application of this synthetic approach in the field of electroanalysis, discussing here the one-pot synthesis of sonogel graphite electrodes containing AuNPs (SG–Au). AuNPs metal cores were obtained directly inside the sol–gel during its formation, by exploiting both a chemical and a thermal reduction method. The so obtained SG–Au electrodes were characterized as to chemical composition, morphology and electrochemical properties. In particular, the effectiveness of the synthetic approach was confirmed by UV–Vis adsorption spectroscopy and by X-ray powder diffraction (XRPD), whereas shape, size and distribution of AuNPs inside the silica matrix were evaluated by scanning electron microscopy (SEM). Electrochemical measurements allowed us to confirm the actual presence of Au<sup>0</sup> centres at the electrode–solution interface and the arising of effective electrocatalytic processes in charge of oxidation of specific analytes. To this aim, the oxidation responses of glucose (Gluc), ascorbic acid (AA) and dopamine (DP) at SG–Au electrodes were compared to those obtained at similar electrode systems not containing AuNPs (SG). These species were chosen in view of heavy drawbacks affecting their electrochemical oxidation at conventional electrode surfaces [22–24] and for their interest as benchmark analytes for the quality control of many food and biological stuffs. Glucose, in fact, is a simple sugar, naturally produced in plants from

photosynthetic processes and, for this reason, present in many foodstuffs, e.g. grapes and honey; it is also an important energy source for our body, although too high level of this sugar in blood indicates the occurrence of disease, widely known as diabetes. As to ascorbic acid, it is one of the main vitamins present in many fruits and vegetables, as well as in the human body; it is also added an antioxidant of many foodstuffs, e.g. fruit juices, to prolong their shelf life. Dopamine, at the end, is a neurotransmitter helping to send signals in the brain; however, low level of this species in blood should indicate the arising of serious disorders, such as schizophrenia or Parkinson's disease.

The results reported here support the possible application of SG–Au electrodes as amperometric sensors to controls levels of glucose, ascorbic acid and dopamine in all these situations.

## Materials and methods

### Synthesis of SG–Au electrodes

The reagents used for the synthesis of SG–Au and SG electrodes were of analytical grade. MTMOS,  $\text{HAuCl}_4 \cdot 3\text{H}_2\text{O}$ ,  $\text{NaAuCl}_4 \cdot 2\text{H}_2\text{O}$  and pure graphite powder (particle size  $< 20 \mu\text{m}$ ) were from Sigma-Aldrich. HCl and sodium citrate ( $\text{Na}_3\text{C}_6\text{H}_5\text{O}_7 \cdot 2\text{H}_2\text{O}$ ) were from Carlo Erba and  $\text{NaBH}_4$  from Fluka.

Figure 1 reports the schematic representation of the process leading to SG–Au electrodes. Briefly, MTMOS and the Au precursor (either 0.1 M  $\text{HAuCl}_4$  or solid  $\text{NaAuCl}_4$ ) were mixed in order to obtain a Si/Au molar ratios of either 50:1 [18] or 24:1 [25]. Since  $\text{HAuCl}_4$  is highly hygroscopic, it was added in the form of water solution. 0.1 M HCl was added as

catalyst, in a 60% vol with respect to MTMOS. The obtained mixture was sonicated in an ultrasonic bath (Bandelin Sonorex RK 100) within intervals of 15 min each, until obtaining a composite with viscosity suitable to be inserted in the glass tubes, avoiding massive liquid leakage. Graphite was then added to the composite to achieve conductivity appropriated to this specific application. The amount of graphite was carefully evaluated in relation to the characteristics of the resulting material and to the analytical performance of the electrodes obtained.

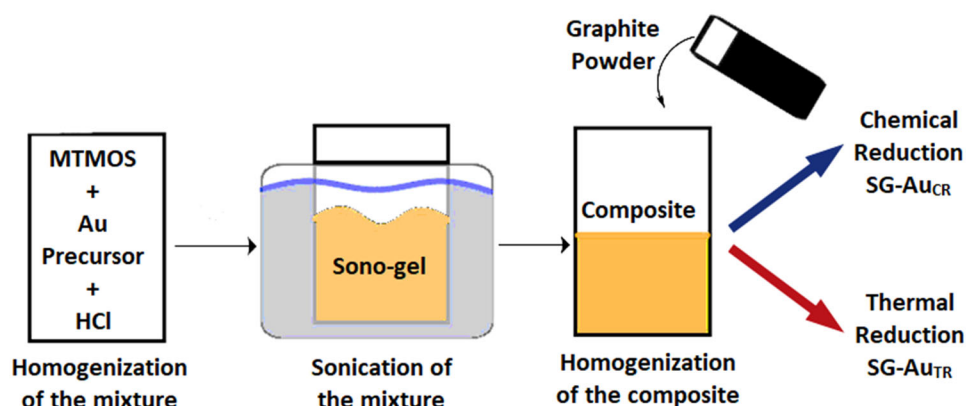
Both chemical and thermal reduction processes were tested to achieve reduction in the Au precursors; the resulting electrodes were named SG–Au<sub>CR</sub> and SG–Au<sub>TR</sub>, respectively.

In the case of SG–Au<sub>CR</sub>, the formation of AuNPs was realized after addition of either 1 mL of 1% (w/w)  $\text{NaBH}_4$  or 1.8 mL of 0.4 M  $\text{Na}_3\text{C}_6\text{H}_5\text{O}_7 \cdot 2\text{H}_2\text{O}$  solutions to the mixture depicted in Fig. 1 under stirring. The synthesis was performed at room temperature or by heating at 80 °C using  $\text{NaBH}_4$  or  $\text{Na}_3\text{C}_6\text{H}_5\text{O}_7 \cdot 2\text{H}_2\text{O}$ , respectively. The composite obtained was then inserted in glass capillary tubes (I.D. = 1.15 mm), compacted with a rigid plastic wire and air-dried to let the sol–gel material forming completely.

In the case of SG–Au<sub>TR</sub>, the mixture described in Fig. 1 was inserted in the glass capillary tubes and air-dried; the tubes were then put in an oven at selected temperatures (150, 250, 350 and 600 °C) for different times (24, 48, 72 h), in order to accomplish the reduction process.

Additional electrodes, named SG, were prepared by following the same procedures but without the addition of Au precursor. They were used as reference electrodes to confirm the effectiveness of AuNPs

**Figure 1** Schematic representation of the steps of the SG–Au electrodes synthesis.



included in the silica matrix in the activation of electrocatalytic processes in charge of the species tested.

### Study of the effect of the thermal treatment

The effect of the thermal treatment was studied by a thermogravimetric method (TG).

This analysis was carried out on the different components of the SG–Au electrodes, namely pure graphite powder, sol–gel matrix and the reaction mixture, consisting of MTMOS, HCl, Au precursor and graphite powder. To this aim, 1 g of each of the mentioned components was placed in an oven, inside a platinum crucible, to evaluate the mass loss at temperatures ranging from 150 to 600 °C.

### Morphological and spectroscopic characterization of AuNPs

Morphological and spectroscopic characterizations were achieved by analysing part of the resulting composite material scratched out from the glass capillaries.

Shape, size and distribution of AuNPs formed inside the silica matrix were defined by SEM micrographs; they were collected by a SEM-FEG microscope (Nova NanoSEM) set up in a scanning transmission electron mode (STEM) and analysed by ImageJ [26] and Gwyddion [27] processing software. The Si/Au molar ratio in the resulting material was estimated by the elemental analysis performed with energy-dispersive spectroscopy (EDS) probe (X-EDS Bruker QUANTAX-200).

Mineralogical studies (phase identification) were performed by XRPD. Spectra were collected with a PANalytical X'Pert Pro Bragg–Brentano diffractometer, using Ni-filtered Cu-K $\alpha$  radiation ( $\lambda = 1.54060 \text{ \AA}$ ) with an X'Celerator detector. The patterns were taken over the diffraction angle  $2\theta$  in the range 5°–70°, with a time step of 50 s and a step size of 0.03° (angular step).

Actual formation of AuNPs was also confirmed by UV–Vis spectra. They were collected with a HP diode-array spectrophotometer (model 8452-A) in the 190–950 nm spectral range, by using the diffuse reflectance technique and a BaSO<sub>4</sub> plate as reflectance standard.

### Electrochemical characterization of SG–Au electrodes

Electrochemical tests were used to confirm the presence of AuNPs at the electrode-solution interface, to test the overall charge-transfer resistance of materials obtained in various conditions and to define the electrocatalytic performance of the relevant electrodes. All electrochemical tests were performed with a potentiostat/galvanostat (PalmSens Instruments), by completing the electrochemical cell with an Ag/AgCl/KCl, 3 M (Amel) reference electrode and a Pt wire counter-electrode.

The chemical species used for electrochemical tests were 1,1-ferrocene dimethanol (Fc-MeOH<sub>2</sub>), LiClO<sub>4</sub>, KOH, D-(+)-glucose (Gluc), ascorbic acid (AA) and dopamine (DP) from Sigma-Aldrich and H<sub>2</sub>SO<sub>4</sub> from Carlo Erba. All solutions were prepared with ultra-pure water (18 M $\Omega$  cm) just before the use.

Charge-transfer resistance of the various electrode materials was tested by recording cyclic voltammetric (CV) traces in 1 mM Fc-MeOH<sub>2</sub>, 0.1 M LiClO<sub>4</sub> aqueous solution, in the 0.0 to + 0.6 V potential range, 0.05 V s<sup>-1</sup> scan rate. This same measurement allowed us to compare the total electroactive surface of electrodes obtained in different conditions.

The presence of Au<sup>0</sup> centres at the electrode-solution interface was verified by recording CV responses in 0.05 M H<sub>2</sub>SO<sub>4</sub> solution, within the – 0.5 to + 1.5 V potential window, 0.05 V s<sup>-1</sup> scan rate: the charge spent in the reduction process, centred at ca. + 0.8 V, is proportional to the area of AuNPs exposed to the solution [28]. These same experimental conditions were also used to define the background currents at SG electrodes obtained in different conditions. To this aim, the difference between the forward (positive) and backward (negative) current values registered at + 1.0 V ( $\Delta i$ ) was calculated from the voltammogram, aiming at evaluating the effect of the thermal treatment on the electrochemical behaviour of the electrodes.

The electrocatalytic performance of SG–Au electrodes was tested with respect to Gluc and AA oxidation. In particular, CV responses in 0.1 M LiClO<sub>4</sub> aqueous solution at pH 12 (0.01 M KOH), in the absence and in the presence of 5 mM Gluc, were registered in the – 0.5 to + 0.6 V potential window, 0.05 V s<sup>-1</sup> potential scan rate. As to AA, differential pulse voltammetric (DPV) traces were recorded in 0.1 M phosphate buffer solution at pH 7.2 (PBS) in

the absence and in the presence of 1 mM AA within potential values between  $-0.3$  and  $+0.5$  V,  $0.015$  V s<sup>-1</sup> scan rate, 0.1 s modulation time and 0.05 V potential impulse.

Student's *t* test and ANOVA test at the confidence limit of 95% ( $\alpha = 0.05$ ) were adopted aiming at evidencing the influence of the various synthetic parameters in the electrochemical and electrocatalytic properties of the resulting materials; to such a purpose, we collected and compared the results arising from at least three electrodes obtained in the same conditions. Comparison between the voltammograms recorded at SG–Au and SG electrodes was also carried out in order to put in light the effectiveness of AuNPs inside the material in the arising of actual electrocatalytic processes.

SG–Au electrodes showing best performance were tested in solutions containing these analytes at different concentration intervals, namely 1.0–20 mM and 0.1–2.0 mM for Gluc and AA, respectively.

The performance of SG–Au and SG electrodes was finally compared with respect to voltammetric traces registered from the simultaneous presence of AA and DP in the same solution. To this aim, DPV responses were registered in 2.5 mM AA, 0.1 M PBS, at DP concentration ranging between 0.0 and 0.4 mM.

## Results and discussion

The mixture used for the synthesis of SG–Au electrodes (see Fig. 1) generally possessed the subsequent composition: 0.3 mL of MTMOS, 0.18 mL of HCl, gold precursor, either in a 24:1 or 50:1 Si/Au molar ratio and 0.3 g of graphite. The use of a different amount of graphite was also attempted, as better described below.

A first screening of the properties of the SG–Au materials obtained in various conditions was achieved by recording voltammetric responses in H<sub>2</sub>SO<sub>4</sub>. In this media, in fact, the possible presence of an electrochemical process correlated with Au<sup>0</sup> oxidation/reduction gives us direct evidence of the effectiveness of either chemical or thermal reduction in the Au precursor. In any case, the voltammetric responses obtained confirm the actual formation of Au<sup>0</sup> metal cores, although better electrochemical results were obtained by using a Si/Au molar ratio of 24:1. A higher (50:1) molar ratio, in fact, resulted in an amount of AuNPs too low to give rise to

electrochemical responses well resolved from the background current. Consequently, 24:1 molar ratio was chosen for all the syntheses reported hereafter.

### Synthesis and characterization of SG–Au<sub>CR</sub> electrodes

As outlined in the experimental section, AuNPs were directly obtained during the sol–gel formation by adding either citrate or borohydride ions as reductant of gold(III) precursor.

In both cases, SEM-FEG micrographs confirm the actual formation of NPs fairly homogeneously distributed inside an amorphous matrix. EDS analyses indicate that NPs actually consist of Au metal cores surrounded by a matrix essentially constituted of Si, C and O (see Online Resource 1). A 24:1 molar ratio between Si and Au is confirmed in the resulting SG–Au material. The percentage of the total surface occupied by AuNPs results, in any case, around 1%.

The reduction process achieved by the addition of citrate ions gives rise to AuNPs with quite a spherical shape (Fig. 2a, b). In particular, the use of NaAuCl<sub>4</sub> (Fig. 2a) leads to the formation of a great amount of AuNPs, more homogeneously dispersed inside the matrix with respect to AuNPs obtained from HAuCl<sub>4</sub> (Fig. 2b). The distribution histograms (Fig. 2c) indicate that AuNPs obtained from HAuCl<sub>4</sub> possess a modal value of diameter in the 10–20 nm range, whereas AuNPs in the range < 10–20 nm are obtained from NaAuCl<sub>4</sub>. The modal values of diameters obtained are in agreement to those reported in the literature for AuNPs synthesized in similar conditions but in the absence of sol–gel [25].

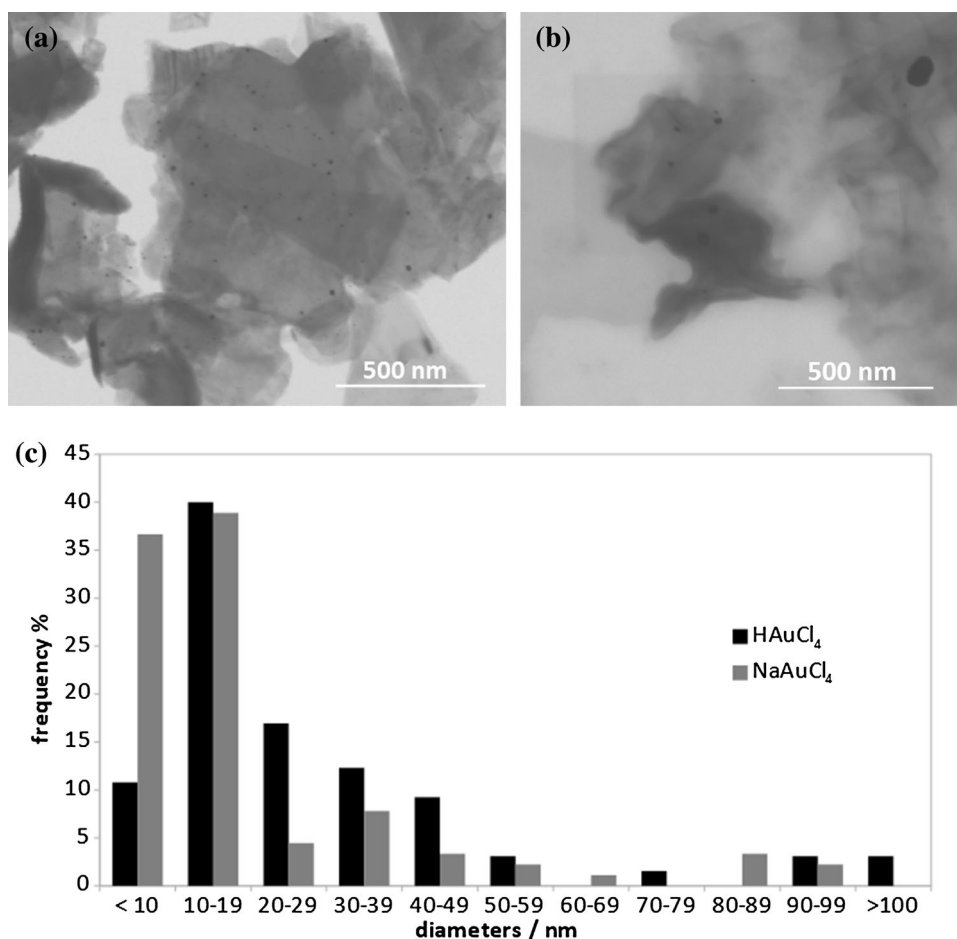
The use of NaBH<sub>4</sub> as a reductant gives rise to AuNPs possessing a wider size dispersion, i.e. ranging between 10 and 45 nm.

As to the performance of the electrodes obtained from these materials, the use of silica-based composites synthesized by NaBH<sub>4</sub> was discarded on the basis of voltammograms registered in the pure electrolyte solution. They show quite high background current values and the presence of undesired oxidation and reduction peaks due to not well-defined side products of the reduction procedure.

Despite finding better results with the use of composites obtained from Na<sub>3</sub>C<sub>6</sub>H<sub>5</sub>O<sub>7</sub>, these electrodes still lead to register quite high background currents. In particular, in CV responses registered in H<sub>2</sub>SO<sub>4</sub> solution, the peak ascribable to AuNPs is only



**Figure 2** SEM-FEG micrographs (transmitted electron) of SG-Au<sub>CR</sub> obtained by reduction with citrate ions of **a** NaAuCl<sub>4</sub> and **b** HAuCl<sub>4</sub>. **c** Relevant size distribution histograms of SG-Au<sub>CR</sub>.



poorly detectable (see Online Resource 2), indicating that this material is not suitable to be used in the electroanalytical frame.

Due to the rather poor electrochemical performance of SG-Au<sub>CR</sub>, we decided to test an alternative reduction approach based on a thermal treatment.

### Synthesis and characterization of SG-Au<sub>TR</sub> electrodes

As outlined in the experimental section, gold(III) reduction was obtained in this case by a thermal treatment of the silica-based composite at defined interval times and temperatures. In general, the compactness of electrodes obtained from HAuCl<sub>4</sub> was rather poor, with evident formation of holes and cracks (see Online Resource 3). This result was ascribed to the requirement to dissolve this precursor in water: massive solvent evaporation occurred during the thermal treatment, leading to spontaneous leakage of the material out from the capillaries. As a

consequence, the electrodes discussed hereafter are obtained from NaAuCl<sub>4</sub> precursor.

As to the effects of the graphite amount on the performance of the resulting electrodes, we studied materials obtained from graphite (g): MTMOS (mL) ratios ranging from 1:1 to 1:4. CV traces registered in the Fc-MeOH<sub>2</sub> solution confirmed that they all show low charge-transfer resistance as far as the amount of graphite was not lower than a 1:2 ratio. Furthermore, voltammetric responses in H<sub>2</sub>SO<sub>4</sub> solution let us to conclude that the amount of graphite did not significantly affect the amount of Au<sup>0</sup> actually formed. We finally chose a 1:1 ratio since the material could be more easily compacted inside the glass capillaries.

The effect of the thermal treatment on the properties of the resulting electrodes was then tested by analysing the different components of the composite by TG: (1) pure graphite powder, (2) sol-gel matrix and (3) the reaction mixture, consisting of MTMOS, HCl, Au precursor and graphite powder.

As expected, evident graphite combustion was observed at temperature values as high as 500 °C, thus preventing the use of so high temperature values for the synthesis of SG–Au<sub>TR</sub> electrodes. As a consequence of this process, in fact, the major part of graphite is lost when attempting to produce SG–Au electrodes at these temperature values: a poorly coherent red powder is finally obtained, however, indicating that AuNPs are actually formed as a consequence of the thermal treatment.

The composite mixture was analysed by TG after being air-dried for 24 h, to simulate the actual preparation of the electrode material. In particular, the residual mass was calculated after heating the sample at a defined temperature values until reaching a steady state: values of 96, 94 and 90% were obtained at 150, 250 and 350 °C, respectively. The effect observed for the composite can not be merely ascribed to the sol–gel itself, because it only shows a mass variation before 150 °C. We have to conclude that the formation of the composite at room temperature leads to strong entrapment of the solvent inside the material, which is progressively desorbed at increasing the temperature of the system. As a consequence of the mass loss, the thermal treatment increases the porosity of the material and affects the mechanical stability of electrodes obtained at 350 °C. Only samples obtained at 150 and 250 °C finally possess adequate mechanical properties to be applied as an electrode material.

The electrochemical performance of the electrodes obtained at these temperatures was firstly investigated by recording electrochemical responses in Fc–MeOH<sub>2</sub> solutions. The peak-to-peak separation close to the theoretical value of 59 mV and the linear correlation between the current peak and the square root of the scan rate (see Online Resource 4) let us conclude that the charge-transfer resistance throughout the electrode body is low and that the materials obtained are suitable for the use in the field of electroanalysis.

In any case, SEM-FEG micrographs (Fig. 3a, b) once more confirm the presence of NPs possessing a spherical shape, more homogeneously dispersed inside the amorphous matrix with respect to AuNPs chemically synthesized from the same gold(III) precursor. The relevant size distribution histograms (Fig. 3c) indicate that, irrespective of the temperature used for the thermal reduction process, a great amount of AuNPs possesses a modal value of

diameter in the 10–20 nm range. EDS elemental analysis once more confirms that NPs actually consist of Au metal cores and that a 24:1 molar ratio between Si and Au is preserved in the final material (see Online Resource 5). In addition, this result was confirmed by the complete absence of black spots in the SEM-FEG micrograph obtained in STEM mode and by EDS analyses of the SG<sub>TR</sub> electrode prepared with thermal reduction at 150 °C for 24 h (see Online Resource 6).

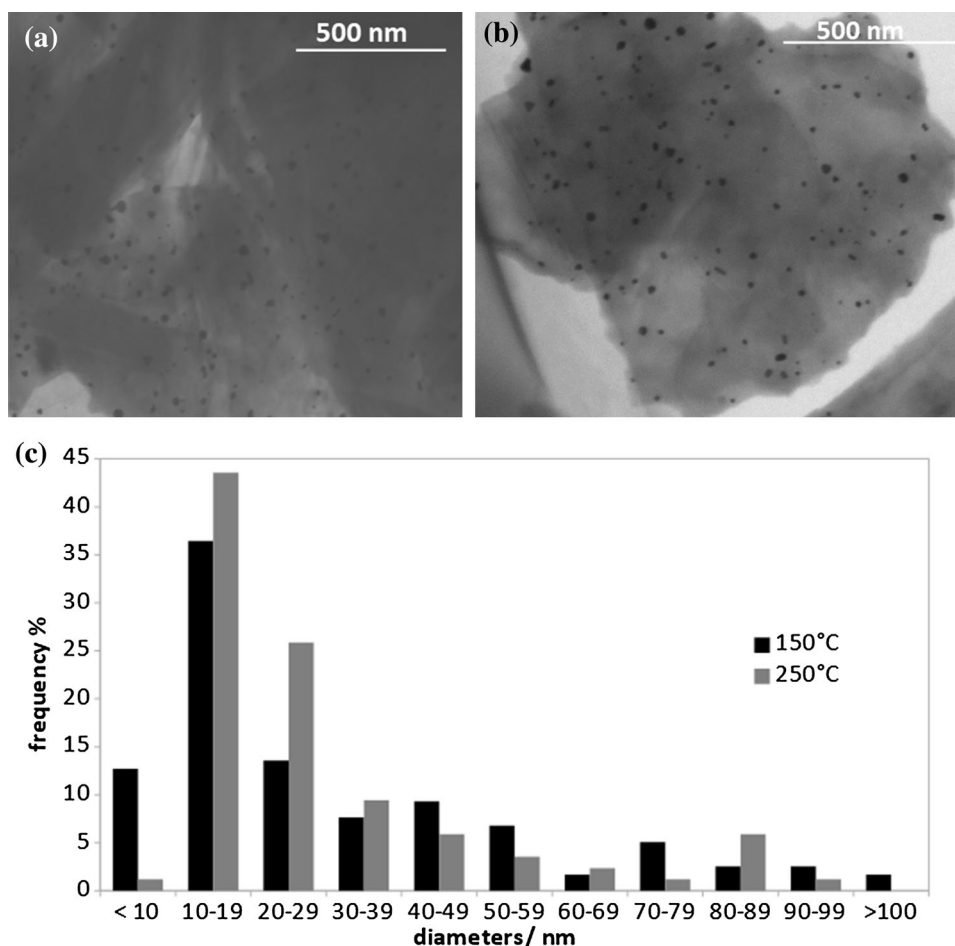
According to the elaboration of SEM-FEG images, the percentage of the total surface finally occupied by AuNPs results, in any case, around 2.6%.

A more punctual comparison of the Au<sup>0</sup> surface present at the electrode-solution interface was once more achieved by evaluating the electrochemical response in H<sub>2</sub>SO<sub>4</sub> solution (see Online Resource 7). To get reliable evaluation of the effect afforded by the different parameters used for the thermal treatment, we decided to perform a two-factor experimental design. Six different sets of electrodes were prepared by changing both the temperature (150 and 250 °C) and the duration (24, 48, 72 h) of the thermal treatment. At least three electrodes for each couple of variables were tested in order to define the significance of these parameters. Table 1 reports the mean values of the charge spent in the reduction response at ca. + 0.8 V, together with the relevant standard deviation. As clearly seen, no evident trend can be evidenced at increasing both the temperature and the duration of the thermal treatment, indicating that these parameters do not affect significantly the amount of AuNPs produced.

As observed, standard deviation values are quite high, indicating that the amount of AuNPs present at the electrode-solution interface changes among the different electrodes obtained in the same experimental conditions. However, due to the intrinsic nature of this material, allowing the registration of well-repeatable voltammetric signals (see hereafter), SG–Au electrodes can act as reusable sensor systems. For this reason, the poor reproducibility of sensor building up does not constitute a drawback in this case.

Table 1 also puts in light that background current values at SG<sub>TR</sub> electrodes ( $\Delta i$ ) increases at increasing the temperature used for the formation of material. A material most suitable for electrochemical purposes was obtained at 150 °C, independently of the duration of the thermal treatment. The electroanalytical

**Figure 3** SEM-FEG micrographs (transmitted electron) of SG-Au<sub>TR</sub> obtained by NaAuCl<sub>4</sub> after 24 h at: **a** 150 °C, **b** 250 °C. **c** Relevant size distribution histograms of SG-Au<sub>TR</sub>.



**Table 1** Average values of the peak area centred at ca. + 0.8 V and of  $\Delta i$  at + 1.0 V calculated from the 10th voltammogram scan registered in 0.05 M H<sub>2</sub>SO<sub>4</sub> at SG-Au<sub>TR</sub> and at SG<sub>TR</sub> electrodes, respectively; the relevant standard deviation calculated from the responses of at least three electrodes obtained in the same experimental conditions is reported within brackets

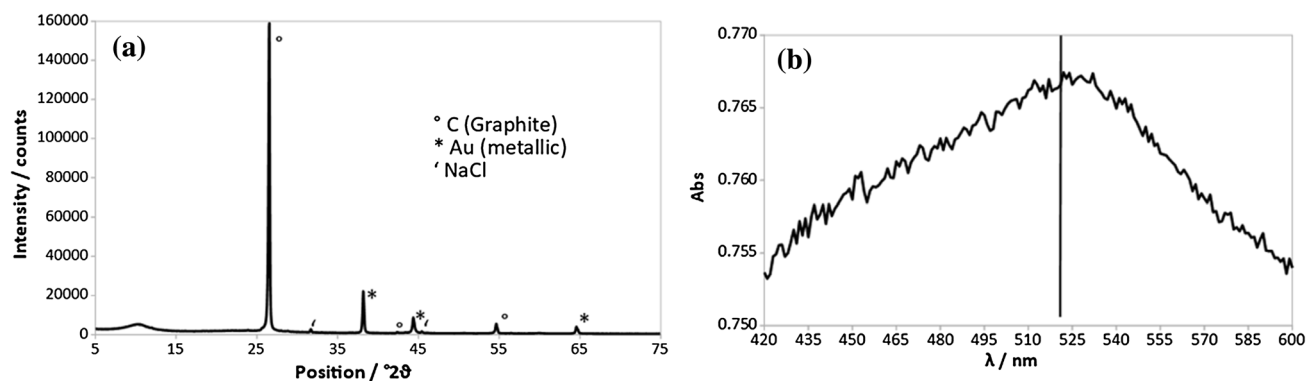
<i>T</i> (°C)	<i>t</i> (h)	Peak area (μC)	$\Delta i$ (μA)
150	24	0.039 (0.026)	0.31 (0.06)
	48	0.031 (0.014)	0.40 (0.21)
	72	0.065 (0.037)	0.51 (0.25)
250	24	0.030 (0.018)	1.44 (0.81)
	48	0.015 (0.016)	0.72 (0.31)
	72	0.032 (0.020)	1.09 (0.48)

performance of the relevant electrode devices (see below) indicates that there is no real advantage in extending the time required for the synthesis over 24 h.

For this reason, although detailed electrochemical investigations were performed with electrodes obtained in the various conditions, the discussion reported below (see “Gluc detection”, “AA and DP detection” sections) will only consider results registered with electrodes achieved by a thermal treatment at 150 °C for 24 h.

The composite obtained in these conditions was also more deeply investigated by spectroscopic analyses. In particular, the presence of AuNPs inside the silica-based matrix, as well as their crystalline nature, was confirmed by X-ray diffraction analysis. Figure 4, in fact, reveals the presence of peak’s characteristic of metallic gold (JCPDS 04-0784) [29]; further, peaks marked in the spectrum are correlated with the presence of graphite (JCPDS 75-2078) [29] and of NaCl (JCPDS 5-0628) [29] deriving from residual reagents.

UV-Vis spectroscopy also confirms the actual formation of AuNPs: an absorption band with a maximum at 525 nm can be ascribed to the characteristic



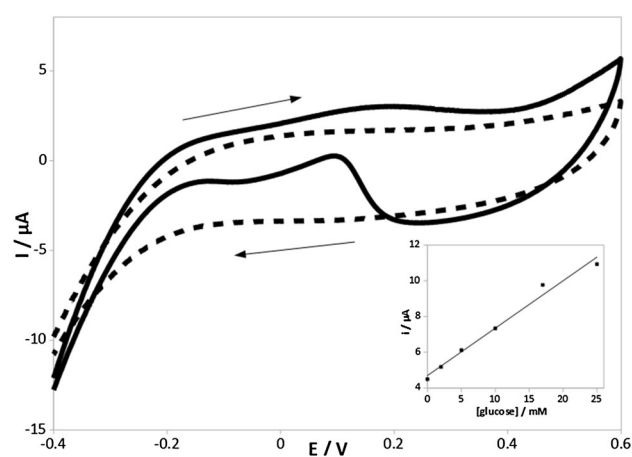
**Figure 4** **a** X-ray powder diffraction and **b** UV spectroscopy of SG–Au<sub>TR</sub> obtained by NaAuCl<sub>4</sub> after 24 h at 150 °C.

plasmon band of AuNPs. Similar adsorption, in fact, is not present in spectra recorded with SG<sub>TR</sub> electrodes.

### Gluc detection

Gluc was chosen as a first species to highlight the electrocatalytic properties of AuNPs included in the sol–gel matrix. Although universally agreed mechanism for non-enzymatic glucose oxidation remains unresolved [30], it is widely accepted that it necessarily requires the presence of hydrous Au oxides. They are formed in highly alkaline solutions during the scan towards positive potentials, and they constitute the actual electrocatalytic sites for glucose oxidation [22, 23]. No oxidation of this species can be, thus, obtained at sol–gel-based electrodes in the absence of AuNPs [14]. Massive electrode passivation often limits the possible detection of this quite important analyte by a non-enzymatic approach. For this reason, although the use of biosensors for Gluc detection is limited by the enzyme lifetime, it is often considered the only choice possible for the detection of this, quite important, analyte.

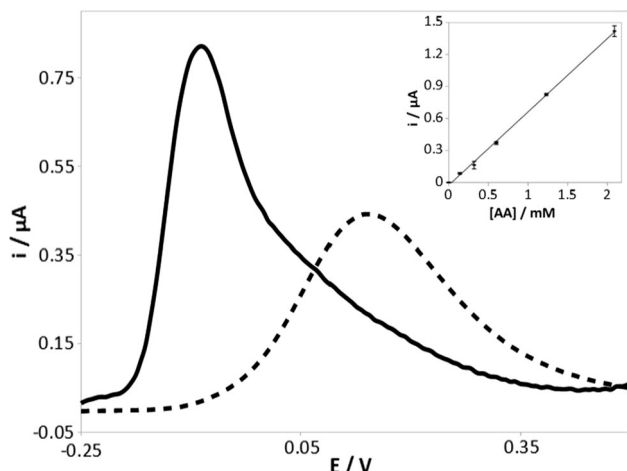
Figure 5 reports the CV trace recorded for Gluc oxidation at SG–Au<sub>TR</sub>. The anodic peak obtained at increasing the potential proves the effectiveness of AuNPs in activating effective electrocatalytic processes in charge of Gluc oxidation. As a consequence of the high standard deviation observed for Au response in H<sub>2</sub>SO<sub>4</sub> solutions, the values of current peak registered for glucose oxidation at five different electrodes obtained in the same conditions possess quite a high relative standard deviation (RSD = 63%). However, well-repeatable voltammetric signals can be registered by repeating four time the analysis with



**Figure 5** CV traces registered at SG–Au<sub>TR</sub> (150 °C, 24 h) electrode in the absence (dotted line) and the presence (solid line) of 5 mM Gluc in 0.1 M LiClO<sub>4</sub> (pH 12); 0.05 V s potential scan rate. Inset reports the relevant calibration plot for the forward current peak at ca. + 0.2 V.

a single SG–Au<sub>TR</sub> electrode (RDS = 10). This result suggests that the sensor can be used in following analytical detections.

The calibration plot, obtained by analysing Gluc solutions at different concentrations (see inset of Fig. 5), indicates that SG–Au<sub>TR</sub> gives a signal directly correlated with the concentration of this analyte, and lets us conclude that it is suitable to be used as a sensor for the detection of this analyte. The calibration plot was obtained both by analysing solutions at increasing concentration of Gluc and by randomizing the measurement in the different solutions; we could observe that the values of slope and intercept in the two cases do not differ significantly ( $\alpha = 0.05$ ), indicating that the electrode system does not suffer of evident surface passivation.



**Figure 6** DPV traces, subtracted for the relevant background current, registered at SG–Au<sub>TR</sub> (150 °C, 24 h, solid line) and SG<sub>TR</sub> (150 °C, 24 h, dotted line) in 1 mM AA, PBS (pH 7.2). Inset reports the relevant calibration plot at different AA concentrations obtained for SG–Au<sub>TR</sub>.

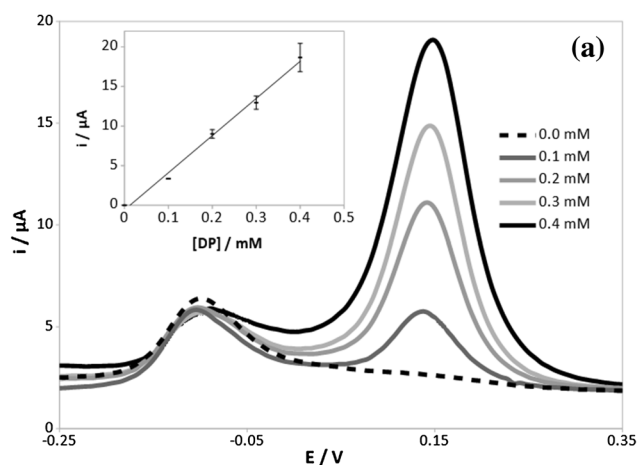
#### AA and DP detection

Unlike Gluc, AA can be electrochemically oxidized at both graphite and AuNPs surfaces [31–33], giving us the possibility to highlight the characteristics of the composite material. DPV responses obtained in 1 mM AA solutions show an oxidation peak centred at + 0.1 V at SG electrode, ascribable to AA oxidation to dehydroascorbic acid. It is significantly ( $\alpha = 0.05$ ) anticipated at – 0.1 V when using SG–Au<sub>TR</sub> (Fig. 6). This finding highlights the effectiveness of AuNPs inside the composite in activating the electrocatalytic

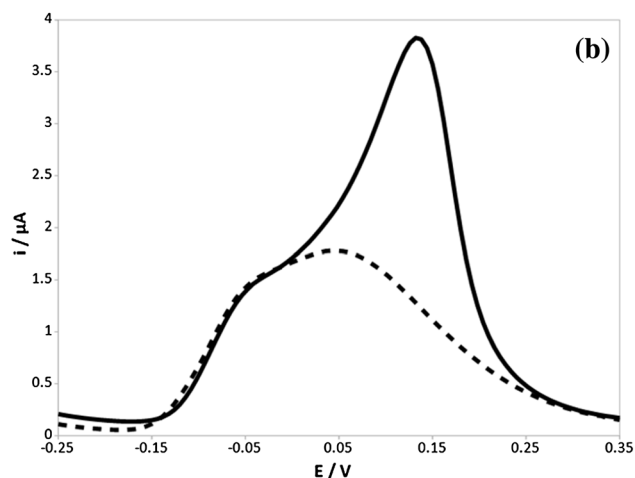
oxidation of AA. As a consequence, the peak intensity obtained at electrodes containing AuNPs is well higher with respect to that obtained at SG electrodes.

Electrochemical measurements carried out both by continuously increasing the concentration of AA in solution and by randomly analysing solutions at different concentrations lead to calibration plots not significantly different from each other ( $\alpha = 0.05$ ), indicating the satisfactory repeatability of the voltammetric responses.

The significant shift of the response due to AA oxidation at lower potential values gives us the opportunity to simultaneously register voltammetric responses ascribable to DP. Figure 7 reports the overlap of DPV traces recorded at either SG–Au<sub>TR</sub> or SG electrodes in solutions of 2.5 mM AA also containing different amounts of DP. As observed, two well-resolved voltammetric signals are obtained only in the first case, i.e. when AuNPs are present inside the composite. Furthermore, the signal due to AA oxidation is very stable and independent of the concentration of DP, demonstrating that the two oxidation processes do not influence each other. The repeatability of the electrochemical responses was tested by recording three subsequent scans in the same solution; calibration plot in the inset of Fig. 7a finally reports the error bars associated with these measurements. The results let us conclude that this electrochemical process is affected by a very low surface passivation [34].



**Figure 7** DPV traces registered at **a** SG–Au<sub>TR</sub> (150 °C, 24 h) and at **b** SG<sub>TR</sub> (150 °C, 24 h) in 2.5 mM AA, PBS (pH 7.2) in the absence (dotted line) and in the presence (black solid line) of



0.4 mM DP. Voltammograms obtained in solutions containing DP at different concentrations are also reported in **a** together with the relevant calibration plot in the inset.

## Conclusions

SG–Au electrodes were obtained by one-pot sono-catalyzed approach, which allows the direct formation of AuNPs during sol–gel synthesis; this approach allows us to strongly reduce the time required for the synthesis of the material with respect to the traditional method.

The compositional and morphological characterization indicates that both chemical and thermal reduction in gold(III) precursor ( $\text{HAuCl}_4$  or  $\text{NaAuCl}_4$ ) causes the formation of AuNPs possessing a spherical shape. Thermal reduction allows the formation of AuNPs characterized by a lower dispersivity with respect to the chemical reduction. The actual formation of AuNPs inside the silica-based matrix was also confirmed by spectroscopic analyses, i.e. by the presence of diffraction peaks and of a plasmon band characteristic of AuNPs.

Irrespective of the temperature used, the major part of the AuNPs possesses a mean diameter in the 10–14 nm range, whereas higher temperatures (250 °C) only increase the amount of NPs possessing diameters larger than 15 nm. The percentage of the electrode surface occupied by AuNPs results ca. 2.6%. For the specific application thought for this material, i.e. in the frame of amperometric sensing, best performance is obtained by the thermal reduction approach performed for 24 h at 150 °C, starting from the  $\text{NaAuCl}_4$  precursor, with a 24:1 Si/Au molar ratio and a 1:1 graphite (g) : MTMOS (mL) ratio. Well-repeatable voltammetric signals, characterized by fairly low background currents, are registered by using electrodes obtained in these conditions.

The effectiveness of AuNPs present inside these electrode systems are highlighted both for the non-enzymatic oxidation of Gluc and for the contemporary detection of AA and DP from the same solution.

## Acknowledgements

This research was financed with funds from the University of Modena e Reggio Emilia, (Project FAR 2015, “Sviluppo Di Materiali A Base Silicatica Per Applicazioni Sensoristiche” Decreto rettorale n. 267/2016 Prot. n. 81676 del 28/06/2016). Authors also thank the “Centro Interdipartimentale Grandi Strumenti” (CIGS) of the University of Modena e

Reggio Emilia for instrument availability and assistance.

**Electronic supplementary material:** The online version of this article (<https://doi.org/10.1007/s10853-019-03580-y>) contains supplementary material, which is available to authorized users.

## References

- [1] Tsionsky M, Gun M, Glezer M, Lev O (1994) Sol-gel-derived ceramic-carbon composite electrodes: introduction and scope of applications. *Anal Chem* 66:1747–1753
- [2] Lev O, Tsionsky M, Rabinovich L, Glezer V, Sampath S, Pankratov I, Gun J (1995) Organically modified sol-gel sensors. *Anal Chem* 67:22A–30A
- [3] Collinson MM, Howells AR (2000) Sol-gels and electrochemistry: research at the intersection. *Anal Chem* 72:702A–709A
- [4] Rabinovich L, Lev O (2001) Sol-gel derived composite ceramic carbon electrodes. *Electroanal Int J Devoted Fundam Pract Asp Electroanal* 13:265–275
- [5] Walcarius A, Mandler D, Cox JA, Collinson M, Lev O (2005) Exiting new directions in the intersection of functionalized sol-gel materials with electrochemistry. *J Mater Chem* 15:3663–3689
- [6] Walcarius A (2001) Electroanalysis with pure, chemically modified, and sol-gel-derived silica-based materials. *Electroanal Int J Devoted Fundam Pract Asp Electroanal* 13:701–718
- [7] Walcarius A (2018) Silica-based electrochemical sensors and biosensors: recent trends. *Curr Opin Electrochem* 10:88–97
- [8] Seeber R, Terzi F, Zanardi C (2014) Functional materials in amperometric sensing: polymeric, inorganic, and nanocomposite materials for modified electrodes. Springer, Heidelberg
- [9] Juan-Díaz MJ, Martínez-Ibáñez M, Hernández-Escolano M, Cabedo L, Izquierdo R, Suay J, Gurruchaga J, Goni I (2014) Study of the degradation of hybrid sol-gel coatings in aqueous medium. *Prog Org Coat* 77:1799–1806
- [10] Brinker CJ, Scherer GW (1990) Sol gel science: the physics and chemistry of sol-gel processing. Academic Press Inc., New York
- [11] Cordero-Rando MM, Hidalgo-Hidalgo de Cisneros JL, Blanco E, Narajo-Rodriguez I (2002) The sonogel-carbon electrode as a sol-gel graphite-based electrode. *Anal Chem* 74:2423–2427

- [12] Ballarin B, Zanardi C, Schenetti L, Seeber R, Hidalgo-Hidalgo de Cisneros JL (2003) Synthesis and electrochemical characterisation of novel sonogel-carbon-polythiophene microstructured electrodes. *Synth Metals* 139:29–33
- [13] Abdelrahim MYM, Benjamin SR, Cubillana-Aguilera LM et al (2013) Study of electrocatalytic activity of cerium oxide and gold-studded cerium oxide nanoparticles using a sonogel-carbon material as supporting electrode: electroanalytical study in apple juice for babies. *Sensors* 13:4979–5007
- [14] Crespo-Rosa JR, Zanardi C, ElKaoutit M, Terzi F, Seeber R, Naranjo-Rodriguez I (2014) Electroanalytical applications of a graphite-Au nanoparticles composite included in a sonogel matrix. *Electrochim Acta* 122:310–315
- [15] Daniel M-C, Astruc D (2014) Gold nanoparticles: assembly, supramolecular chemistry, quantum-size-related properties, and applications toward biology, catalysis, and nanotechnology. *Chem Rev* 104:293–346
- [16] Wang J, Pamidi PVA (1997) Sol-gel-derived gold composite electrodes. *Anal Chem* 69:4490–4494
- [17] Jena BR, Raj CR (2006) Enzyme-free amperometric sensing of glucose by using gold nanoparticles. *Chem Eur J* 12:2702–2708
- [18] Maduraiveeran G, Ramaraj R (1951) Gold nanoparticles embedded in silica sol-gel matrix as amperometric sensor for hydrogen peroxide. *J Electroanal Chem* 608:52–58
- [19] Turkevich J, Stevenson PC, Hillier J (1951) A study of the nucleation and growth processes in the synthesis of colloidal gold. *Discuss Faraday Soc* 11:55–75
- [20] McFarland AD, Haynes CL, Mirkin CA, Van Duyne RP, Godwin HA (2004) Color my nanoworld. *J Chem Educ* 81:544A–544B
- [21] Lusvardi G, Malavasi G, Menabue L, Aina V, Bertinetti L, Cerrato G, Morterra C (2010) Bioactive glasses containing Au nanoparticles. Effect of calcination temperature on structure, morphology, and surface properties. *Langmuir* 26:10303–10314
- [22] Larew LA, Johnson DC (1989) Concentration dependence of the mechanism of glucose oxidation at gold electrodes in alkaline media. *J Electroanal Chem* 262:167–182
- [23] Burke LD, Ryan TG (1992) The role of incipient hydrous oxides in the oxidation of glucose and some of its derivatives in aqueous media. *Electrochim Acta* 37:1363–1370
- [24] Bello A, Giannetto M, Mori G, Seeber R, Terzi F, Zanardi C (2007) Optimization of the DPV potential waveform for determination of ascorbic acid on PEDOT-modified electrodes. *Sens Act B* 121:430–435
- [25] Zhao J, Griederich B (2015) Synthesis of gold nanoparticles via chemical reduction methods. In: 7th Nanocon, Brno, Czech Republic, EU
- [26] Rasband W, ImageJ Version 1.32J, National Institute of Mental Health, Bethesda, Maryland, USA
- [27] Gwyddion Version 2.53. <http://gwyddion.net/>. Accessed 2 Apr 2019
- [28] Angerstein-Kozłowska H, Conway BE, Hamelin A, Stolicoviciu L (1987) Filamentary steps of electrochemical oxidation of single crystal planes of Au. Part II: a chemical and structural basis of oxidation of the (111) plane. *J Electroanal Chem* 228:429–453
- [29] PCPDFWIN 2.3. JCPDS International center for diffraction data, 637 Swarthmore 2002
- [30] Toghiani KE, Compton RG (2010) Electrochemical non-enzymatic glucose sensors: a perspective and an evaluation. *Int J Electrochem Sci* 5:1246–1301
- [31] Rueda M, Aldaz A, Sanchez-Burws F (1978) Oxidation of L-ascorbic acid on a gold electrode. *Electrochim Acta* 23:419–424
- [32] Hu IF, Kuwana T (1986) Oxidative mechanism of ascorbic acid at glassy carbon electrodes. *Anal Chem* 58:3235–3239
- [33] Manzanares MI, Solfs V, de Rossi RH (1986) Effect of cyclodextrins on the electrochemical behaviour of ascorbic acid on gold electrodes. *J Electroanal Chem* 407:141–147
- [34] Zanardi C, Terzi F, Seeber R (2010) Composite electrode coatings in amperometric sensors. Effects of differently encapsulated gold nanoparticles in poly(3,4-ethylenedioxythiophene) system. *Sens Actuators B* 148:277–282

**Publisher's Note** Springer Nature remains neutral with regard to jurisdictional claims in published maps and institutional affiliations.

## **Chapter 3**

**Silica-based pellets containing copper nanoparticles as disposable systems for electrocatalytic glycerol oxidation**



# Silica-based pellets containing copper nanoparticles as disposable systems for electrocatalytic glycerol oxidation

## 3.1. Introduction

Copper-based materials are largely reported to be effective systems for the anodic oxidation of different organic species, such as alcohols, carbohydrates and polyols in general [1-5]. Due to this property, Cu electrodes have been introduced as efficient and cheap alternative to noble metal-based electrodes in alkaline fuel cells [6,7]; these organic species, in fact, possess high energy volumetric density and easiness of transport and storage with respect to hydrogen. Among the various species of interest for such an application, glycerol is a promising alternative to methanol due the low flammability and volatility, nontoxicity, low crossover flux through the membrane and bio-renewability [8-12]; additionally, glycerol is obtained in large amounts as a by-product of the biodiesel production process [11].

In this respect, it has to be underlined that the strict monitoring of glycerol concentration during the industrial production of biodiesel is of outmost importance, since large amounts of this species can affect vehicle performance and can cause storage problems, formation of carbon deposits on the engine, clogging of the nozzles in the engine, deterioration of the fuel and emissions of aldehydes into the atmosphere [13]. Accurate quantification of glycerol can be effectively achieved by amperometric sensors exploiting the electrocatalytic properties of different metals, *e.g.* Au, Pt, Ni and Cu [14]; among these, Cu is preferred due to the low cost and the wider availability.

Thanks to the recent interests in nanosized materials, the use of copper nanoparticles (CuNPs) is often preferred to the bulk material for many applications, such as catalyst in organic synthesis [15-22], electrocatalysis [23-28], and electrochemical sensing [5,29-31]. Since CuNPs tend to aggregate and are characterized by a low mechanical strength, they are generally used as composites, mixed to carbon-based materials, *e.g.* carbon paste [32-34], activated carbon [35] and ceramic-carbon [36,37]. The appropriate choice of the supporting matrix can also lead to the enhancement of the catalytic properties of CuNPs [5].

Here we describe the preparation of a composite material that can be utilized for disposable electrochemical systems for electrocatalytic oxidation of glycerol. These devices are composed by CuNPs, graphite ( $C_{gr}$ ), silica-based sol-gel and polystyrene (PS).  $C_{gr}$  was added to support CuNPs and to confer adequate electrical conductivity; silica-based sol-gel, obtained from

methyltrimethoxysilane (MTMOS) was included to enhance the electrocatalytic performance of metal NPs, because their silanol groups facilitate the binding with CuNPs [38-41]; finally, PS was used as a binder to improve the mechanical stability. The ratio among the components was optimised by an experimental design to achieve the best peak intensity of the voltammetric signal due to glycerol oxidation and the stability of the device. The samples prepared according to this approach were used as pellets, representing an effective alternative configuration to common disposable electrodes and sensing systems, due to the fabrication simplicity and easiness to use. The commercial availability of the components and their relatively low cost make possible an efficient production of these disposable electrode systems.

## **3.2. Materials and Methods**

### **3.2.1. Chemicals**

All chemicals, of pure or puriss. grade, were supplied from Sigma Aldrich, except for CuNPs (70 nm nominal size) supplied from Iolitec (product number: NM-0044-UP).  $C_{gr}$  powder was  $< 20 \mu\text{m}$ . All solutions were prepared using Millipore ultrapure water,  $18 \text{ M}\Omega \times \text{cm}$  resistivity.

### **3.2.2. Composite material synthesis**

CuNPs and  $C_{gr}$  were mixed in a 40:60% w/w ratio [5]. Sol-gel was obtained from MTMOS by the addition of a basic catalyst, namely NaOH; the use of an alkaline catalyst rather than conventional acid ones avoids corrosion of the CuNPs. MTMOS and 0.1 M NaOH solution were mixed in the 5:3 volumetric ratio. The reaction was extremely fast [42]: the sol-gel was obtained within 5 minutes, without the use of any additional organic solvent (e.g. ethanol), heating or sonication of the sample. The use of NaOH solutions at higher concentration (1 M) leads to a too dry material since the reaction proceeds too quickly. The resulting sol-gel was mixed with the  $C_{gr}$ +CuNPs powders before complete dryness and the resulting composite material was air-dried overnight at room temperature.

PS ( $M_n=35,000$ ), added to enhance the mechanical strength of the composite [43], was dissolved in toluene, that is volatile enough to allow faster drying of the dispersions. 1 g of the above prepared mixture ( $C_{gr}$ , CuNPs and sol-gel) was suspended in 4 mL of the PS solution and ground in an agate mortar; this last mixture was air-dried at room temperature for at least 30 minutes. The total final mass for a typical batch was *ca.* 0.75 g.

### 3.2.3. Electrode preparation

Pellets were prepared using a standard IR pellet die equipped with a hydraulic press (PerkinElmer, IR Accessory Hydraulic Press) employing a  $75 \text{ kN cm}^{-2}$  force for 15 min.

The pellets were fixed on the top of a steel rod using conductive glue (Bare Conductive Electric Paint). The rod, the conductive glue and the lateral surface of the pellet were insulated from the solution employing a fast-drying nail polish to fix the area of the electrode. The resulting system was used as the working electrode of a three-electrode cell. The process afforded working electrodes with a fixed weight of *ca.* 200 mg, a diameter of 13 mm and a thickness of *ca.* 1.5 mm.

### 3.2.4. Electrochemical investigations

Electrochemical measurements were performed with an Autolab PGSTAT12 (Ecochemie) potentiostat/galvanostat, at room temperature in a single-compartment three-electrode cell. An aqueous Ag/AgCl/KCl 3 M electrode, from Omega Engineering (PHE 1304), was the reference electrode; all the given potential values are referred to it. The solution (50 mL) was contained in a hollow hemisphere (AISI 430 18/C steel), also acting as the auxiliary electrode. The ratio between the area of the counter electrode and that of the working one was *ca.* 10.

Voltammograms were recorded in 0.1 M KOH solutions in absence and in presence of glycerol; the choice of the solvent was related to the well-known electroactivity of glycerol in alkaline solutions [1-4]. To gain substantial signals, 25 mM solution of glycerol was employed.

Voltammetric curves were recorded starting from open circuit potential, at  $50 \text{ mVs}^{-1}$  potential scan rate. The lowest and highest potential limits were -0.40 and +0.85 V, respectively; these values were selected to avoid any solvent discharge. The solution was magnetically stirred for 30 s and left quiescent for 20 s before each voltammetric scan.

Amperometric tests at constant potential value were registered polarizing the electrode at +0.75 V for 20 s. In any case, the current values reported for glycerol oxidation are the mean of three replicates obtained on the same electrode surface; the relative standard deviation of the analysis was, thus, calculated.

All electrochemical tests were carried out in solutions in contact with the atmosphere, i.e. in presence of dissolved oxygen. The removal of oxygen through de-aeration, performed by bubbling nitrogen through the solution for 15 min, does not lead to significant variation of the electrochemical responses.

Experimental design calculations were carried out using the R statistical package [44]. Each set of voltammetric tests of the experimental design required the acquisition of 40 potentials sweeps: 4

sweeps in the pristine 0.1 M KOH solution were followed by 4 sweeps in 25 mM glycerol; this protocol was repeated 5 times on the same electrode and in the same solutions.

### **3.2.5. Characterisation of the pellets**

SEM images were acquired using a FEI Nova NanoSEM 450 and FEI Quanta 200 electron microscopes, equipped with Energy Dispersive Spectrometer (EDS, Quantax 200 from Bruker and INCA System from Oxford Instrument, respectively), in high vacuum condition. Images were acquired using secondary and backscattered electrons, before and after the electrochemical investigation; the samples were anchored on an aluminium stub using carbon glue. Scanning transmission electron microscopy (STEM) was employed for the powder samples; in this case, a tiny amount of material was dispersed in ultrapure water and skimmed onto the surface of a Ni/C grid. X-Ray diffraction measurements of the powder (XRPD) were carried out using a PANAnalytical X'pert PRO system. Qualitative analysis was performed using X'Pert High Score Plus [45,46], whereas QPA was obtained by mixing 0.9 g of the composite with 0.1 g of Al<sub>2</sub>O<sub>3</sub> or SnO<sub>2</sub> powder, from NIST, as a standard reference. Rietveld method was employed for QPA, using General Structure Analysis System program [47].

Room temperature DC conductivity was estimated in air by an Autolab PGSTAT12 (Ecochemie) potentiostat/galvanostat. The experiment was carried out placing each pellet on a stainless-steel plate, using a copper tip as a second electrode and applying a constant potential of +0.2 V between the two electrodes. The current passing throughout the pellet was converted to the relevant value of resistance by Ohm's Law; the values of the conductivity in different points of the pellet were similar.

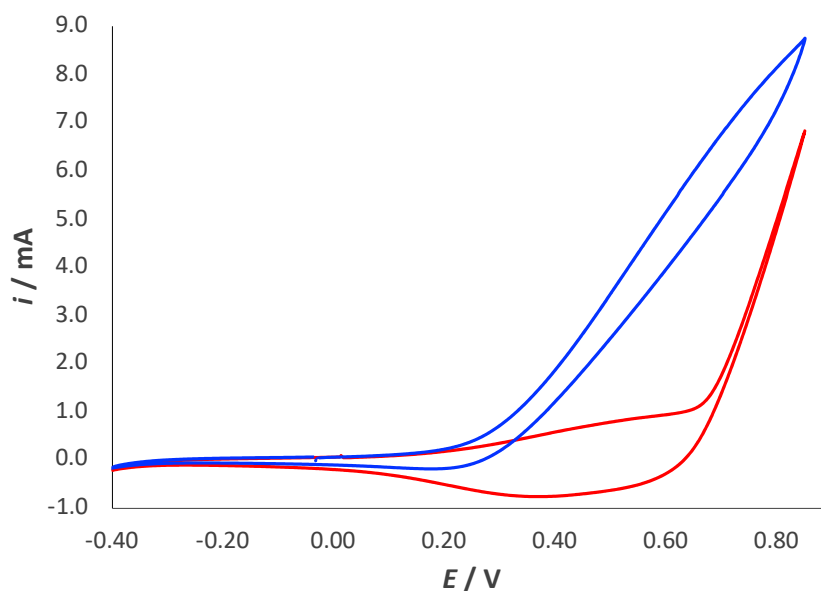
The amount of Cu released from the pellet during the electrochemical experiments was estimated by Inductively Coupled Plasma (ICP) spectroscopy equipped with an optical emission detector (Optima 4200 DV from Perkin Elmer). Before the execution of the analysis, the samples were acidified by adding 1% w/w HNO<sub>3</sub>.

### 3.3. Results and Discussion

#### 3.3.1. Voltammetric behaviour of the pellets

Preliminary voltammetric investigations of the silica-based pellets were carried out using a composite prepared with 126 mg of the C<sub>gr</sub>+CuNPs powder, 54 mg of MTMOS and 20 mg of polystyrene; this formulation was adopted on the basis of our previous studies on CuNPs inks [5]. The voltammetric response in a 0.1 M KOH solution (**Figure 1**), shows a broad anodic peak at *ca.* +0.60 V, ascribed to the oxidation of the CuNPs, with the associated cathodic peak between +0.20 and +0.30 V. These results indicate that CuNPs are in physical contact with the solution and in electrical contact with the conductive C<sub>gr</sub>, proving that PS chains and sol-gel do not form a passivating layer on the CuNPs surface.

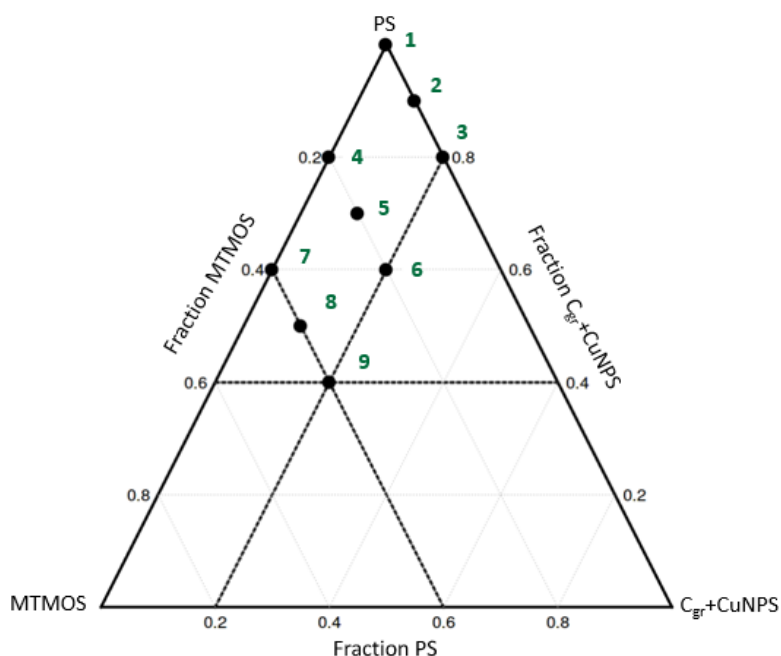
The voltammetric responses in a 25 mM glycerol solution shows a significant anodic current from *ca.* +0.25 V onwards in the forward and in the backward potential scans. This shape, already reported in the case of copper and noble metals-based electrodes [48-51], is ascribed to glycerol oxidation. A clear definition of the voltammetric responses is not possible, since the reaction mechanism involved in this oxidation, as well as of other oxygenated electroactive species, is not known in detail even in the case of conventional electrode materials such as gold [52-54].



**Figure 1.** Exemplificative voltammetric curves recorded at silica-based pellet in 0.1 M KOH, in absence (red traces) and presence (blue traces) of 25 mM glycerol. Bullet points indicate the starting OCP.

### 3.3.2. Experimental design

The experimental design (**Figure 2**) was carried out to optimize the formulation of the composite material to achieve highest oxidation currents and repeatability in a 25 mM glycerol solution. Preliminary experiments indicate that: *i*) small amounts of CuNPs led to low signals for glycerol oxidation; *ii*) conductivity of the material drops if the concentration of CuNPs is too high, due to the non-negligible contact resistance among CuNPs; *iii*) limited amount of  $C_{gr}$  leads to an excessive resistivity; *iv*) mechanical stability of the pellets decreases when PS is below 10% w/w; *v*) PS higher than 20% w/w or MTMOS higher than 58% w/w leads to an excessive reduction of CuNPs amount. In order to reduce the parameters to be optimized, the ratio (% w/w) between CuNPs and  $C_{gr}$  was fixed to 40:60 as previously reported [5].



**Figure 2.** Ternary diagram with the compositions (% w/w) of the silica-based pellets

The composition and characteristics of the pellets studied are reported in **Table 1**. Each pellet was tested in the glycerol solution by recording four following CV traces and repeating the procedure five times. Due to the absence of a proper current peak related to glycerol oxidation, for each experiment we evaluated the current flowing at +0.85 V, finally calculating the average current value ( $i_{ox}$ ) from experiments collected with the same electrode device; the associated relative standard deviation (RDS) quantifies the stability of the electrochemical response device.

**Table 1.** Composition (% w/w) and characteristics of the silica-based pellets

Pellet #	Composition <sup>[a]</sup>	$i_{ox}$ (mA) <sup>[b]</sup>	RSD (%) <sup>[b]</sup>	Conductivity (S)
1	100:0:0	N/A	N/A	7.14
2	90:0:10	5.6	9.1	5.88
3	80:0:20	2.5	8.5	3.33
4	73:27:0	7.6	7.1	3.13
5	63:27:10	8.3	6.0	2.70
6	53:27:20	3.3	5.6	1.11
7	46:54:0	5.5	6.9	0.11
8	36:54:10	5.2	1.8	0.03
9	26:54:20	3.9	4.5	0.03

<sup>[a]</sup> the composition is referred to this sequence: C<sub>gr</sub>+CuNPs : MTMOS : PS.

<sup>[b]</sup> average current recorded at +0.85V and associated RSD calculated from tests 1 to 5 and scans 1 to 4 of CV responses recorded in 25 mM glycerol solution

Pellet #1, composed entirely of PS, was characterized by very low current values and failed mechanically after the first eight potential sweeps; it was then discarded due to poor electrochemical performance and mechanical stability.

The highest current values associated were registered for Pellet #5; however, the voltammetric signal exhibited a significant decrement over five subsequent tests, evidencing an evolution of the material when undergoing polarization.

High current values were also registered for Pellets #2, #4 and #7, but the drift of the current intensity was well evident also in these cases.

The best compromise between current intensity and repeatability was achieved by Pellet #8. In this case, the results are highly repeatable (RSD 1.8%). To check its reproducibility, five additional pellets were prepared starting from different synthetic batches with similar composition, obtaining an overall RSD of 6.2%. This proves the high reproducibility of this kind of electrode systems. The mean current obtained for Pellet #8 was normalized by the geometric area and for actual amount of Cu

(expressed as %Cu w/w), obtaining  $0.252 \text{ mA cm}^{-2} \% \text{Cu}^{-1}$ . This value is larger than that obtained from conventional Cu electrodes in similar conditions [49,50], demonstrating the improvement conferred by the components of the pellet to the electrocatalytic properties of CuNPs.

Further electrochemical experiments were recorded by polarising the different pellets at a constant potential value (+0.75 V) and evaluating the current values flowing after 20 s. The analysis was repeated four times on the same pellet, in order to define the repeatability of the oxidation process (**Table 2**).

Data were once more normalized by the actual amount of Cu (expressed as %Cu w/w), to define its role in the electrocatalytic performance of the material. The highest current values were obtained using Pellets #8 and #9, whose RSD is around 5%.

Similarly, to the case of CVs, five pellets obtained from different batches were tested to check the reproducibility for Pellet #8 when working in these experimental conditions. The mean current value was  $0.236 \text{ mA cm}^{-2} \% \text{Cu}^{-1}$  with RSD of 5%.

**Table 2.** Average current values and associated RSD for Pellets #2-9 calculated from amperometric responses and normalized by %Cu w/w.

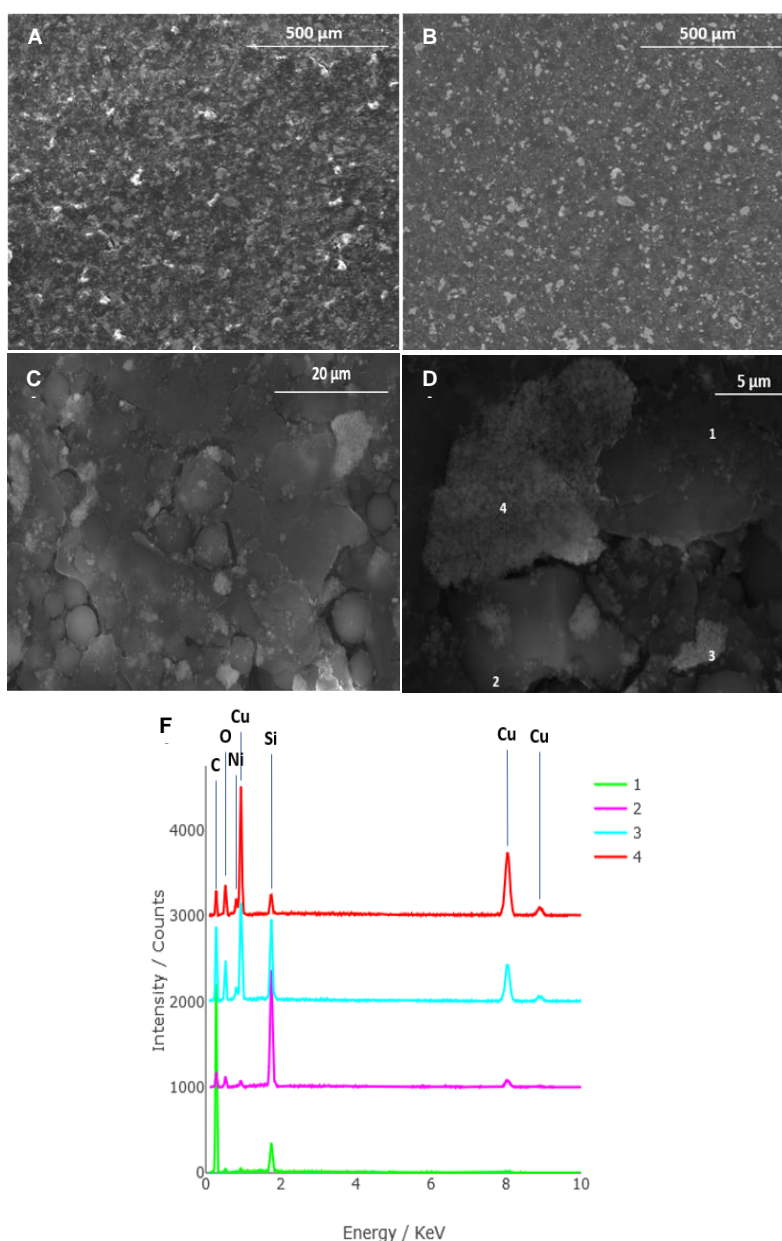
Pellet # <sup>[a]</sup>	$i$ ( $\text{mA cm}^{-2} \% \text{Cu}^{-1}$ )	RSD (%)
2	0.105	9.5
3	0.063	6.7
4	0.163	9.3
5	0.226	5.5
6	0.117	4.6
7	0.206	8.6
8	0.252	6.2
9	0.251	4.5

<sup>[a]</sup> Pellet #1 was discarded due to the poor mechanical stability



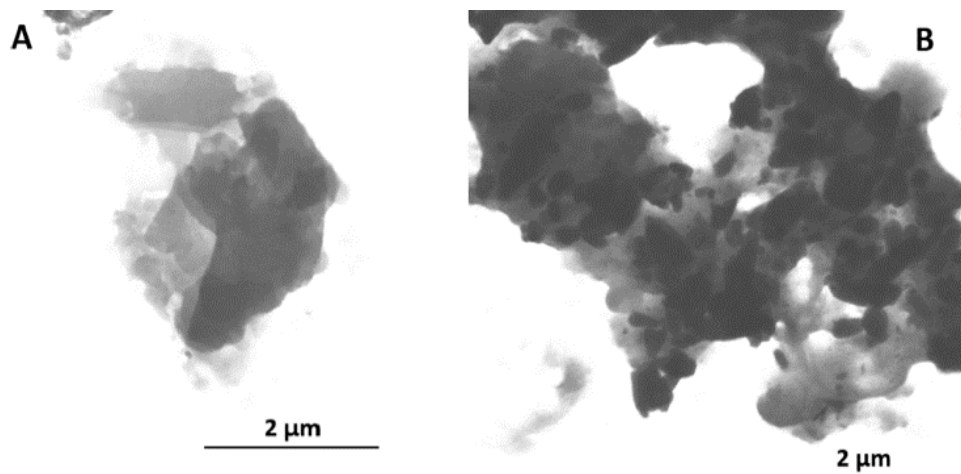
### 3.3.3. Characterisation

**Figure 3** reports scanning electron investigation performed on Pellet #8. Images derived from secondary (**Figure 3A**) and backscattered (**Figure 3B**) electrons at higher magnification show that the surface is homogeneous, since evident separation of the different phases or large pores are absent. The components are homogeneously mixed and inhomogeneities are only observable at the micron scale (**Figures 3C** and **3D**). Images (not showed) acquired immediately after the preparation of the pellets and at the end of the electrochemical characterisation are quite similar, indicating that the electrochemical process does not induce variations to the morphological structure of the surface.



**Figure 3.** SEM micrographs of Pellet #8 at different magnification obtained from secondary (A, C, D) and backscattered (B) electrons. E) EDS spectra of micrograph D.

Images obtained from secondary electrons (**Figures 3C and 3D**) show that CuNPs are dispersed as aggregates on the surface of the  $C_{gr}$  and, in some cases, they form a coating. The area occupied by the CuNPs is *ca.* 10% of the total electrode surface, estimated on the basis of different SEM images. STEM images confirm the presence of CuNPs in the sol-gel matrix possessing a dimension of *ca.* 200 nm (**Figures 4A and 4B**).



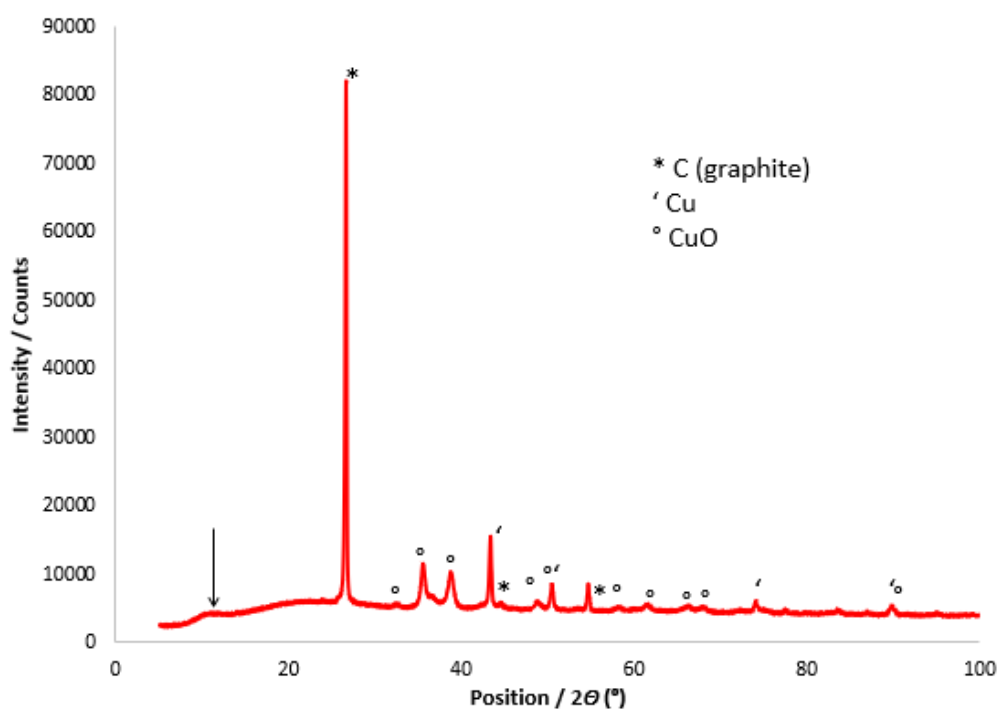
**Figure 4.** STEM micrographs of pristine sol-gel material (A) and Pellet #8 (B).

EDS spectra collected in different positions of the surface show that the sol-gel is distributed on the whole electrode surface (**Figure 3E**), forming granules possessing both irregular and spherical shape. The formation of these structures was also previously observed for conventional sol-gel materials undergoing an ageing process [55] and it was ascribed to reticulation of the silicate matrix occurring in the solution phase. In our case, however, the absence of solvent led to the formation of small-reticulated clusters, which can't grow further.

Similar characterisations performed on both pristine  $C_{gr}$  flakes and on a composite material not containing CuNPs confirmed the results previously discussed. It is worth noticing that it is not possible to distinguish between  $C_{gr}$  flakes and the polymeric binder (PS) since they are both composed uniquely of C and H atoms.

XRPD spectra were acquired to identify the phases present in the powders; the diffractogram of Pellet #8 (**Figure 5**), shows the presence of  $C_{gr}$  [45], (PDF 41-1487) and a broad band located at *ca.*  $10^\circ$  ( $2\theta$ ) ascribable to small amount of amorphous phase due to silicate fraction and PS. Copper is present both in the form of Cu, (PDF 4-836) and CuO, (PDF 41-254) [45]. Quantitative phase analysis (QPA) indicated that the ratio between Cu and CuO is *ca.* 0.6 w/w, demonstrating that the surface of the CuNPs is partially oxidised [56]. By analogy to what demonstrated for the electrocatalytic

oxidation of hydrocarbons [49] and of methanol [50], this oxidised phase should represent the actual electrocatalyst of glycerol.



**Figure 5.** XRPD pattern of Pellet #8: arrow indicates the amorphous area.

It is worth noticing that the presence of CuO does not hamper the electrical conductivity of the system. The conductivity of the overall material can be ascribed to the large number of defects in the oxide coating of CuNPs, its thickness and the closeness of the particles to the highly conducting  $C_{gr}$  phase.

On the basis of the electrochemical, microscopic and spectroscopic characterisations of Pellet #8, it is possible to affirm that: *i*) CuNPs are in electrical contact with  $C_{gr}$ ; *ii*) no evidence of encapsulation from sol-gel matrix and PS towards  $C_{gr}$  and CuNPs *iii*) the intimate contact between the sol-gel matrix and the CuNPs improves the electrochemical performance of the system thanks to the exploitation of synergic effects most likely strong metal support interaction (SMSI) [57].

Finally, ICP analysis was employed to evaluate the amount of Cu released from Pellet #8 during the voltammetric investigations. The results showed that only 9 and 14 ppb of Cu were released after 20 scans in the blank and in the 25 mM glycerol solutions, respectively. This amount is roughly equivalent to a layer of 1 nm thickness of a planar pellet surface based on the composite (CuO+ $C_{gr}$ +PS+sol-gel) assuming a homogeneous dissolution of Cu; moreover, re-deposition of Cu

during the potential sweeps is negligible. This partial dissolution phenomenon may explain the evolution of the voltammetric signal observed in some cases previously discussed.

### 3.4. Conclusion

Pellet electrodes based on CuNPs were successfully manufactured/developed by a very simple synthetic approach. The optimal formulation of the composite was identified by an experimental design, affording a stable material with effective electrocatalytic activity for glycerol oxidation. The optimal formulation is ascribed to Pellet #8 and corresponds to 63 g of C<sub>gr</sub>+CuNPs (60:40% w/w), 27 mL of MTMOS and 10 g of PS. The synergic action between CuNPs and the sol-gel matrix leads to a significant improvement of the electrocatalytic properties with respect to pristine CuNPs-based electrodes.

These devices are simple and fast to prepare, do not require high temperature for the sintering of CuNPs, is easy to use and mechanically stable. Moreover, their electrochemical response is highly reproducible allowing the proposition of these devices as disposables.

The composite materials proposed here for the first time allows the formation of disposable electrodes for the oxidation of glycerol. Maybe of note, these devices also pave the way to the development of similar electrodes for other organic species.

### 3.5. References

- [1] J.M. Marioli, T. Kuwana, Electrochemical characterisation of carbohydrate oxidation at copper electrodes, *Electrochim. Acta*, 37 (1992) 1187-1197.
- [2] M.Z. Luo, R.P. Baldwin, Characterization of carbohydrate oxidation at copper electrodes, *J. Electroanal. Chem.*, 387 (1995) 87-94.
- [3] N. Torto, Recent progress in electrochemical oxidation of saccharides at gold and copper electrodes in alkaline solutions, *Bioelectrochemistry*, 76 (2009), 195-200.
- [4] M.B. Gawande, A. Goswami, F.-X. Felpin, T. Asefa, X. Huang, R. Silva, X. Zou, R. Zboril, R.S. Varma, Cu and Cu-Based Nanoparticles: Synthesis and Applications in Catalysis, *Chem. Rev.*, 116 (2016), 3722-3811.
- [5] F. Terzi, B. Zanfognini, S. Ruggeri, N. Dossi, G.M. Casagrande, E. Piccin, Amperometric paper sensor based on Cu nanoparticles for the determination of carbohydrates, *Sens. Act. B* 245 (2017) 352-358.

- [6] C. Ottoni, R. Fernando, B. De Souza, S. Silva, Glycerol and Ethanol Oxidation in Alkaline Medium Using PtCu/C Electrocatalysts. *International journal of electrochemical science, Int J Electrochem Sci* 13 (2018) 1893–1904.
- [7] F. Munoz, C. Hua, T. Kwong, L. Tran, T.Q. Nguyen, J.L. Haan, Palladium–copper electrocatalyst for the promotion of the electrochemical oxidation of polyalcohol fuels in the alkaline direct alcohol fuel cell, *Appl Catal B - Environ* 174–175 (2015) 323–328.
- [8] E. Habibi, H. Razmi, Glycerol electrooxidation on Pd, Pt and Au nanoparticles supported on carbon ceramic electrode in alkaline media, *Int J Hydrog Energy* 37 (2012) 16800–16809
- [9] M.S.E. Houache, E. Cossar, S. Ntais, E.A. Baranova, Electrochemical modification of nickel surfaces for efficient glycerol electrooxidation, *J Power Sources* 375 (2018) 310–319.
- [10] J. Hu, X. Wu, Q. Zhang, M. Gao, H. Qiu, K. Huang, Preparation of a highly active palladium nanoparticle/polyoxometalate/reduced graphene oxide nanocomposite by a simple photoreduction method and its application to the electrooxidation of ethylene glycol and glycerol, *Electrochem Commun* 83 (2017) 56–60.
- [11] O.O. Fashedemi, H.A. Miller, A. Marchionni, F. Vizza, K.I. Ozoemena, Electro-oxidation of ethylene glycol and glycerol at palladium-decorated FeCo@Fe core–shell nanocatalysts for alkaline direct alcohol fuel cells: functionalized MWCNT supports and impact on product selectivity, *J Mater Chem A* 3 (2015) 7145–7156
- [12] Y. Kang, W. Wang, Y. Pu, J. Li, D. Chai, Z. Lei, An effective Pd-NiOx-P composite catalyst for glycerol electrooxidation: Co-existed phosphorus and nickel oxide to enhance performance of Pd, *Chem Eng J* 308 (2017) 419–427.
- [13] A.H. Maruta, T.R.L.C. Paixão, Flow injection analysis of free glycerol in biodiesel using a copper electrode as an amperometric detector, *Fuel* 91 (2012) 187–191.
- [14] F. Terzi, L. Pigani, C. Zanardi, Unusual metals as electrode materials for electrochemical sensors, *Curr. Opin. Electrochem.* 16 (2019) 157-163.
- [15] M.R. Decan, S. Impellizzeri, M.L. Marin, J.C. Scaiano, Copper Nanoparticle Heterogeneous Catalytic ‘Click’ Cycloaddition Confirmed by Single-Molecule Spectroscopy, *Nat. Commun.* 5 (2014) 4612 (1-8)
- [16] Q. Hu, G. Fan, L. Yang, F. Li, Aluminum-Doped Zirconia-Supported Copper Nanocatalysts: Surface Synergistic Catalytic Effects in the Gas-Phase Hydrogenation of Esters, *ChemCatChem* 6 (2014) 3501–3510.
- [17] A. Ahmed, P. Elvati, A. Violi, Size-and Phase-Dependent Structure of Copper (II) Oxide Nanoparticles, *RSC Adv.* 5 (2015) 35033–35041.

- [18] S.S. Acharyya, S. Ghosh, S. Adak, D. Tripathi, R. Bal, Fabrication of  $\text{CuCr}_2\text{O}_4$  Spinel Nanoparticles: A Potential Catalyst for the Selective Oxidation of Cycloalkanes via Activation of  $\text{C}_{\text{sp}^3}\text{-H}$  Bond, *Catal. Commun.* 59 (2015) 145–150.
- [19] B. Mohan, C. Yoon, S. Jang, K.H. Park, Copper Nanoparticles Catalyzed Se(Te)-Se(Te) Bond Activation: A Straight-forward Route Towards Unsymmetrical Organochalcogenides from Boronic Acids, *Chem. Cat. Chem.* 7 (2017) 405–412.
- [20] D.B. Alves, R. Silva, D. Voiry, T. Asefa, M. Chhowalla, Copper Nanoparticles Stabilized by Reduced Graphene Oxide for  $\text{CO}_2$  Reduction Reaction, *Mater. Renew. Sustain. Energy* 4 (2015) 1-8.
- [21] B.R. Buckley, R. Butterworth, S.E. Dann, H. Heaney, E.C. Stubbs, Copper-in-Charcoal Revisited: Delineating the Nature of the Copper Species and Its Role in Catalysis, *ACS Catal.* 5 (2015) 793–796.
- [22] M. Nasrollahzadeh, B. Jaleh, P. Fakhri, A. Zahraei, E. Ghadery, Synthesis and Catalytic Activity of Carbon Supported Copper Nanoparticles for the Synthesis of Aryl Nitriles and 1,2,3-triazoles, *RSC Adv.* 5 (2015) 2785–2793.
- [23] T.J. Meyer, Chemical Approaches to Artificial Photosynthesis, *Acc. Chem. Res.* 22 (1989) 163–170.
- [24] A.J. Bard, M.A. Fox, Artificial Photosynthesis - Solar Splitting of Water to Hydrogen and Oxygen, *Acc. Chem. Res.* 28 (1995) 141–145.
- [25] A.C. Dillon, K.M. Jones, T.A. Bekkedahl, C.H. Kiang, D.S. Bethune, M.J. Heben, Storage of Hydrogen In Single-Walled Carbon Nanotubes, *Nature* 386 (1997) 377–379.
- [26] C.Y. Wang, Fundamental Models for Fuel Cell Engineering, *Chem. Rev.* 104 (2004) 4727–4765.
- [27] D. Gust, T.A. Moore, A.L. Moore, Solar Fuels via Artificial Photosynthesis, *Acc. Chem. Res.* 42 (2009) 1890–1898.
- [28] F.T. Wagner, B. Lakshmanan, M.F. Mathias, Electro-chemistry and the Future of the Automobile. *J. Phys. Chem. Lett.* 1 (2010) 2204–2219.
- [29] F.J. Arévalo, Y. Osuna-Sánchez, J. Sandoval-Cortés, A. Di Tocco, A.M. Granero, S.N. Robledo, M.A. Zon, N.R. Vettorazzi, J.L. Martínez, E.P. Segura, A. Iliná, H. Fernández, Development of an electrochemical sensor for the determination of glycerol based on glassy carbon electrodes modified with a copper oxide nanoparticles/multiwalled carbon nanotubes/pectin composite, *Sens Act B* 244 (2017) 949-957.
- [30] S. Ayaz, S. Karakay, G. Emir, D.G. Dilgin, Y. Dilgin, A novel enzyme-free FI-amperometric glucose biosensor at Cu nanoparticles modified graphite pencil electrode, *Microchem. J* 154 (2020) 104586 (1-10).

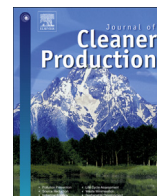
- [31] M. Rahman, A.J.S. Ahammad, J.H. Jin, S.J. Ahn, J.J. Lee, A Comprehensive Review of Glucose Biosensors Based on Nanostructured Metal-Oxides, *Sensors* 10 (2010) 4855-4886.
- [32] M. Javanbakht, A. Badiei, M. Reza Ganjali, P. Norouzi, A. Hasheminasab, M. Abdouss, Use of organofunctionalized nanoporous silica gel to improve the lifetime of carbon paste electrode for determination of copper(II) ions, *Analytica Chimica Acta* 601 (2007) 172-181.
- [33] K. Vytřas, I. Švancara, R. Metelka, Carbon paste electrodes in electroanalytical chemistry, *J. Serb. Chem. Soc.* 74 (2009) 1021-1033.
- [34] I. Švancara, K. Vytřas, K. Kalcher, A. Walcarius, J. Wang, Carbon Paste Electrodes in Facts, Numbers, and Notes: A Review on the Occasion of the 50-Years Jubilee of Carbon Paste in Electrochemistry and Electroanalysis, *Electroanalysis*, 21 (2009) 7-28.
- [35] F. Alonso, Y. Moglie, G. Radivoy, M. Yus, Multicomponent Click Synthesis of 1,2,3-Triazoles from Epoxides in Water Catalyzed by Copper Nanoparticles on Activated Carbons, *J. Org. Chem.* 76 (2011) 8394-8405.
- [36] L. Rabinovich, O. Lev, Sol-Gel derived composite ceramic carbon electrodes, *Electroanalysis* 13 (2001) 265-275.
- [37] D. Bellido-Milla, L.M. Cubillana-Aguilera, M. El Kaoutit, M.P. Hernández-Artiga, J.L. Hidalgo-Hidalgo de Cisneros, I. Naranjo-Rodríguez, J.M. Palacios-Santander, Recent advances in graphite powder-based electrodes, *Anal Bioanal Chem.* 405 (2013) 3525-3539.
- [38] R.J. White, R. Luque, V.L. Budarin, J.H. Clark, D.J. Macquarrie, Supported metal nanoparticles on porous materials. Methods and applications, *Chem Soc Rev* 38 (2009) 481-494.
- [39] S.H. Wu, C.Y. Mou, H.P. Lin, Synthesis of mesoporous silica nanoparticles, *Chem Soc Rev* 42 (2013) 3862-3875.
- [40] Q. Huang, L.M. Zhou, X.H. Jiang, Y.F. Zhou, H.W. Fan, W.C. Lang, Synthesis of Copper Graphene Materials Functionalized by Amino Acids and Their Catalytic Applications, *ACS Appl Mater Inter* 6 (2014) 13502-13509.
- [41] C.A. Borgo, R.T. Ferrari, L.M.S. Colpini, C.M.M. Costa, M.L. Baesso, A.C. Bento, Voltammetric response of a copper(II) complex incorporated in silica-modified carbon-paste electrode, *Analytica Chimica Acta*, 385 (1999) 103-109.
- [42] L.L. Hench, J.K. West, The sol-gel process, *Chem. Rev.* 90 (1990) 33-72.
- [43] R.G. Jones, J. Kahovec, R.F.T. Stepto, E.S. Wilks, M. Hess, T. Kitayama, W.V. Metanomski, A. Jenkins, P. Kratochvil, *Compendium of Polymer Terminology and Nomenclature: IUPAC Recommendations (first ed.)*, International Union of Pure and Applied Chemistry, Durham (2008)

- [44] <https://www.r-project.org>. Accessed 31<sup>st</sup> October, 2020.
- [45] T. Degen, M. Sadki, E. Bron, U. König, G. Nénert, The HighScore suite, Powder Diffraction, 29 (2014) S13-S18.
- [46] A. J. Markvardsen, K. Shankland, W. I. F. David, J. C. Johnston, R. M. Ibberson, M. Tucker, H. Nowell, T. Griffin., ExtSym: a program to aid space-group determination from powder diffraction data, J. Appl. Cryst. 41 (2008) 1177-1181.
- [47] A.C. Larson, R.B. Von Dreele, General Structure Analysis System (GSAS), Los Alamos National Laboratory Report LAUR, 1-231.
- [48] J.R. Crespo-Rosa, C. Zanardi, M. El Kaoutit, F. Terzi, R. Seeber, I. Naranjo-Rodriguez, Electroanalytical applications of a graphite-Au nanoparticles composite included in a sonogel matrix, Electrochim Acta 122 (2014) 310-315.
- [49] F. Terzi, B. Zanfognini, S. Ruggeri, N. Dossi, Nanostructured Au/Ti bimetallic electrodes in selective anodic oxidation of carbohydrates, Electrochim. Acta 188 (2016) 262-268.
- [50] S. Ruggeri, E. Miles, F. Poletti, L. Pigani, C. Zanardi, B. Zanfognini, E. Corsi, N. Dossi, R. Seeber, F. Terzi, Voltammetric behaviour of Cu alloys toward hydrogen peroxide and organic species, Electrochemistry Communications 90 (2018) 56–60.
- [51] M.L. Ligabue, F. Terzi, C. Zanardi, G. Lusvardi, One-pot sonocatalyzed synthesis of sol–gel graphite electrodes containing gold nanoparticles for application in amperometric sensing, J. Mater. Sci. 54 (2019) 9553-9565.
- [52] L.D. Burke, N.F. Nugent, The electrochemistry of gold: I the redox behaviour of the metal in aqueous media, Gold Bull. 30 (1997) 43-53.
- [53] L.D. Burke, Scope for new applications for gold arising from the electrocatalytic behaviour of its metastable surface states, Gold Bull. 37 (2004) 125-135.
- [54] L.D. Burke, N.F. Nugent, The electrochemistry of gold: II the electrocatalytic behaviour of the metal in aqueous media, Gold Bull. 31 (1998) 39-50.
- [55] J. Lin, C. W. Brown, Sol-gel glass as a matrix for chemical and biochemical sensing, TrAC 16 (1997) 200-211.
- [56] K.B. Male, S. Hrapovic, Y. Liu, D. Wang, J.H.T. Luong, Electrochemical detection of carbohydrates using copper nanoparticles and carbon nanotubes, Analytica Chimica Acta 516 (2004) 35–41.
- [57] C.-J. Pan, M.-C. Tsai, W.-N. Su, J. Rick, N.G. Akalework, A.K. Agegnehu, S.-Y. Cheng, B.-J. Hwang, Tuning/exploiting strong metal-support interaction (SMSI) in heterogeneous catalysis, J. Taiwan Inst. Chem. Eng. 74 (2017) 154-186.



## **Chapter 4**

**Recycling of thermally treated cement-asbestos for the production of  
porcelain stoneware slabs**



# Recycling of thermally treated cement-asbestos for the production of porcelain stoneware slabs

Maria Laura Ligabue<sup>a</sup>, Alessandro F. Gualtieri<sup>a,\*</sup>, Magdalena Lassinantti Gualtieri<sup>b</sup>, Daniele Malferrari<sup>a</sup>, Gigliola Lusvardi<sup>a</sup>

<sup>a</sup> Department of Chemical and Geological Sciences, University of Modena and Reggio Emilia, Via G. Campi 103, 41125, Modena, Italy

<sup>b</sup> Department of Engineering "Enzo Ferrari", University of Modena and Reggio Emilia, Via P. Vivarelli 10, 41125, Modena, Italy

## ARTICLE INFO

### Article history:

Received 26 May 2019

Received in revised form

21 October 2019

Accepted 27 October 2019

Available online 31 October 2019

Handling editor Prof. Jiri Jaromir Klemes̄

### Keywords:

End of waste

Cement-asbestos

Frit

Secondary raw material

Ceramic tiles

Porcelain stoneware slabs

## ABSTRACT

The directives of the European Commission Environment on the management of hazardous asbestos-containing materials (ACM) are pointing towards treatment and recycling other than disposal in landfills. KRY·AS is a secondary raw material obtained by the thermal transformation of cement-asbestos (CA) and can be inserted in the production line of e.g. concrete, clay bricks, ceramics, and plastic materials. This being a possible future solution to the huge "CA-emergency" in Italy, additional recycling options are sought. In this work, KRY·AS was used for the production of glass-ceramic frits destined for the manufacturing of porcelain stoneware slabs. Two novel frits were obtained by vitrifying KRY·AS together with minor amounts of natural raw materials as well as glass waste. The resulting frits were added in a ceramic body formulation (0, 1, 3, 5 wt.%). Phase composition, microstructure and technological properties of fired samples were evaluated and the results were compared to those obtained when using a standard commercial frit. According to water absorption tests, the novel products can be classified as *Bla*-type. Comparable or even improved technological properties were found between the standard body and the frit-bearing ones. More precisely, the addition of 5 wt.% of the novel frits led to better stain resistance as well as higher productivity due to reduction of the linear firing shrinkage. Improved mechanical strength (ca. 75 MPa compared to ca 60 MPa for the standard) was also obtained. The novel recycling route of KRY·AS supports a conclusive solution for the management of hazardous CA in Italy.

© 2019 Elsevier Ltd. All rights reserved.

## 1. Introduction

The commercial term "asbestos" includes six mineral species characterised by a fibrous-asbestiform crystal habit (Gualtieri, 2017); chrysotile (serpentine asbestos) and five amphiboles (actinolite asbestos, tremolite asbestos, anthophyllite asbestos, amosite and crocidolite). Asbestos minerals have been extensively used since ancient times for various industrial applications. Unfortunately, it is now proven that respirable asbestos fibers may promote adverse effects leading to several lung diseases (Manning et al., 2002; Røe and Stella, 2015; Gualtieri, 2017b). For this reason, the six commercial forms of asbestos have been included in Group 1 as carcinogens (mainly mesothelioma) for humans by the International Agency for Research on Cancer (IARC) (IARC, 1987).

Although all asbestos minerals are banned in Italy since 1992 (Italian D. Lgs. 257/92), a massive amount of asbestos-containing material (ACM) is still found on national territory, in particular cement-asbestos (CA) slates (Gualtieri and Elmi, 2006; D'Orsi, 2007). Phase analyses of slates from 27 various CA reclamation sites in Italy showed a rather complex phase composition, with calcite, quartz and hydrated cement phases in addition to anhydrous cement phases and asbestos minerals (Viani et al., 2013a). Chrysotile was found in all samples in concentrations ranging from ca. 2–13 wt.% whereas amphibole asbestos was detected in 17 of the 29 sample, generally in concentrations less than 3 wt.%. Chrysotile, with the ideal chemical formula  $Mg_3(OH)_4Si_2O_5$ , was thus the most employed asbestos phase in the production of CA.

According to existing laws, a policy of abatement and disposal of ACM in landfills in the last 40 years has been followed, but ACM waste management has become an emergency today also considering disaster events (Kim and Hong, 2017).

\* Corresponding author.

E-mail address: [alessandro.gualtieri@unimore.it](mailto:alessandro.gualtieri@unimore.it) (A.F. Gualtieri).

As a matter of fact, disposal in controlled landfills cannot be the ultimate solution as zero risk of fiber dispersion in air and water in the long run cannot be guaranteed. Their maintenance and disposal of the percolate for an indefinite time is also economically unviable. Besides, this process is conflicting with the agenda and directives of the European Commission (2008/98/EC), pointing towards recycling of the wastes (*End of Waste concept*) instead of their disposal (Pongrácz and Pohjola, 2004). Treatment and recycling should be the preferred solution, as it may produce new secondary raw materials and reduces environmental impact and consumption of primary raw materials.

Asbestos phases recrystallize in non-hazardous phases at high temperature (Gualtieri et al., 2008a, 2008b), rendering thermal treatment a promising route for ACM handling. Several industrial processes for thermal transformation of CAs have been proposed in the past (a few examples: Abruzzese et al., 1998; Downey and Timmons, 2005; Gualtieri et al., 2008a) and many different recycling routes for the obtained products have been proposed (Gualtieri et al., 2011a; Gualtieri and Boccaletti, 2011b; Pérez-Estébanez et al., 2014; Kusiorowski et al., 2016). One of the most realistic processes was patented by Gualtieri and Zanatto (2009) and involves prolonged annealing (>24 h) of sealed packages of CA in a tunnel kiln at temperatures in the range 1200–1300 °C. The obtained product, named KRY·AS, is free of asbestos phases and contains newly-formed clinker phases (Gualtieri et al., 2008a; Viani and Gualtieri, 2013b) with cytotoxic effects comparable to commercial clinker (Giantomassi et al., 2010; Pugnali et al., 2015). As discussed for CA above, a rather important compositional variability was observed for samples obtained following heat-treatment of slates collected from various sites on national territory (Viani and Gualtieri, 2013b). In particular, three groups of KRY·AS could be identified based on the phase composition: akermanite-rich products, bredigite-rich products and larnite (C2S)-rich products (Viani and Gualtieri, 2013b).

The presence of low-temperature clinker (i.e. C2S) renders the product suitable as substitute for ordinary Portland cement in quantities as high as 20 wt.% (Gualtieri and Boccaletti, 2011). This secondary raw material has also been successfully applied for the production of calcium sulfoaluminate clinker (Viani and Gualtieri, 2013), geopolymers (Gualtieri et al., 2012) and various other materials such as clay bricks, ceramic pigments, ceramic frits, rock/glass wool (Gualtieri et al., 2011) as well as porcelain stoneware (Gualtieri and Tartaglia, 2000; Gualtieri et al., 2008a).

The cost of thermal treatment for the production of KRY·AS (including pre-heating processing, thermal treatment, post-heating processing, personnel, amortization costs) was estimated to be 63 Euros/t which is highly competitive with landfill disposal (150–200 Euros/t) (Gualtieri and Zanatto, 2009). In particular, the thermal consumption (including recovered energy) and the specific absorbed power was estimated to be 550 kcal/t and 26 kWh/t, respectively. Considering the huge amount of technically verified recycling options described above, the process has the potential to transform a waste to an added value product. In this scenario, the final cost for waste handling is even more competitive. An estimated sales price of KRY·AS, taking into account the raw materials market for e.g. the production of cement, is 20 Euros/t. Hence, the real cost of the inertization process is 43 Euros/t (Gualtieri and Zanatto, 2009).

Porcelain stoneware (group *Bla*, water absorption <0.5% according to ISO 13006) is one of the most important industrial developments within the ceramic industry and has steadily increased its market share, today being 88% of the Italian product portfolio (Canetti, 2018). The large success of this product, following its introduction in the late seventies and early eighties, is the outstanding technological properties and high aesthetic standard

(Sánchez et al., 2010; Romero and Pérez, 2015). The compact microstructure, obtained by viscous liquid sintering at high temperatures (1180–1250 °C), is generally composed of a glassy phase formed mainly by the melting of feldspars (up to 80 wt.%) with embedded residual quartz crystals and newly-formed mullite (Lassinantti Gualtieri et al., 2011; Zanelli et al., 2011; dos Santos Conserva et al., 2016). Today, the aesthetic and applicative versatility of porcelain stoneware has gone one step further thanks to new and improved technologies for both forming, decoration and post-firing treatments. For example, the porcelain stoneware tile industry is moving towards the production of large-sized slabs not only finding new applications such as outdoor facades and kitchen worktops but also offering higher versatility towards specific market requests and customer-oriented product design. The fast industrial developments have motivated new scientific investigations specifically aimed at aspects related to large formats (e.g. Soldati et al., 2018; Campione et al., 2019).

As discussed above, many recycling options for KRY·AS in the ceramic sector have been explored in the past, including glass-ceramics (Gualtieri et al., 2011) and traditional porcelain stoneware tiles (Gualtieri and Tartaglia, 2000; Gualtieri et al., 2008a). It was shown that thermal treatment at temperatures higher than 1200 °C, gave a product which was suitable for direct recycling as secondary raw material in porcelain stoneware ceramic mixtures (Gualtieri and Tartaglia, 2000; Gualtieri et al., 2008a). In fact, the authors showed that the addition of up to 5 wt.% of thermally treated asbestos slates did not yield significant variations to the standard production parameters of white porcelain stoneware tile mixtures (Gualtieri et al., 2008a).

In Italy, porcelain stoneware manufacturing is particularly interesting as recycling option due to the short geographical distance between the major disposal sites and landfills of ACM waste to one of the most important ceramic clusters in Europe situated in the Sassuolo district in northern Italy. In fact, transportation distance is important when evaluating the economic/environmental impact of a process. From this aspect, waste management through thermal treatment and subsequent recycling in the ceramic industry has the potential of offering a viable solution to the ACM waste emergency in Italy.

The present paper focuses on the recycling of KRY·AS to prepare ceramic frits for the production of porcelain stoneware slabs. Waste management and recycling through the preparation of frits which subsequently can be used in traditional ceramics is an interesting option as the chemical composition and thus glass properties (e.g. viscosity, surface tension, crystallization behavior) can be tailored for specific purposes (Karamanova and Karamanov, 2009; Bernardo et al., 2008).

Here, a commercial ceramic frit used as sintering modifier in the production of porcelain stoneware slabs was used as reference and compositional adjustments of KRY·AS was performed by adding natural raw materials (kaolin, K-feldspar) as well as glass waste from the processing of soda-lime glass from domestic recycling. Two novel waste-containing frits were designed. Ceramic bodies were prepared using the novel frits and compared to those obtained with the reference (0, 1, 3 and 5 wt.%). Technological properties such as water absorption and linear firing shrinkage were determined using standard methods. Instead, the sintering process and microstructure developments were studied by optical dilatometry, scanning electron microscope (SEM) analyses and full quantitative phase analyses using X-ray powder diffraction (XRPD) and the Rietveld method. The results will show that the type and amount of frit have important effects on the sintering behavior and final properties of the ceramic body, affirming its importance for process tailoring. In addition, it will be shown that recycling of KRY·AS for the production of a vitreous substitute for synthetic frits

in porcelain stoneware slabs is a promising route for ACM waste management.

## 2. Materials and methods

### 2.1. Raw materials for frits and ceramic bodies

The raw materials used to prepare the ceramic frits were KRY·AS, kaolin from Ukraine, K-feldspar from Italy and recycled glass (Emiliana Rottami, Modena, Italy). The glass is the fine particulate (<100 µm) that is removed from the sieve filters of the mills used to grind glass from domestic recycling. Due to the small grain size, recovery for glass production is not an option and the product is thus generally considered as waste. The chemical composition remains quite constant over time, which is an important advantage considering future recycling and scale-up. The product of thermal inertization (i.e. KRY·AS) was obtained by thermal treatment of a package of cement-asbestos slates placed in a discontinuous industrial kiln and exposed to a heating program with a total duration of 40 h. The experiment was repeated three times. The heating (ca. 1.8 °C/min) up to the maximum firing temperature of 1200 °C was followed by an 21 h long isotherm and subsequent cooling down to RT (2.4 °C/min). Each single slate had the dimensions of approximately 122 × 57 × 1 cm. Following treatment, the slate fragments were crushed and homogenized in a hammer mill (Pulverisette 16 Fritsch) to obtain a powder with grains <200 µm. The product was further reduced to a finer powder in agate mortar for the various laboratory experiments (see below).

The ceramic frit used as a reference ( $F_{ref}$ ) is commercially available (Esmalglass-Itaca, Italy). The standard ceramic body (SCB) mixture, used as base to which frits were added, is a spray-dried powder used for the production of large porcelain stoneware slabs. According to the manufacturer, the raw materials composition of this powder is: 36.0 wt.% kaolinite-illite clay from Ukraine, 8.0 wt.% kaolin from Spain, 25.0 wt.% Na-K-feldspar (albite and microcline) from Italy, 15.5 wt.% floated Na-feldspar, 15.5 wt.% Na-feldspar (albite) from Turkey.

### 2.2. Preparation of the frits

Two frits (F1, F2) obtained from different raw materials, were prepared in this work. The compositions were designed (see Section 3.1) in order to, as closely as possible, match the chemical composition of the reference frit ( $F_{ref}$ ). The frits were prepared by melting of the raw materials mixtures in a laboratory kiln for 1 h at 1350 °C followed by rapid quenching in water. The fragments were recovered from the water bath, dried and subjected to a pre-milling step for 4 min. The obtained powder was subsequently used for the preparation of ceramic bodies.

### 2.3. Preparation of ceramic bodies

The standard ceramic body (SCB) mixture was mixed with each one of the three frits ( $F_{ref}$ , F1 and F2) in the weight proportions 100:0, 99:1, 97:3 and 95:5. A total of 9 frit-containing ceramic body mixtures were thus obtained:  $F_{ref-1}$ ,  $F_{ref-3}$ ,  $F_{ref-5}$  (SCB with addition of 1, 3 and 5 wt.% of  $F_{ref}$ ); F1\_1, F1\_3, F1\_5 (SCB with addition of 1, 3 and 5 wt.% of F1); F2\_1, F2\_3, F2\_5 (SCB with addition of 1, 3 and 5 wt.% of F2). As the relatively high iron content in KRY·AS (further discussed in section 3.1) could have compromised the color of the fired ceramic body, a maximum of 5 wt.% was added.

The various mixtures were subsequently wet-milled (50 wt.% deionized water and 0.3 wt.% sodium tripolyphosphate as dispersant) in a porcelain jar charged with alumina balls as grinding media. The obtained slips were dried overnight at 105 °C and

successively powdered. Following humidification of the powders with 6 wt.% deionized water, ceramic tiles (100 × 50 × 6 mm<sup>3</sup>) were prepared by uniaxial pressing (143 kg/cm<sup>2</sup>). For each mixture, 5–10 tiles were prepared. The green bodies were dried in an oven at 100 °C for 24 h before the firing step in a muffle furnace. The maximum firing temperature and the duration of the isotherm at maximum firing temperature were optimized in the laboratory (see section 2.4). The rest of the heating profile followed standard industrial settings: a first heating step from room temperature (RT) to 900 °C in 10 min followed by a second heating step from 900 °C to 1200 °C in 8 min, isotherm (10 min) at the maximum temperature (i.e. 1200 °C) followed by a first cooling step down to 650 °C in 10 min and a second one from 650 °C down to RT in 14 min.

### 2.4. Characterization techniques

Chemical analyses of the major elements were carried out on pressed powders using a wavelength dispersive Philips PW 1480 X-ray fluorescence (XRF) spectrometer.

The frits were analyzed by Differential Scanning Calorimetry (DSC) in order to determine the glass transition ( $T_g$ ) and the peak crystallization temperatures. Measurements were carried out using a Netzsch DSC 404 instrument. The measurement range was 20–1400 °C and the analyses were performed in air using a heating rate of 10 °C/min. In order to identify the newly-formed crystalline phases giving rise to exothermic peaks in the DSC traces, XRPD analyses (see below) were performed on recrystallized frits specially prepared for this purpose (30 min thermal treatment at the peak temperature, i.e. 990 °C for  $F_{ref}$  and F1 and 860 °C for F2).

An optical dilatometer (Expert Lab Service, Modena, Italy) was used to investigate the sintering behavior of the dry ceramic tiles and to optimize the firing cycle using the standard ceramic body (SCB) mixture. Specimens were cut from dry tiles in the shape of trapezoidal parallelepiped and had the dimensions 50 mm × 5 mm × 5 mm. Optimization of the firing cycle was carried out in two main steps. First, a heating ramp up to ca. 1350 °C was applied in order to determine the temperature at which maximum sintering velocity was obtained (Fig. 1 SI). This temperature was considered suitable as maximum firing temperature. The heating rate was set to 80 °C/min which is typically used in industrial firing. The maximum sintering velocity was easily identified from the first derivative curve (Fig. 1 SI), which in this case was 1200 °C. In order to verify that small variations in the maximum firing did not result in expansion/deformation of the ceramic piece due to bloating, the stability range of the ceramic mix around the temperature corresponding to the maximum velocity of sintering was investigated (Fig. 2 SI) through successive temperature increments starting from 1195 °C (heating rate 80 °C/min). From the resulting sintering curve (Fig. 2 SI), we observed that the ceramic body only started to expand at temperatures higher than 1215 °C, indicating a relatively good temperature stability around the maximum firing temperature (i.e. 1200 °C). The duration of the isotherm at maximum firing temperature was set to 10 min (maximum shrinkage was guaranteed).

XRPD data for the qualitative phase analyses were collected using a Philips PW 1730 instrument with a Ni-filtered Cu K $\alpha$  radiation generated with 40 kV and 30 mA. A step scan of 0.02 °2 $\theta$  was performed using a high counting statistic (5s/step) in the 3–80 °2 $\theta$  range. XRPD data for the quantitative phase analyses were collected using a  $\theta/\theta$  diffractometer (PANalytical, Cu K $\alpha$  radiation, 40 kV and 40 mA), equipped with a real time multiple strip (RTMS) detector. A virtual step scan (0.0167 °2 $\theta$ ) was performed in the 3–90 °2 $\theta$  range. Each sample was thoroughly mixed with a standard (10 wt.% corundum NIST 676a) and mounted in an aluminum sample holder by side-loading. The refinements for the quantitative phase

analyses were performed using the GSAS package (Larson and von Dreele, 1994) and its graphical interface EXPGUI (Toby, 2001). The determination of both crystalline and amorphous fractions was possible using the combined Rietveld-R.I.R. method (Gualtieri, 2000). The refined weight fractions of each crystalline phase ( $X_{ic}$ ) was rescaled with respect to the known weight fraction of added standard ( $X_s$ ) in order to obtain the real crystalline phase weight fraction ( $X_i$ ):

$$X_i = \frac{1}{1 - X_s} \left[ \left( \frac{X_s}{X_{sc}} \right) X_{ic} \right] \quad (1)$$

where  $X_{sc}$  is the refined weight fraction of the internal standard. Knowing the weight fractions of all crystalline phases, the amorphous content ( $X_a$ ) is calculated using the following equation:

$$X_a = 1 - \sum_i X_i \quad (2)$$

The fired apparent density ( $\rho_{bulk}$ ) of the ceramic samples was determined based on the weight and sample dimensions using an analytical balance and a digital caliper ( $>0.01$  mm), respectively. Prior to measurements, the ceramic pieces were kept at  $105^\circ\text{C}$  overnight.

True density ( $\rho_t$ ) was determined on fine powders using a gas displacement pycnometer (AccuPyc 1330, Micrometrics Inc. USA). The powders, obtained by dry-milling in an agate jar (planetary ball mill), were dried at  $105^\circ\text{C}$  overnight and subsequently kept in a desiccator prior to analyses.

Total porosity ( $TP$ , %) was calculated according to:

$$TP = \left( 1 - \frac{\rho_{bulk}}{\rho_t} \right) \cdot 100 \quad (3)$$

The linear firing shrinkage ( $LFS$ , %) defines the dimensional change of the ceramic sample after firing. It was calculated according to the following formula:

$$LFS(\%) = \frac{(w_i - w_f)}{w_i} \cdot 100 \quad (4)$$

where  $w_i$  is the initial tile width and  $w_f$  is the final tile width.

The CIE Lab (Commission Internationale d'Eclairage  $L^* a^* b^*$  color space dimensions) were determined according to ISO 10545–16:2012 using a Medical High Technology Pikko colorimeter. The differences in color between the standard ceramic body (SCM) and the frit-bearing ones were evaluated using  $\Delta E^*$ :

$$\Delta E^* = \sqrt{\Delta L^{*2} + \Delta a^{*2} + \Delta b^{*2} + \Delta c^{*2}} \quad (5)$$

where  $\Delta L^*$ ,  $\Delta a^*$  and  $\Delta b^*$  are the differences between the color parameters of the SCB and the ones recorded for the frit-bearing ceramic body.

Water absorption ( $WA$ , %) was determined according to the ISO 10545–3:2018 protocol.

Modulus of rupture ( $MOR$ ) was determined by a three-point bending test using equipment from Ceramic Instruments, model MOR/1-M/E (Sassuolo, Italy) which applies the following formula for calculation of  $MOR$ :

$$MOR = \frac{3FL}{2wh^2} \quad (6)$$

where  $F$  is the load (N),  $L$  is the span,  $w$  is the width (mm) and  $h$  is the thickness (mm).

The stain resistance was determined according to ISO

10545–14:2015. This protocol involves staining of the ceramic tile surface with an organic dye followed by three cleaning steps: in warm water followed by warm aqueous solution of a commercial cleaning agent and finally a combination of commercial cleaning agent and brushing. The stain resistance is classified as 5, 4 or 3 depending on which of the three consequent steps managed to restore the aesthetic appearance of the surface.

The three-point bending test method was used to calculate the so-called *pyroplastic index* ( $PI$ ) (dos Santos Conserva et al., 2016). Specimens with the dimensions  $85 \times 7 \times 5$  mm<sup>3</sup> were obtained from dried green tiles. They were placed on 2 bars 7 mm apart and fired using the same heating cycle as that used for the tile samples (see section 2.3).  $PI$  was calculated with the following formula:

$$PI = \frac{4h^2S}{3L^4} \quad (7)$$

where  $h$  (cm) is the initial thickness of the body,  $S$  (cm) is the maximum deflection of the sample and  $L$  (cm) is the distance between the two supports.

The microstructure of the fired bodies was investigated by an environmental scanning electron microscope (ESEM, FEI Quanta-200 instrument). The surface and bulk of one tile from each ceramic body mixture were investigated. The specimens were attached on aluminum stubs using carbon glue and subsequently coated with a 10 nm thick gold film.

### 3. Results and discussion

#### 3.1. Frits-chemical design and thermal behavior

Table 1 shows the XRF analyses results of raw materials and frits. The chemical composition of KRY·AS is rather different with respect to the industrial frit ( $F_{ref}$ ). When designing novel frit compositions, the objective was to optimize the amount of recycled materials without deviating too much from the composition of the reference frit. Several constraints had to be considered: i) Presence of volatile components in KRY·AS (mainly  $H_2O$  and  $CO_2$  from hydration and carbonation reactions during long-time storage); ii) The high content of fluxes (Ca, Na) and the low content of Si and Al with respect to  $F_{ref}$ ; iii) The significant amounts of Fe which possibly could compromise the color of the ceramic body. Two frits named F1 and F2 were developed, different in terms of waste recovery and expected results.

F1 was prepared by vitrifying KRY·AS (37.0 wt.%) together with recycled glass (18.0 wt.%) in addition to the natural raw materials kaolin (25.0 wt.%) and K-feldspar (20.0 wt.%). The final chemical composition of F1 was quite close to that of  $F_{ref}$  although some discrepancies were observed, mainly regarding the concentration of some glass modifiers. As observed in Table 1, the concentration of  $Na_2O$ ,  $K_2O$  and  $Fe_2O_3$  were higher in F1 with respect to the reference frit whereas  $MgO$  was lower.

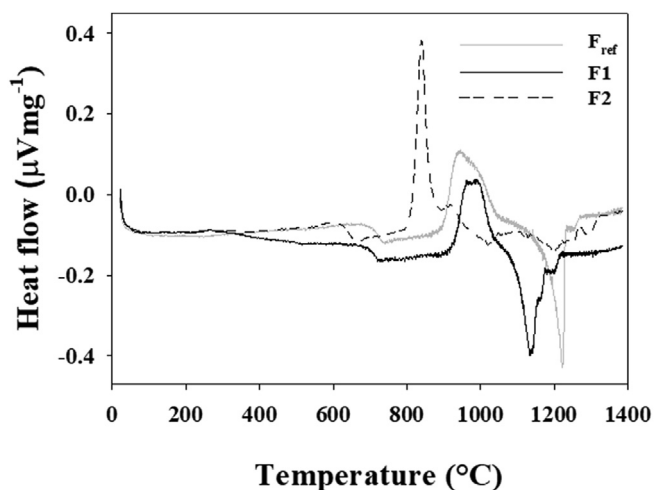
F2 was obtained by vitrifying KRY·AS (43.5 wt.%) with recycled glass (56.5 wt.%), leading to a totally waste-based frit and thus total absence of raw materials consumption. Some major differences in chemical composition between F2 and  $F_{ref}$  were observed (Table 1). In particular, the waste-based frit was much richer in  $CaO$ ,  $Na_2O$  and  $Fe_2O_3$  whereas depleted in  $MgO$  and  $Al_2O_3$ .

Fig. 1 shows the DSC curves for the novel ceramic frits (F1 and F2) as well as for  $F_{ref}$ . First of all, comparable traces are observed for F1 and  $F_{ref}$ , which is expected considering similar chemical compositions (see Table 1). The glass transition temperature ( $T_g$ ) for both frits are observed just above  $700^\circ\text{C}$  ( $725^\circ\text{C}$  for  $F_{ref}$  and  $710^\circ\text{C}$  for F1). They both display at least two overlapping exothermic peaks at around  $950^\circ\text{C}$  and  $990^\circ\text{C}$ , the first one being at slightly

**Table 1**  
Chemical composition (wt.%) of the novel frits (F1, and F2) as well as the raw materials used to prepare them (KRY·AS, recycled glass, kaolin, K-feldspar).

	Na <sub>2</sub> O	MgO	Al <sub>2</sub> O <sub>3</sub>	SiO <sub>2</sub>	P <sub>2</sub> O <sub>5</sub>	K <sub>2</sub> O	CaO	TiO <sub>2</sub>	Mn <sub>2</sub> O <sub>3</sub>	Fe <sub>2</sub> O <sub>3</sub>	Lo.I <sup>a</sup>
KRY·AS	0.26	9.52	4.07	24.86	0.00	0.29	48.34	0.21	0.07	2.72	9.65
recycled glass	12.26	2.50	2.84	69.31	0.02	0.77	9.24	0.14	0.05	0.47	2.42
kaolin	0.30	0.30	33.50	51.30	/	0.90	0.20	0.50	/	0.70	12.30
K-feldspar	0.70	/	17.00	65.50	/	14.00	/	/	/	/	0.10
F1	2.50	4.22	14.55	52.46	0.00	3.47	21.14	0.22	0.04	1.40	0.00
F2	6.53	5.51	4.25	54.57	0.00	0.80	26.47	0.16	0.05	1.65	0.00
F <sub>ref</sub>	1.32	9.54	18.49	50.01	0.00	1.07	19.24	0.0	0.01	0.22	0.00

<sup>a</sup> Obtained from thermogravimetric measurements.



**Fig. 1.** DSC curve for the reference frit F<sub>ref</sub> (grey solid line), sample F1 (black solid line) and sample F2 (black dashed line).

lower temperature for F<sub>ref</sub>. The reference frit shows an important endothermic peak at 1220 °C with a small shoulder at ca. 1255 °C. The novel frit F1 also displays important endothermic events, but at slightly lower temperatures with respect to the standard. The main event is observed at 1137 °C whereas two minor ones are centered at 1160 °C and 1197 °C. The endothermic peaks are surely relative to melting of both residual glassy phase and newly-formed crystalline phases.

The DSC trace for F2 is completely different with respect to the standard and F1, probably due to the different chemical composition (see Table 1). Not only is T<sub>g</sub> found at a much lower temperature (640 °C compared to 710–725 °C) but an important crystallization peak is observed already at 838 °C with a shoulder at 918 °C. Another obvious difference is the refractory behavior of the frit, showing only very weak endothermic peaks at 1025 °C and 1202 °C.

XRPD analyses were performed on recrystallized frits in order to identify the phases formed during heating (see section 2.4). As expected, similarities were found between F<sub>ref</sub> and F1. Both frits showed crystallization of calcium magnesium silicates (diopside, JCPDS 00-041-1370 in F<sub>ref</sub> and akermanite-gehlenite, JCPDS 01-079-2423 in F1) and anorthite (JCPDS 01-089-1460). F1 also showed newly-formed wollastonite (wollastonite-2M, JCPDS file 00-027-0088 and possibly also wollastonite-1T, JCPDS file 00-029-0372), which is not surprising considering the higher CaO and lower Al<sub>2</sub>O<sub>3</sub> content in F1 with respect to F<sub>ref</sub> (see Table 1).

The thermally treated F2 showed the presence of imandrite, a sodium calcium iron silicate (JCPDS file 00-039-0403), in addition to akermanite-gehlenite and wollastonite that were also found for F1. The considerably higher content of Na<sub>2</sub>O in F2 with respect to the other frits, motivates the presence of a sodium-bearing phase.

Anorthite was not observed in this sample, surely due to the much lower content of Al<sub>2</sub>O<sub>3</sub> (see Table 1).

### 3.2. Standard ceramic body (SCB) characterization

Table 2 shows the chemical and mineralogical composition of the standard ceramic body (SCB) mixture. The type of minerals and their quantity are in line with what is expected from a raw materials mixture for porcelain stoneware tiles. The clay fraction, composed of kaolinite and illite, gives plasticity and mechanical strength to the green body. Whereas both clay phases act as aluminosilicate source for the crystallization of mullite, illite also introduced potassium oxide in the ceramic body which modifies the composition of the liquid melt (Ferrari and Gualtieri, 2006). The feldspar portion, playing a key role in the process of viscous sintering and responsible for the highly vitreous nature of the final product, is mainly composed of plagioclase with a minor amount of K-feldspar. The main function of quartz is to control the firing shrinkage and dimensional stability of the tile, although partial melting during firing also leads to modification of the liquid melt.

### 3.3. Sintering behaviour of the ceramic bodies

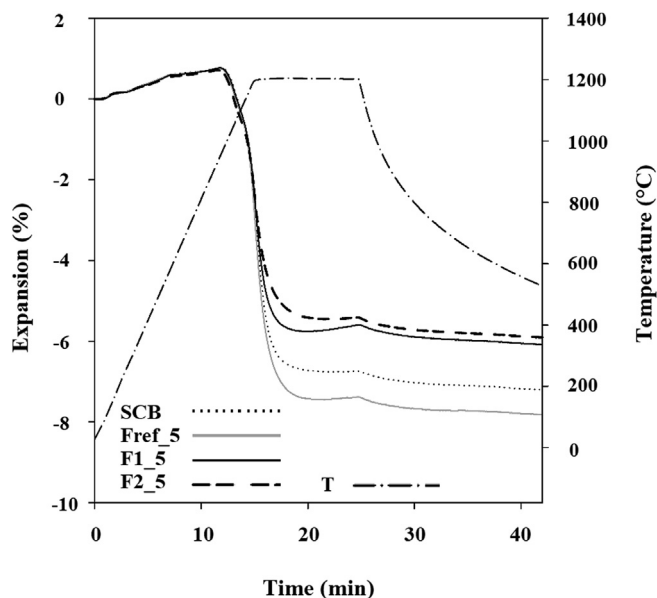
Fig. 2 reports the results from the optical dilatometry analyses carried out on SCB, F<sub>ref\_5</sub>, F1\_5 and F2\_5 using a heating rate of 80 °C/min up to 1200 °C (the temperature corresponding to the maximum velocity of sintering of SCB) and an isothermal step for 10 min, as reported in section 2.4. Except for the α- to β-quartz transition around 573 °C, the samples expand in a linear manner up to ca. 920 °C after which a first contraction step is observed. The first derivative curve (not shown here) presented a minimum at around 1040 °C. According to Gualtieri (2007) who studied a traditional porcelain stoneware tile formulation, this minor contraction may be associated with the following events; i) crystallization of primary mullite from metakaolinite; ii) structural collapse of dehydroxylated illite with subsequently crystallization of primary mullite and the formation of a viscous glass. According to DSC analyses of the ceramic frits (Fig. 1) described in section 3.1, crystallization occurs in the temperature range 800–950 °C for F2 and 900–1050 °C for F<sub>ref</sub> and F1 which corresponds rather well with the first contraction step observed in the expansion curves. Hence, a contribution from these events is also possible. Between this temperature and the second minimum at 1200 °C the contraction of the systems is mainly related to viscous sintering, resulting from the formation of a liquid glassy phase from the melting of feldspars and partial melting of quartz.

Maximum contraction is obtained after ca. 5–6 min of the isothermal segment. The values obtained for the different compositions are rather different (Fig. 2). The largest contraction is observed for sample F<sub>ref\_5</sub> (7.4%) followed by F1\_5 (5.8%) and F2\_5 (5.4%). The value for the SCB alone without the addition of a frit was 6.7%. The observed discrepancies are likely explained by different

**Table 2**  
Chemical and mineralogical composition of SCB.

Chemical composition (wt.%)										
Lo.I. <sup>a</sup>	Na <sub>2</sub> O	MgO	Al <sub>2</sub> O <sub>3</sub>	SiO <sub>2</sub>	P <sub>2</sub> O <sub>5</sub>	K <sub>2</sub> O	CaO	TiO <sub>2</sub>	Mn <sub>2</sub> O <sub>3</sub>	Fe <sub>2</sub> O <sub>3</sub>
4.66	3.74	0.56	22.84	64.53	0.23	1.81	0.60	0.51	0.02	0.50
Mineralogical composition (wt.%)										
kaolinite			illite/mica		K-feldspar		plagioclase		quartz	
22.7 (4)			19.2 (6)		3.0 (3)		34.6 (3)		20.5 (2)	

<sup>a</sup> Loss on ignition (LoI) obtained from thermogravimetric measurements.



**Fig. 2.** Expansion as a function of time for the standard ceramic body (SCB), and samples F<sub>ref\_5</sub>, F1<sub>5</sub>, F2<sub>5</sub>. The temperature (T) corresponding to each point in the curves can be extracted from the temperature vrs. time curve shown in the Figure.

flow behaviors of the liquid phase during viscous sintering and/or differences in the porous structure of the pressed piece (Amorós et al., 2007). In fact, densification mainly depends on the liquid phase viscosity, which in turn depends on the temperature, the chemical composition as well as size, shape and fraction of dispersed solid phases (e.g. newly-formed mullite and residual quartz) (Lassinanti Gualtieri et al., 2018a; Conte et al., 2018; Sanchez et al., 2019; dos Santos Conserva et al., 2016).

A good dimensional stability is observed following complete densification (see Fig. 2), which is highly desirable from a technological point of view.

### 3.4. Technological properties of the fired ceramic bodies

Many technological properties of porcelain stoneware tiles such as water absorption (WA), mechanical properties (e.g. MOR), and stain resistance are governed by microstructure, which in turn depends on the raw materials composition, physical properties of the particles, physical properties of the pressed body as well as processing parameters such as heating cycle etc (Romero and Pérez, 2015). The most important microstructural characteristic for porcelain stoneware tiles is the absence of open porosity ( $\leq 0.5$  wt.% according to ISO 13006/2012), giving this product an excellent resistance to chemical attack, staining, frost damage etc. Nevertheless, the bulk density as well as total porosity may vary in ceramic tiles due to closed porosity (Romero and Pérez, 2015).

Fig. 3 shows the water absorption (WA) and the linear firing shrinkage (LFS) as a function of frit content. Table 3 summarizes bulk and real density ( $\rho_{bulk}$  and  $\rho_{true}$ , respectively) as well as total porosity (TP) and the class of stain resistance (SR) determined for the investigated tiles.

First of all, the tiles have a WA less than 0.05% which is well below the limit set by the standard (Fig. 3a). Hence, the tiles can be classified as *Bla* ceramic tiles (i.e. porcelain stoneware). As a consequence of the close to zero water absorption, the total porosity can be considered closed (i.e. not connected to the tile surface).

The LFSs for the ceramic body compositions containing the commercial frit (i.e. F<sub>ref</sub>) are not statistically different from the standard (SCB) although there appears to be a negative trend with amount of added frit (Fig. 3b). Instead, the addition of F1 and F2 in higher percentages (i.e. 3% and 5%) leads to a lower LFS with respect to the standard (SCB). Also, for these frits, a negative trend is observed between LFS and amount of added frit. The successive decrease in LFS with increasing amount of frit is mirrored in the opposite trend for the TP (Table 3), although the values (ca. 4.5–8.5%) are still perfectly in line with those expected from traditional porcelain stoneware (Romero and Pérez, 2015).

The LFS values are in concert with the results obtained from the sintering curves collected from the ceramic bodies containing the highest amount of added frit (i.e. 5 wt.%), i.e. the contraction increases in the order F<sub>ref\_5</sub> > F1<sub>5</sub> > F2<sub>5</sub>.

The increased residual porosity observed for the frit-bearing ceramic bodies is possibly related to changes in the viscous sintering process due to physical properties of the liquid melt and/or differences in the porous structure of the dry piece. For example, both viscosity and surface tension affecting capillary flow within the ceramic compact during liquid phase sintering depend on the chemical composition of the melt as well as dispersed solid phases (e.g. newly-formed microcrystals) as already discussed in the previous section.

A good stain resistance was observed for all samples, in particular for the ceramic bodies containing the highest amount of frit and for which rinsing in warm water was enough to completely remove the staining agent (see Table 3). A close correlation exists between stain resistance and the amount, size and shape of surface pores as well as surface roughness (e.g. Dondi et al., 2005). The overall higher stain resistance observed for frit-bearing bodies is surely related to the lower amount of open pores (i.e. lower water absorption, see Fig. 3a).

Fig. 4 shows the CIE Lab color parameters determined for the reference and for the frit-bearing ceramic bodies. No significant differences can be observed between the various tiles. In fact, values of  $\Delta E^*$  are lower than 2.3 which can be considered the limit under which no difference in color can be distinguished by the human eye (Sharma, 2003). It is interesting to notice that the slightly higher amount of Fe in the novel frits (see Table 1) did not significantly affect the color.

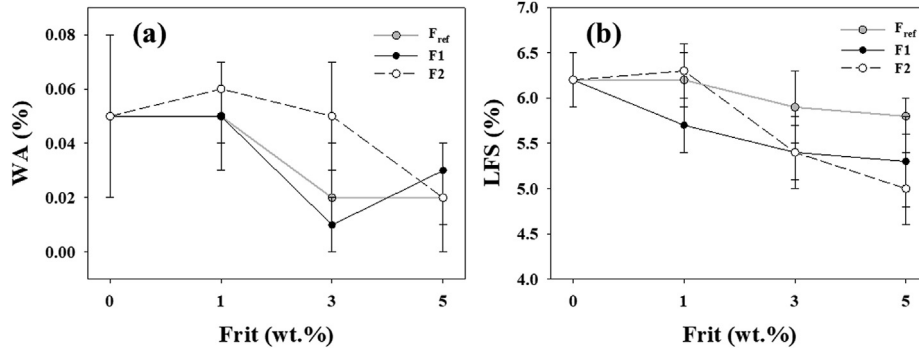


Fig. 3. Water absorption (WA) and linear firing shrinkage (LFS) (a and b, respectively) as a function of frit content.

Table 3

Bulk density ( $\rho_{bulk}$ ), true density ( $\rho_{true}$ ), total porosity (TP) and class of stain resistance (SR) of the fired ceramic tiles.

Sample	$\rho_{bulk}$ (g·cm <sup>-3</sup> )	$\rho_{true}$ (g·cm <sup>-3</sup> )	TP (%)	SR <sup>a</sup>
SCB	2.39 (2)	2.4980 (9)	4.4 (6)	3
F <sub>ref_1</sub>	2.38 (2)	2.4994 (7)	4.7 (2)	3
F <sub>ref_3</sub>	2.35 (2)	2.4991 (4)	6.0 (6)	4
F <sub>ref_5</sub>	2.34 (2)	2.5060 (7)	6.7 (7)	5
F1_1	2.325 (8)	2.4987 (8)	7.0 (3)	4
F1_3	2.31 (1)	2.4933 (5)	7.4 (5)	4
F1_5	2.31 (2)	2.4999 (3)	7 (1)	5
F2_1	2.370 (7)	2.4933 (9)	5.0 (3)	4
F2_3	2.306 (2)	2.4908 (9)	7.42 (7)	4
F2_5	2.28 (1)	2.4959 (9)	8.6 (4)	5

<sup>a</sup> Surface can be cleaned with just water (class 5), with a commercial cleaning agent (class 4), with a rough sponge and a commercial cleaning agent (class 3).

As observed in Fig. 5, the modulus of rupture (MOR) for all tiles are considerably higher (>51 MPa) than the limit dictated for porcelain stoneware tiles (35 MPa, see ISO 10545-4/2012). Comparing the frit-bearing compositions with the reference, only the novel frits added in the highest amount (i.e. 5 wt.%) are statistically different from the reference (60 ± 8, 75 ± 6, 72 ± 3 MPa for SCB, F1\_5 and F2\_5, respectively). These results are peculiar considering that the total porosity of the reference (ca. 4%) was much lower than the frit-bearing ceramic bodies (ca. 8%). Apparently, microstructural parameters other than porosity are important here. Generally, the high mechanical strength of porcelain stoneware tiles is considered the upshot of several contributing factors such as the presence of interlocking mullite needles or other newly-formed crystals such as anorthite (Taskiran et al., 2005; Karamanova and Karamanov, 2009). or wollastonite (Lassinantti Gualtieri et al., 2018b) and matrix reinforcement due to the compressive residual

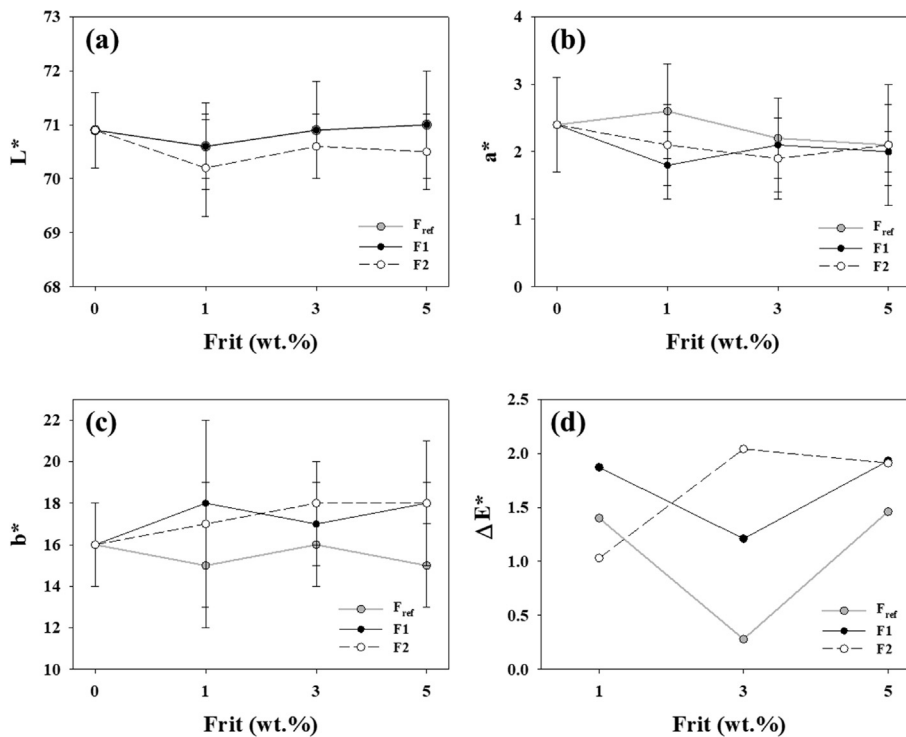


Fig. 4. CIELab color parameters as a function of frit content of the fired tiles: (a) L\*; (b) a\*; (c) b\*; (d) ΔE\*.



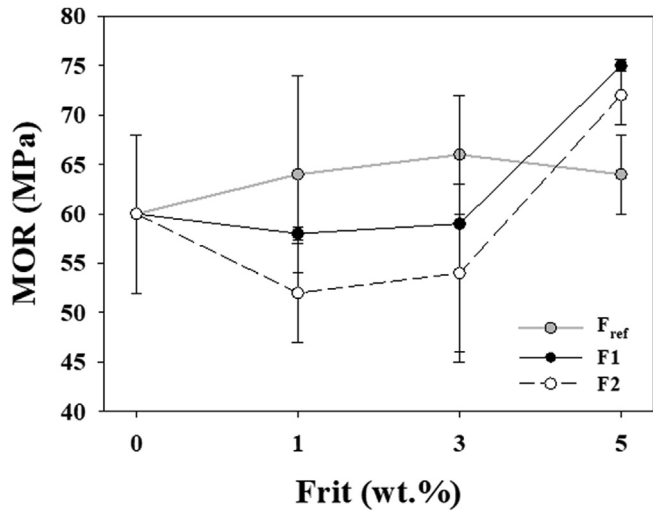


Fig. 5. Modulus of rupture (MOR, MPa) of the fired tiles as a function of frit content.

stress of the glassy phase (Carbajal et al., 2007).

### 3.5. Microstructural characterization-SEM and XRPD

Fig. 6 shows representative SEM micrographs recorded from the cross-section of all the samples. As can be observed from these micrographs, the ceramic bodies are highly sintered. The pores are regularly distributed, isolated and small, most of them having a diameter  $<5 \mu\text{m}$ , never exceeding  $30 \mu\text{m}$ . This porous structure is compatible with residual porosity from the viscous sintering process (Romero and Pérez, 2015). The tile surfaces were also investigated and the micrographs taken from some of the samples (SCB, F<sub>ref\_5</sub>, F1\_5 and F2\_5) are shown as supporting information (Fig. 3 SI). In concert with the close to zero water absorption found for the samples (Fig. 3a), the micrographs show highly vitrified surfaces.

### 3.6. Phase composition (XRPD and Rietveld-RIR) and pyroplastic index

Fig. 7 shows the wt.% of the various phases present in the fired bodies as a function of amount of added frit. The exact values are

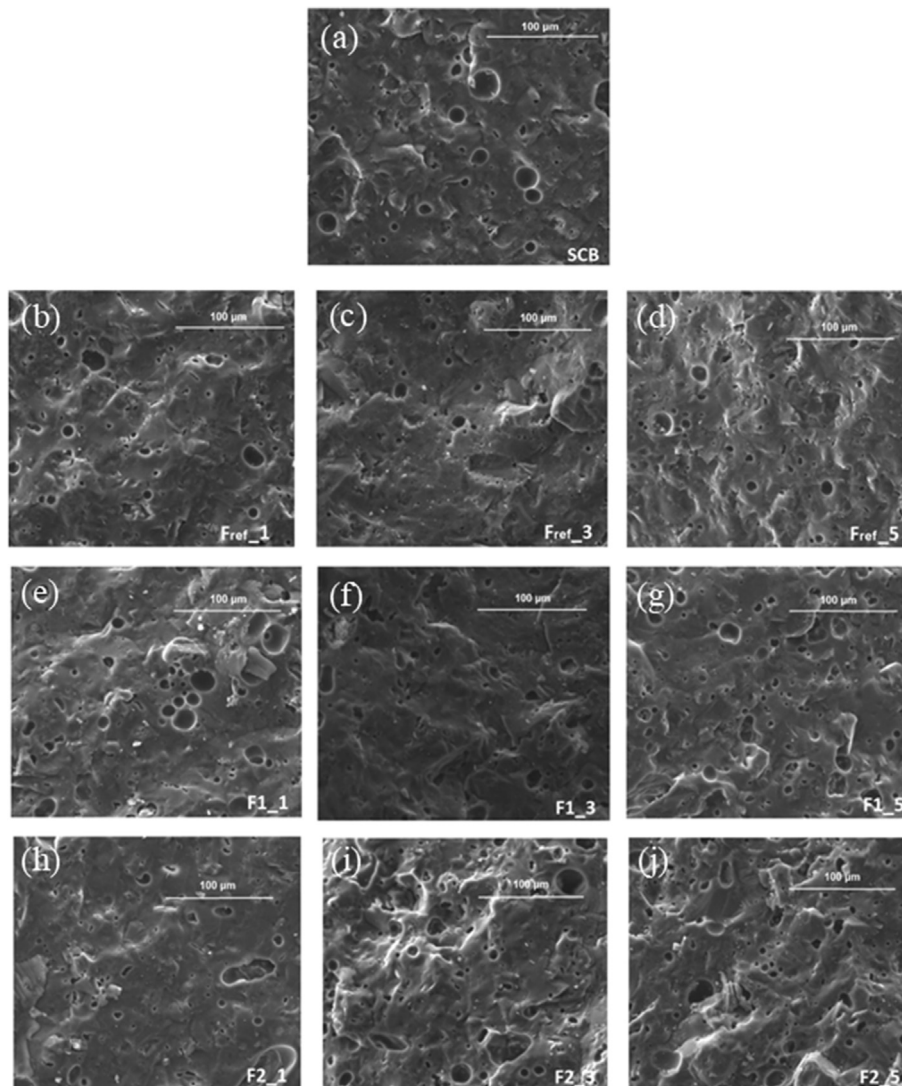
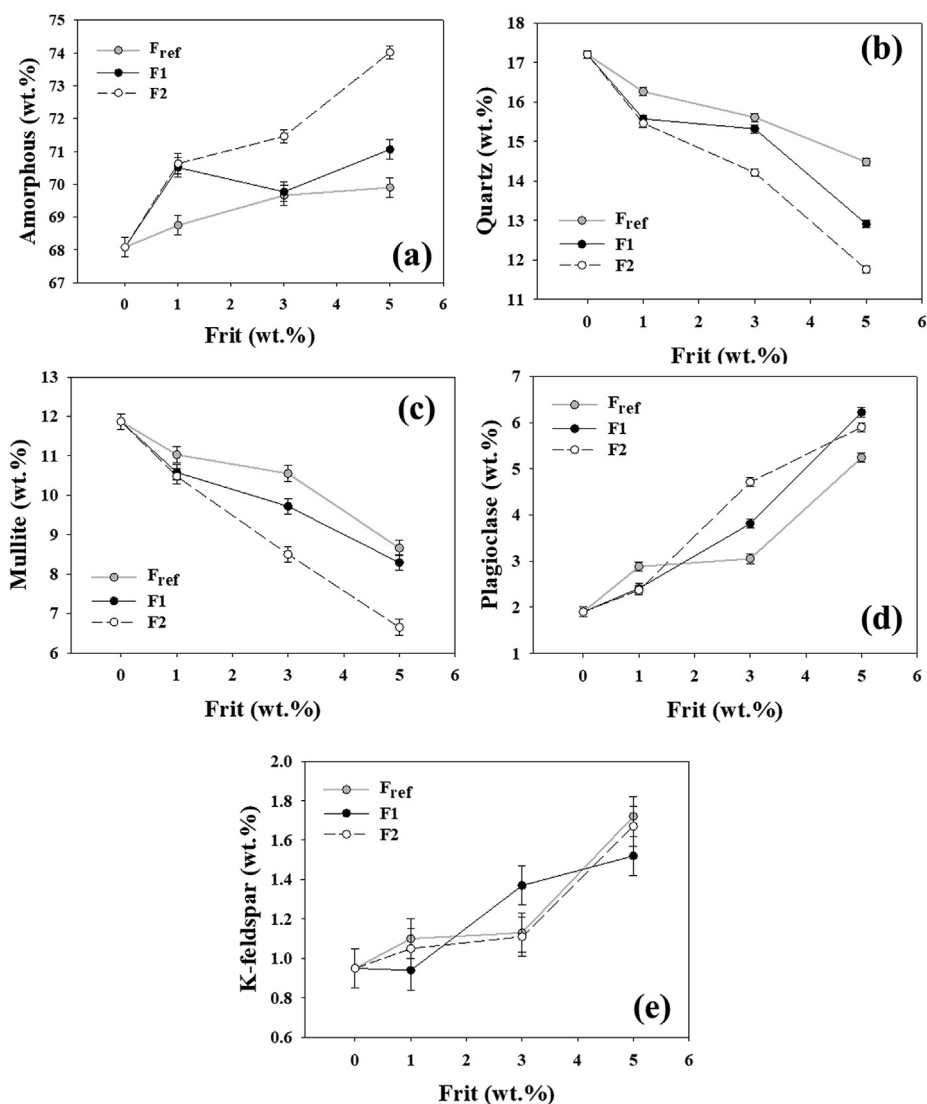
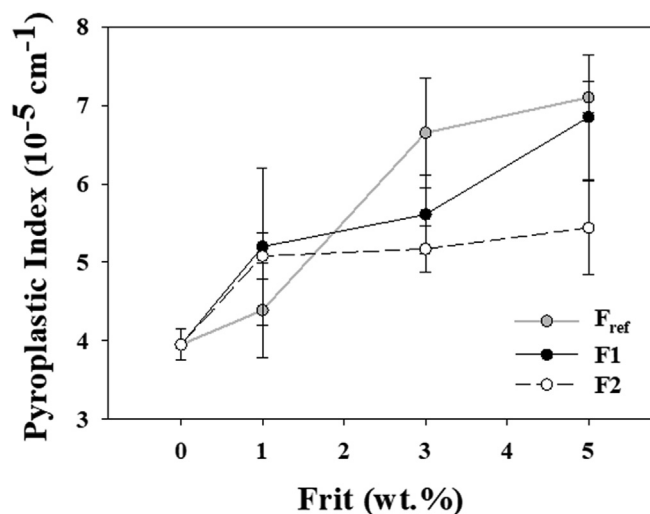


Fig. 6. Secondary electron SEM micrographs of the cross-section of each fired ceramic body: (a) SCB; (b) F<sub>ref\_1</sub>; (c) F<sub>ref\_3</sub>; (d) F<sub>ref\_5</sub>; (e) F1\_1; (f) F1\_3; (g) F1\_5; (h) F2\_1; (i) F2\_3; (j) F2\_5.



**Fig. 7.** Phase content of fired tiles (determined by XRPD and Rietveld-RIR), as a function of added frit. The figures show the following phases: (a) amorphous; (b) quartz; (c) mullite; (d) plagioclase; (e) K-feldspar. Agreement factors of the Rietveld refinements were in the range:  $R_{wp} = 5.25\text{--}5.74\%$ ,  $R_p = 3.66\text{--}4.06\%$ ,  $\chi^2 = 2.154\text{--}2.54$ .

also displayed in Table 1S1. The phase compositions of the ceramic bodies were qualitatively in line with what is expected from porcelain stoneware tiles, the major phase being amorphous (68–74 wt.%) with residual quartz (11.5–17.5 wt.%) and newly-formed mullite (6.5–12 wt.%). Some minor amount of residual K-feldspar was also observed (1–2 wt.%) together with residual albite in addition to newly formed anorthite (i.e. plagioclase 2–6 wt.%). The following general trends (more accentuated for F2) can be observed with increasing amounts of added frits (Fig. 7); i) amorphous content increases; ii) quartz content decreases; iii) mullite content decreases; iii) plagioclase content increases in a similar fashion for each sample series. The changes are too large to be simply explained by a dilution effect provoked by the addition of the frits. Instead, chemical interactions between the frits and the phases constituting the SCB determines some modifications of the phase evolution during firing. In particular, the high Ca-content in the frits leads to crystallization of newly-formed calcium aluminosilicate crystals (i.e. anorthite) following interaction with the dehydroxylated clay phases as observed by others (Lassinantti Gualtieri et al., 2018a). As a consequence, the mullite content decreases whereas the amount of plagioclase increases (Fig. 7 d and



**Fig. 8.** The pyroplastic index (PI) as a function of added frit.

e). This is particularly evident for the frit F2, which not only have a high content of Ca but is also depleted in Al (see Table 1). The stability of the quartz crystals decreases upon addition of the frits, in particular when the frit F2 is inserted in the SCB (see Fig. 7b). The decreased amount of quartz matches rather well with the increased amount of amorphous fraction (Fig. 7a).

A common defect in traditional ceramics obtained by viscous sintering, e.g. porcelain and porcelain stoneware, is pyroplastic deformation. This type of defect is of major industrial importance, in particular for large slabs, and is verified by loss of planarity of the fired product. Fig. 8 shows the pyroplastic index ( $PI$ , eq. (7)) as a function of added frit. The ceramic bodies containing frits all have a  $PI$  slightly higher than the standard body ( $4.1 \pm 0.2$ ).  $PI$  tends to increase with amount of added frit for the sample series including the commercial frit ( $F_{ref}$ ) (from  $4.4 \pm 0.6$  to  $7.1 \pm 0.2$ ). Such a trend is also observed in the other sample series although not statistically valid. The best results are observed for F2 where the  $PI$  remains rather stable ( $5.1$ – $5.4$ ) and close to the standard body. In a recent work, dos Santos Conserva et al. (2016) studied the influence of the grain size of quartz as well as flux composition (K-feldspar, Na-feldspar) on the  $PI$  of a traditional porcelain stoneware tile formulation and found an important correlation between  $PI$  and viscosity of the liquid phase calculated from its chemical composition using theoretical models. The authors found a  $PI$  (wet route) in the range  $7.4$ – $9.5 \text{ cm}^{-1} \cdot 10^{-5}$  and hence considerably higher with respect to the values found here (Fig. 8). In order to further investigate the relationship between  $PI$  and shear viscosity, the chemical composition of the amorphous fraction was calculated for each ceramic body by subtracting the contribution of the crystalline phases from the overall chemical composition of the ceramic body. Subsequently, the shear viscosity at  $1200 \text{ }^\circ\text{C}$  (maximum firing temperature) was calculated according to the model suggested by Giordano et al. (2008) and previously verified as suitable for porcelain stoneware (Conte et al., 2018). Table 2SI shows the results from these calculations. Fig. 9 shows the  $PI$  as a function of the calculated melt viscosity. A rather good linear trend can be observed, confirming previous results (dos Santos Conserva et al., 2016). The amorphous fraction of the frit-bearing bodies had a somewhat higher content of alkaline earth metals (Ca, Mg) with respect to the SCB (Table 2SI). Being glass modifiers, this brought on a decreased viscosity which explains the somewhat higher values

of  $PI$  observed for these ceramic pieces.

#### 4. Conclusions

In this work, we explored the possibility of using thermally transformed asbestos slates (KRY·AS) for the production of ceramic frits. The frits were specifically designed to be included in raw materials mixtures for the production of large formats of porcelain stoneware, a product with increasing market trend. The scale-up from traditional tiles to large slabs, made possible through novel process technologies, often necessities modification of traditional raw materials mixtures through e.g. addition of ceramic frits. Considering the increasingly higher product demand of large formats, new recycling opportunities in the ceramic industry through waste vitrification is thus opened. Mixtures of KRY·AS and natural raw materials (kaolin, feldspars) and waste from the processing of recycled glass lead to two novel ceramic frits (F1 and F2) that were inserted in a porcelain stoneware slab formulation (up to 5 wt.%). The frit F2 was particularly interesting considering that it was obtained only from a mixture of KRY·AS and glass processing waste without any addition of natural raw materials. First of all, the investigated compositions led to a water absorption less than what is required for porcelain stoneware (i.e.  $<0.5 \text{ wt.}\%$ ) using the temperature cycle optimized for the standard ceramic body. The technological properties were comparable or improved when frits were added. In particular, the addition of 5 wt.% of the novel frits leads to: i) A higher class of stain resistance (class 5 instead of class 3); ii) Reduction of the linear firing shrinkage ( $LFS$ ) leading to higher productivity, in particular for the novel frit containing only recycled waste (F2). In fact,  $LFS$  decreased from 6.2% for the standard ceramic body to 5.0% for the ceramic body containing F2; iii) Increased values of modulus of rupture ( $MOR$ ), going from  $60 \pm 8 \text{ MPa}$  for the standard body mixture to  $75 \pm 6$  and  $72 \pm 3 \text{ MPa}$  for bodies containing F1 and F2, respectively.

In summary, we can conclude that the production of ceramic frits from thermally treated asbestos is a technically viable recycling option of this secondary raw material and geographically advantageous considering the short distance between major Italian ceramic industries and potential waste sources.

In a broader perspective, the results reinforce the argumentations in favor for the implementation of a thermal treatment plant in the Northern Italy and safe recycling in regional industries such as the ceramic cluster of Sassuolo. Economic assessment, together with industrial tests, are challenges to be met in future work.

#### Declaration of competing interest

None.

#### Acknowledgements

This work was financially supported by Ministero dell'Ambiente e della Tutela del Territorio e del Mare, Italy, Decr. Dir. Min. Ric-Dec\_2017\_0000196, 22/12/17, "Tecnologie di trattamento di rifiuti contenenti amianto (RCA) e riciclo per la produzione di piastrelle ceramiche, nell'ottica di una economia circolare". We kindly acknowledge P. Miselli for collecting the DSC traces.

#### Appendix A. Supplementary data

Supplementary data to this article can be found online at <https://doi.org/10.1016/j.jclepro.2019.119084>.

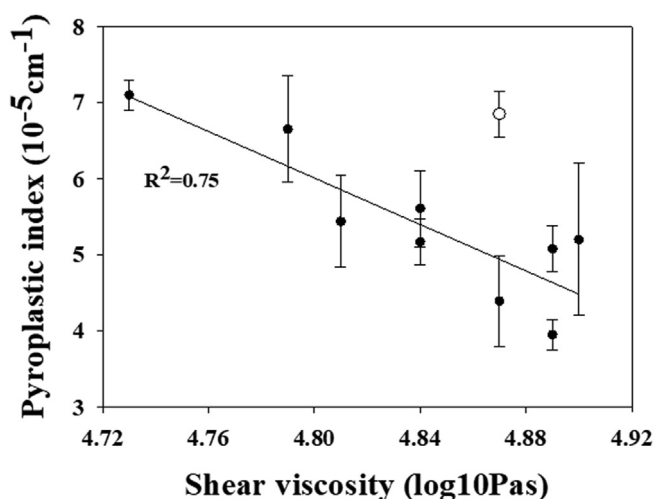


Fig. 9. The pyroplastic index ( $PI$ ) as a function of shear viscosity at  $1200 \text{ }^\circ\text{C}$ , the latter calculated from chemical composition of the amorphous fraction and theoretical models (Giordano et al., 2008). The point represented by a white symbol (F1\_5) was not included in the linear fit.

## References

- Abruzzese, C., Marabini, A.M., Paglietti, F., Plescia, P., 1998. CORDIAM process: a new treatment for asbestos wastes. In: Mishra, B. (Ed.), EPD Congress Book, the Minerals, Metals and Materials Society. San Antonio TX USA. TMS Springer, Boston, pp. 563–577.
- Amorós, J.L., Orts, M.J., García-Ten, Gozalbo, A., Sánchez, E., 2007. Effect of the green porous texture on porcelain tile properties. *J. Eur. Ceram. Soc.* 27, 2295–2301. <https://doi.org/10.1016/j.jeurceramsoc.2006.07.005>.
- Bernardo, E., Esposito, L., Rambaldi, E., Tucci, A., Hreglich, S., 2008. Recycle of waste glass into “Glass-Ceramic stoneware”. *J. Eur. Ceram. Soc.* 91, 2156–2162. <https://doi.org/10.1111/j.1551-2916.2008.02460.x>.
- Campione, I., Fragassa, C., Martini, A., 2019. Kinematics optimization of the polishing process of large-sized ceramic slabs. *Int. J. Adv. Manuf. Technol.* <https://doi.org/10.1007/s00170-019-03623-3>.
- Canetti, A., 2018. Produzione ceramica e prospettive di sviluppo. *Ecoscienza* 2, 36–37.
- Carbajal, L., Rubio-Marcos, F., Bongochea, M.A., Fernandez, J.F., 2007. Properties related phase evolution in porcelain ceramics. *J. Eur. Ceram. Soc.* 27, 4065–4069. <https://doi.org/10.1016/j.jeurceramsoc.2007.02.096>.
- Conte, S., Zanelli, C., Artid, M., Cruciani, G., Dondi, M., 2018. Predicting viscosity and surface tension at high temperature of porcelain stoneware bodies: a methodological approach. *Materials* 11, 2475–2780. <https://doi.org/10.3390/ma11122475>.
- Dondi, M., Ercolani, G., Guarini, G., Melandri, C., Raimondo, M., Rocha e Almendra, E., Tenorio Cavalcante, P.M., 2005. The role of surface microstructure on the resistance to stains of porcelain stoneware tiles. *J. Eur. Ceram. Soc.* 25, 357–365. <https://doi.org/10.1016/j.jeurceramsoc.2004.01.017>.
- D’Orsi, F., 2007. Amianto Valutazione, Controllo, Bonifica. EPC Libri, Rome (in Italian).
- Dos Santos Conserva, L.R., Melchiades, F.G., Natri, S., Boschi, A., Dondi, M., Guarini, G., Raimondo, M., Zanelli, C., 2016. Pyroplastic deformation of porcelain stoneware tiles: wet vs. dry processing. *J. Eur. Ceram. Soc.* 37, 333–342. <https://doi.org/10.1016/j.jeurceramsoc.2016.08.015>.
- Downey, A., Timmons, D.M., 2005. Study into the applicability of thermochemical conversion technology to legacy asbestos wastes in the U.K. In: Waste Management 2005 Abstract Conference Book, Tucson.
- Ferrari, S., Gualtieri, A.F., 2006. The use of illitic clays in the production of stoneware tile ceramics. *Appl. Clay Sci.* 32, 73–81. <https://doi.org/10.1016/j.clay.2005.10.001>.
- Giantomassi, F., Gualtieri, A.F., Santarelli, L., Tomasetti, M., Lusvardi, G., Lucarini, G., et al., 2010. Biological effects and comparative cytotoxicity of thermal transformed asbestos-containing materials in a human alveolar epithelial cell line. *Toxicol. In Vitro* 24, 1521–1531. <https://doi.org/10.1016/j.tiv.2010.07.009>.
- Giordano, D., Russell, J.K., Dingwell, D.B., 2008. Viscosity of magmatic liquids: a model. *Earth Planet. Sc. Lett.* 271, 123–134. <https://doi.org/10.1016/j.epsl.2008.03.038>.
- Gualtieri, A.F., 2000. Accuracy of XRPD QPA using the combined Rietveld-RIR method. *J. Appl. Crystallogr.* 33, 267–278. <https://doi.org/10.1107/S002188989901643X>.
- Gualtieri, A.F., Tartaglia, A., 2000. Thermal decomposition of asbestos and recycling in traditional ceramics. *J. Eur. Ceram. Soc.* 20, 1409–1418. [https://doi.org/10.1016/S0955-2219\(99\)00290-3](https://doi.org/10.1016/S0955-2219(99)00290-3).
- Gualtieri, A.F., Elmi, G., 2006. Understanding the high temperature reaction sequence during the thermal treatment of cement–asbestos slates. In: Proceedings of the European Conference on Asbestos Risks and Management. December 4–6, 2006. ARAM, Rome.
- Gualtieri, A.F., 2007. Thermal behavior of the raw materials forming porcelain stoneware mixtures by combined optical and in situ X-ray dilatometry. *J. Am. Ceram. Soc.* 90, 1222–1231. <https://doi.org/10.1111/j.1551-2916.2007.01614.x>.
- Gualtieri, A.F., Cavenati, C., Zanatto, I., Meloni, M., Elmi, G., Lassinantti Gualtieri, M., 2008a. The transformation sequence of cement–asbestos slates up to 1200 °C and safe recycling of the reaction product in stoneware tile mixtures. *J. Hazard Mater.* 152, 563–570. <https://doi.org/10.1016/j.jhazmat.2007.07.037>.
- Gualtieri, A.F., Lassinantti Gualtieri, M., Tonelli, M., 2008b. In situ ESEM study of the thermal decomposition of chrysotile asbestos in view of safe recycling of the transformation product. *J. Hazard Mater.* 156, 260–266. <https://doi.org/10.1016/j.jhazmat.2007.12.016>.
- Gualtieri, A.F., Zanatto, I., 2009. Industrial Process for the Direct Temperature Induced Recrystallization of Asbestos and/or Mineral Fibers Containing Waste Products Using a Tunnel Kiln and Recycling, European Patent, EP 2 027943 B1.
- Gualtieri, A.F., Giacobbe, C., Sardisco, L., Saraceno, M., Lassinantti Gualtieri, M., Lusvardi, G., Cavenati, C., Zanatto, I., 2011. Recycling of the product of thermal inertization of cement–asbestos for various industrial applications. *Waste Manag.* 31, 91–100. <https://doi.org/10.1016/j.wasman.2010.07.006>.
- Gualtieri, A.F., Boccaletti, M., 2011. Recycling of the product of thermal inertization of cement–asbestos for the production of concrete. *Constr. Build. Mater.* 25, 3561–3569. <https://doi.org/10.1016/j.conbuildmat.2011.03.049>.
- Gualtieri, A.F., Veratti, L., Tucci, A., Esposito, L., 2012. Recycling of the product of thermal inertization of cement–asbestos in geopolymers. *Constr. Build. Mater.* 31, 47–51. <https://doi.org/10.1016/j.conbuildmat.2011.12.087>.
- Gualtieri, A.F., 2017. Introduction. In: Mineral Fibres: Crystal Chemistry, Chemical-Physical Properties, Biological Interaction and Toxicity, vol. 18. European Mineralogical Union, London, UK, pp. 1–15.
- IARC, International Agency for Research on Cancer, 1987. Monograph. Suppl. 7, 106–116.
- Karamanov, E., Karamanov, A., 2009. Glass-ceramic frits from fly ash in terracotta production. *Waste Manag. Res.* 27, 87–92. <https://doi.org/10.1177/0734242X08088694>.
- Kim, Y.-C., Hong, W.-H., 2017. Optimal management program for asbestos containing building materials to be available in the event of a disaster. *Waste Manag.* 64, 272–285. <https://doi.org/10.1016/j.wasman.2017.03.042>.
- Kusiorowski, R., Zaremba, T., Piotrowski, J., 2016. Influence of the type of pre-calced asbestos containing wastes on the properties of sintered ceramics. *Constr. Build. Mater.* 106, 422–429. <https://doi.org/10.1016/j.conbuildmat.2015.12.110>.
- Larson, A.C., von Dreele, R.B., 1994. GSAS Generalized Structure Analysis System. *Laur* 86–748. Los Alamos National Laboratory, Los Alamos, NM.
- Lassinantti Gualtieri, M., Romagnoli, M., Gualtieri, A.F., 2011. Influence of body composition on the technological properties and mineralogy of stoneware: a DOE and mineralogical-microstructural study. *J. Eur. Ceram. Soc.* 31, 673–685. <https://doi.org/10.1016/j.jeurceramsoc.2010.12.002>.
- Lassinantti Gualtieri, M., Mugoni, C., Guandalini, S., Cattini, A., Mazzini, D., Alboni, C., Siligardi, C., 2018a. Glass recycling in the production of low-temperature stoneware tiles. *J. Clean. Prod.* 197, 1531–1539. <https://doi.org/10.1016/j.jclepro.2018.06.264>.
- Lassinantti Gualtieri, M., Colombini, E., Mazzini, D., Alboni, C., Manfredini, T., Siligardi, C., 2018b. The effect of alkaline earth carbonated on the microstructure and mechanical properties of impermeable and lightweight ceramics. *J. Eur. Ceram. Soc.* 38, 5563–5568. <https://doi.org/10.1016/j.jeurceramsoc.2018.08.011>.
- Manning, C.B., Vallyathan, V., Mossman, B.T., 2002. Diseases caused by asbestos: mechanisms of injury and disease development. *Int. Immunopharmacol.* 2, 191–200. [https://doi.org/10.1016/S1567-5769\(01\)00172-2](https://doi.org/10.1016/S1567-5769(01)00172-2).
- Pérez-Estébanez, M., Mácova, P., Šašek, P., Viani, A., Gualtieri, A., 2014. Mg-phosphate ceramics produced from the product of thermal transformation of cement-asbestos. *Inzynieria Mineralna* 15, 187–192.
- Pongrácz, E., Pohjola, V.J., 2004. Re-defining waste, the concept of ownership and the role of waste management. *Resour. Conserv. Recycl.* 40, 141–153. [https://doi.org/10.1016/S0921-3449\(03\)00057-0](https://doi.org/10.1016/S0921-3449(03)00057-0).
- Pugnalon, A., Lucarini, G., Rubini, C., Smorlesi, A., Tomasetti, M., Straffella, E., Armeni, T., Gualtieri, A.F., 2015. Raw and thermally treated cement-asbestos exerts different toxicity effects on A549 cells in vitro. *Acta Histochem.* 117, 29–39. <https://doi.org/10.1016/j.acthis.2014.10.007>.
- Røe, O.D., Stella, G.M., 2015. Malignant pleural mesothelioma: history, controversy and future of a manmade epidemic. *Eur. Respir. Rev.* 24, 115–131. <https://doi.org/10.1183/09059180.00007014>.
- Romero, M., Pérez, J.M., 2015. Relation between the microstructure and technological properties of porcelain stoneware. A review. *Mater. Construcción* 65, 320–338. <https://doi.org/10.3989/mc.2015.05915>.
- Sánchez, E., García-Ten, J., Sanz, V., Moreno, A., 2010. Porcelain tile: almost 30 years of steady scientific-technological evolution. *Ceram. Int.* 36, 831–845. <https://doi.org/10.1016/j.ceramint.2009.11.016>.
- Sanchez, E., Sanz, V., Cañas, E., Sales, J., Kayaci, K., Taşkıran, M.U., Anil, Ü.E., Türk, Ş., 2019. Revisiting pyroplastic deformation. Application for porcelain stoneware tile bodies. *J. Eur. Ceram. Soc.* 39, 601–609. <https://doi.org/10.1016/j.jeurceramsoc.2018.09.032>.
- Sharma, G., 2003. Digital Color Imaging Handbook. CRC Press, Webster New York, pp. 30–32 (Chapter 1).
- Soldati, R., Zanelli, C., Guarini, G., Piancastelli, A., Melandri, C., Fazio, S., Bignozzi, M.C., Dondi, M., 2018. Pore evolution and compaction behaviour of spray-dried bodies for porcelain stoneware slabs. *J. Eur. Ceram. Soc.* 38, 4127–4136. <https://doi.org/10.1016/j.jeurceramsoc.2018.04.058>.
- Taskiran, M.U., Dermirkol, N., Capoglu, A., 2005. A new porcelainised stoneware material based on anorthite. *J. Eur. Ceram. Soc.* 25, 293–300. <https://doi.org/10.1016/j.jeurceramsoc.2004.03.017>.
- Toby, B.H., 2001. EXPGUI, a graphical user interface for GSAS. *J. Appl. Crystallogr.* 34, 210–213. <https://doi.org/10.1107/S0021889801002242>.
- Viani, A., Gualtieri, A.F., Secco, M., Peruzzo, L., Artioli, G., Cruciani, G., 2013a. Crystal chemistry of cement-asbestos. *Am. Mineral.* 98, 195–1105. <https://doi.org/10.2138/am.2013.4347>.
- Viani, A., Gualtieri, A.F., Pollastri, S., Rinaudo, C., Croce, A., Urso, G., 2013b. Crystal chemistry of the high temperature product of transformation of cement-asbestos. *J. Hazard Mater.* 248–249. <https://doi.org/10.1016/j.jhazmat.2012.12.030>.
- Viani, A., Gualtieri, A.F., 2013. Recycling the product of thermal transformation of cement-asbestos for the preparation of calcium sulfoaluminate clinker. *J. Hazard Mater.* 260, 813–818. <https://doi.org/10.1016/j.jhazmat.2013.06.020>.
- Zanelli, C., Raimondo, M., Guarini, G., Dondi, M., 2011. The vitreous phase of porcelain stoneware: composition, evolution during sintering and physical properties. *J. Non-Cryst. Solids* 357, 3251–3260. <https://doi.org/10.1016/j.jnoncrsol.2011.05.020>.

## **Chapter 5**

**Synthesis of blue and black ceramic pigments from KRY·AS**

# Synthesis of blue and black ceramic pigments from KRY·AS

## 6.6. Introduction

### 6.6.1. Ceramic pigments

Nowadays inorganic natural and synthetic pigments are widely applied in decorations and coatings, and they are preferred to organic pigments because of their higher stability under chemical corrosion, high temperatures and UV radiations. They are used for many materials, such as glazes ceramic bodies, porcelain enamels, glasses, paints and plastics. [1-6]

In the field of ceramic materials there are three general ways used to colour a sample. Firstly, organometallic dyes (soluble salts), which contain transition metal ions. [7-9] A second method, which is used mainly to produce an opaque white colour, is to induce precipitation of the crystalline phase during the sintering. For example, the solubility of zirconium and titanium dioxide is reduced at the decrease of the temperature, and precipitation occurs. The last method consists in dispersing the pigment inside the material or in the glaze; the pigment is a coloured crystalline phase that is insoluble in the matrix. For this application pigments require specific properties: resistance at high temperature (a melting point generally  $> 1500^{\circ}\text{C}$ ) and to be inert respect to the liquid phase of ceramic bodies or molten glaze.

### 6.6.2. Blue ceramic pigments

Blue ceramic materials traditionally owe their colour to cobalt (II) in a tetrahedral coordination. The most used cobalt pigments are  $\text{CoAl}_2\text{O}_4$  [10] and olivine  $\text{Co}_2\text{SiO}_4$  [11]. The first, named cobalt blue, has a spinel structure and is synthesised as a pure alumina-based pigment or through co-precipitation of aluminium and cobalt hydroxides with a subsequent treatment at high temperature [12]. Its colour can be modified toward turquoise or green with the addition of chromium oxide instead of alumina and zinc replacing cobalt. The pigment  $\text{Co}_2\text{SiO}_4$  requires a higher amount of cobalt compared to the spinel, and it is principally used in glaze, where  $\text{Co}^{2+}$  has a quadruple coordination. Unfortunately, at high temperature cobalt tends to precipitate, giving a defect called "cobalt bleeding" [13]. Because of these problems cobalt pigments in glaze can be substituted by vanadium-doped zirconium pigments. These are synthesised starting from a mixture of zirconia, ammonium metavanadate and silica, which is calcined [14,15]. Other types of cobalt blue pigments are based on silicates and oxides, for example hibonite  $\text{CaAl}_{12}\text{O}_{19}$  [16], hardystonite  $\text{Ca}_2(\text{Zn},\text{Co})\text{Si}_2\text{O}_7$  [17] and willemite  $(\text{Zn},\text{Co})_2\text{SiO}_4$  [14, 18]. A turquoise dye is hibonite doped with nickel [19]. A grey–

blue colour characterizes the mordant molybdena–alumina pigment ( $\text{MoO}_x\text{-Al}_2\text{O}_3$ ) [20]. Other dyes are: cobalt magnesium borate  $(\text{Co,Mg})_2\text{B}_2\text{O}_5$  and cobalt phosphates [21].

### 6.6.3. Black ceramic pigments

The main problem in the production of black pigments is the complexity of this colour: black is the consequence of an absorption of most wavelengths of the visible spectrum. Industrially the common solution is the use of several transition metal ions (chromophores), that are introduced in crystal sites with different coordinations. This method is meant to multiply the colour centres in order to absorb at different wavelength ranges and consequently to obtain the black colour of the pigment [22]. The most frequently used cations are  $\text{Cr}^{3+}$ ,  $\text{Fe}^{3+}$ ,  $\text{Co}^{2+}$ ,  $\text{Ni}^{2+}$ ,  $\text{Fe}^{2+}$ ,  $\text{Mn}^{2+}$ ,  $\text{Mn}^{3+}$ , and the energy of their optical bands changes once they are octahedrally or tetrahedrally coordinated [23-25]. The structures used for black pigments are spinel (solid solutions of chromite and magnetite in the Co-Cr-Fe-Mn-Ni-(Cu-V) system) [23,26] and corundum (solid solutions of eskolaite and hematite  $(\text{Cr,Fe})_2\text{O}_3$ ) [8,9]. The first structure is the most common for black pigments in ceramic products [27,28], while the second tends to create stability problems in glaze [29,30].

Among the most effective black pigments there are spinels containing nickel [31-33], but unfortunately nickel-precursors have been classified as carcinogenic by health regulations [34], therefore research for nickel-free black pigments have increased in the past decades [23,35].

### 6.6.4. Production of ceramic pigments with recycled raw materials

Due to present economic and environmental conditions, the search for less expensive ceramic pigments is a matter of great interest [36]. The attention is devoted to lower the production costs, using waste instead of raw materials and to develop environmentally friendly products. The recycling of industrial waste in the production of ceramic pigments has increased in the last decades [37-39]. In literature there are various examples of this application such as: Ni/Cr galvanizing [40], marble sawing [41], titania synthesis [42] and foundries [43], red mud (RM) [44], electroplating sludge [38,45], steel waste [46], leather sludge [47], Al anodizing sludge [37], foundry sand [48] and marble saw dust [39]. KRY·AS is the product of thermal transformation of cement asbestos (CA) slates, this process consists of a thermal treatment of the CA in a tunnel kiln at annealing temperatures between 1200 and 1300°C [49-51]. The raw material obtained does not longer contain asbestos phases and it is composed of newly-formed minerals mainly consisting of clinker phases containing Ca, Mg, Al and Fe [50,51]. KRY·AS has already been successfully used, among other applications, in the production of Ca-silicate based ceramic pigments as green uvarovite

(Ca<sub>3</sub>Cr<sub>2</sub>(SiO<sub>4</sub>)<sub>3</sub>) and pink malayaite (Ca(Sn,Cr)SiO<sub>5</sub>) [52]. This study shows the application of thermally treated cement-asbestos in the production of blue and black ceramic pigments, using KRY·AS in the range between 50 and 90 wt. % based on other additional components. Each pigment was synthesised considering the interaction of different variables: the type of raw materials, their ratio, the temperature and the time of the thermal treatment.

On the basis of literature reference [53] we decided to synthesised blue pigments from KRY·AS, MgO, SiO<sub>2</sub> and Co<sub>3</sub>O<sub>4</sub> in different ratios.

Regarding black pigments the focus of this research is to obtain Ni-free black pigments starting from KRY·AS, with the addition of other raw materials as Co<sub>3</sub>O<sub>4</sub>, MnO<sub>2</sub> and Cr<sub>2</sub>O<sub>3</sub>. The molar ratios between Fe (present in KRY·AS), Co, Mn, Cr in the samples is defined from literature data [23].

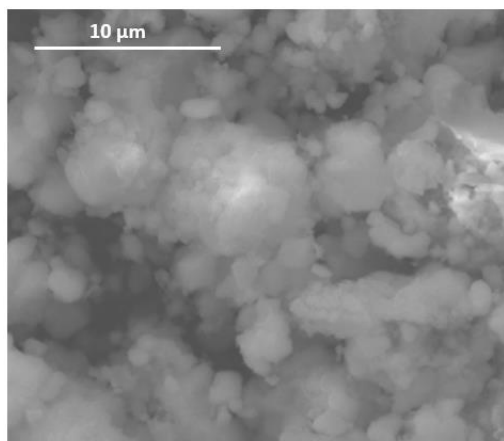
### 6.6.5. Mineralogical, chemical and morphological characteristics of KRY·AS

KRY·AS has been already characterized in previous studies [50-54]. However, taking into account the potential variability depending both on the compositions of the starting material (asbestos) and on the environmental conditions applied during the thermal treatment, it was again characterized through chemical and mineralogical analysis. (Table 1).

**Table 1.** Chemical composition and mineralogical phases of the used batch of KRY·AS.

Chemical composition (wt. %)										
Na <sub>2</sub> O	MgO	Al <sub>2</sub> O <sub>3</sub>	SiO <sub>2</sub>	P <sub>2</sub> O <sub>5</sub>	K <sub>2</sub> O	CaO	TiO <sub>2</sub>	MnO	Fe <sub>2</sub> O <sub>3</sub>	L.o.I.
0.22	7.76	3.26	21.53	0.00	0.30	52.28	0.21	0.07	2.66	11.71
Mineralogical composition [PDF]										
Larnite (Ca <sub>2</sub> SiO <sub>4</sub> ) [33-0302]	Brownmillerite (Ca <sub>2</sub> (Al,Fe <sup>3+</sup> ) <sub>2</sub> O <sub>5</sub> ) [30-0226]		Hatrurite (Ca <sub>3</sub> SiO <sub>5</sub> ) [86-0402]		CaO [37-1497]		MgO [43-1022]			





**Figure 1.** SEM macrograph of a KRY·AS sample treated at 1250°C for 4h.

A SEM micrograph of a KRY·AS sample treated at 1250°C for 4h is reported in **Figure 1** in order to evaluate the changes in the morphology and elements distribution after the synthesis of the pigments. The sample appears to be quite inhomogeneous with aggregates of different shapes and dimensions, with diameters from 2 μm to bigger irregular ones beyond 6 μm. The morphological inhomogeneity is followed by an inhomogeneous distribution of the elements. Through EDS analysis, we obtain that the mol % of iron and magnesium are in the subsequent intervals: Fe 0.5 – 1.5% and Mg 1.2 – 3.0 %.

## 6.7. Experimental

### 6.7.1. Synthesis and preparation of the samples

The samples were prepared mixing up KRY·AS and reagent-grade powders (from Sigma-Aldrich). For the blue colour (**series A**) MgO, SiO<sub>2</sub> and Co<sub>3</sub>O<sub>4</sub>, CoCO<sub>3</sub> or Co(OH)<sub>2</sub> were used according to the stoichiometry of a Co-doped åkermanite (Ca<sub>2</sub>Co<sub>x</sub>Mg<sub>1-x</sub>Si<sub>2</sub>O<sub>7</sub>) [55,56]. For the black colour two different type of pigments were prepared with Co<sub>3</sub>O<sub>4</sub> and MnO<sub>2</sub> as chromophores, in the first (**series B**) the stoichiometry was Co<sub>1.0</sub>Fe<sub>1.0</sub>Mn<sub>1.0</sub>O<sub>4</sub>; in the second (**series C**) Cr<sub>2</sub>O<sub>3</sub> was also added, with stoichiometry Co<sub>1.0</sub>Fe<sub>1.0</sub>Mn<sub>1.0</sub>Cr<sub>1.0</sub>, Co<sub>4.0</sub>Fe<sub>4.0</sub>Mn<sub>4.0</sub>Cr<sub>3.0</sub>, Co<sub>6.0</sub>Fe<sub>6.0</sub>Mn<sub>6.0</sub>Cr<sub>1.0</sub>, Co<sub>3.0</sub>Fe<sub>3.0</sub>Mn<sub>3.0</sub>Cr<sub>1.0</sub>.

The synthesis followed these steps, considering the changes in the variables reported in **Table 2, 3 and 4**:

- 1) based on the elements already present in KRY·AS, weigh the raw materials in order to obtain the desired molar ratio KRY·AS.
- 2) mix the components inside an agate mortar for at least 5 minutes.
- 3) transfer the mixture inside a porcelain crucible.

4) treat the sample in an oven under proper conditions of time and temperature.

The final samples were grounded into a fine powder with a mortar before their characterisation.

**Table 2.** Synthesis parameters for sample series A: experimental molar ratios of the elements and reaction temperature. The rate of the firing is 5°C/min in heating and cooling and the duration of the treatment at the maximum temperature is 6 h.

Sample A	Ca : Mg : Co : Si molar ratios				T (°C)
	Ca	Mg	Co	Si	
A1	1.00	1.00	/	1.99	1200
A2	2.01	1.00	/	2.01	1200
A3	2.42	0.50	0.50	2.00	1200
A4	2.00	0.50	0.49	1.99	1200
A5	2.00	0.75	0.25	2.00	1200
A6	2.00	0.90	0.10	2.00	1200
A7	2.42	0.50	0.24	1.99	1250
A8	2.00	0.50	0.49	2.00	1250
A9 <sup>[a]</sup>	2.42	0.50	0.25	2.00	1250
A10 <sup>[b]</sup>	2.42	0.50	0.25	1.99	1250

<sup>[a]</sup> use of Co(OH)<sub>2</sub> instead of Co<sub>3</sub>O<sub>4</sub>

<sup>[b]</sup> use of CoCO<sub>3</sub> instead of Co<sub>3</sub>O<sub>4</sub>

**Table 3.** Synthesis parameters for sample series B (Co : Fe : Mn molar ratio = 1 : 1 : 1): reaction temperature and time. The rate of the firing is 20°C/min in heating and 5°C/min in cooling and the ratio between the chromophore (Fe, Mn, Co) is always 1.

Sample B	Temperature and time of isotherm
B1	1250°C, 2h
B2	1300°C, 4h
B3	1300°C, 2h
B4	1250°C, 6h
B5	1250°C, 12h

**Table 4.** Synthesis parameters for sample series C: experimental molar ratios of the chromophore metal elements, reaction temperature and time. The rate of the firing is 20°C/min in heating and 5°C/min in cooling.

Sample C	Fe : Mn : Co : Cr molar ratio				Temperature and time of isotherm
	Fe	Mn	Co	Cr	
C1	1.00	1.00	0.99	0.99	1300°C, 2h
C2	4.00	4.00	4.03	3.07	1300°C, 2h
C3	6.00	6.00	5.99	1.00	1300°C, 2h
C4	3.00	2.99	3.03	1.00	1300°C, 2h
C5	3.00	3.02	2.99	0.99	1250°C, 6h

### 6.7.2. Characterisation

The specific colour of a pigment is usually the main purpose of its synthesis, but it is also strictly related to analytical information. The CIELAB (Commission Internationale d'Eclairage L\* a\* b\* colour space dimensions) is an objective method used to measure the chromatic characteristics of a sample. The colour coordinates were determined according to ISO 10545e16:2012 using a Medical High Technology Pikko colorimeter. L\* for the lightness from black (0) to white (100), a\* from green (-) to red (+), and b\* from blue (-) to yellow (+).

Ultraviolet-visible spectroscopy (UV-Vis) allows investigation of the electronic transitions caused by the absorption of light, especially in the visible range (380-720 nm), which are related to the colour of a pigment. Transition metal ions often produce an electronic spectrum in the visible region. The instrument used for this characterisation is UV-Vis spectrophotometer Jasco V-570 with a total reflection sphere installed for the solid samples analysis. Mineralogical studies performed by XRPD (X-Ray Powder Diffraction) were carried out with a PANalytical X'Pert Pro Bragg-Brentano diffractometer (Panalytical, Malvern, UK), using Ni-filtered Cu K $\alpha$  radiation ( $\lambda = 1.54060 \text{ \AA}$ ) with an X'Celerator detector. The patterns were taken over the diffraction angle range of  $2\theta = 5-75^\circ$ , with a time step of 50 s and a step size of  $0.03^\circ$  (angular step). In this work the attention is focused on the synthesis of a pigment of a specific colour, consequently the mineralogical studies are only qualitative, and the following considerations are semi-quantitative.

An Environmental Scanning Electron Microscope (FEI ESEM Quanta-200) in high vacuum condition was used to obtain a morphological and compositional analysis of the samples. The images were acquired in secondary electron mode (SE) to observe the morphology and the elements distribution and abundance (mol %) were elaborated through an EDS detector. EDS analyses were performed in quadruplicate for each examined agglomerate onto the surface; the result was a mean of the replicates and a standard deviation of 0.5%.

### 6.7.3. Application in mass coloration of ceramic tiles

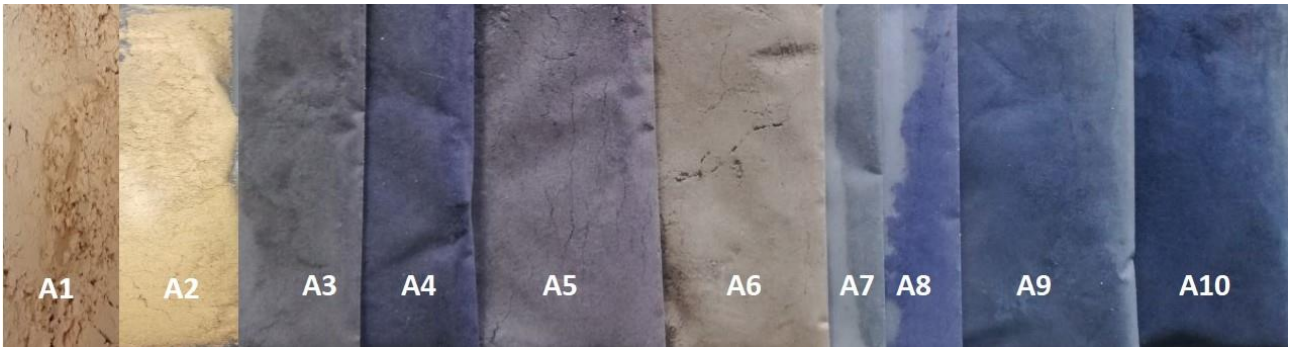
The stability and performance of the pigments were evaluated applying them as mass colorant for ceramic tiles.

The ceramic samples were prepared with the addition of the pigment in an amount of 1, 3 and 5 wt. % to a standard ceramic body mixture (SBC). The SBC, the process and the firing conditions are the same as the ones described in chapter 4 "Recycling of thermally treated cement-asbestos for the production of porcelain stoneware slabs" [54].

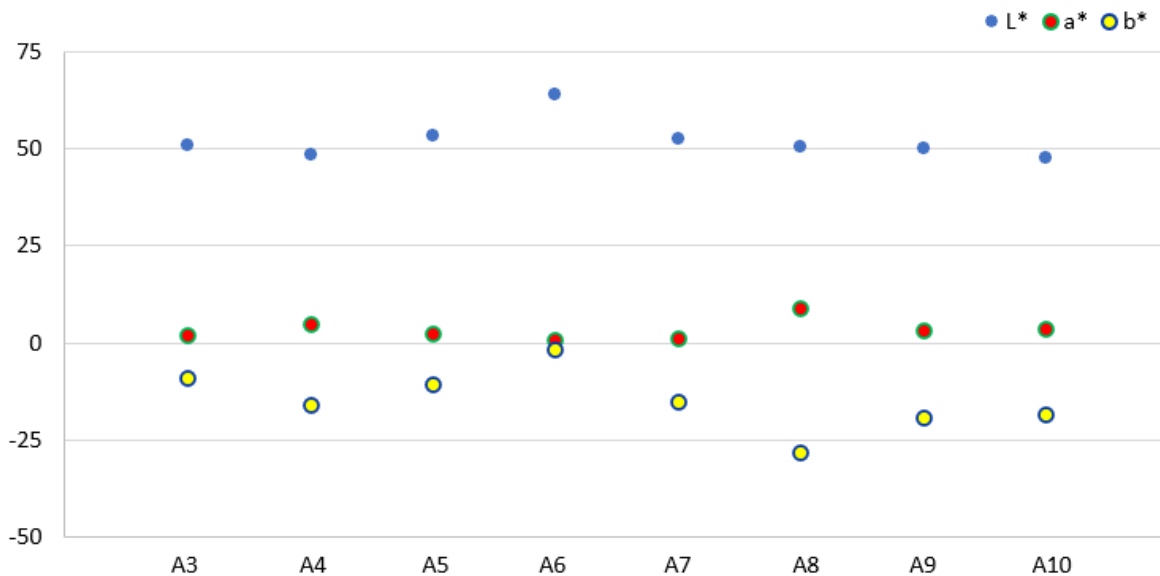
## 6.8. Blue pigment: Results and discussion

The images reported in **Figure 2** show the impact of the different variables, especially the amount of Co, on the colour of pigments A. The samples A1 and A2 were prepared without Co, and they present respectively a fleshy pink and a beige colour. A6 is light grey because it contains a very low amount of Co with a Mg/Co ratio of 9. The other samples show different shades of blue related to an Mg/Co ratio  $\leq 3$ , accordingly a higher amount of the chromophore.

The values of the colour parameters (**Figure 3**) confirm the previous observations.  $L^*$  is around 50 for all samples that are deep blue, while A6 that is a bright grey is associated to  $L^* = 64$ . The values of  $a^*$  are all positive, therefore they shift towards red, and  $b^*$  are negative, which indicates a blue colour. As a matter of fact, these pigments show a blue-violet tint. The best shades belong to A4 and A8 which present a Mg/Co ratio of 1 and the lowest values of  $b^*$  (-16.1 and -28.2 respectively). Furthermore, also samples A9 and A10 (Mg/Co = 2) have negative  $b^*$  value (-19.1 and -18.5 respectively) and an interesting colour.



**Figure 2.** Photographs for sample series A [57]



**Figure 3.**  $L^*$ ,  $a^*$  and  $b^*$  parameters for series A

The presence of multiple phases, with overlapped or very close peaks, makes the diffractograms interpretation slightly difficult.

As can be observed in **Table 5** in every sample is present åkermanite, which is a new phase completely absent from KRY·AS, however the reaction conditions and the reactants are compatible with its formation. Its synthesis is not due to changes of KRY·AS alone, at high temperature, because it was already observed that this material does not possess this characteristic. The reason for this change is due to the addition of  $\text{SiO}_2$  and  $\text{MgO}$ , which modifies the phases equilibrium, and it induces a solid-state reaction at high temperature [58].

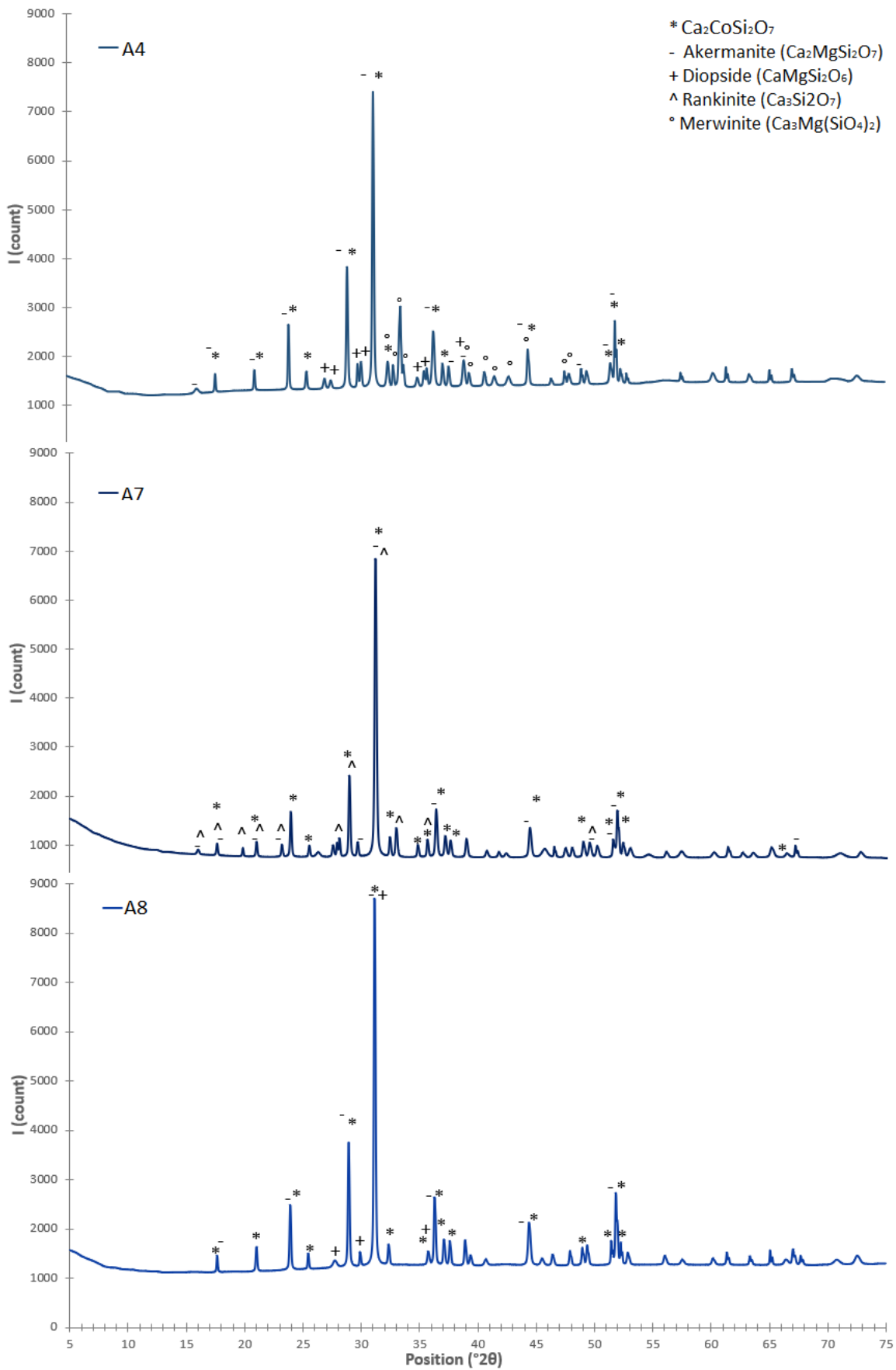
With the addition of  $\text{Co}_3\text{O}_4$ , cobalt replaces magnesium and the phase named Co-åkermanite ( $\text{Ca}_2\text{CoSi}_2\text{O}_7$ ) is formed; with  $\text{Mg}/\text{Co} \leq 3$  this becomes the first phase (**Table 5**). This effect is evident observing a characteristic peak of the åkermanite at  $16^\circ 2\theta$ , that practically disappear at the increasing of the amount of cobalt from A4 to A8 (**Figure 4**).

It is clear from the results that both the amount of Co and the reaction temperature are relevant variables in the formation of  $\text{Ca}_2\text{CoSi}_2\text{O}_7$ . A4 and A7 are very similar in terms of colour coordinate (**Figure 3**) and diffraction pattern (**Figure 5**), despite the difference in Mg/Co ratio, which is respectively 1 and 2; however A7 is treated at a higher temperature (1250°C instead of 1200°C). A8 was synthesised with both Mg/Co = 1 and a temperature of 1250°C; its counts are much higher respect to the other samples which indicate, from a semi-quantitative point of view, the presence of a higher amount of the first phase ( $\text{Ca}_2\text{CoSi}_2\text{O}_7$ ). Furthermore, the number of secondary phases is much lower than the other pigments and its colour is the brightest and bluest.

Similar results can be achieved with A9 and A10, and they can also be considered better in economical terms. In fact, they have been prepared with less amount of chromophore (Mg/Co=2) and, in addition, in case of A9, it was prepared with  $\text{Co}(\text{OH})_2$  that cost 5 time less than  $\text{Co}_3\text{O}_4$  (price from Sigma Aldrich) [59-61]

**Table 5.** Mineralogical phases for series A samples.

	Principal phase [PDF]	Secondary phases (PDF)
<b>A1</b>	Quartz ( $\text{SiO}_2$ ) [83-0539]	åkermanite ( $\text{Ca}_2\text{MgSi}_2\text{O}_7$ ) [83-1815]; merwinite ( $\text{Ca}_3\text{Mg}(\text{SiO}_4)_2$ ) [74-0382]; diopside ( $\text{CaMg}(\text{SiO}_3)_2$ ) [75-0945]; cristobalite ( $\text{SiO}_2$ ) [75-0945]; bredigite ( $\text{Ca}_{14}\text{Mg}(\text{SiO}_4)_8$ ) [36-0399]
<b>A2</b>	Åkermanite	merwinite; quartz; bredigite; diopside; cristobalite
<b>A3</b>	$\text{Ca}_2\text{CoSi}_2\text{O}_7$ [75-2059]	bredigite; merwinite; quartz; åkermanite; diopside
<b>A4</b>	$\text{Ca}_2\text{CoSi}_2\text{O}_7$	merwinite; åkermanite; diopside; bredigite
<b>A5</b>	$\text{Ca}_2\text{CoSi}_2\text{O}_7$	merwinite; åkermanite; diopside; bredigite
<b>A6</b>	Åkermanite	merwinite; bredigite; diopside; $\text{Ca}_2\text{CoSi}_2\text{O}_7$ ; cristobalite
<b>A7</b>	$\text{Ca}_2\text{CoSi}_2\text{O}_7$	åkermanite; rankite ( $\text{Ca}_3\text{Si}_2\text{O}_7$ ) [22-0539]; diopside
<b>A8</b>	$\text{Ca}_2\text{CoSi}_2\text{O}_7$	diopside; åkermanite
<b>A9</b>	$\text{Ca}_2\text{CoSi}_2\text{O}_7$	åkermanite; diopside
<b>A10</b>	$\text{Ca}_2\text{CoSi}_2\text{O}_7$	åkermanite; diopside

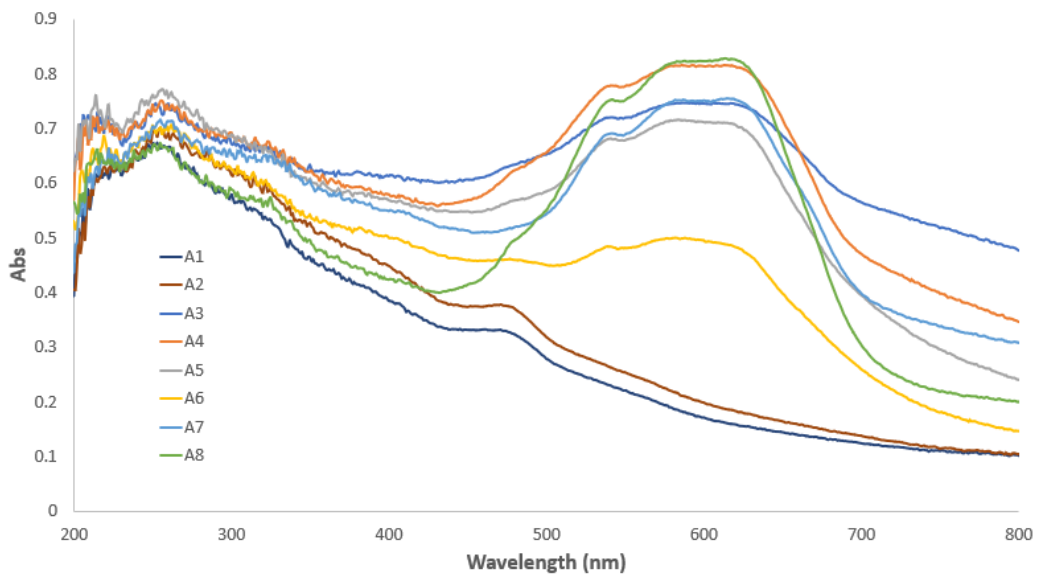


**Figure 4.** Diffraction pattern of A4, A7 and A8.

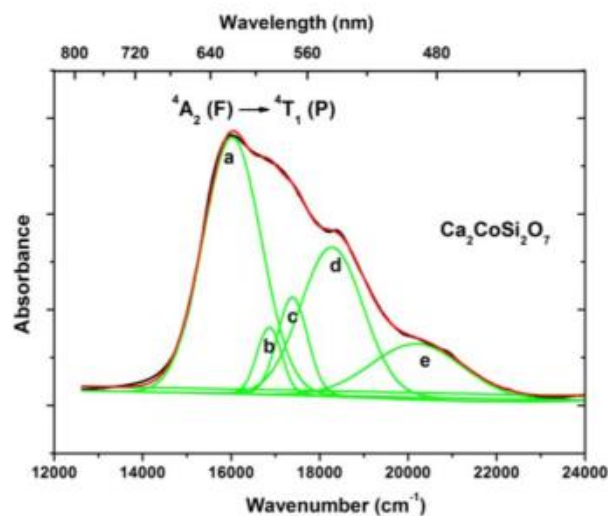
In **Figure 5** and **Table 6** one we can observe the influence of cobalt on the absorption bands of the samples in the UV-vis range. In A1 and A2 (without Co) there is only one peak at 478 nm. With the substitution of part of Mg with Co, this peak remains but another larger one starts to appear between 540 and 630 nm (A6, with Mg/Co = 9). With a higher amount of Co (Mg/Co  $\leq$  3) this larger band splits in three (around 540, 580 and 620 nm). A8 has the better profile in the spectrum, in terms of intensity and separation of the peaks.

As confirmed from literature work [53,56] the major amount of the peaks is related to  $\text{Ca}_2\text{CoSi}_2\text{O}_7$  (Co-åkermanite).

In Co-åkermanite,  $\text{Co}^{2+}$  is in a tetrahedral coordination, which implied the presence of an allowed triple band in visible region between 520 and 640 nm. This band, represented in **Figure 6** (literature work), is exactly the one shown by our samples (**Figure 5**).



**Figure 5.** UV-vis spectra of series A samples



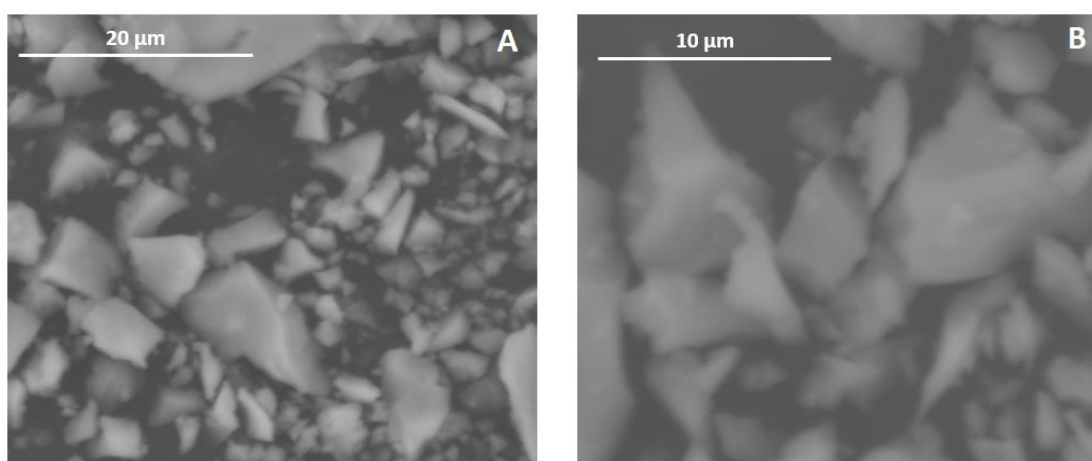
**Figure 6.** UV-Vis spectra of Co-åkermanite with an attempt of deconvolution [56]



**Table 6.** Intensity of the absorbance peak at a specific wavelength ( $\lambda$  in nm) from the UV-vis spectrum for sample series A

Absorbance at selected $\lambda$						
	217 nm	252 nm	475 nm	540 nm	580 nm	621 nm
<b>A1</b>	/	0.670	0.327	/	/	/
<b>A2</b>	/	0.693	0.374	/	/	/
<b>A3</b>	0.719	0.746	/	0.720	0.746	0.744
<b>A4</b>	0.701	0.732	0.620	0.778	0.815	0.812
<b>A5</b>	0.734	0.758	0.567	0.681	0.715	0.705
<b>A6</b>	0.661	0.692	0.459	0.484	0.500	0.483
<b>A7</b>	0.636	0.704	/	0.691	0.751	0.752
<b>A8</b>	0.654	0.668	0.496	0.752	0.821	0.825

For A9, **Figure 7**, the aggregates have different shapes, like splinters, and dimensions between 0.5 and 8  $\mu\text{m}$ . The Mg/Co average experimental ratio = 1.49, has been calculated confronting the value (obtained with EDS) of mol% of magnesium and calcium. This value is lower respect to the theoretical one (Mg/Co = 2). The ratio is also different between the larger and the smaller aggregates, in the former is near the real value, while in the latter is almost half. These results are greatly influenced by the inhomogeneity of KRY·AS.

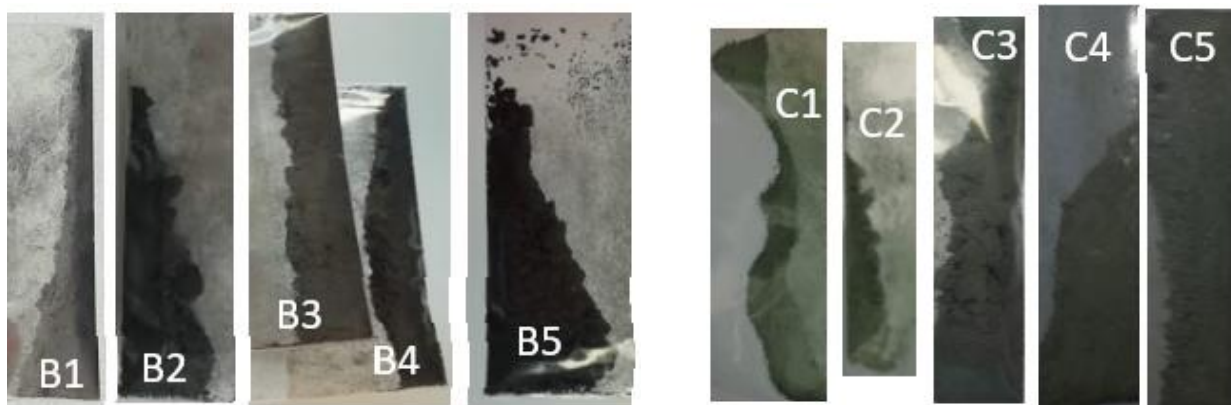


**Figure 7.** Micrographs of sample A9 at different magnitude

### 6.9. Black pigments: Results and discussion

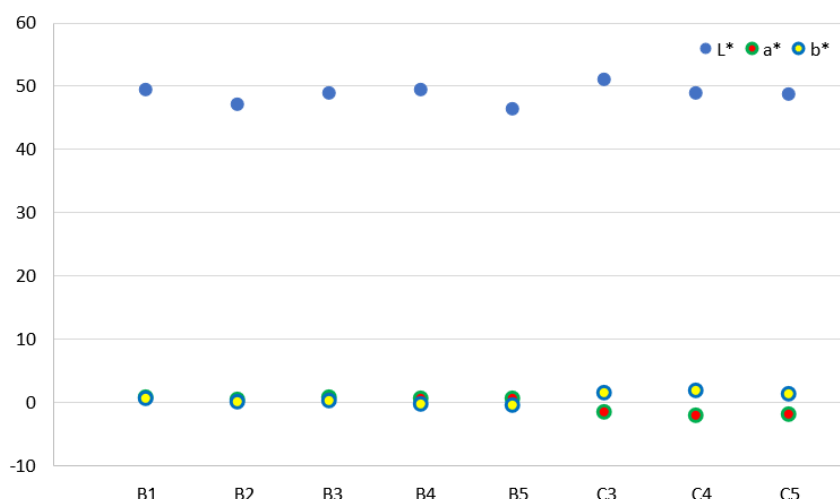
In order to obtain a black pigment in series B we changed the temperature and time of the thermal treatment, while the molar ratio between the chromophores was maintained equal to 1. In **Figure 8** we observe that the sample with the best colour is B5, which is anthracite black, and it was synthesised at 1250 °C for 12 h. The samples B1 (1250 °C, 2 h) and B3 (1300 °C, 2 h) are grey and B2 (1300 °C, 4 h) and B4 (1250 °C, 6 h) are dark grey. The colour of the pigments seems to be mostly influenced by the duration of the treatment rather than the temperature.

The colour of samples C (**Figure 8**) is clearly afflicted by the presence of chrome. C1 and C2 are both green, since they have a high amount of Cr, with a molar ratio Co/Cr respectively of 1 and 1.3, while the other chromophores maintain a molar ratio of 1. At the increase of the Co/Cr molar ratio (C3 = 6, C4 and C5 = 3) the samples present a darker colour with a green shade.



**Figure 8.** Photographs of sample series B, C [57]

The values of the colour parameters (**Figure 9**) confirm the previous observations. Samples B and C have an  $L^*$  parameter around 50, and B5 possesses the lowest value with  $L^* = 46.4$ . The values of  $a^*$  and  $b^*$  are close to 0 for B samples, which is a confirmation of the grey and black anthracite tint. The same parameters for C pigments have a highest module, they are indeed brighter than B with a slight green shade ( $a^* < 0$  and  $b^* > 0$ ).



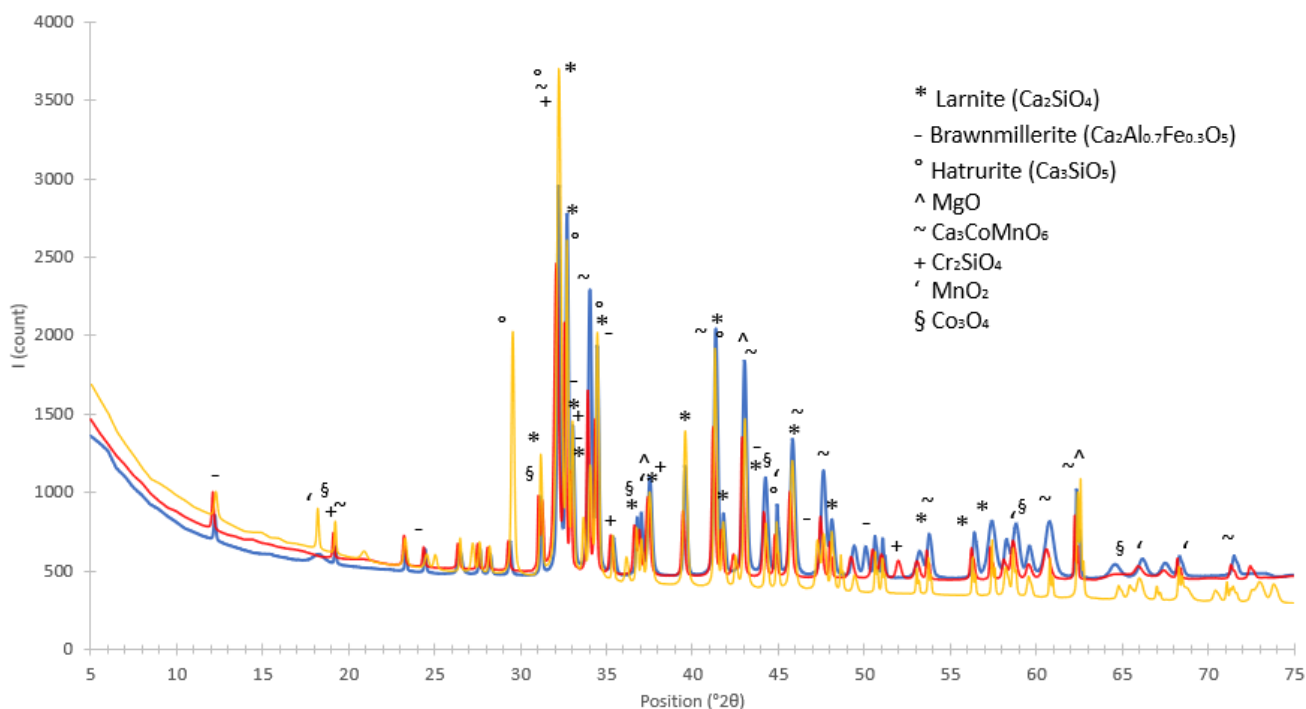
**Figure 9.**  $L^*$ ,  $a^*$  and  $b^*$  parameters for sample series B, C

Also, in these cases the interpretation of the diffractogram is complex because of the presence of phases, with overlapped or very close peaks.

The samples are compared to KRY·AS (**Figure 10**) to show the changes in the raw materials under the synthesis conditions. The first phase of each sample (**Table 7**) is larnite, which is reported to be the same as KRY·AS. In addition, among the secondary phases brownmillerite is also present inside KRY·AS from the beginning. The addition of cobalt and manganese help the formation of  $\text{Ca}_3\text{CoMnO}_6$  in both series, while the addition of chromium in series C formed  $\text{Cr}_2\text{SiO}_4$ . In all samples a low amount of unreacted raw materials can be found, such as  $\text{Co}_3\text{O}_4$  and  $\text{MnO}_2$ .

**Table 7.** Mineralogical phases for sample series B and C

	First phase [PDF]	Secondary phases (PDF)
<b>B1</b>	Larnite ( $\text{Ca}_2\text{SiO}_4$ ) [33-0302]	$\text{Ca}_3\text{CoMnO}_6$ [51-1776]; brownmillerite ( $\text{Ca}_2(\text{Al},\text{Fe}^{3+})_2\text{O}_5$ ) [30-0226]; $\text{Co}_3\text{O}_4$ [65-3103]
<b>B2</b>	Larnite ( $\text{Ca}_2\text{SiO}_4$ )	$\text{Ca}_3\text{CoMnO}_6$ ; brownmillerite; $\text{MnO}_2$ [17-0510]
<b>B3</b>	Larnite ( $\text{Ca}_2\text{SiO}_4$ )	$\text{Ca}_3\text{CoMnO}_6$ ; brownmillerite; $\text{Co}_3\text{O}_4$
<b>B4</b>	Larnite ( $\text{Ca}_2\text{SiO}_4$ )	$\text{Ca}_3\text{CoMnO}_6$ ; brownmillerite; $\text{Co}_3\text{O}_4$
<b>B5</b>	Larnite ( $\text{Ca}_2\text{SiO}_4$ )	$\text{Ca}_3\text{CoMnO}_6$ ; brownmillerite; $\text{Co}_3\text{O}_4$
<b>C1</b>	Larnite ( $\text{Ca}_2\text{SiO}_4$ )	$\text{Cr}_2\text{SiO}_4$ [82-1545]; brownmillerite; $\text{Co}_3\text{O}_4$ ; $\text{MnO}_2$
<b>C2</b>	Larnite ( $\text{Ca}_2\text{SiO}_4$ )	Brownmillerite; $\text{Ca}_3\text{CoMnO}_6$ ; $\text{Co}_3\text{O}_4$ ; $\text{MnO}_2$
<b>C3</b>	Larnite ( $\text{Ca}_2\text{SiO}_4$ )	$\text{Ca}_3\text{CoMnO}_6$ ; brownmillerite; $\text{Cr}_2\text{SiO}_4$ ; $\text{Co}_3\text{O}_4$
<b>C4</b>	Larnite ( $\text{Ca}_2\text{SiO}_4$ )	$\text{Ca}_3\text{CoMnO}_6$ ; brownmillerite; $\text{Cr}_2\text{SiO}_4$ ; $\text{Co}_3\text{O}_4$
<b>C5</b>	Larnite ( $\text{Ca}_2\text{SiO}_4$ )	$\text{Ca}_3\text{CoMnO}_6$ ; brownmillerite; $\text{Cr}_2\text{SiO}_4$ ; $\text{MnO}_2$ ; $\text{Co}_3\text{O}_4$

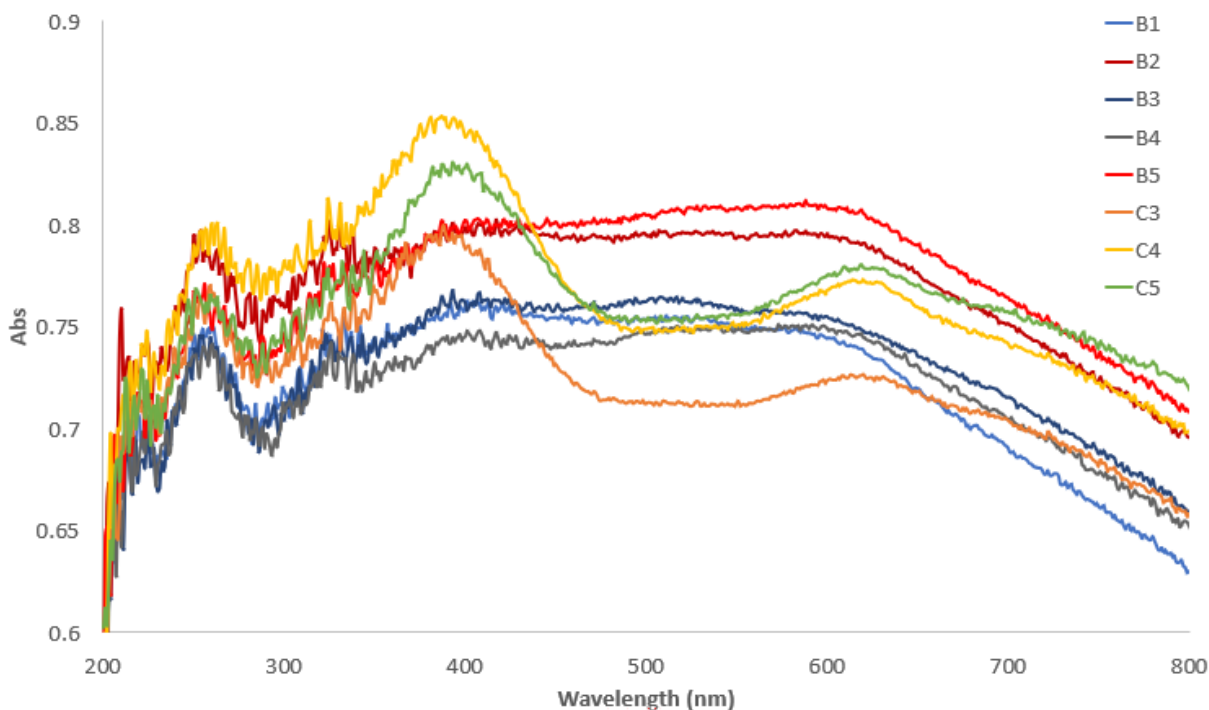


**Figure 10.** Diffraction pattern of B5 (blue), C5 (red) and KRY-AS (yellow).

**Figure 11** and **Table 8** and **9** show two different type of absorption spectra for series B and C. In the first case there are some difficulties to assign precise wavelengths to each peak. We can identify five different positions, as reported in **Table 8**, with low intensity, but a better shape for B1, B3 and B4. As described in literature most of them can be related to  $\text{Co}_3\text{O}_4$  (337 and 608 nm) [62] and  $\text{MnO}_2$  (410 nm) [63].  $\text{Co}_3\text{O}_4$  shows a band between 277 and 375 nm which involves the charge transfer transitions from  $\text{O}^{2-}$  to Co (II) and Co (III), and electronic transition of Co (III) in octahedral site [64]. Also, it shows a second band around 600 nm which is assigned to the second peak of Co (III) in octahedral site and Co (II) in tetrahedral [65].

**Table 9** shows the absorption intensity of three peaks at 259, 396 and 623 nm. Even in this case they eventually can be assigned to  $\text{Co}_3\text{O}_4$ , but it is not a perfect match.  $\text{Cr}_2\text{SiO}_4$  cannot be considered a possible match because its absorption bands are positioned at 505, 552 and 606 nm [66].

There is the possibility that, in case of both series B and C, part of the peaks is related to the inclusion of the chromophores inside larnite or brownmillerite. However, it is difficult to find other research able to confirm the exact structure that shows these absorptions.



**Figure 11.** UV-vis spectra for sample in series B and C

**Table 8.** Intensity of the absorbance peak at specific wavelength for the UV-vis spectrum of samples in series B

	Absorbance at specific $\lambda$				
	259 nm	337 nm	410 nm	518 nm	608 nm
<b>B1</b>	0.756	0.741	0.760	0.749	0.741
<b>B2</b>	0.782	0.789	0.801	/	0.793
<b>B3</b>	0.750	0.741	0.760	0.762	0.754
<b>B4</b>	0.750	0.731	0.743	0.747	0.748
<b>B5</b>	0.762	0.771	0.801	/	0.808

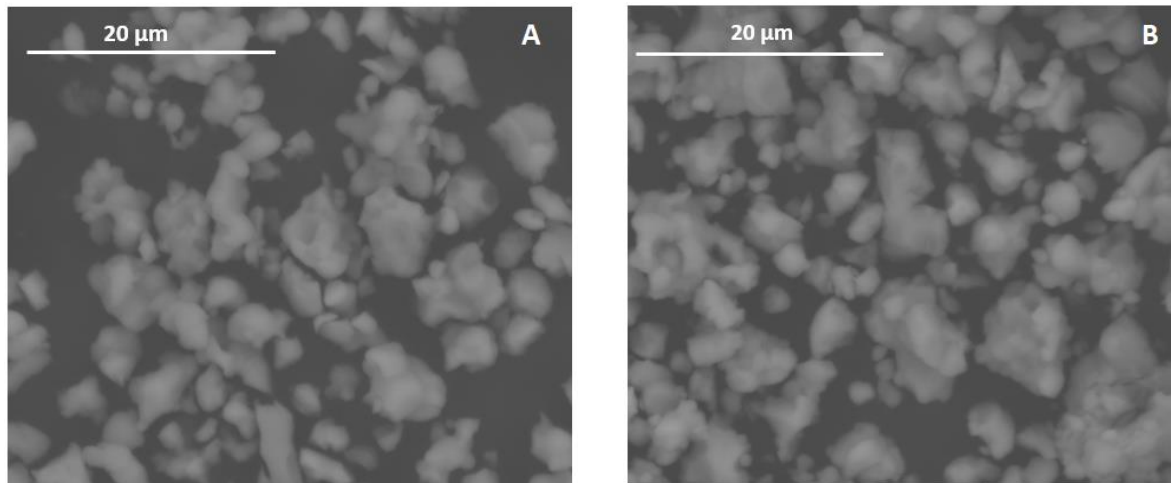
**Table 9.** Intensity of the absorbance peak at specific wavelength for the UV-vis spectrum of samples in series C

	Absorbance at specific $\lambda$		
	259 nm	396 nm	623 nm
<b>C3</b>	0.792	0.791	0.724
<b>C4</b>	0.765	0.848	0.771
<b>C5</b>	0.765	0.825	0.778

In case of B5 (**Figure 12 A**) the sample is formed by aggregates of different dimensions, with irregular shapes, mainly rounded. There are two types of aggregates: big and irregular, with an average diameter of 8  $\mu\text{m}$ , and small and more regular, with an average of 3  $\mu\text{m}$ . With EDS we obtain the measure of the experimental values of the molar ratio of the chromophores, which are close to the theoretical ones: Fe/Mn = 1.33 (theoretical value = 1) and Fe/Co = 0.77 (theoretical value = 1). The real value is closer to the theoretical mostly in the smaller aggregates, while in the bigger ones the values are detaches from it.

The morphology of C5 (**Figure 12 B**) is similar to B5, with the presence of aggregates of different dimensions (from 10  $\mu\text{m}$  to 2  $\mu\text{m}$  of diameter) and rounded shapes. Also, in this sample the elements distribution is inhomogeneous. The bigger aggregates have a much variable composition, respect to the smaller ones, and the molar ratio between the elements, in some cases, is far from the theoretical value. The average values of the molar ratio are Fe/Mn = 1.11 (theoretical value = 1), Fe/Co = 0.97 (theoretical value = 1) and Fe/Cr = 2.03 (theoretical value = 3).

Also, in these samples the inhomogeneity of KRY·AS is probably the main cause of a different punctual reactivity of the materials, which leads to these results.

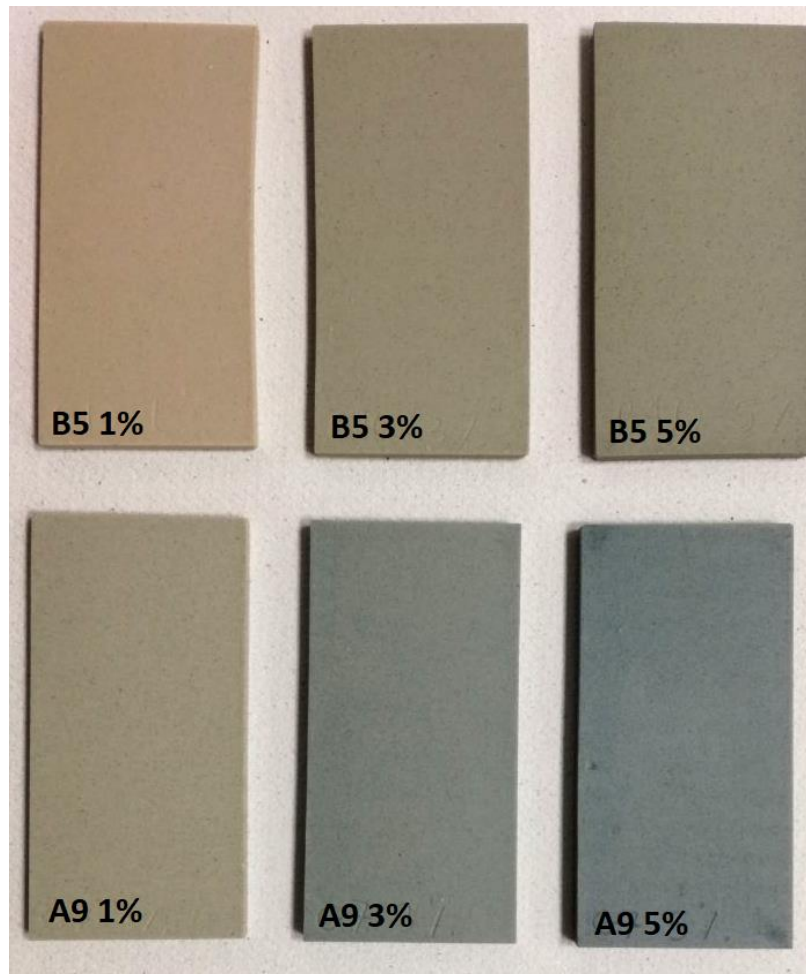


**Figure 12.** Micrographs of B5 (A) and C5 (B)

### 6.10. Ceramic tiles

We chose samples A9 and B5 to test the effect of the pigments inside a ceramic matrix. The reasons for these choices were: the homogeneous colour and the high amount of KRY·AS (respectively 85 and 94 wt. %) used for their synthesis. Moreover, in case of the blue pigment it is constituted of almost a single phase (Co-åkermanite).

B5 and A9 were used to prepare three ceramic samples each at a concentration 1, 3 and 5 wt. % (Figure 14).



**Figure 14.** Ceramic samples prepared with 1, 3 and 5 wt. % of A9 and B5

The ceramic samples with 1 wt. % of pigments have a light colour, but in any case, the different colouration is visible. The intensity of the colour, both A9 and B5, increases from 1 to 5 wt. %.

The required stability of the pigment is satisfied for both samples, as a matter of fact none of them react with the ceramic matrix.

During the process of preparation of the ceramic bodies, because of the addition of the pigments, the viscosity of the slips suffered a drastic change and the temperature of the mixture increased, especially in case of B5.

These effects are related to calcium silicate phases and their interaction with water with formation of colloidal hydrated calcium silicates, found in Portland cement. As highlighted by XRD analysis, our samples have for example larnite, brownmillerite and bredigite which are phases derived from KRY·AS [49-52,54].

The high viscosity of the slips was avoided increasing the amount of water added in the preparation process. The liquid excess was eliminated by the drying process in the stove. The procedure to prepare the ceramic samples was not influenced by these changes, because of that the rheology of these systems was not elaborated further.

### **6.11. Conclusion**

The present work shows the possibility to use high amount of KRY·AS in the synthesis of inorganic ceramic pigments. Different parameters have been evaluated: molar ratio between the components, especially with the chromophore, and/or temperature and time of the thermal treatment.

The first researched pigment is a blue one (A) with åkermanite structure and cobalt as chromophore, named Co-åkermanite ( $\text{Ca}_2\text{CoSi}_2\text{O}_7$ ). MgO, SiO<sub>2</sub> and Co<sub>3</sub>O<sub>4</sub> were added to KRY·AS in order to synthesis these pigments. A wide range of blue shades was observed, and these colours were confirmed with colorimetric analysis. The mineralogical composition of these samples showed the formation of  $\text{Ca}_2\text{CoSi}_2\text{O}_7$  as principal phase. In some case Co-åkermanite was also the phase in the highest amount (from a semi-quantitative analysis).

Pigments B and C were synthesized after. They were black pigments with iron, cobalt, manganese and, in case of the latter, even chromium used as chromophores. The observation of the samples reported that series B showed a varied grey-black coloration, and the darkest was B5 (anthracite black), while series C were grey with green shades, because of the chromium. The same results were confirmed with the CIELab method through colorimetric analysis.

In these samples KRY·AS composition was not significantly changed, with larnite as the first phase for each and every sample and the presence of unreacted brownmillerite, MnO<sub>2</sub> and Co<sub>3</sub>O<sub>4</sub>. It was also observed the formation of low amounts of Ca<sub>3</sub>CoMnO<sub>6</sub> (in B and C) and Cr<sub>2</sub>SiO<sub>4</sub> (only in C), which were the phases probably related to the observed colours.

ESEM/EDS analysis indicated a morphological and compositional heterogeneity of all the pigments, due to the characteristic of KRY·AS.



For both blue and black pigments, the best synthesis conditions were slow heating and cooling rate, with isotherm at 1250°C for 6/12 h. The purpose for an optimal molar ratio that can enhance the KRY·AS was achieved: for all the samples the amount of the thermally treated cement asbestos was around 90 wt. %.

In the second part of the project the best pigments (A9 and B5) were used to colour ceramic samples. Both pigments showed chemical stability in contact with the ceramic matrix and they produced, in an amount  $\geq 3$  wt. %, the researched change in the colour of the tiles.

The aim of the project was reached, with the production of interesting pigments, produced with a high amount of raw material (KRY·AS  $\approx 90$  wt. %) in respect to the chromophores.

## 5.7. References

- [1] G. Buxbaum, *Industrial Inorganic Pigments* (2<sup>nd</sup> edition), Wiley-VCH, Weinheim, Germany (1997).
- [2] M. Jansen, H.P. Letschert, *Inorganic yellow-red pigments without toxic metals*, *Nature* 404 (2000) 980.
- [3] J.H. Kim, B.R. Son, D.H. Yoon, K.-T. Hwang, H.-G. Noh, W.-S. Cho, U.-S. Kim, *Characterization of blue CoAl<sub>2</sub>O<sub>4</sub> nano-pigment synthesized by ultrasonic hydrothermal method*, *Ceram Int.* 38 (2012) 5707-5712.
- [4] C.M. Alvarez-Docio, J.J. Reinoso, A.D. Campo, J.F. Fernández, *2D particles forming a nanostructured shell: a step forward cool NIR reflectivity for CoAl<sub>2</sub>O<sub>4</sub> pigments*, *Dyes Pigm.* 137 (2017) 1-11.
- [5] M. Yoneda, K. Gotoh, M. Nakanishi, T. Fujii, T. Nomura, *Influence of aluminum source on the color tone of cobalt blue pigment*, *Powder Technol.* 323 (2018) 574-580.
- [6] S. Kurajica, J. Popović, E. Tkalčec, B. Gržeta, V. Mandić, *The effect of annealing temperature on the structure and optical properties of sol-gel derived nanocrystalline cobalt aluminate spinel*, *Mater Chem Phys.* 135 (2012) 587-593.
- [7] A. Burgyan, R.A. Eppler, *Classification of Mixed-Metal-Oxide Inorganic Pigments*, *Am. Ceram. Soc. Bull.* 62 (1983) 1001-1003.
- [8] P. Escribano, J.B. Carda, E. Cordoncillo: *Esmaltes y pigmentos ceramicos*, Faenza Editrice Iberica, Castellon (2001).
- [9] *Colour, Pigments and Colouring in Ceramics*, Italian Ceramic Society, SALA, Modena (2003).
- [10] M. Ardit, G. Cruciani, M. Dondi, *Structural relaxation in tetrahedrally coordinated Co<sup>2+</sup> along the gahnite-Co-aluminate spinel solid solution*, *Am. Mineral.* 97 (2012) 1394-1401.

- [11] M. Llusar, A. Forés, J.A. Badenes, J. Calbo, M.A. Tena, G. Monrós, Colour analysis of some cobalt-based blue pigments, *J. Eur. Ceram. Soc.* 21 (2001) 1121-1130.
- [12] F. Habashi, *Pigments through the Ages*, *Interceram* 65 (2016) 4-5.
- [13] M. Dondi, R.A. Eppler, *Ceramic Colorants*, in book: *Ullmann's Encyclopedia of Industrial Chemistry*, eds. Wiley-VCH Verlag GmbH & Co. KGaA, Weinheim (2014) 1-18.
- [14] M. Ocaña, A.R. González-Elipe, V.M. Orera, P. Tartaj, C.J. Serna, Spectroscopic Studies on the Localization of Vanadium(IV) in Vanadium-Doped Zircon Pigments, *J. Am. Ceram. Soc.* 81 (1998) 395-400.
- [15] M. Llusar, J.B. Vicent, J. Badenes, M.A. Tena, G. Monros, Environmental optimisation of blue vanadium zircon ceramic pigment, *J. Eur. Ceram. Soc.* 19 (1999) 2647-2657.
- [16] A. Leite, G. Costa, W. Hajjaji, M.J. Ribeiro, M.P. Seabra, J.A. Labrincha, Blue cobalt doped-hibonite pigments prepared from industrial sludges: Formulation and characterization, *Dyes Pigm.* 81 (2009) 211-217.
- [17] M. Dondi, C. Zanelli, M. Ardit, G. Cruciani, Co-Doped Hardystonite,  $\text{Ca}_2(\text{Zn,Co})\text{Si}_2\text{O}_7$ , a New Blue Ceramic Pigment, *J. Am. Ceram. Soc.* 94 (2011) 1025-1030.
- [18] E. Ozel, H. Yurdakul, S. Turan, M. Ardit, G. Cruciani, M. Dondi, Co-doped willemite ceramic pigments: Technological behaviour, crystal structure and optical properties, *J. Eur. Ceram. Soc.* 30 (2010) 3319-3329.
- [19] G. Costa, M.J. Ribeiro, W. Hajjaji, M.P. Seabra, J.A. Labrincha, M. Dondi, G. Cruciani, Ni-doped hibonite ( $\text{CaAl}_{12}\text{O}_{19}$ ): A new turquoise blue ceramic pigment, *J. Eur. Ceram. Soc.* 29 (2009) 2671-2678.
- [20] M. Dondi, F. Matteucci, G. Baldi, A. Barzanti, G. Cruciani, I. Zama, C.L. Bianchi, Gray-blue  $\text{Al}_2\text{O}_3$ - $\text{MoO}_x$  ceramic pigments: Crystal structure, colouring mechanism and performance, *Dyes Pigm.* 76 (2008) 179-186.
- [21] S. Meseguer, M.A. Tena, C. Gargori, J.A. Badenes, M. Llusar, G. Monrós, Structure and colour of cobalt ceramic pigments from phosphates, *Ceram. Int.* 33 (2007) 843-849.
- [22] K. Nassau, *The Physics and Chemistry of Color* (2<sup>nd</sup> edition), Wiley, New York, (2001).
- [23] M. Dondi, C. Zanelli, M. Ardit, G. Cruciani, L. Mantovani, M. Tribaudino, G.B. Andreozzi, Ni-free, black ceramic pigments based on Co—Cr—Fe—Mn spinels: A reappraisal of crystal structure, colour and technological behaviour, *Ceramics International* 39 (2013) 9533-9547.
- [24] R.G. Burns, *Mineralogical Applications of Crystal Field Theory* (2<sup>nd</sup> edition), Cambridge University Press, Cambridge (1993).
- [25] M. Wildner, M. Andrut, C.Z. Rudowicz, Optical absorption spectroscopy in geosciences. Part I: Basic concepts of crystal field theory, in *Spectroscopic Methods in Mineralogy*, eds. A. Beran, E. Libowitzky, Eötvös University Press, Budapest (2004) 93-144.
- [26] R.A. Eppler, Cobalt-free black pigments, *Am. Ceram. Soc. Bull.* 60 (1981) 562-565.

- [27] R.A. Eppler, Colorants for ceramics, in Encyclopedia of Chemical Technology, eds. R.E. Kirk, D.F. Othmer, Wiley, New York, (1998) 877-892.
- [28] G.N. Maslennikova, Pigments of the spinel type, *Glass and Ceramics* 58 (2001) 5-6.
- [29] R.A. Eppler, Selecting ceramic pigments, *American Ceramic Society Bulletin* 66 (1987) 1600-1604.
- [30] E. Ozel, S. Turan, Production and characterisation of iron-chromium pigments and their interactions with transparent glazes, *Journal of the European Ceramic Society* 23 (2003) 2097-2104.
- [31] G. Costa, V.P. Della, M.J. Ribeiro, A.P.N. Oliveira, G. Monrós, J.A. Labrincha, Synthesis of black ceramic pigments from secondary raw materials, *Dyes and Pigments* 77 (2008) 137-144.
- [32] J. Calbo, M. A. Tena, G. Monrós, M. Llusar, J. A. Badenes, Synthesis of nickel-iron spinel by non-conventional methods, *J Sol-Gel Sci Techn* 38 (2006) 167-177.
- [33] O.O. Vasilkov, O.P. Barinova, S.V. Kirsanova, N.A. Marnautov, A.B. Elfimov, Ceramic black pigments based on chromium-nickel spinel  $\text{NiCr}_2\text{O}_4$ , *Glass and Ceramics*, Vol. 74 (2017) 7-8.
- [34] H. Lu, X. Shi, M. Costa, C. Huang, Carcinogenic effect of nickel compounds, *Molecular and Cellular Biochemistry*, Volume 279, Issue 1-2 (2005) 45-67.
- [35] A.F. Gualtieri, E. Mazzucato, P. Venturelli, A. Viani, P. Zannini, L. Petras, Determination of Nickel(II) Oxide in Ceramic Pigments by In Situ X-ray Diffraction Quantitative Analysis, *J. Am. Ceram. Soc.* 82 (1999) 2566-2568.
- [36] M. Yoneda, K. Gotoh, M. Nakanishi, T. Fujii, Y. Konishi, T. Nomura, Solid-state synthesis and characterization of cobalt blue core-shell pigment particles, *Journal of the American Ceramic Society*, Volume 102, Issue 6 (2019) 3468-3476.
- [37] G. Costa, M.J. Ribeiro, T. Trindade, J.A. Labrincha, J.A., Development of waste-based ceramic pigments. *Bol. Soc. Esp. Ceram.* 46 (2007) 7-13.
- [38] C. Gargori, S.R. Prim, M. Llusar, M.V. Folgueras, G. Monrós, Recycling of Cr/Ni/Cu plating wastes as black ceramic pigments, *Mater. Lett.* 218 (2018) 341-345.
- [39] W. Hajjaji, G. Costa, C. Zanelli, M.J. Ribeiro, M.P. Seabra, M. Dondi, J.A. Labrincha, An overview of using solid wastes for pigment industry, *J. Eur. Ceram. Soc.* 32 (2012) 753-764.
- [40] A. Ribeiro, W. Hajjaji, M.P. Seabra, J.A. Labrincha, Malayaite ceramic pigments prepared from industrial wastes: formulation and characterization, *J. Mater. Sci. Forum* 636-637 (2010) 1371-1376.
- [41] M.A. Montero, M.M. Jordán, M.S. Hernández-Crespo, T. Sanfeliu, The use of sewage sludge and marble residues in the manufacture of ceramic tile bodies, *J. Appl. Clay Sci.* 46 (2009) 404-408.
- [42] M. Dondi, G. Guarini, M. Raimondo, C. Zanelli, D. Dalle Fabbriche, A. Agostini, Recycling the insoluble residue from titania slag dissolution (tionite) in clay bricks, *J. Ceram. Int.* 36 (2010) 2461-2467.
- [43] R. Siddique, A. Noumowe, Utilization of spent foundry sand in controlled low-strength materials and concrete, *J. Conserv. Recycling* 53 (2008) 27-35.

- [44] N. Yalçın, V. Sevinç, Utilization of bauxite waste in ceramic glazes, *Ceram. Int.* 26 (2000) 485-493.
- [45] W. Hajjaji, M.P. Seabra, J.A. Labrincha, Evaluation of metal-ions containing sludges in the preparation of black inorganic pigments, *J. Hazard. Mater.* 185 (2011) 619-625.
- [45] G.C. Díaz, E.A. Reynoso, M.C. Castanon-Bautista, O. Novelo, R. Jordan, Synthesis of  $MgFe_2O_4$  spinel using steel waste as iron resource, *Int. J. Eng. Inn. Technol.* 4 (2015) 1-4.
- [47] Z. Chen, Y. Du, Z. Li, D. Sun, C. Zhu, Synthesis of black pigments containing chromium from leather sludge, *Ceram. Int.* 41 (2015) 9455-9460.
- [48] D. Esteves, W. Hajjaji, M.P. Seabra, J.A. Labrincha, Use of industrial wastes in the formulation of olivine green pigments, *J. Eur. Ceram. Soc.* 30 (2010) 3079-3085.
- [49] Gualtieri, A.F., Zanatto, I, Industrial process for the direct temperature induced recrystallization of asbestos and/or mineral fibres containing waste products using a tunnel kiln and recycling. European Patent, EP. 2 027943 B1 (2009).
- [50] A.F. Gualtieri, C. Cavenati, I. Zanatto, M. Meloni, G. Elmi, M. Lassinantti Gualtieri, The transformation sequence of cement-asbestos slates up to 1200°C and safe recycling of the reaction product in stoneware tile mixtures, *Journal of Hazardous Materials* 152 (2008) 563-570.
- [51] A. Viani, A.F. Gualtieri, S. Pollastri, C. Rinaudo, A. Croce, G. Urso, Crystal chemistry of the high temperature product of transformation of cement-asbestos, *Journal of Hazardous Materials* 248-249 (2013) 69- 80.
- [52] A.F. Gualtieri, C. Giacobbe, L. Sardisco, M. Saraceno, M. Lassinantti Gualtieri, G. Lusvardi, C. Cavenati, I. Zanatto, Recycling of the product of thermal inertization of cement-asbestos for various industrial applications, *Waste Manag.* 31 (2011) 91-100.
- [53] C. Gori, L. Mantovani, M. Tribaudino, C. Zanelli, M. Dondi, Colour of  $Ca(Co_xMg_{1-x})Si_2O_6$  pyroxenes and their technological behaviour as ceramic colorants, *Ceramics International* 44 (2018) 12745-12753.
- [54] M.L. Ligabue, M. Lassinantti Gualtieri, G. Lusvardi, D. Malferrari, A.F. Gualtieri, Innovative recycling route of thermally treated cement-asbestos for the production of porcelain stoneware slabs, *J. Cleaner Production*, 247 (2020) 119084.
- [55] E. Burzo, Melilites and related silicates, in *Magnetic properties of non-metallic inorganic compounds based on transition elements*, eds. Landolt-Börnstein - Group III Condensed Matter (2005).
- [56] L. Mantovani, PhD Thesis: Synthesis and characterization of  $CaCoSi_2O_6$ - $Co_2Si_2O_6$  pyroxenes, Tutor: M. Tribaudino, Co-Tutor: D. Bersani, (2013), Università degli Studi di Parma.
- [57] A. Iodice, Tesi Triennale: Sintesi e caratterizzazione pigmenti inorganici ottenuti da amianto inertizzato, Thesis supervisors: G.Lusvardi, A.F. Gualtieri, (2019), Università di Modena e Reggio Emilia.

- [58] B. Joachim, E. Gardes, R. Abart, W. Heinrich, Experimental growth of akermanite reaction rims between wollastonite and monticellite: evidence for volume diffusion control, *Contrib Mineral Petrol* 161 (2011) 389-399.
- [59] <https://www.sigmaaldrich.com/catalog/product/aldrich/221643?lang=it&region=IT>. Accessed 3<sup>rd</sup> September 2020.
- [60] <https://www.sigmaaldrich.com/catalog/product/aldrich/379956?lang=it&region=IT>. Accessed 3<sup>rd</sup> September 2020.
- [61] <https://www.sigmaaldrich.com/catalog/product/aldrich/342440?lang=it&region=IT> Accessed 3<sup>rd</sup> September 2020.
- [62] K.H. Mahmoud, Synthesis and Spectroscopic Investigation of Cobalt Oxide Nanoparticles, *Polymer Composites* 37 (2016) 1881-1885.
- [63] V. Hoseinpour, M. Souri, N. Ghaemi, Green synthesis, characterisation, and photocatalytic activity of manganese dioxide nanoparticles, *Micro & Nano Letters*, Vol. 13, Iss. 11 (2018) 1560-1563.
- [64] A.F. Osorio, A.V. Olmos, R.S. Berru, and R. Escudero, *Rev. Adv. Mater. Sci.* 22 (2008) 60.
- [65] L.G.A. van de Water, G.L. Bezemer, J.A. Bergwerff, M.V. Helder, B.M. Weckhuysen, K.P. de Jong, Spatially resolved UV–vis microspectroscopy on the preparation of alumina-supported Co Fischer–Tropsch catalysts: Linking activity to Co distribution and speciation, *J. Catal.* 242, 287 (2006).
- [66] B.E. Scheetz, W.B. White, Synthesis and Optical Absorption Spectra of Cr<sup>2+</sup> -Containing Orthosilicates, *Contr. Mineral. und Petrol.* 37 (1972) 221-227.

## **Chapter 6**

**Innovative use of thermally treated cement-asbestos in the production of foaming materials: effects of composition, reducing agent, temperature, and reaction time**

## **Innovative use of thermally treated cement-asbestos in the production of foaming materials: effects of composition, reducing agent, temperature, and reaction time**

### **6.1. Introduction**

Hazardous asbestos-containing materials (ACM), especially cement-asbestos (CA) slates, are still present in everyday life and working environment of many European countries, resulting in potential exposure of the population to carcinogenic respirable fibres [1].

In the last 40 years, a policy of abatement and disposal of ACM in landfills has been followed. Unfortunately, the use of landfills cannot be the ultimate solution at zero risks of fibres dispersion in air and water; in the long run, the safety cannot be guaranteed. Furthermore, it conflicts with the directives of the European Commission, pointing to the recycling other than disposal of the wastes (End of Waste concept) [2].

The ultimate solution to this problem is the removal of all the asbestos-containing materials from the environment and the transformation of this hazardous wastes into a secondary raw material [3,4]. There are many viable conversion processes that realize the crystal-chemical transformation of CA slates. Among them, the KRY·AS process represents a successful and economical solution [5-7] and consists of a thermal treatment of CA slates in a tunnel kiln at annealing temperatures between 1200 and 1300 °C; the raw material, so obtained, has been given the commercial name of KRY·AS.

The mineralogical composition of CA can be summarized as follows: calcite ( $\text{CaCO}_3$ ), cement hydration products, mainly portlandite ( $\text{Ca(OH)}_2$ ), amorphous calcium silicate hydrates (C-S-H), asbestos minerals and inert aggregates [7]. As reported [6,7], chemical and mineralogical composition of KRY·AS shows that it does no longer contain asbestos minerals. It is composed of newly formed phases mainly consisting of clinker phases containing Ca, Mg, Al and Fe. Moreover, *in vitro* tests demonstrated that KRY·AS has the same toxic potential of a commercial clinker [8,9].

KRY·AS can replace natural raw materials, in quantities from 10 to 40 wt. %, in the process to obtain clay bricks, rock-wool glasses for insulation and glass-ceramics for the production of ceramic tiles [10], concrete [11], traditional porcelain stoneware tiles [12, 13] and frits [14].

In recent years, the attention has been focused also on the foam glass, that is becoming increasingly popular in the construction of civil and industrial buildings and structures [15,16]. Foam glass is a multi-phase material constituted of three components: amorphous phase, gaseous phase and crystalline phase [17]. Due to the low conductivity of glass and the presence of porosity up to 90%

vol, foamed glass is a very good insulating material. Its advantages include low density, good mechanical properties, low thermal conductivity, and incombustibility [18,19].

In general, foam glass is prepared from a finely ground glass powder, an eventual flux agent and a pore-forming agent. The fluxing (carbonate or sulphate of alkaline metals) and foaming agents (coke, graphite or SiC) react at high temperature (between 800 and 1100 °C) to produce gases and consequently pores in the amorphous matrix [20].

Recycled materials like soda-lime and bottle glass waste [21-25], cathode ray tube panels [26], mineral wool waste [27], red mud [28], mine and industrial tailings [23, 29], slag [24], coal fly and bottom ashes [21, 30], rice husk [25], eggshell wastes [31], oyster shell wastes [32] has already been used to prepare foam glass, as source of amorphous phase or foaming agent. KRY·AS, thanks to its chemical composition (see paragraph 2.1) could be also proposed as interesting supplier of SiO<sub>2</sub> (~20 wt. %) in foam glass, even if the typical amount of SiO<sub>2</sub> required is > 50 wt. % [33]. Therefore, the present study focuses on the use of KRY·AS and glass waste (deriving from the processing of soda-lime glass from domestic recycling, RG), for the manufacture of foam glass. The fusion behaviour of KRY·AS and RG was examined as key property in foam glass preparation. Optimization of the foaming conditions (temperature and time) was reached using KRY·AS, RG, SiC and fluxing agent in different ratios. The physical, microstructural, and mineralogical properties of the final products was analysed and subsequently compared to a standard industrial product, to evaluate their practical suitability as insulating materials.

## **6.2. Materials and methods**

### **6.2.1. Materials**

KRY·AS and RG were used to prepare glass powder at the laboratory scale. KRY·AS was previously obtained by thermal treatment of a package of CA slates in a discontinuous industrial kiln at 1200°C for 40 hours [5,6]. Subsequently, the slate fragments were crushed and homogenized in a hammer mill (Pulverisette 16 Fritsch, Germany) to obtain a powder of dimensions < 200 µm. RG was the fine fraction (< 100 µm) collected in the fabric filter of the mills used to grind domestic glass waste (from Emiliana Rottami, Modena, Italy); this fraction due to its small size (the average grain size is about 50µm), to the occurrence of Mg and Fe (**Table 1**) that may impart unwanted chromatic tones and to specific laws that limit their reuse to produce food containers, is not easily recoverable and must be considered like a waste. KRY·AS was already characterized in previous studies [5,6,34]. However, considering the variability in the composition of the starting material (CA slates) and the reaction



during the thermal treatment, it was again characterized along with the recycled glass (RG) (**Table 1**).

**Table 1.** Chemical composition (wt. %) of KRY-AS and RG as well as mineralogical composition of KRY-AS

	<b>KRY-AS</b>		<b>RG</b>		
<b>Na<sub>2</sub>O</b>	0.22		12.26		
<b>MgO</b>	7.76		2.50		
<b>Al<sub>2</sub>O<sub>3</sub></b>	3.26		2.84		
<b>SiO<sub>2</sub></b>	21.53		69.31		
<b>P<sub>2</sub>O<sub>5</sub></b>	0.00		0.02		
<b>K<sub>2</sub>O</b>	0.30		0.77		
<b>CaO</b>	52.28		9.24		
<b>TiO<sub>2</sub></b>	0.21		0.14		
<b>MnO</b>	0.07		0.05		
<b>Fe<sub>2</sub>O<sub>3</sub></b>	2.66		0.47		
<b>KRY-AS Mineralogical Phases</b>					
<b>Larnite</b>	<b>Brownmillerite</b>	<b>Calcite</b>	<b>Lownsonite</b>	<b>Periclase</b>	<b>Reyerite</b>
Ca <sub>2</sub> SiO <sub>4</sub>	Ca <sub>2</sub> (Fe,Al) <sub>2</sub> O <sub>5</sub>	CaCO <sub>3</sub>	CaAl <sub>2</sub> Si <sub>2</sub> O <sub>7</sub> (OH) <sub>2</sub> ·H <sub>2</sub> O	MgO	(KCa <sub>14</sub> Si <sub>24</sub> O <sub>60</sub> (OH) <sub>5</sub> ·5H <sub>2</sub> O

Powdered SiC-1500 ( $D_{50} < 2.5 \mu\text{m}$ ), SiC-600 ( $D_{50} = 9.3 \mu\text{m}$ ) and SiC-320 ( $D_{50} = 29.2 \mu\text{m}$ ) from Thermo Fisher Scientific were selected as foaming agents; SiC releases CO<sub>2</sub> due to the oxidation reaction of the C with the oxygen of the air during the firing process [56].

Appropriate doses of pure powdered (purity > 99%) Na<sub>2</sub>CO<sub>3</sub> and Li<sub>2</sub>CO<sub>3</sub> (from Quimiamel, Quox Corporation, Spain) were used as fluxing agents to reduce the melting temperature [35], as well as to improve thermal expansion [36,37] It should be highlighted that the carbonates, during the thermal decomposition, release CO<sub>2</sub>, therefore they may also act as foaming agents, provided that the thermal decomposition occurs after the foaming glass mixture melts. Furthermore, it is important to point out the characteristics of lithium, compared with other alkali metal ions. The use of lithium minerals in ceramics and glass is well established because Li<sup>+</sup> ions helps to improve the chemical resistance of the glass substrates [38]. Unfortunately, the main drawback nowadays is the

increase in the costs of these minerals due to the high demand in the manufacture of lithium-ion batteries. In this study, however, the authors also considered its use; if these results and the following production are to go on an industrial scale, costs will be considered as optimization.

### 6.2.2. Characterisation of the raw materials

Thermogravimetric (TGA) and first derivative of the thermo-gravimetric curve (DTG) measurements were carried out with a thermal analyser (Seiko SSC 5200, Japan) coupled with a quadrupole mass spectrometer (ESS, GeneSys Quadstar 422, UK) which allows the qualitative determination of the volatile compounds ( $H_2O$ ,  $CO_2$  and  $SO_2$ ) evolved during heating (MS-EGA). Thermal behaviour was investigated in the thermal range 25-1300°C at a heating rate 20°C/min using ultrapure helium at a flow rate of 100  $\mu$ L/min as purging gas.

The determination of the expansion-contraction curve was obtained with a vertical optical dilatometer MISURA. Recrystallised alumina was the standard used for the calibration. The samples tested are prismatic specimens of RG and KRY·AS with approximative dimensions of 29x8x8 mm<sup>3</sup>.

Chemical analysis was carried out on powder pressed pellets via a wavelength dispersive Philips PW 1480 X-ray fluorescence (XRF) spectrometer [39,40].

### 6.2.3. Foam glass mixtures preparation

The preparation and optimisation of the foam glass is summarized in **Table 2** and details will be reported in the following paragraphs.

Phase 1 (paragraph 3.2): interaction between RG and KRY·AS at different ratios. Each mixture has been treated for 6 min at 950, 1000, 1050, 1100 °C. Chosen composition: 60 RG: 40 KRY·AS (wt. %).

Phase 2 (paragraph 3.3): partial substitution of RG with flux agent:  $Na_2CO_3$  (5 and 10% wt. %) or  $Li_2CO_3$  (5 wt. %). Treatment time and temperatures as in phase 1. Optimized raw composition, with better behaviour between 1000 and 1100°C: 55 RG: 40 KRY·AS: 5  $Li_2CO_3$  (wt. %).

Phase 3 (paragraph 3.4): addition of SiC (0.5, 1, 5 wt. %) at different sizes (SiC-320, SiC-600, SiC-1500) to the optimized composition. Each new mixture has been treated at 1000, 1050, 1070, 1100°C for 6 min. Most performing agent at every temperature value: SiC-1500.

Phase 4 (paragraph 3.5): addition of SiC 1500 (1, 2.5, 5 wt. %) to the optimized composition 55 RG : 40 KRY·AS : 5  $Li_2CO_3$  (wt. %); treatment for each mixture at 1000, 1050, 1100°C for 1, 6 and 30 min. Optimized mixture used for further characterizations: 55 RG : 40 KRY·AS : 5  $Li_2CO_3$  (wt. %) with the addition of 2.5 wt. % SiC 1500 treated between 700 and 1100 °C for 6 min (paragraph 3.6).

To prepare the mixtures, 400 g of RG was wet milled for 10 min in a porcelain jar with ~ 180 g of alumina balls (12-14 mm of diameter) as grinding media. The obtained slurry was dried overnight, dry-crushed and sieved at 500  $\mu\text{m}$ . Also, KRY·AS was dried for at least 2 h under an IR light to low the humidity content. The mixtures were dried mixed and homogenised using a planetary mill. Successively, they were humidified with water up until approx. 8 wt. %, sieved at 750  $\mu\text{m}$  and kept in a sealed plastic bag for 24 h. Specimens of 40 mm diameters x 6 mm thick were obtained from each mixture by uniaxial pressing at a pressure of 24.5 MPa using a laboratory press machine. These specimens were dried overnight at 110°C, treated at the selected temperatures and time using a computer-controlled electric laboratory kiln, with heating rate of 25°C/min. All the fired specimens were cooled down to room temperature. At least three specimens for each combination of composition, time and temperature have been prepared and tested; average values of the properties tested and their standard deviation have been calculated.

**Table 2.** Compositions (wt. %) of the studied mixtures

	Phase 1			Phase 2			Phase 3					Phase 4		
	A	B	C	B1	B2	B3	FG1	FG2	FG3	FG4	FG5	FG4	FG5	FG6
<b>RG</b>	70	60	50	55	50	55	55	55	55	55	55	55	55	55
<b>KRY·AS</b>	30	40	50	40	40	40	40	40	40	40	40	40	40	40
<b>Na<sub>2</sub>CO<sub>3</sub></b>	-	-	-	5	10	-	-	-	-	-	-	-	-	-
<b>Li<sub>2</sub>CO<sub>3</sub></b>	-	-	-	-	-	5	5	5	5	5	5	5	5	5
<b>SiC – 320<sup>[a]</sup></b>	-	-	-	-	-	-	0.5	-	-	-	-	-	-	-
<b>SiC – 600<sup>[a]</sup></b>	-	-	-	-	-	-	-	0.5	1	-	-	-	-	-
<b>SiC – 1500<sup>[a]</sup></b>	-	-	-	-	-	-	-	-	-	1	5	1	2.5	5

<sup>[a]</sup> SiC was additive to the compositions

#### 6.2.4. Characterisation of the mixtures

Loss on ignition (LOI), water absorption (WA) and apparent density (AD) were measured in all cases. The optimization of the composition of the mixtures has led to the following more performing composition: 55 RG: 40 KRY·AS: 5 Li<sub>2</sub>CO<sub>3</sub> (wt. %) with the addition of 2.5 wt. % SiC 1500 (details reported in the next paragraphs). To evaluate the foaming process, a set of specimens with this composition was produced for further in-depth characterization including microstructure and

mineralogy. The samples have been prepared using different thermal treatment, changing the firing temperature (700, 800, 900, 950, 1000, 1050, 1100 °C), with a soaking time of 6 min.

The foam glass specimens were cut and the images of transversal section have been measured and analysed by ImageJ [41] processing software to obtain the dimensions of the pores.

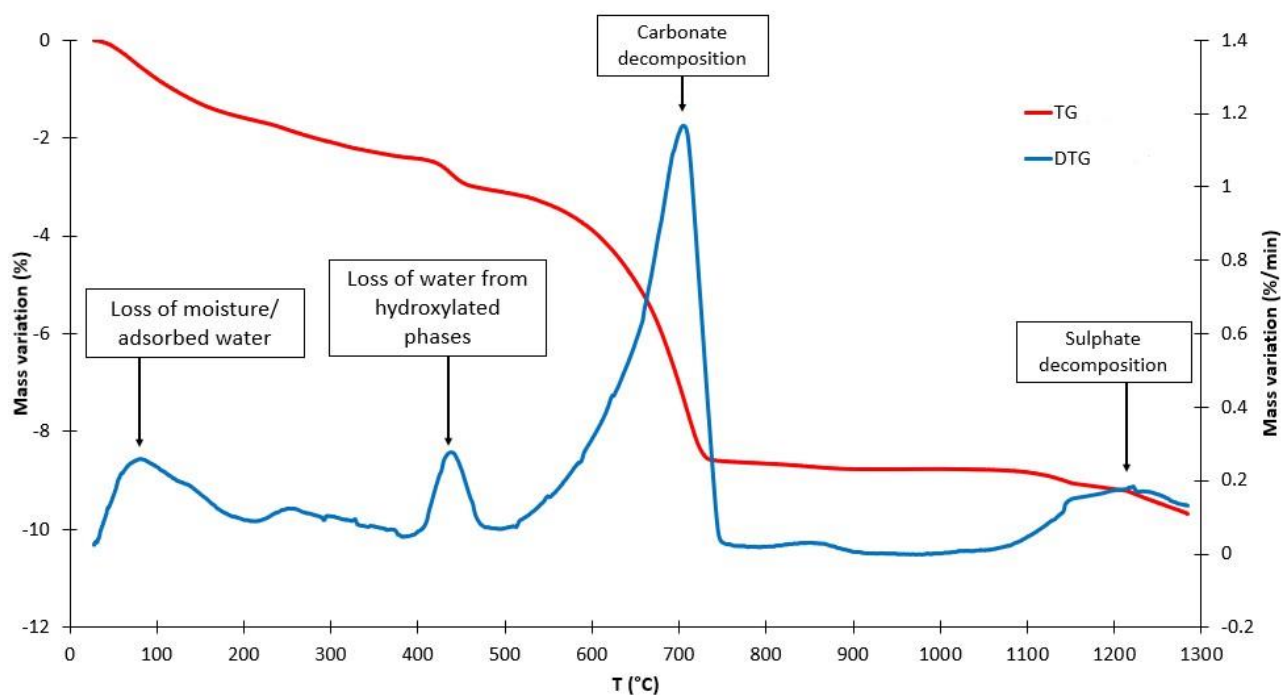
The identification of the crystalline structure and quantitative analysis of the samples were performed by powder X-Ray diffraction (Bruker D8 Advance, Germany) with a  $\text{CuK}\alpha$  radiation generated with 30 kV and 40 mA. A step scan of  $0.023^\circ 2\theta$  was performed in 334s in the  $5\text{-}90^\circ 2\theta$  range. Each sample was thoroughly mixed with a standard (corundum SRM1976) to perform quantitative analysis. The determination of both crystalline and amorphous fractions was possible using the Rietveld-RIR method. [42]

The foam glass microstructure was assessed through the stereoscopic microscope integrated with a three-dimensional computer program, in which the microscope images were displayed and stored. The microstructure and composition of the foam-glass samples were investigated by a scanning electron microscope equipped with an energy dispersive X-ray probe (FEG-ESEM, Quattro S de Thermo Fisher Scientific). The foam glass specimens were cut, the transversal section was englobed in an epoxy resin, then the surface was polished with sandpaper.

### 6.3. Results and discussion

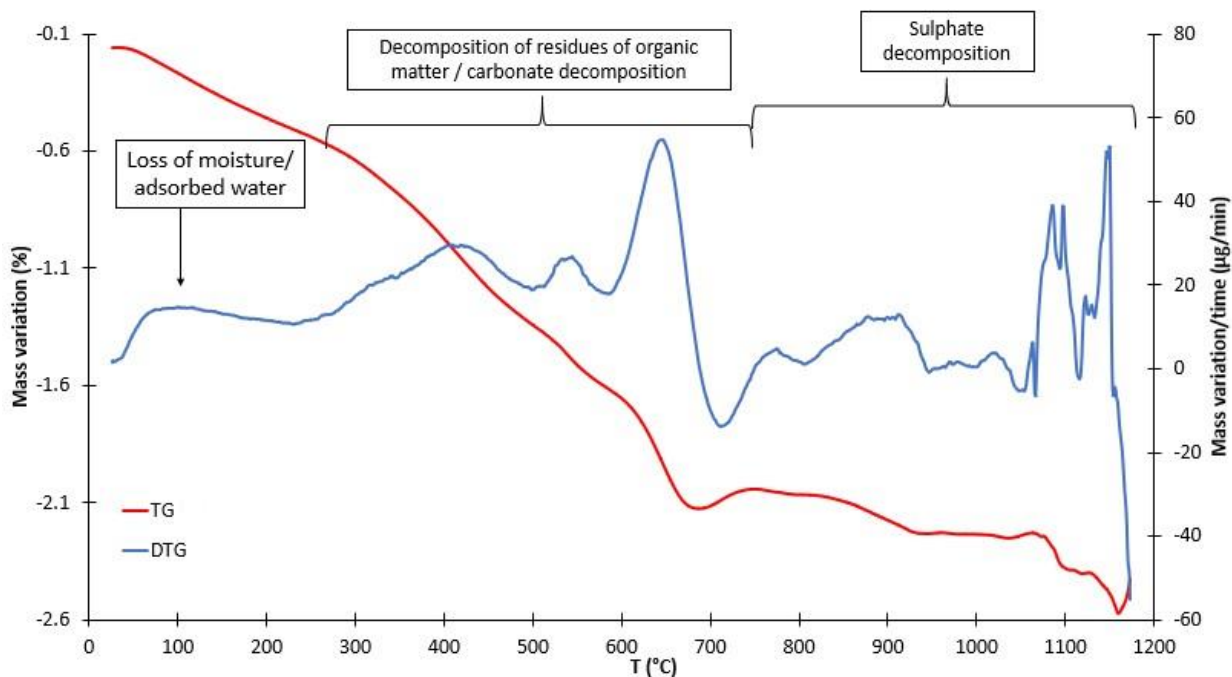
#### 6.3.1. Firing behaviour of raw materials

**Figure 1** shows the TGA and DTG of KRY·AS. The first derivative of the thermo-gravimetric curve points out at least four main thermal events: i) a bands between 25 and 214°C with maximum rate at 82°C and a mass variation of 1.69 wt. % which is due to the release of adsorbed and bonded  $\text{H}_2\text{O}$  molecules ( $m/z=18$ ); ii) a well-defined thermal reaction between 343 and 490°C with a mass variation of 0.71 wt. % that is indicative of hydroxylated phases, as proved by the release of water; iii) a second well-defined reactions between 495 and 780°C related to the thermal decomposition of carbonates and therefore producing the release of  $\text{CO}_2$  ( $m/z=44$ ), with a mass variation of 5.56 wt. %; iv) an high-temperature (1050-1300°C) event (weight loss 0.91 wt. %) related to the thermal decomposition of (calcium) sulphate as highlighted by the release of  $\text{SO}_2$  ( $m/z=64$ ).



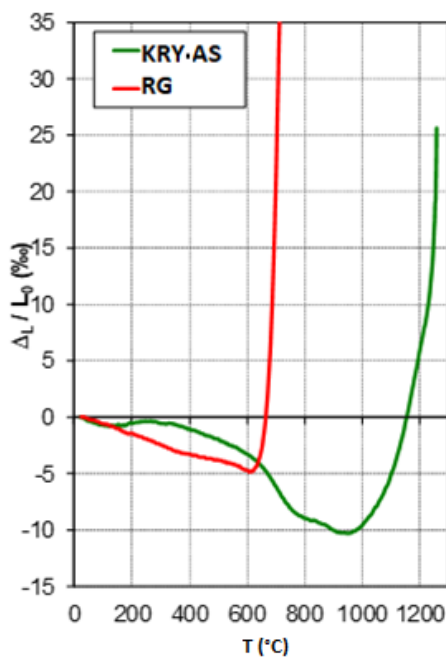
**Figure 1.** TGA (red) and DTG (blue) curves for KRY·AS.

The TGA-DTG curve of RG (**Figure 2**) points out: i) a composite bands between 25 and 235°C with maximum at about 82°C and a mass variation of 0.52 wt. %, due to the release of H<sub>2</sub>O ( $m/z=18$ , Figure SI-2, Supplementary Material) physio-adsorbed on the particles surface; ii) a series of thermal reactions (overall weight loss of 1.55 wt. %) between 235 and 720°C, with a shoulder at 314°C and maxima at 410, 547 and 651°C, which could be indicative of the thermal decomposition of residues of organic matter (e.g., paper, plastic, etc) and carbonates as proved by the simultaneous release of H<sub>2</sub>O ( $m/z=18$ ), NO ( $m/z=30$ ), CO<sub>2</sub> ( $m/z=44$ ) and NO<sub>2</sub> ( $m/z=46$ ); iii) several other poorly defined thermal events between 720 and 1200°C, that are not easy to interpret and producing a mass variation of about 0.35 wt. %; the release in the same thermal range of SO<sub>2</sub> ( $m/z=64$ ) could suggest that they derive from thermal decomposition of sulphates.



**Figure 2.** TGA (red) and DTG (blue) curves for RG.

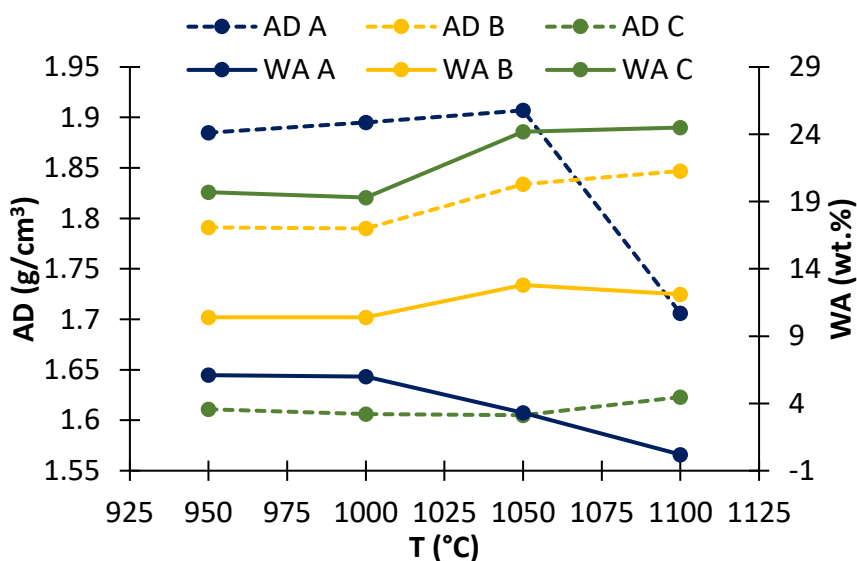
The expansion-contraction curve (**Figure 3**) shows that both raw materials contract steadily until 610 and 950°C for RG and KRY·AS, respectively. These can be considered the softening points ( $T_{S0}$ ). From these temperatures both materials largely expand in a relative short period. The high softening point and fusion temperature ( $T_F > 1200^\circ\text{C}$ ) of KRY·AS may be attributed to the high CaO and  $\text{Al}_2\text{O}_3$  and low  $\text{Na}_2\text{O}$  and  $\text{K}_2\text{O}$  contents (**Table 1**). This behaviour is confirmed by the mineralogical composition of KRY·AS (**Table 1**), which indicates that it is composed by phases characterized by high thermal stability [43].



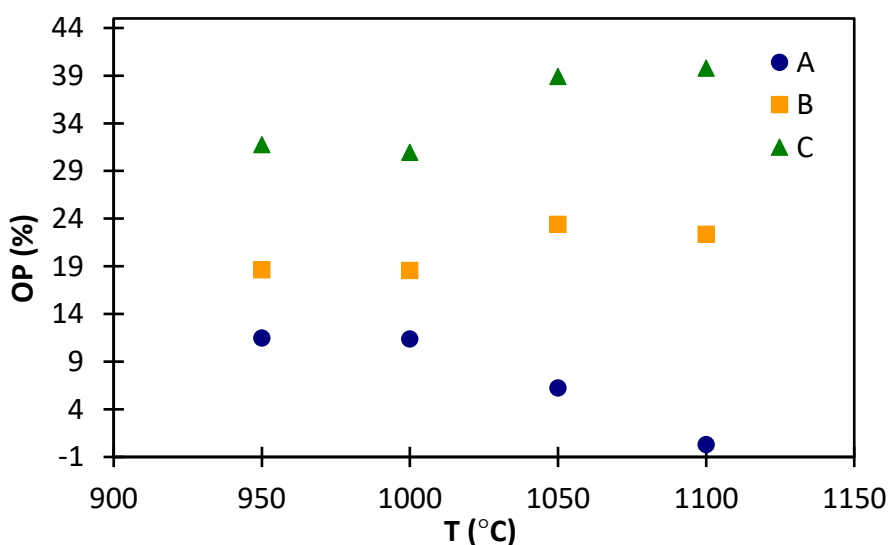
**Figure 3.** Expansion-contraction curve of KRY·AS (green) and RG (red)

### 6.3.2. Phase 1: KRY·AS: RG wt. % ratio

The interaction between KRY·AS and RG is the key step in the foam glass preparation. Three different mixtures with RG:KRY·AS ratios of 70:30 (A), 60:40 (B), 50:50 (C) wt. % were treated for 6 min at 950, 1000, 1050 and 1100°C. For all samples AD and WA were measured, and open porosity (OP % = AD · WA %) was calculated (Figures 4, 5). Foaming would occur only if enough amounts of CO<sub>2</sub> are emitted and trapped inside the melted mixture. The proprieties of the mixture must be such as to prevent the release of the gas once added the foaming agent, therefore the values of WA, and consequently of OP, must be as lower as possible ( $\leq 1\%$ ). [20]



**Figure 4.** AD, WA of mixtures RG:KRY·AS 70:30 (A), 60:40 (B), 50:50 (C) wt.% treated at 950, 1000, 1050, 1100°C for 6 min.



**Figure 5.** OP of mixtures RG:KRY·AS 70:30 (A), 60:40 (B), 50:50 (C) wt. % treated at 950, 1000, 1050, 1100°C for 6 min

**Figures 4, 5** indicate that as the amount of KRY·AS increased, AD decreased and WA increased, and consequently OP increase. At the increase of the temperature AD, WA and OP slightly increase for the samples with 40 and 50 wt. % of KRY·AS, while for the sample with the highest amount of RG the trend is the opposite. The error related to the value of AD, WA and OP is extremely low, therefore the three compositions can be considered significantly different.

The substitution of RG with KRY·AS (**Table 2**) decreases the amount of Na<sub>2</sub>O and SiO<sub>2</sub> that are responsible of the amorphous phase formation. Moreover, the significant increase of CaO could favour the formation of crystalline phases.

These results show that the composition with RG: KRY·AS 70:30 has the lowest values of OP (11-0.3%) and WA (6-0.2%) at all temperatures. However, the RG: KRY·AS 60:40 mixture will be successively optimized, despite the higher OP (23 -18%) and WA (10-12%), as the main objective of the research is to obtain foam glass recovering as much as KRY·AS possible.

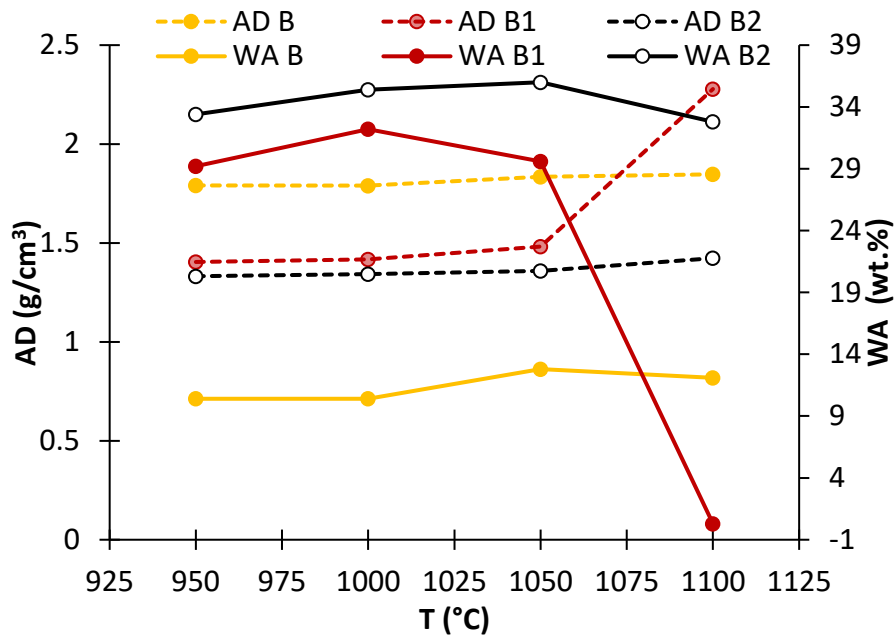
**Table 2.** Chemical composition (wt. %) from XRF data of mixtures RG:KRY·AS 70:30 (A), 60:40 (B), 50:50 (C)

	Na <sub>2</sub> O	MgO	Al <sub>2</sub> O <sub>3</sub>	SiO <sub>2</sub>	P <sub>2</sub> O <sub>5</sub>	K <sub>2</sub> O	CaO	TiO <sub>2</sub>	MnO	Fe <sub>2</sub> O <sub>3</sub>
<b>A</b>	8.65	4.08	2.97	54.98	0.01	0.63	22.15	0.161	0.06	1.13
<b>B</b>	7.44	4.60	3.01	50.20	0.01	0.58	26.46	0.168	0.06	1.35
<b>C</b>	6.24	5.13	3.05	45.42	0.01	0.54	30.76	0.175	0.06	1.57

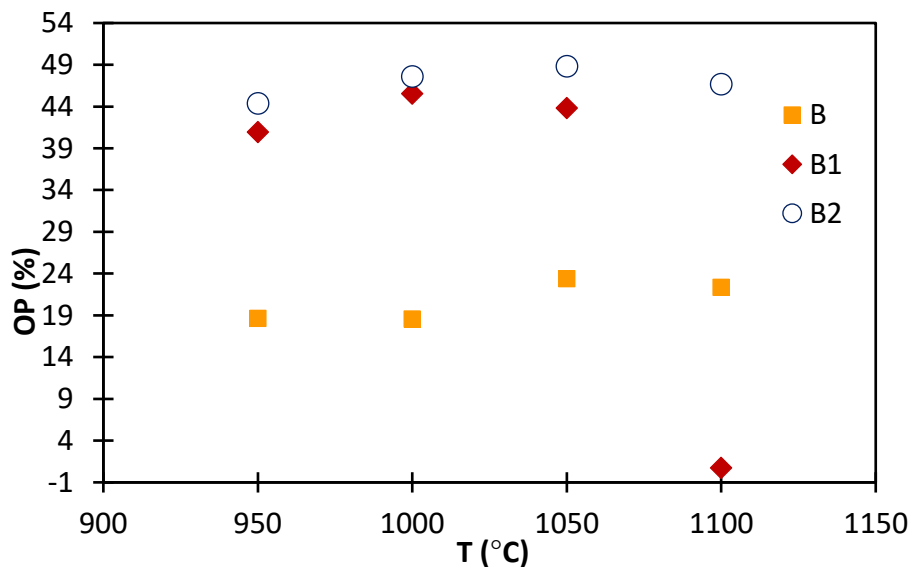
### 6.3.3. Phase 2: flux agents

Na<sub>2</sub>CO<sub>3</sub> is added as partial substituent of RG to RG: KRY AS 60:40 composition in the amount of 5 wt. % (mixture B1) and 10 wt. % (mixture B2). WA (**Figure 6**) and OP clearly increased (**Figure 7**) with the Na<sub>2</sub>CO<sub>3</sub> content. **Figures 6, 7** show that at T ≤ 1050 °C, AD decreases with the amount of Na<sub>2</sub>CO<sub>3</sub>, while WA and OP increase, with significant differences between the sample B, B1 and B2. However, at the highest temperature WA and OP of the sample B1 abruptly drop near zero, while its AD grows up to 2.3 g/cm<sup>3</sup>. The other samples do not show variations at higher temperatures.





**Figure 6.** AD, WA of mixtures RG:KRY·AS 60:40 wt. % (B), RG:KRY·AS 55:40 wt. % with  $\text{Na}_2\text{CO}_3$  5 wt. % (B1), RG:KRY·AS 50:40 wt. % with  $\text{Na}_2\text{CO}_3$  10 wt. % (B2) treated at 950, 1000, 1050, 1100°C for 6 min

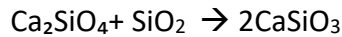


**Figure 7.** OP of mixtures RG:KRY·AS 60:40 (B) wt. %, RG:KRY·AS 55:40 wt. % with  $\text{Na}_2\text{CO}_3$  5 wt. % (B1), RG:KRY·AS 50:40 wt. % with  $\text{Na}_2\text{CO}_3$  10 wt. % (B2) treated at 950, 1000, 1050, 1100°C for 6 min.

Quantitative phase analysis (QPA) (**Table 3**) indicates that with the increase of  $\text{Na}_2\text{CO}_3$ , wollastonite ( $\text{CaSiO}_3$ ) diminishes whereas åkermanite ( $\text{Ca}_2\text{MgSi}_2\text{O}_7$ ) and combeite ( $\text{Na}_2\text{Ca}_2\text{Si}_3\text{O}_9$ ) increase. Samples B and B1 showed the highest amount of amorphous phase, exceeding 50 wt. %.

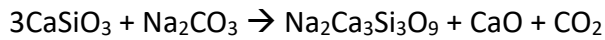
According to a literature review, wollastonite derives from larnite ( $\text{Ca}_2\text{SiO}_4$ ) presents in the KRY·AS, thanks to the addition of  $\text{SiO}_2$  from RG (**Table 4**) [43].

The increase of temperature favours the formation of åkermanite from wollastonite basing on the following reaction [44]:



Moreover, considering the free energies of formation for wollastonite ( $\Delta G_f, 1100^\circ\text{C} = -1726 \text{ KJ/mol}$ ) and åkermanite ( $\Delta G_f, 1100^\circ\text{C} = -4114 \text{ KJ/mol}$ ), the formation of the latter phase is thermodynamically favoured, but with a slow kinetic as described in Joachim et al. (2011) [44].

On the other hand, the mechanism proposed by Dawson et al. (1989) [45] can be used to explain the increase in combeite amount, as it shows the modification that may occur to wollastonite in presence of rich alkali phases. The reaction can be simplified as follow:



**Table 3.** Quantitative phase analysis (wt. %) of RG:KRY·AS 60:40 wt. % (B) 55:40 wt. % with  $\text{Na}_2\text{CO}_3$  5 wt. % (B1), 10 wt. % (B2) treated at  $1100^\circ\text{C}$  for 6min.

	Phases (wt. %)			
	Wollastonite	Åkermanite	Combeite	Amorphous
<b>B</b>	43 ± 4	6 ± 1	0	51 ± 3
<b>B1</b>	25 ± 2	12 ± 1	11 ± 1	52 ± 3
<b>B2</b>	/	22 ± 2	40 ± 4	38 ± 4

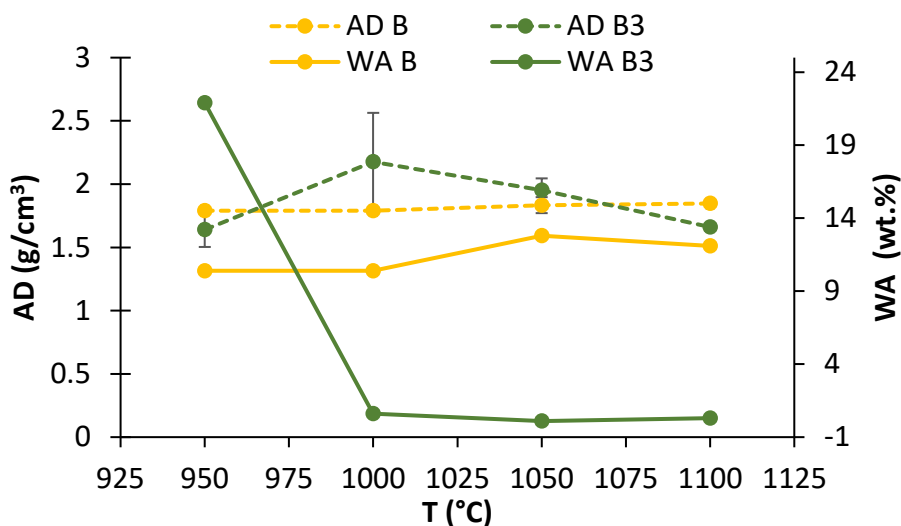
**Table 4.** Chemical composition (wt. %) of  $\text{Na}_2\text{CO}_3$ , RG:KRY·AS 60:40 wt. % (B) RG:KRY·AS 55:40 wt. % with  $\text{Na}_2\text{CO}_3$  5 wt. % (B1), RG:KRY·AS 50:40 wt. % with  $\text{Na}_2\text{CO}_3$  10 wt. % (B2), calculated from the XRF data

	$\text{Na}_2\text{O}$	$\text{MgO}$	$\text{Al}_2\text{O}_3$	$\text{SiO}_2$	$\text{P}_2\text{O}_5$	$\text{K}_2\text{O}$	$\text{CaO}$	$\text{TiO}_2$	$\text{MnO}$	$\text{Fe}_2\text{O}_3$
<b><math>\text{Na}_2\text{CO}_3</math></b>	58.3	<dl <sup>a</sup>	<dl	<dl	<dl	<dl	<dl	<dl	<dl	<dl
<b>B</b>	7.44	4.60	3.01	50.20	0.01	0.58	26.46	0.17	0.06	1.35
<b>B1</b>	9.76	4.48	2.87	46.73	0.01	0.54	25.99	0.16	0.06	1.32
<b>B2</b>	12.07	4.35	2.72	43.27	0.01	0.51	25.53	0.15	0.05	1.30

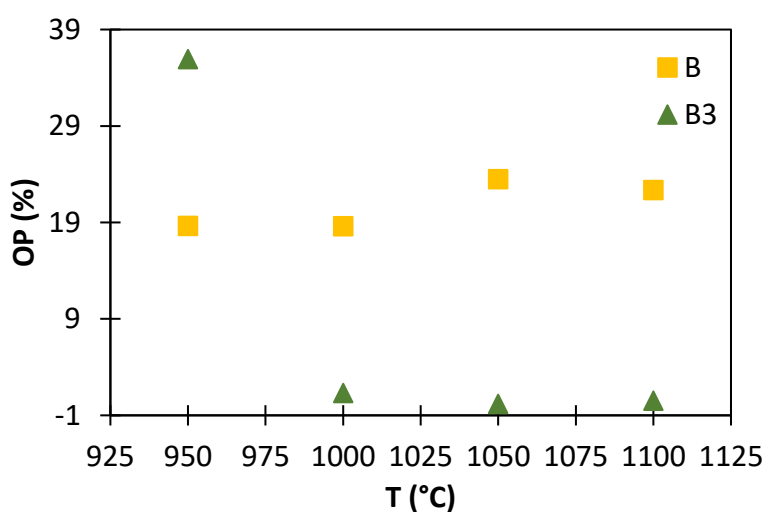
<sup>a</sup> <dl = under detection limit

The addition of  $\text{Na}_2\text{CO}_3$ , in general, favours the crystallization processes, increases the OP (%) and reduces the quality of a foam glass. Therefore, the crystallization process should be avoided, or at least be controlled.

The addition of  $\text{Li}_2\text{CO}_3$  drives to an evident decrease of WA and OP, while AD undergoes to little variations (**Figures 8,9**). As shown in **Figure 8** the values of AD for the composition with  $\text{Li}_2\text{CO}_3$  (B3) at  $T \leq 1050^\circ\text{C}$  are not significantly different from the composition B. The results of WA and OP, below 1% even at  $1000^\circ\text{C}$ , it is the necessary starting point to create foam glass at lower temperatures and in a larger temperature range. The main drawback in the use of  $\text{Li}_2\text{CO}_3$  is the current cost, as stated above, but to produce foam glass, low quality lithium raw materials, poorly appreciated for other applications, may be used [46, 47].



**Figure 8.** AD, WA of mixtures RG:KRY·AS 60:40 wt. % (B) and RG:KRY·AS 55:40 wt. % with  $\text{Li}_2\text{CO}_3$  5 wt. % (B3) treated at 950, 1000, 1050, 1100°C for 6 min.

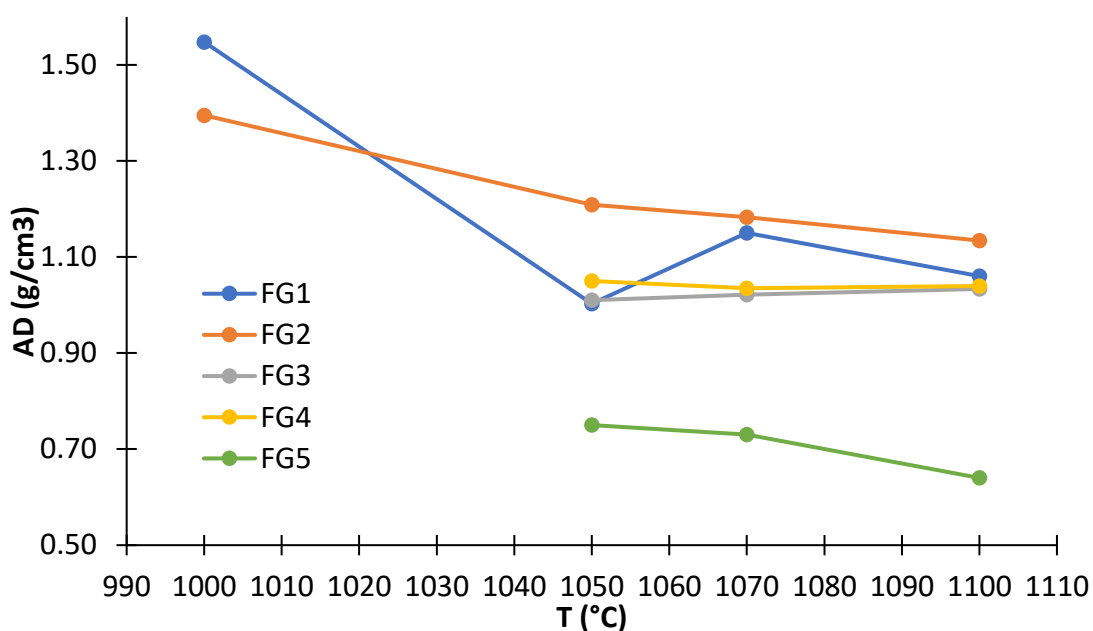


**Figure 9.** AD, WA of mixtures RG:KRY·AS 60:40 wt. % (B) and RG:KRY·AS 55:40 wt. % with  $\text{Li}_2\text{CO}_3$  5 wt. % (B3) treated at 950, 1000, 1050, 1100°C for 6 min.

At the end of this phase, because of its low WA and OP at  $T \geq 1000^\circ\text{C}$ , RG:KRY·AS 55:40 wt. % with  $\text{Li}_2\text{CO}_3$  5 wt. % has been chosen as the appropriate composition to test the foaming agents and to prepare the final product.

### 6.3.4. Phase 3: effect of foaming agent

The foaming agent, namely SiC, was added in different size and amount at the mixture RG:KRY·AS 55:40 wt. % with  $\text{Li}_2\text{CO}_3$  5 wt. %. Specifically, we used SiC-320 at 0.5 wt. % (FG1), SiC-600 at 0.5 (FG2) and 1 wt. % (FG3), SiC-1500 at 1 (FG4) and 5 wt. % (FG5). The samples have been treated for 6 min at 1000, 1050, 1070, 1100 °C and the aim was to obtain AD values comparable to those of commercial products ( $\text{AD} \leq 0.5 \text{ g/cm}^3$ ) [20]. AD decreases (**Figure 10**), with the increase of the amount and decrease of the dimensions of SiC, in agreement with the literature [48]. AD reaches values between 0.75 and 0.64  $\text{g/cm}^3$  with 5 wt. % of SiC-1500. As a result, SiC-1500 has been chosen as foaming agent for the optimised composition.



**Figure 10.** AD, WA of mixtures RG:KRY·AS 55:40 wt. % with  $\text{Li}_2\text{CO}_3$  5wt. % and: SiC-320 0.5 wt. % (FG1), SiC-600 0.5 wt. % (FG2), SiC-600 1 wt. % (FG3), SiC-1500 1 wt. % (FG4), SiC-1500 5 wt. % (FG5) at 950, treated at 1000, 1050, 1100°C for 6 min.

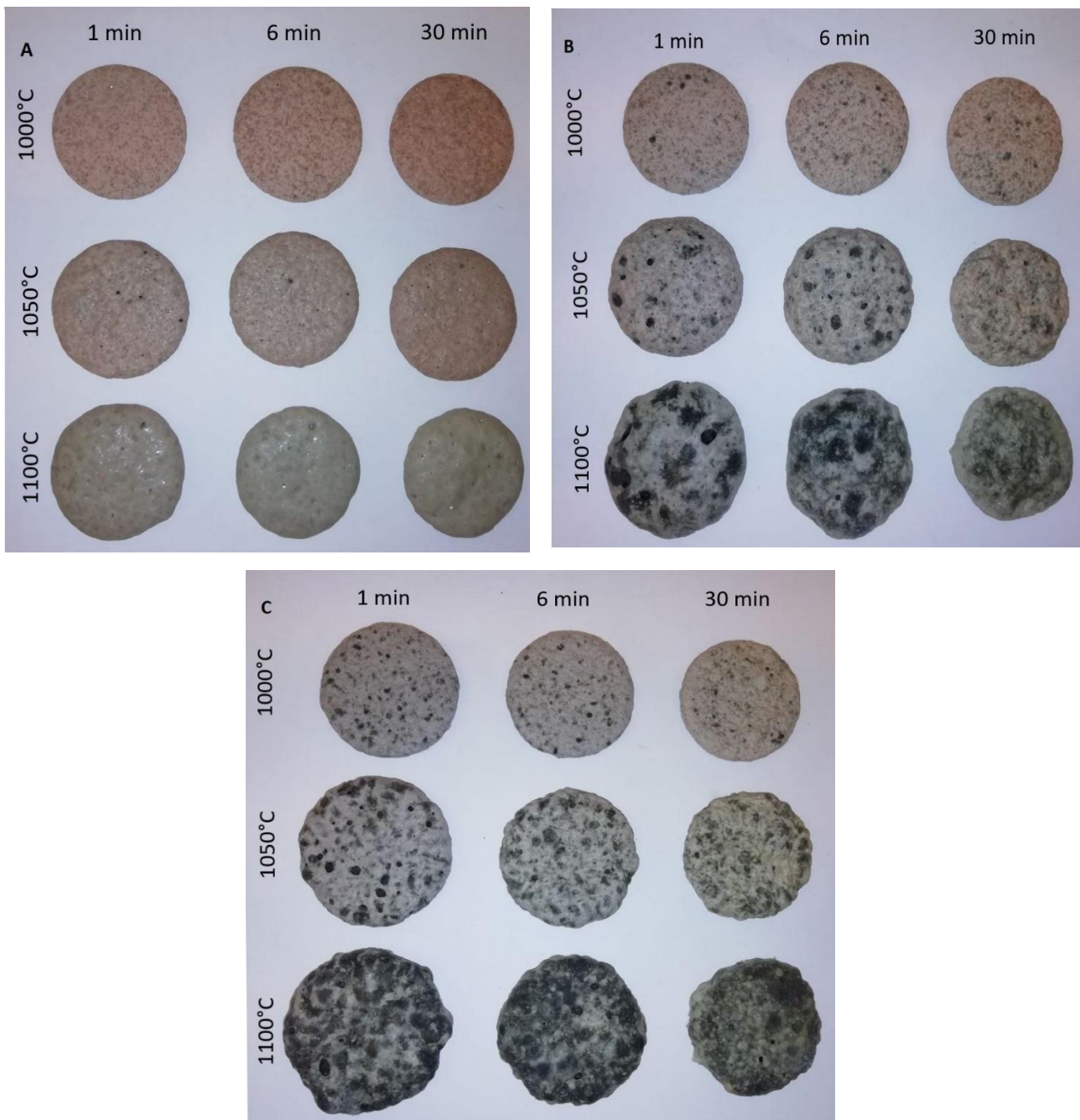
### 6.3.5. Phase 4: synthetic variables

Twenty-seven samples were prepared and studied with the optimized composition RG:KRY-AS 55:40 wt. % with  $\text{Li}_2\text{CO}_3$  5wt. % and different amount of SiC (1, 2.5, 5 wt. %), firing temperature (1000, 1050, 1100°C) and soaking time (1, 6, 30 min). Images of the samples (**Figures 11** and **12**) and data of AD (**Table 5** and **Figures 13, 14** and **15**) were used to evaluate the influence of the different variables.

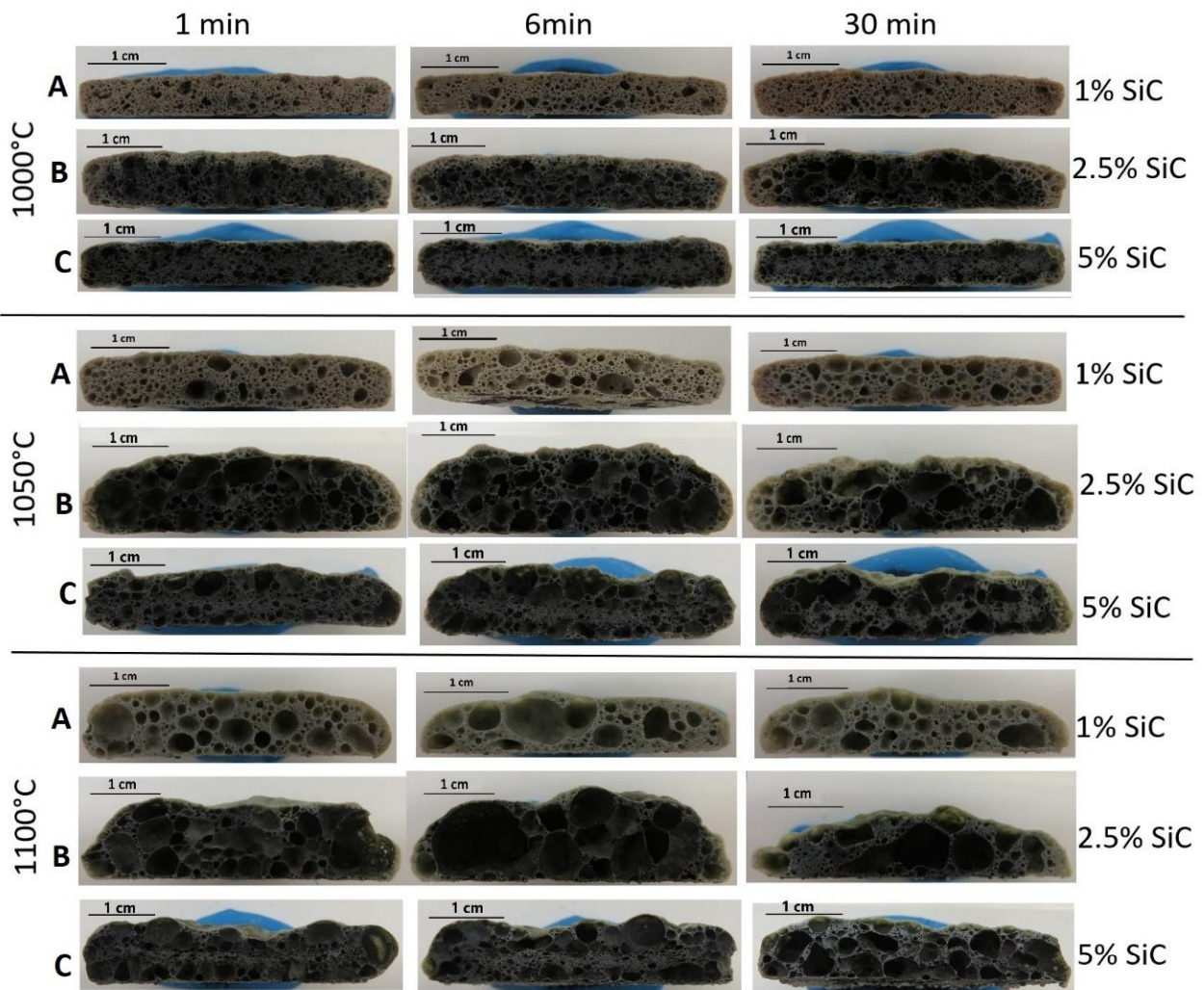
#### 6.3.5.1. External and internal structure

**Figures 11** and **12** show an increase of amount and diameters of pores, with the increase of temperature and percentage of SiC. At each temperature and time, 1 wt. % SiC gives rise to foam glasses with a light colour (**Figure 11 A**); with 2.5 and 5 wt. % the samples are darker with a greenish shade, due the presence of iron. Inside of some samples the colour is grey-black, this is due to products formed after SiC reduction.

Observing the section of the samples (**Figure 12**) 2.5 wt. % of SiC seemed to be the adequate amount to give effective foaming, thus suggesting to avoid a further increase in the amount of the foaming agent, as it will not provide significant improvements [49]. The pores of all the samples in **Figure 12** have been measured with an appropriate software, and they can be classified as macroporous ( $\varnothing > 50 \mu\text{m}$ ) (IUPAC classification), which is common in foam glass [50,51]. Varying the temperature, the pores pass from  $\varnothing < 1 \text{ mm}$  at 1000°C, to 3-7 mm at 1050°C, until they reach up to 1 cm at 1100°C; this is also evident at the increasing of soaking time. This trend can be explained with the model of the particle coarsening during the sintering process: smaller particles tend to contract and disappear while the average size of the remaining particles increases. This result is brought by interparticle mass transport caused by surface diffusion and evaporation-condensation [20,52]. In our case the observation is that the most voluminous pores grow at the expense of the smaller ones. The effect of the increasing temperature and soaking time of the process produced a rise in the pressure of the gas inside the pores with as a consequence the collapse of the microstructures, in particular the break of the walls of the pores and formation of connections between pores.



**Figure 11.** Photographs of external surface of samples with RG:KRY-AS 55:40 with  $\text{Li}_2\text{CO}_3$  5wt. % and SiC 1 wt. % (A), 2.5 wt. % (B), 5 wt. % (C), treated at 1000, 1050, 1100°C for 1, 6, 30 min.



**Figure 12.** Photographs of the section of samples with RG:KRY·AS 55:40 with  $\text{Li}_2\text{CO}_3$  5wt. % and SiC 1 wt. % (A), 2.5 wt. % (B), 5 wt.% (C), treated at 1000, 1050, 1100°C for 1, 6, 30 min.

### 6.3.5.2. Apparent density

Figures 13, 14, 15 and Table 5 report the AD values; as can be observed in Table 5 the lowest value of AD ( $0.55 \pm 0.02 \text{ g/cm}^3$ ) was obtained with SiC 2.5 wt. % at 1100°C for 1 min and, in general, the samples with this amount of SiC have the lowest AD at each temperature and time. These data are comparable with those of the commercial products ( $0.5 \text{ g/cm}^3$ ) and previous works [20,22,53].

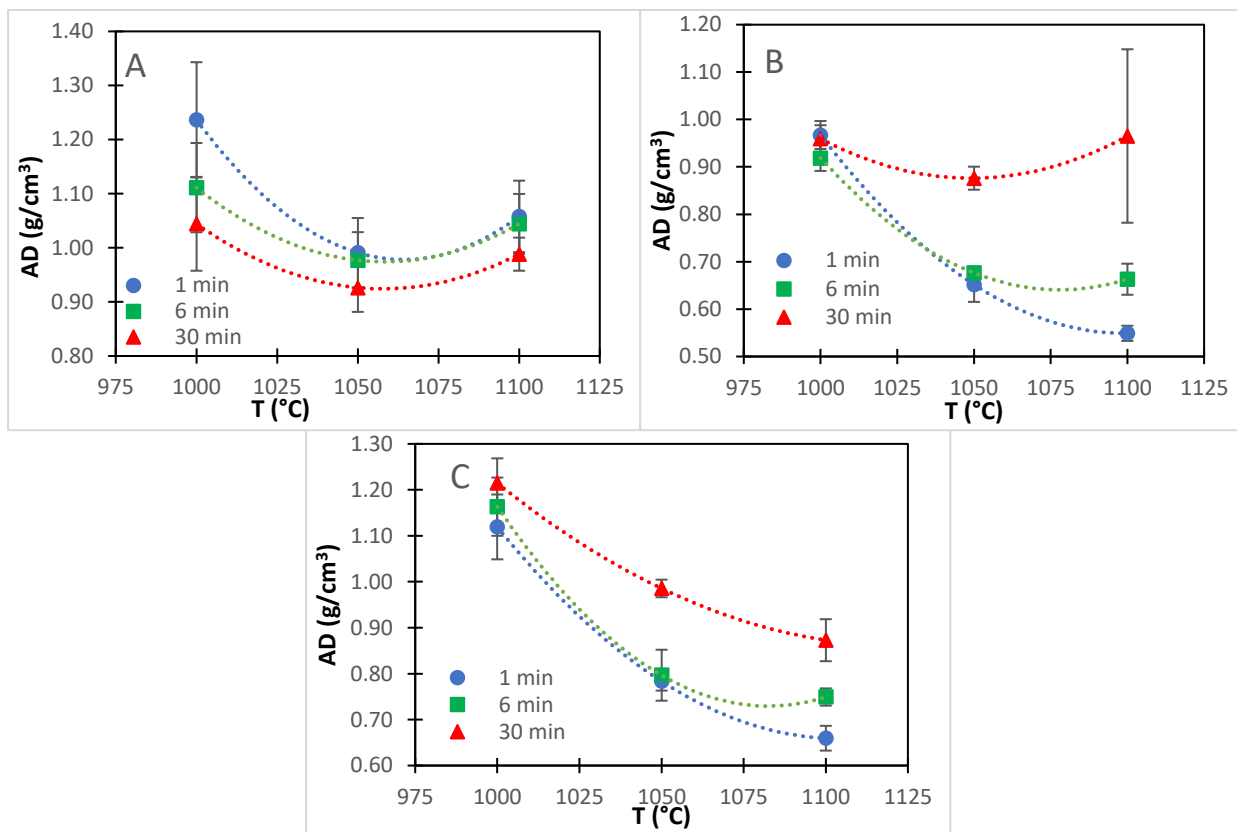
**Table 5.** Mean values of AD as a function of amount of SiC, temperatures and time for samples with RG:KRY·AS 55:40 with  $\text{Li}_2\text{CO}_3$  5 wt. % and SiC 1 wt. % (A), 2.5 wt. % (B), 5 wt.% (C), treated at 1000, 1050, 1100°C for 1, 6, 30 min.

SiC (wt. %)	t (min)	AD ( $\text{g/cm}^3$ ) 1000°C	AD ( $\text{g/cm}^3$ ) 1050°C	AD ( $\text{g/cm}^3$ ) 1100°C
1	1	$1.24 \pm 0.11$	$0.99 \pm 0.08$	$1.06 \pm 0.09$
	6	$1.11 \pm 0.08$	$0.98 \pm 0.05$	$1.04 \pm 0.04$
	30	$1.04 \pm 0.09$	$0.93 \pm 0.06$	$0.99 \pm 0.03$
2.5	1	$0.97 \pm 0.03$	$0.65 \pm 0.04$	$0.55 \pm 0.02$
	6	$0.92 \pm 0.03$	$0.68 \pm 0.00$	$0.66 \pm 0.03$
	30	$0.96 \pm 0.03$	$0.88 \pm 0.02$	$0.97 \pm 0.18$
5	1	$1.12 \pm 0.07$	$0.78 \pm 0.02$	$0.66 \pm 0.03$
	6	$1.16 \pm 0.06$	$0.80 \pm 0.06$	$0.75 \pm 0.02$
	30	$1.21 \pm 0.05$	$0.99 \pm 0.02$	$0.87 \pm 0.05$

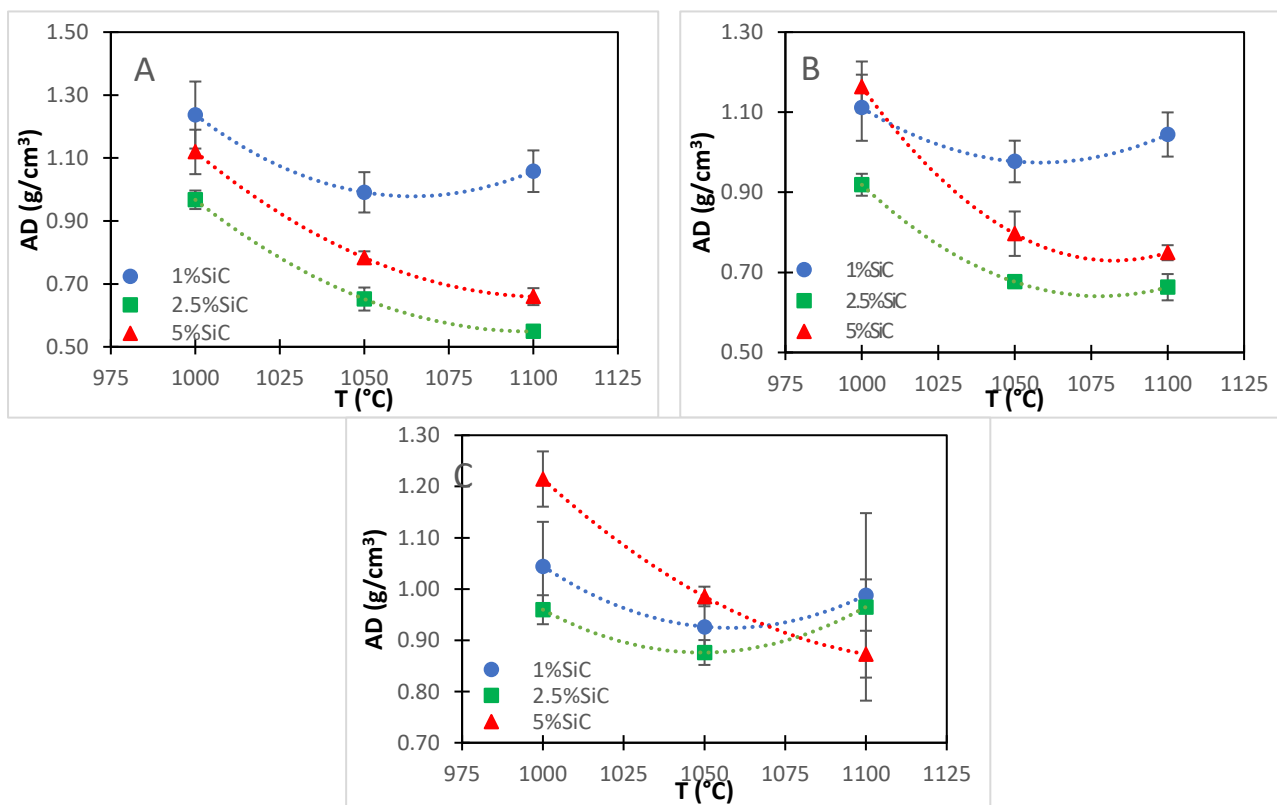
Figure 13 reports the influence of temperature and soaking time on each batch; with the 1 wt. % of SiC (A), the AD values do not differ significantly from each other and the lower values are at 1050°C. In contrast an increase of SiC at 2.5 and 5% (B and C, respectively), drives to AD decreases with the increase of the temperature and, therefore, an increase with the time.

The influence of the amount of foaming agent can be observed in Figure 14. In A (1 min) and B (6 min) the samples with 2.5 wt. % of SiC have the lowest values of AD, while with 1 wt. % of SiC they have the highest. At a soaking time of 30 min the data are not significantly different.





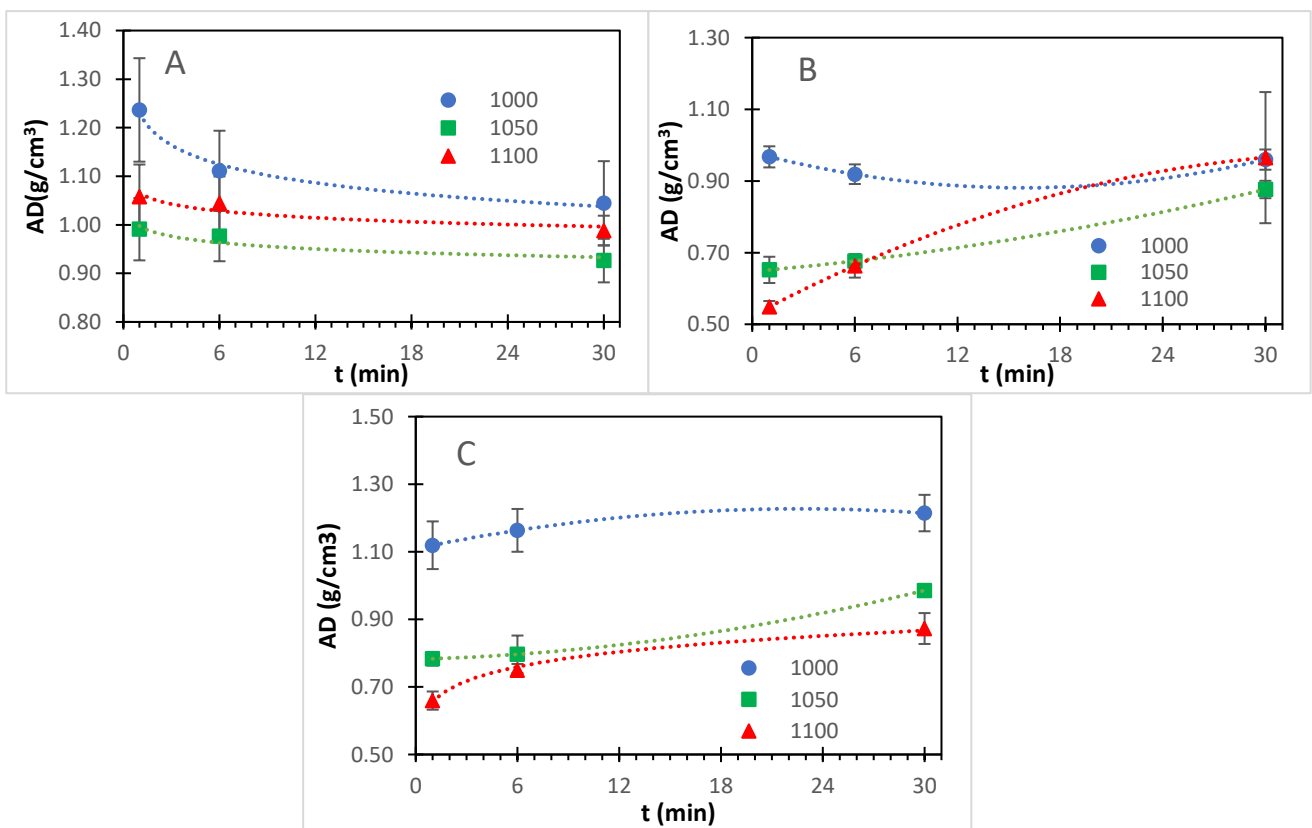
**Figure 13.** AD for the composition RG:KRY-AS 55:40 with Li<sub>2</sub>CO<sub>3</sub> 5 wt. % and 1wt. % (A), 2.5 wt. % (B), 5 wt. % (C) of SiC treated at 1000, 1050 and 1100°C.



**Figure 14.** AD for the composition RG:KRY-AS 55:40 wt. % with Li<sub>2</sub>CO<sub>3</sub> 5 wt. % and 1wt. %, 2.5 wt. %, 5 wt. % of SiC treated at 1000,1050 and 1100°C after 1 min (A), 6 min (B), 30 min (C)

As previously described [56], the dependence of AD on the duration of the thermal treatment is represented by a convex parabolic trend. During the realising of gas, the density decreases up to a minimum, then the coalescence phenomenon begins, and the pores start to collapse. This process leads to a reduction of the volume, hence to a new increase in the density. Consequently, observing the trend of AD in **Figure 15** we can evaluate which reaction time is the best to obtain the minimum in the AD. In **A** there is a general downward trend, thus with 1 wt. % of SiC is probably necessary a higher amount of time at each temperature. With 2.5 wt. % of SiC (**B**): at 1000°C the perfect time is probably higher than 6 min but lower than 30 min, while at higher temperatures, the minimum is at 1 min. The same observation can be done with 5 wt. % of SiC (**C**), in which the best soaking time is 1 min.

It is possible to conclude that the best foaming glass, with the lowest AD, have been obtained with 2.5 wt. % of SiC, treated at 1100°C.



**Figure 15.** AD of the composition RG:KRY-AS 55:40 with  $\text{Li}_2\text{CO}_3$  5 wt. % and 1wt. % (A), 2.5 wt. % (B), 5 wt. % (C) of SiC after 1, 6 and 30 min, treated at 1000, 1050 and 1100°C.

### 6.3.6. Study of the foaming mechanism

To study the foaming mechanisms, specimens of the selected composition RG:KRY·AS 55:40 with  $\text{Li}_2\text{CO}_3$  5 wt. %, SiC 2.5 wt. % were treated at different temperatures between 700 and 1100°C for 6 min. The samples obtained were analysed through a stereoscopic and a scanning electron microscope. The raw samples, observed with the stereoscopic microscope (**Table 6 A1**), present a homogeneous appearance and some small white areas, heterogeneous in shape. When studied with SEM, the surface appears to be composed by a mixture of different agglomerates (**Table 6 D1 and E1**). Through X-ray powder diffraction (XRPD, **Figure 16**) and Energy Dispersive X-ray Analysis (EDX, **Figures 17 and 18**), they can be identified as KRY·AS (small white particles), RG and SiC (sharp dark particles), and  $\text{Li}_2\text{CO}_3$  (darker areas in **Figure 17**).

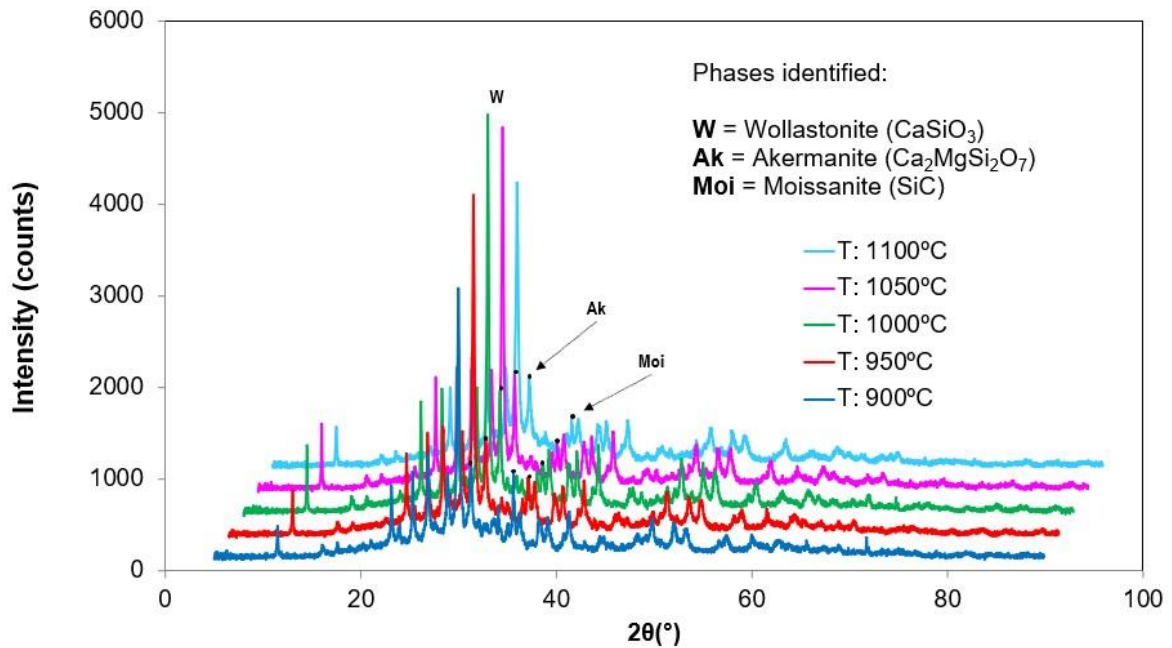
At 700°C (**Table 6 row 2, Figure 19**) it is possible to distinguish smooth vitrified areas with very small pores (<40  $\mu\text{m}$ ), which are formed by melting of  $\text{Li}_2\text{CO}_3$  and RG. The interaction between SiC and the amorphous phase creates larger pores (50-200  $\mu\text{m}$ ). In addition, particles of SiC are also evident as small shiny dots homogeneously distributed in the sample, and we can detect calcium rich phases (besides the åkermanite) derived from KRY·AS.

At the increasing of the temperature (800-900°C) the amount of the liquid phase increases (**Figures 20 and 21**) and SiC starts to react originating bigger and irregular pores (< 400  $\mu\text{m}$ ). Clear-toned crystals, probably wollastonite, begin to form at the edge of the vitreous matrix (**Table 6 D3 and E3**) and inside it (**Table 6 D4 and E4**). KRY·AS is still present in the matrix at 800°C, otherwise at 900°C it seems to be completely integrated in the glass phase, together with SiC particles.

Starting from 950°C the samples acquire a green tone because of iron in the glass phase (**Table 1, Table 6 A5 and C5**). Small round pores, with dimensions < 100  $\mu\text{m}$  (**Table 6 D5**), are well evident and, at high temperature in consequence of SiC oxidation, the pores dimension increases up to about 1mm (not observable as they are larger than the optical field of the microscope). In the vitrified areas particles of SiC and crystals of wollastonite are still present and homogeneously distributed (**Table 6 E5**).

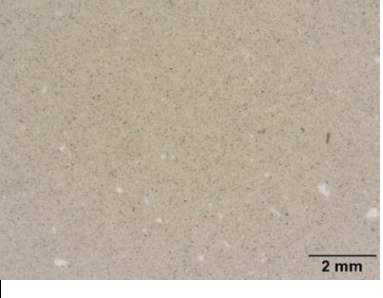
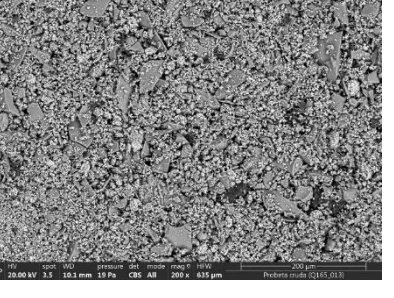
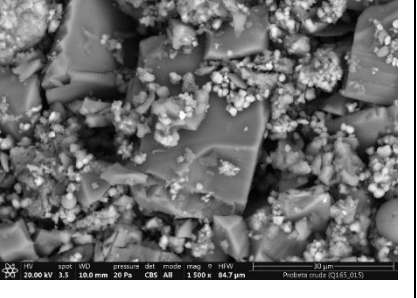

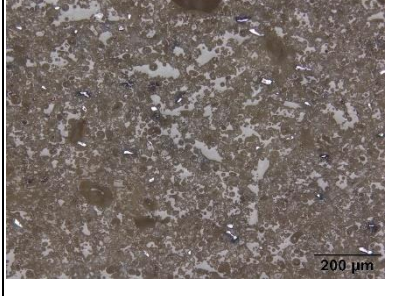
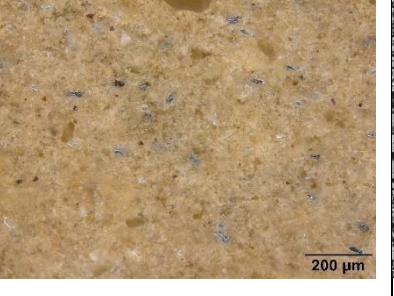
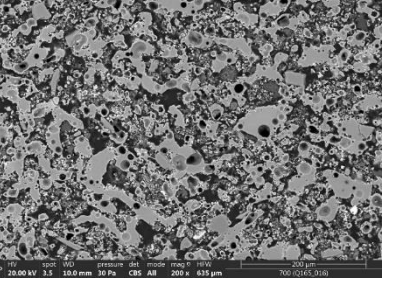
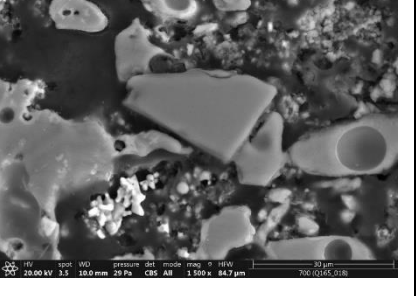
Starting from 1000°C we can observe closed round pores (<100  $\mu\text{m}$ ) (**Table 6 A6 and D6**) and larger pores (> 400  $\mu\text{m}$ ), with SiC particles located at their border (**Table 6 D6 and E6**). At 1100°C the presence of small, white, spherical and iron rich particles can be appreciated, which are probably formed by the partial or total reduction of iron oxide by SiC (**Table 6 E8, Figure 22**).

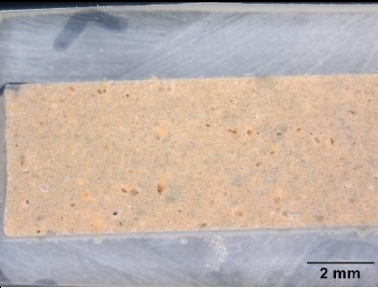
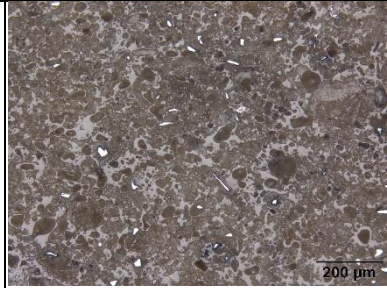
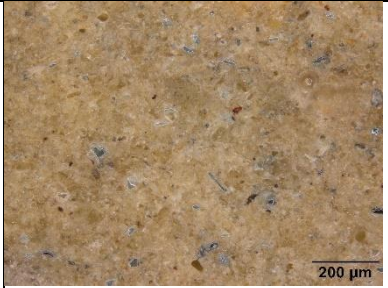
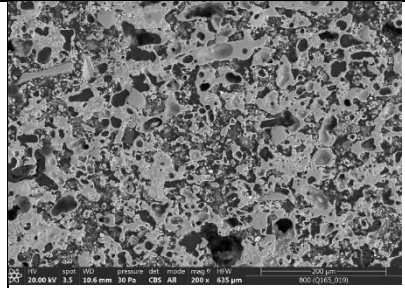
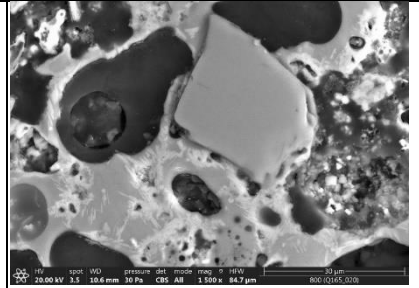
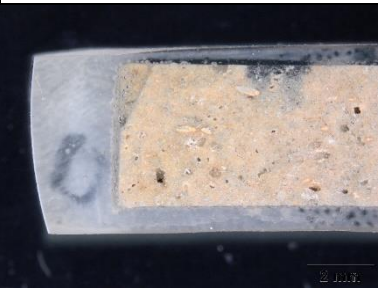
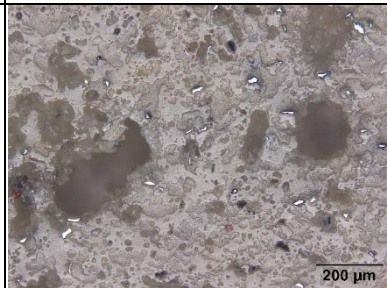
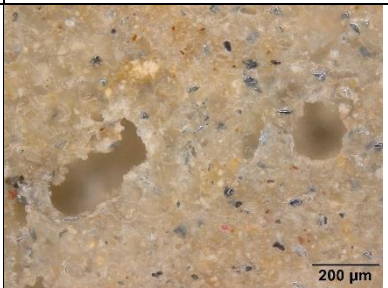
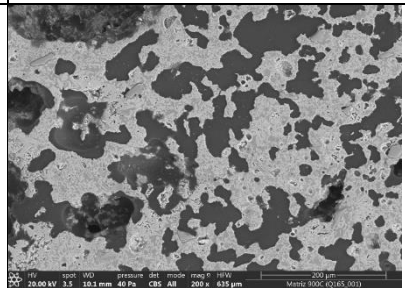
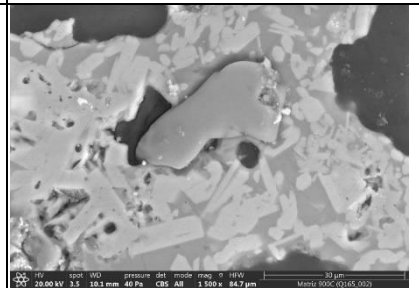

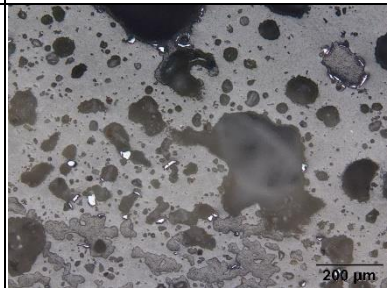

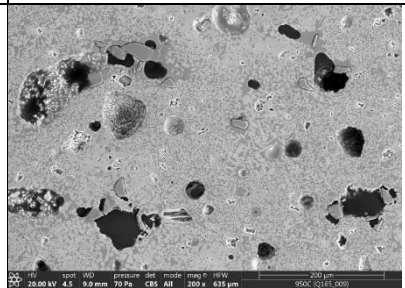
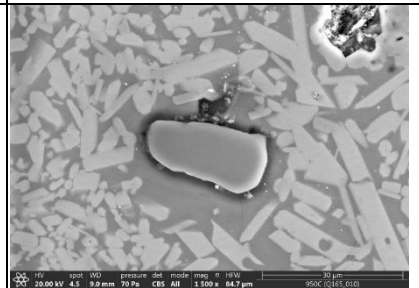
The incorporation of KRY-AS in the liquid phase at a relative high temperature makes the foaming process more difficult. A high amount of gas is formed at lower temperature from the oxidation of SiC and it is released because of the porous structure, which persists up to 900°C. The actual foaming process starts only at 950°C, provided that there is a liquid phase capable of entrap the generated gases.

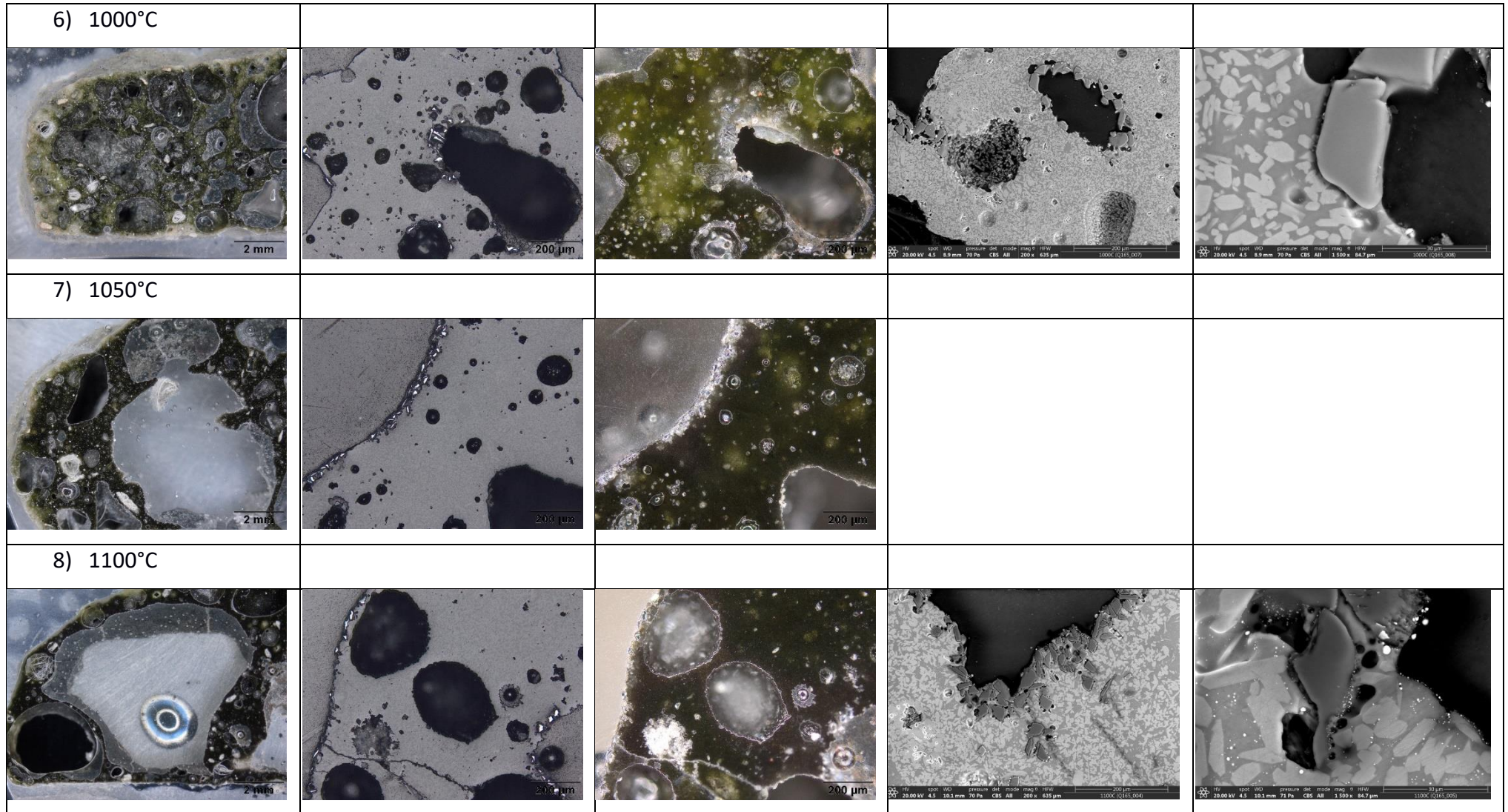


**Figure 16.** Diffraction pattern of the samples at RG:KRY-AS 55:40 with  $\text{Li}_2\text{CO}_3$  5 wt. % with SiC 2.5 wt. % treated for 6 min at different temperature values.

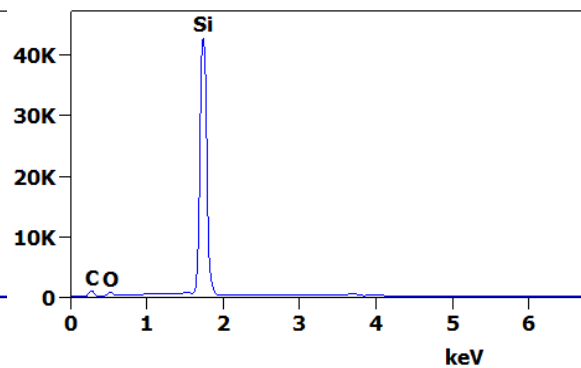
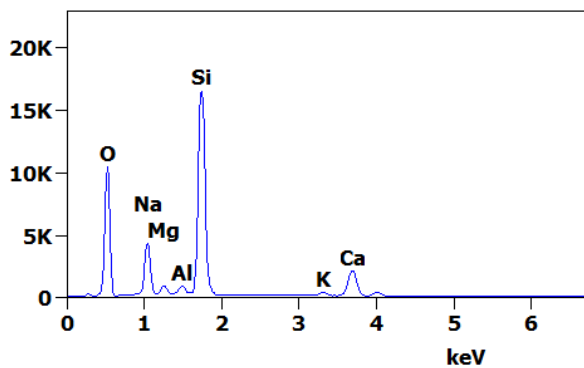
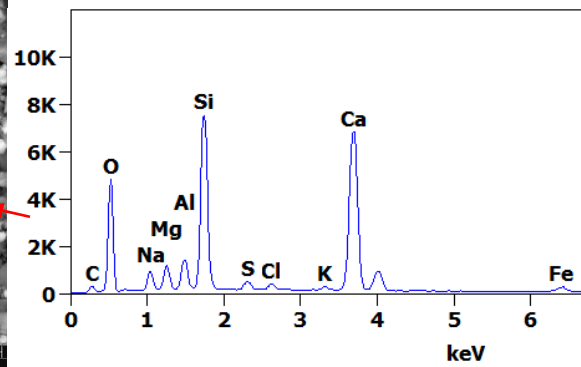
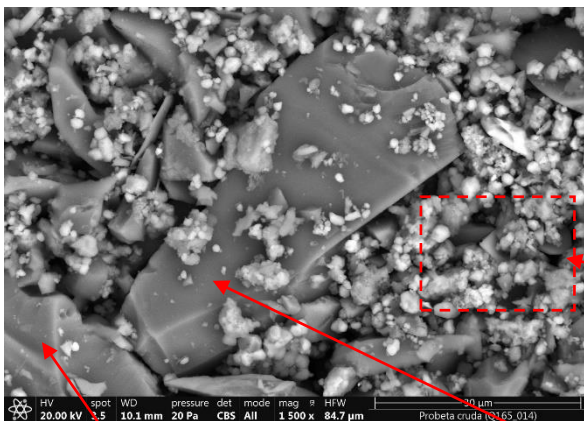
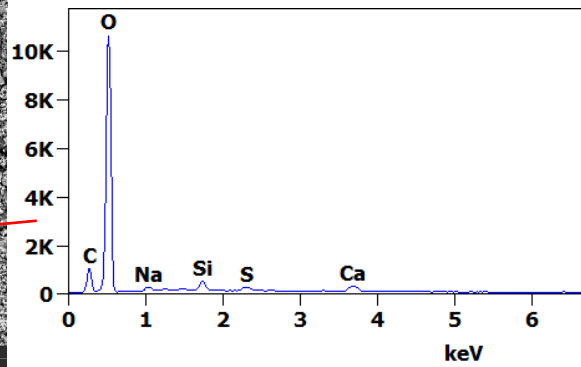
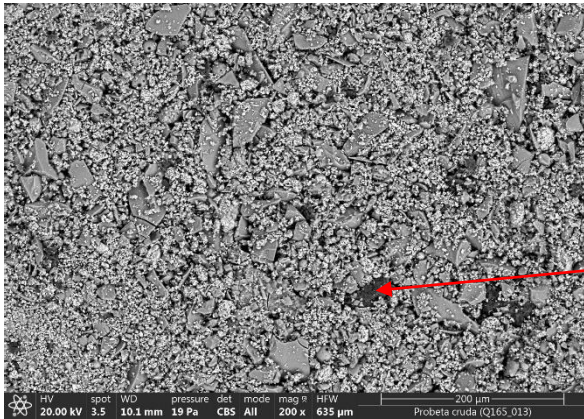
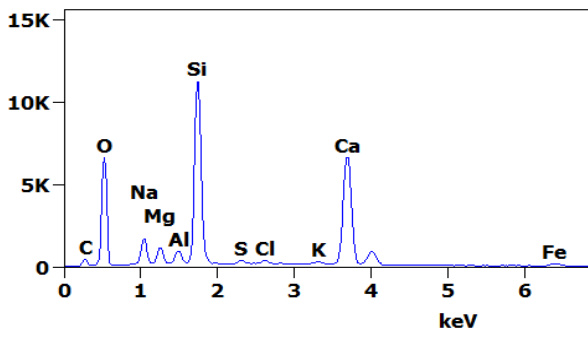
**Table 6** Images<sup>[a]</sup> of the sample RG:KRY·AS 55:40 wt. % with Li<sub>2</sub>CO<sub>3</sub> 5 wt. %, SiC 2.5 wt. % raw (row 1) and treated for 6 min at 700°C (row 2), 800°C (row 3), 900°C (row 4), 950°C (row 5), 1000°C (row 6), 1050°C (row 7), 1100°C (row 8)

A) Stereoscopic microscope	B) Optical microscope bright field	C) Optical microscope dark field	D) SEM (magnified x200)	E) SEM (magnified x1500)
1) Raw				
				
2) 700°C				
				

<p>3) 800°C</p> 				
<p>4) 900°C</p> 				
<p>5) 950°C</p> 				

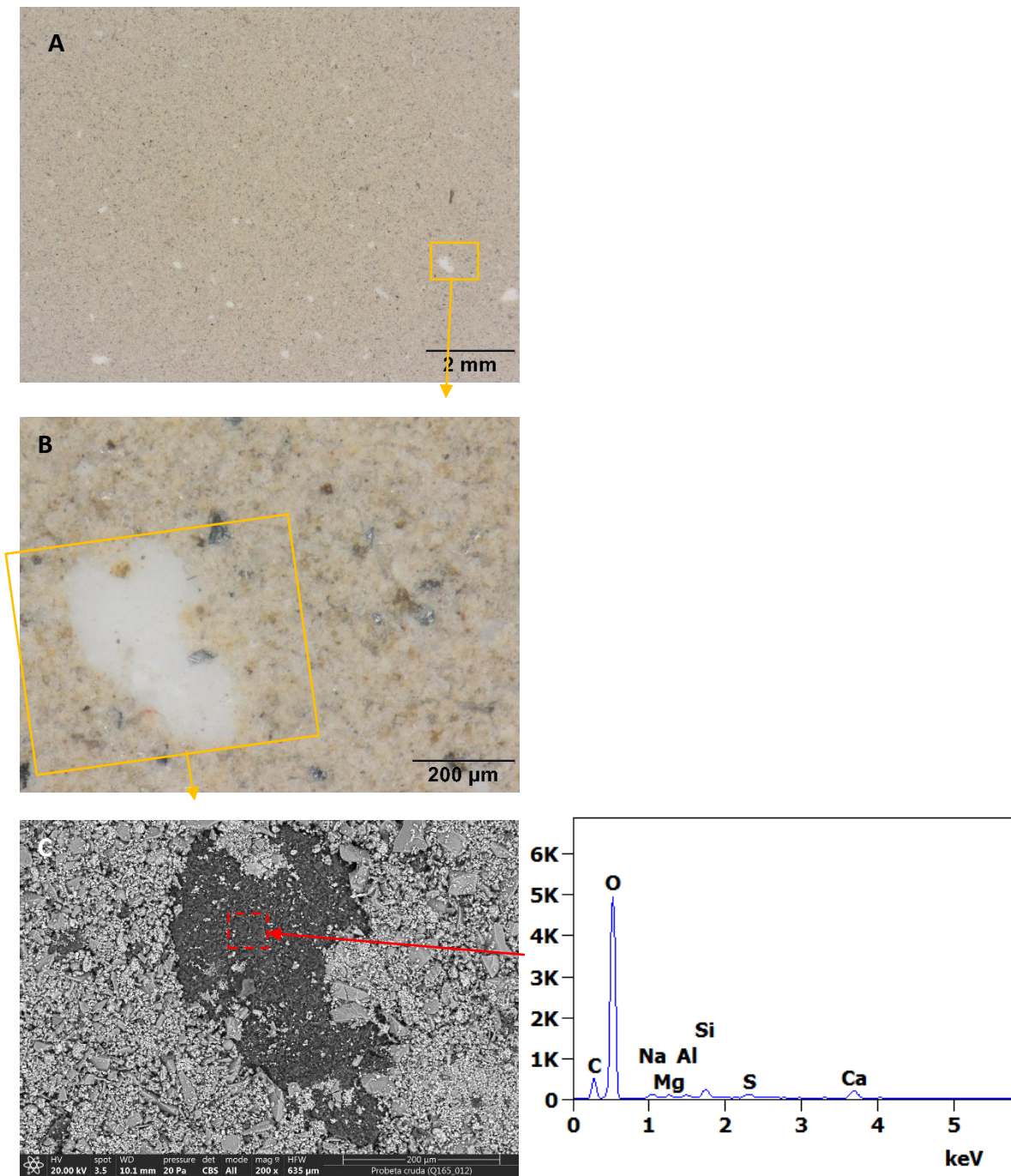


<sup>[a]</sup> stereoscopic microscope (column A), optical microscope in bright field (column B) and dark field (column C), SEM at different magnification x200 (column D) and x1500 (column E)

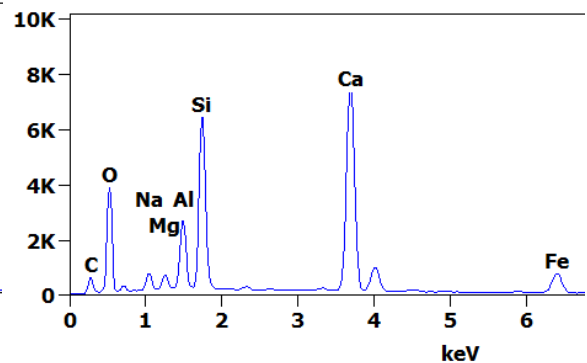
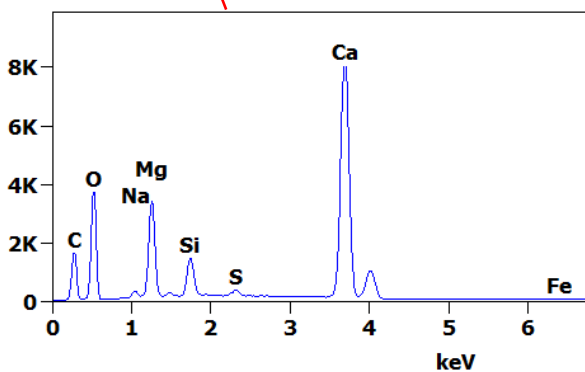
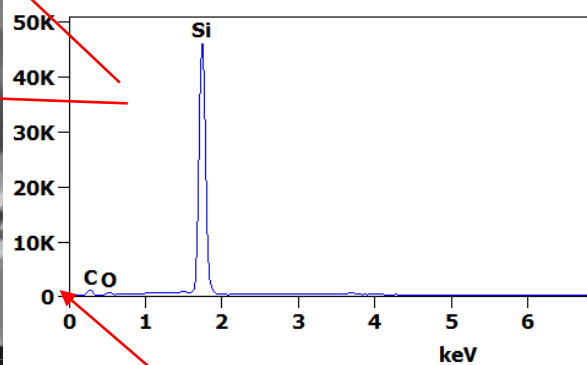
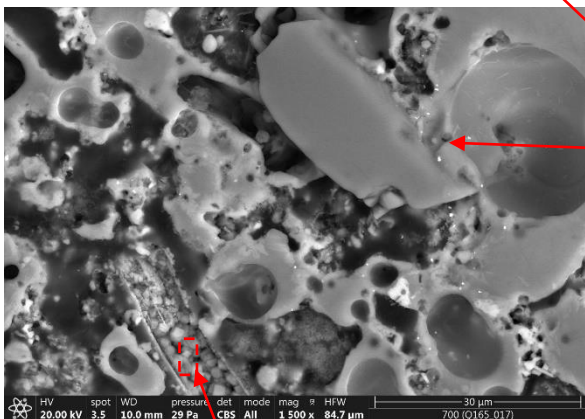
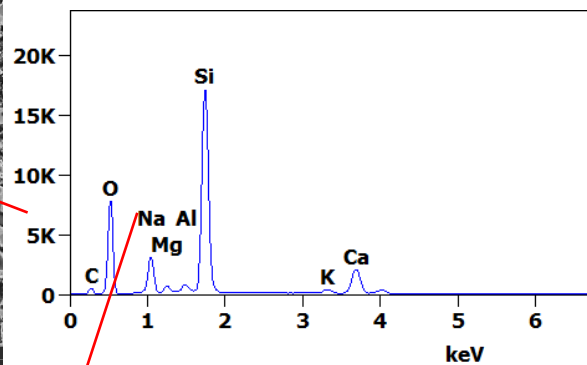
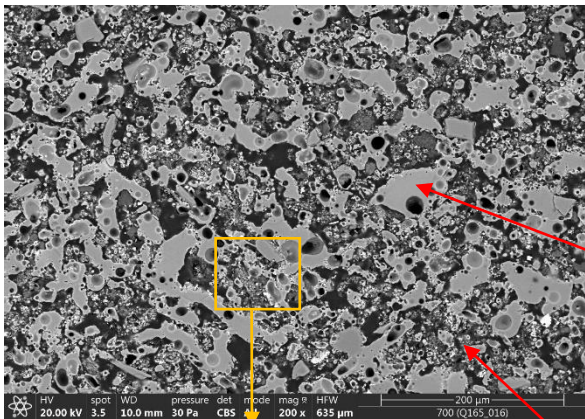
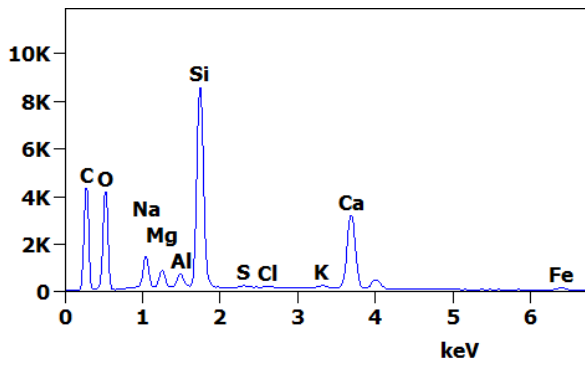


**Figure 17.** SEM micrograph of the surface of the raw sample RG:KRY·AS 55:40 with  $\text{Li}_2\text{CO}_3$  5 wt. % and SiC 2.5 wt. %, EDX analysis and identification of the principal constituents.

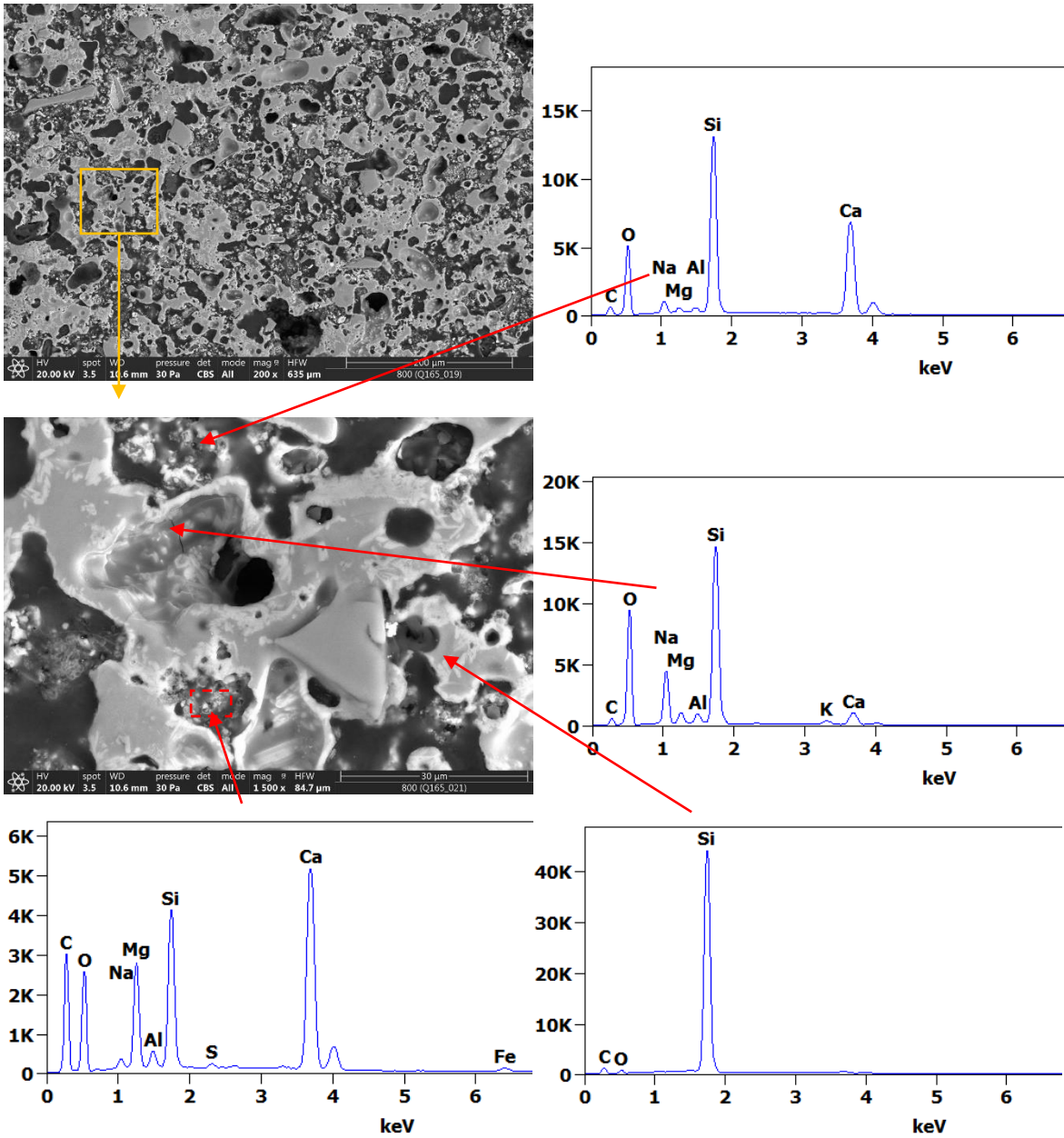




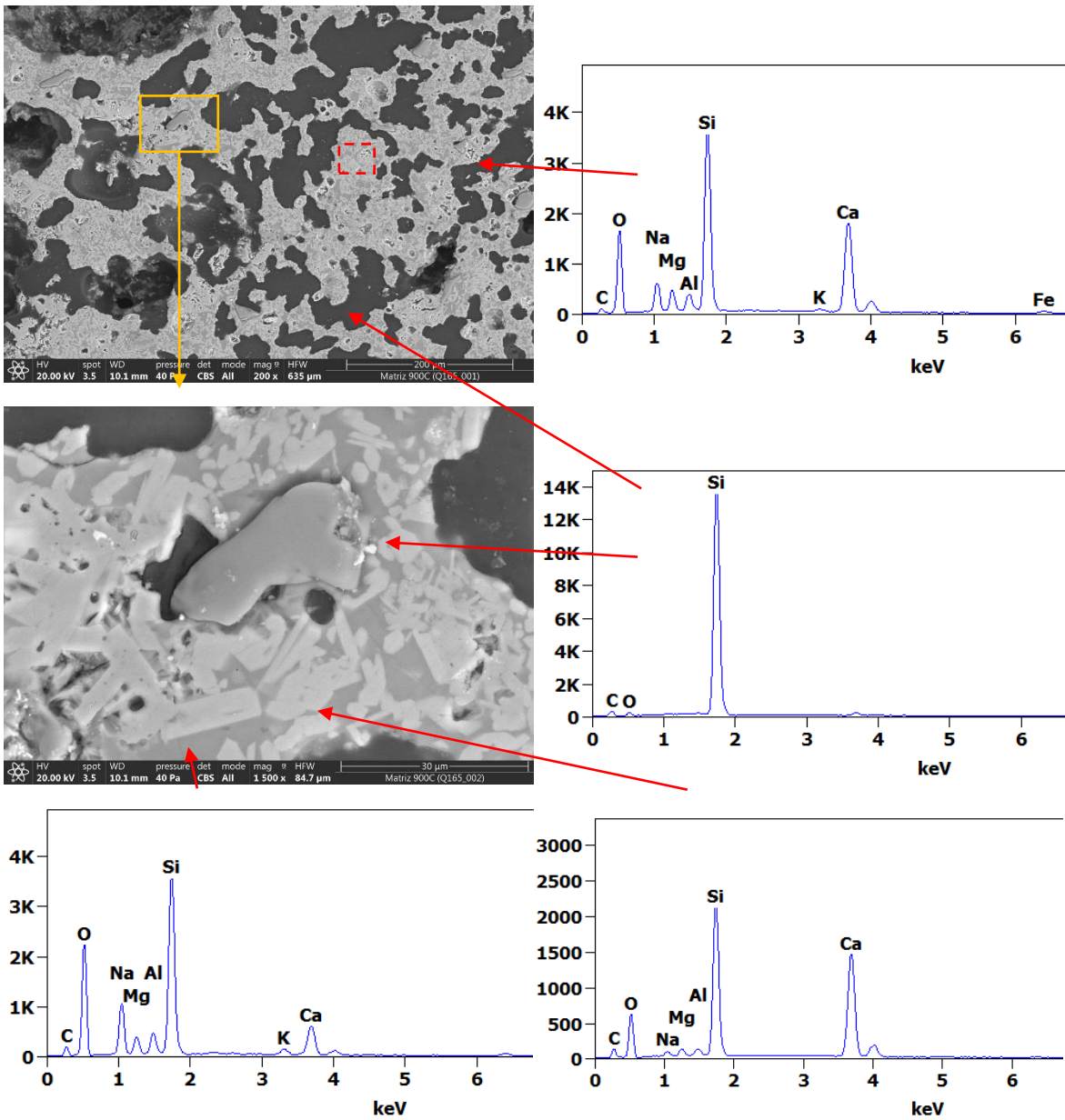
**Figure 18.** Photo of the surface of the raw sample RG:KRY-AS 55:40 with  $\text{Li}_2\text{CO}_3$  5 wt. % and  $\text{SiC}$  2.5 wt. %, analysed the stereoscopic microscope (A,B) and SEM. EDX analysis and identification of the principal constituents of the darkest area (C) (white in A and B)



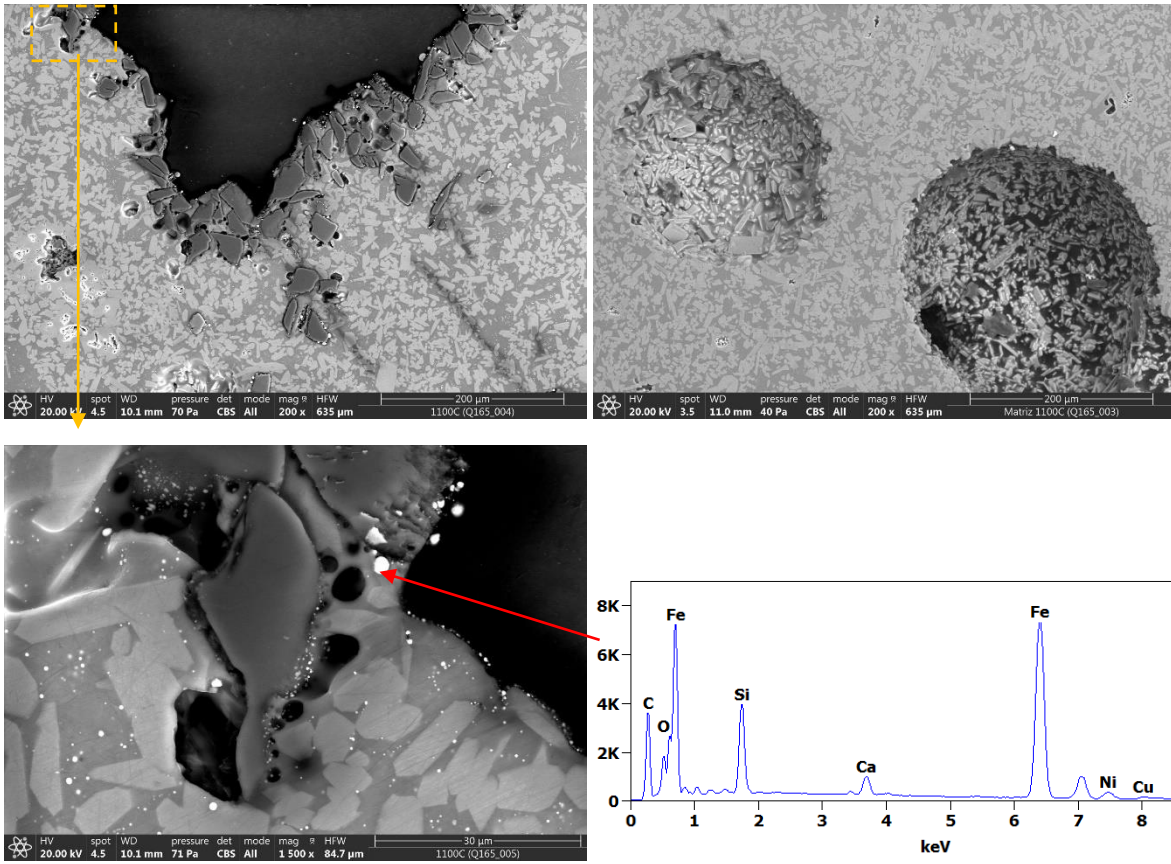
**Figure 19.** SEM micrographs of the transversal section of the sample RG:KRY-AS 55:40 with  $\text{Li}_2\text{CO}_3$  5 wt. % and  $\text{SiC}$  2.5 wt. % treated at  $700^\circ\text{C}$  for 6 min. EDX analysis and identification of the principal constituents.



**Figure 20.** SEM micrographs of the transversal section of the sample RG:KRY·AS 55:40 with  $\text{Li}_2\text{CO}_3$  5 wt. % and  $\text{SiC}$  2.5 wt. % treated at  $800^\circ\text{C}$  for 6 min. EDX analysis and identification of the principal constituents.



**Figure 21.** SEM micrographs of the transversal section of the sample RG:KRY-AS 55:40 with  $\text{Li}_2\text{CO}_3$  5 wt. % and  $\text{SiC}$  2.5 wt. % treated at  $900^\circ\text{C}$  for 6 min. EDX analysis and identification of the principal constituents.



**Figure 22.** SEM micrographs of the transversal section of the sample RG:KRY-AS 55:40 with  $\text{Li}_2\text{CO}_3$  5 wt. % and  $\text{SiC}$  2.5 wt. % treated at  $1100^\circ\text{C}$  for 6 min. EDX analysis and identification of the principal constituents.

#### 6.4. Conclusion

Foam glass has been demonstrated to be a promising way to recycle thermal treated asbestos (KRY·AS) and glass waste (RG). Interesting samples were obtained with a ratio between RG and KRY·AS of 55:40 (wt. %), with  $\text{Li}_2\text{CO}_3$  at 5 wt. % as flux agent and SiC 2.5 wt. % as foaming agent, when fired between 1000 and 1100°C with a soaking time of 1-6 min. The obtained product presented a slightly higher apparent density (0,55-0,68 g/cm<sup>3</sup>) when compared to a commercial foam glass.

The behaviour and final properties of the foam glass were strongly influenced by the ratio RG: KRY·AS, the flux agent ( $\text{Li}_2\text{CO}_3$  or  $\text{Na}_2\text{CO}_3$ ), the grit and amount of the foaming agent (SiC), the firing temperature and the soaking time, as established at each phase of the research.

The results of the interaction between different amount of RG and KRY·AS at 950, 1000, 1050, 1100°C for 6 min have been shown at the end of phase 1. At the increase of KRY·AS WA and OP increased because there was a higher content of CaO that favour the formation of crystalline phases instead of the amorphous. The chosen mixture was RG: KRY·AS 60:40 (wt. %). In phase 2, to obtain lower values of WA and OP, part of RG was substituted with a flux agent:  $\text{Na}_2\text{CO}_3$  (5 and 10% wt. %) or  $\text{Li}_2\text{CO}_3$  (5 wt. %). It was observed an interaction between  $\text{Na}_2\text{CO}_3$  and KRY·AS that, in general, favours the crystallization processes, increased the OP (%) and, consequently, it reduced the quality of the foam glass. On the contrary, the addition of  $\text{Li}_2\text{CO}_3$  gave rise to an evident decrease of WA and OP at 1000, 1050 and 1100°C for a soaking time of 6 min. At the end of this phase the optimized composition was RG: KRY·AS 55:40 with 5  $\text{Li}_2\text{CO}_3$  (wt. %). In phase 3, the addition of the foaming agent, namely SiC, at different grit and amount permitted the study of the first foam glass products. It was observed that at a lower size of SiC corresponded lower values of AD of the samples, so SiC-1500 was chosen. The final tests were done in phase 4, where we tested the composition RG: KRY·AS 55:40 with 5  $\text{Li}_2\text{CO}_3$  (wt. %) with the addition of SiC 1500 (1, 2.5, 5 wt. %), at 1000, 1050, 1100°C for 1, 6 and 30 min. It was observed a decrease of the AD with the firing temperature, but an increase with the soaking time. Moreover, the foaming glass were better optimized with an amount of SiC of 2.5 wt. %, but if it were to reach 5 wt. % the performances would drop.

The best mixture RG: KRY·AS 55:40 with 5  $\text{Li}_2\text{CO}_3$  and 2.5 SiC-1500 (wt. %) was studied to define the evolution of the foaming process between 700 and 1100°C for 6 min. In first place, at a slightly lower temperature than 700°C, RG and  $\text{Li}_2\text{CO}_3$  started to form the liquid phase. This phase surrounded the porosity originally present in the piece, giving rise to small pores ( $\varnothing < 100 \mu\text{m}$ ). At higher

temperature, it started to interact with SiC, and the subsequent production of gas formed larger pores ( $\varnothing > 400 \mu\text{m}$ ). At the increase of the temperature, the amount of liquid phase increased, this phase started to interact with KRY·AS and dissolved it. At 900°C a major part of the KRY·AS was integrated in the liquid phase. Starting from 950°C the oxidation of SiC took place and the amount and dimensions of pores increased with the temperature, up to diameters over 1 mm. A greenish colour, caused by the partial or total reduction of iron oxide by SiC, was also observed.

## 6.5. References

- [1] Monographs on the Evaluation of Carcinogenic Risks to Humans, vol 14, Asbestos.
- [2] E. Pongrácz, V.J. Pohjola, Re-defining waste, the concept of ownership and the role of waste management, *Resour., conserv. and recycl.* 40 (2004) 141-153.
- [3] Art. 5 italian law 27 march 1992 n.257, GU Serie Generale n.87 del 13-04-1992 - Suppl. Ordinario n. 64 (in italian).
- [4] Decreto ministeriale nr. 248/2004 (in italian).
- [5] A.F. Gualtieri, I. Zanatto, Industrial process for the direct temperature induced recrystallization of asbestos and/or mineral fibres containing waste products using a tunnel kiln and recycling. European Patent, EP. 2 027943 B1 (2009).
- [6] A.F. Gualtieri, C. Cavenati, I. Zanatto, M. Meloni, G. Elmi, M. Lassinantti Gualtieri, The transformation sequence of cement–asbestos slates up to 1200°C and safe recycling of the reaction product in stoneware tile mixtures, *Journal of Hazardous Materials* 152 (2008) 563–570.
- [7] A. Viani, A.F. Gualtieri, S. Pollastri, C. Rinaudo, A. Croce, G. Urso, Crystal chemistry of the high temperature product of transformation of cement-asbestos, *Journal of Hazardous Materials* 248–249 (2013) 69– 80.
- [8] F. Giantomassi, A.F. Gualtieri, L. Santarelli, M. Tomasetti, G. Lusvardi, G. Lucarini, Biological effects and comparative cytotoxicity of thermal transformed asbestos-containing materials in a human alveolar epithelial cell line, *Toxicol. In Vitro* 24 (2010) 1521–31.
- [9] A. Pugnaroni, G. Lucarini, C. Rubini, A. Smorlesi, M. Tomasetti, E. Strafella, T. Armeni, A.F. Gualtieri, Raw and thermally treated cement-asbestos exerts different toxicity effects on A549 cells in vitro, *Acta Histochemica* 117 (2015) 29-39.
- [10] A. Viani, A.F. Gualtieri, Preparation of magnesium phosphate cement by recycling the product of thermal transformation of asbestos containing wastes, *Cement and Concrete Research*, 58 (2014) 56-66.

- [11] A.F. Gualtieri, C. Giacobbe, L. Sardisco, M. Saraceno, M. Lassinantti Gualtieri, G. Lusvardi, C. Cavenati, I. Zanatto, I., Recycling of the product of thermal inertization of cement–asbestos for various industrial applications, *Waste Manag.* 31 (2011) 91-100.
- [12] A.F. Gualtieri, A. Tartaglia, Thermal decomposition of asbestos and recycling in traditional ceramics. *J. Eur. Ceram. Soc.* 20 (2000) 1409-1418.
- [13] A.F. Gualtieri, L. Veratti, C. Cavenati, I. Zanatto, KRY·AS, materia prima secondaria del processo di trasformazione termica del cemento-amianto: caratteristiche e proposta di riciclo nel grès porcellanato, *Ceramica Informazione* (2008).
- [14] M.L. Ligabue, M. Lassinantti Gualtieri, G. Lusvardi, D. Malferrari, A.F. Gualtieri, Innovative recycling route of thermally treated cement-asbestos for the production of porcelain stoneware slabs, *J. Cleaner Production*, 247 (2020) 119084-119085.
- [15] R. Ji, Z. Zhang, Y. He, L. Liu, X. Wang, Synthesis, characterization and modelling of new building insulation material using ceramic polishing waste residue, *Constr. Build. Mater.* 85 (2015) 119–126.
- [16] J. Hurley, S. Consultant, A UK Market Survey for Foam Glass. Glass Development and Research Final Report, WRAP Creating Markets for Recycled Resources, GLA-0015, Published by: The Waste and Resources Action Programme, Oxon, England (2003).
- [17] I. S. Grushko, M. P. Maslakov; Crystalline phase formation in a foam glass matrix and its effect on material performance. *Glass and Ceramics*, 75 (2019) 465-470.
- [18] R. Ji, Z. Zhang, Y. He, L. Liu, X. Wang, Synthesis, characterization and modelling of new building insulation material using ceramic polishing waste residue, *Constr. Build. Mater.* 85 (2015) 119–126.
- [19] J.S. Morgan, J.L. Wood, R.C. Bradt, Cell size effects on the strength of foamed glass, *Mater. Sci. Eng.* 47 (1981) 37–42. [https://doi.org/10.1016/0025-5416\(81\)90038-0](https://doi.org/10.1016/0025-5416(81)90038-0)
- [20] G. Scarinci, G. Brusatin, E. Bernardo, Glass Foams, in *Cellular Ceramics: Structure, Manufacturing, Properties and Applications*, Edit. Wiley-Vch, M. Scheffler and P. Colombo, chapter 2.7 (2005) 158-176
- [21] E. Bernardo, R. Castellan, S. Hreglich, I. Lancellotti, Sintered sanidine glass-ceramics from industrial wastes, *J. Eur. Ceram. Soc.* 26 (2006) 3335–3341.
- [22] J. Li, X. Zhuang, E. Monfort, X. Querol, A.S. Llaudis, O. Font, N. Moreno, F.J.G. Ten, M. Izquierdo, Utilization of coal fly ash from a Chinese power plant for manufacturing highly insulating foam glass: Implications of physical, mechanical properties and environmental features, *Construction and Building Materials* 175 (2018) 64–76.
- [23] C. Xi, F. Zheng, J. Xu, W. Yang, Y. Peng, Y. Li, P. Li, Q. Zhen, S. Bashir, J.L. Liu, Preparation of glass-ceramic foams using extracted titanium tailing and glass waste as raw materials; *Construction and Building Materials* 190 (2018) 896–909.



- [24] H. Wang, K. Feng, Q. Sun, Effect of calcium carbonate on the preparation of glass ceramic foams from water-quenched titanium-bearing blast furnace slag and waste glass; *Adv. In App. Ceram.* 117 (2018) 312-318. <https://doi.org/10.1080/17436753.2017.1412120>
- [25] F.A. da Silva Fernandes, S. Arcaro, E.F. Tochtrop Jr, J.C. Valdés Serra, C. Pérez Bergmann, Glass foams produced from soda-lime glass waste and rice husk ash applied as partial substitutes for concrete aggregates, *Process Safety and Environmental Protection* 128 (2019) 77–84.
- [26] Synthesis of Foam Glass-Ceramic from CRT Panel Glass using One-step Powder Sintering Hao Yuan, Hongcheng Wu, Jie Guan; *IOP Conf. Series: Earth and Environmental Science* 186 (2018) 012020. doi :10.1088/1755-1315/186/2/012020
- [27] Z. Chen, H. Wang, R. Ji, L. Liu, C. Cheeseman, X. Wang, Reuse of mineral wool waste and recycled glass in ceramic foams, *Ceramics International* 45 (2019) 15057–15064.
- [28] X. Chen, A. Lu, G. Qu, Preparation and characterization of foam ceramics from red mud and fly ash using sodium silicate as foaming agent, *Ceram. Int.*, 39 (2013) 1923–1929. doi 10.1016/j.ceramint.2012.08.042
- [29] T. Liu, C. Lin, J. Liu, L. Han, H. Gui, C. Li, X. Zhou, H. Tang, Q. Yang, A. Lu, Phase evolution, pore morphology and microstructure of glass ceramic foams derived from tailings wastes; *Ceramic International* 44 (2018) 14393-14400. <https://doi.org/10.1016/j.ceramint.2018.05.049>
- [30] C.D.S. Goncalves, A.M. Bernardin, R.A.A. Boca Santa, C. Leoni, G.J.M. Martins, C.T. Kniess, H.G. Riella, Production of vitreous materials from mineral coal bottom ash to minimize the pollution resulting from the waste generated by the thermoelectrical industry. *Boletín la Soc. Española Cerámica y Vidr.* 57 (2018) 142–150. <http://dx.doi.org/10.1016/j.bsecv.2017.10.007>
- [31] A.P. Oliveira, Glass foams produced from glass bottles and eggshell wastes, *Process Saf. Environ. Prot.* 111 (2017) 60–64. <http://dx.doi.org/10.1016/j.psep.2017.06.011>
- [32] L. B. Teixeira, V.K. Fernandes, B.G.O. Maia, S. Arcaro, A.P.N. Oliveira, Vitrocrystalline foams produced from glass and oyster shell wastes. *Ceram. Int.* 43 (2017) 6730–6737. <http://dx.doi.org/10.1016/j.ceramint.2017.02.078>
- [33] Kaz'mina, O.V., Vereshchagin, V.I. Physicochemical modeling of composition of foam glass-crystal materials. *Glass Phys Chem* 41, 122–126 (2015).
- [34] A. Viani, A.F. Gualtieri, M. Secco, L. Peruzzo, G. Artioli, G. Cruciani, Crystal chemistry of cement-asbestos, *American Mineralogist*, 98 (2013) 1095–1105.
- [35] A. Tucci, L. Esposito, E. Rastelli, C. Palmonari, E. Rambaldi, Use of soda-lime scrap-glass as a fluxing agent in a porcelain stoneware tile mix, *J. Eur. Ceram. Soc.* 24 (2004) 83–92.
- [36] B. Swain, Recovery and recycling of lithium: a review, *Sep. Purif. Technol.* 172 (2017) 388–403.
- [37] S. Shang, L.G. Hector, S. Shi, Y. Qi, Z. Liu, Lattice dynamics, thermodynamics and elastic properties of monoclinic  $\text{Li}_2\text{CO}_3$  from density functional theory, *Acta Mater.* 60 (2012) 5204–5216.

- [38] J. Neeway, S. Kerisit, S. Gin, Z. Wang, Z. Zhu, J.V. Ryan, Low-temperature lithium diffusion in simulated high-level boroaluminosilicate nuclear waste glasses, *J. Non-Cryst. Solids* 405 (2014) 83–90.
- [39] M. Franzini, L. Leoni, M. Saitta, M. Revisione di una metodologia analitica per fluorescenza-X, basata sulla correzione completa degli effetti di matrice, *Rendiconti della Società Italiana di Mineralogia e Petrografia*, 31 (1975) 365–378.
- [40] L. Leoni, M. Saitta, X-ray fluorescence analysis of 29 trace elements in rock and mineral standards. *Rendiconti della Società Italiana di Mineralogia e Petrografia*, 32 (1976) 497–519.
- [41] Rasband W, ImageJ Version 1.32J, National Institute of Mental Health, Bethesda, Maryland, USA
- [42] U. Kolb, K. Shankland, L. Meshi, A. Avilov, W. David, *Uniting Electron Crystallography and Powder Diffraction*, Ed. Springer, 2012. DOI 10.1007/978-94-007-5580-2
- [43] J.L. Haas Jr., G.R. Robinson Jr., B.S. Hemingway, Thermodynamic tabulations for selected phases in the system  $\text{CaO-Al}_2\text{O}_3\text{-SiO}_2\text{-H}_2$  at 101.325 kPa (1 atm) between 273.15 and 1800 K, *Journal of Physical and Chemical Reference Data* 10 (1981) 575-669. doi: 10.1063/1.555645
- [44] B. Joachim, E. Gardés, R. Abart, W. Heinrich, Experimental growth of åkermanite reaction rims between wollastonite and monticellite: evidence for volume diffusion control, *Contrib Mineral Petrol* 161 (2011) 389–399. DOI 10.1007/s00410-010-0538-7
- [45] J. B. Dawson, J. V. Smith, I. M. Steele, Combeite ( $\text{Na}_{2.33}\text{Ca}_{1.74}\text{Others}_{0.12}$ ) $\text{Si}_3\text{O}_9$  from Oldoinyo Lengai, Tanzania, *Journal Of Geology*, 97 (1989) 365-372.
- [46] J. Jandová, P. Dvořák, J. Kondás, L. Havlák, Recovery of lithium from waste materials, *Ceramics – Silikaty* 56 (2012) 50-54.
- [47] S. Natarajan, V. Aravindan, Burgeoning Prospects of Spent Lithium-Ion Batteries in Multifarious Applications, *Advanced Energy Materials*, 8 (2018) 1802303-1802319.
- [48] G. Bayer, S. Koese, Reaction of foaming additives with glass powders in the preparation of lightweight materials, *Riv. Staz. Sperim. Vetro*, 9 (1979) 310-320
- [49] B. Xu, K.M. Liang, J.W. Cao, Y.H. Li, Preparation of Foam Glass Ceramics from Phosphorus Slag. *Advanced Materials Research*, 105–106 (2010) 600–603. <https://doi.org/10.4028/www.scientific.net/amr.105-106.600>
- [50] L. Cot, A. Ayral, J. Durand, C. Guizard, N. Hovnanian, A. Julbe, A. Larbot, *Inorganic membranes and solid state sciences*, *Solid state sciences* 2 (2000) 313-334.
- [51] D.U. Tulyaganov, H.R. Fernandes, S. Agathopoulos, J.M.F. Ferreira, Preparation and characterization of high compressive strength foams from sheet glass, *J. Porous. Mater.* 13 (2006). 133–139 DOI 10.1007/s10934-006-7014-9
- [52] G. Brusatin, G. Scarinci, *Proceed. IVth Int. Congress “Valorisation and Recycling of Industrial Wastes (VARIREI)”, L’Aquila, Italy, 2003.*

[53] A.S. Llaudis, M.J. Orts Tari, F.J. Garcia Ten, E. Bernardo, P. Colombo, Foaming of flat glass cullet using  $\text{Si}_3\text{N}_4$  and  $\text{MnO}_2$  powders, *Ceramics International* 35 (2009) 1953–1959. doi:10.1016/j.ceramint.2008.10.022

## **Appendix A**

# Supplementary Materials: Preparation and Luminescence Properties of Ba<sub>5</sub>Si<sub>8</sub>O<sub>21</sub> Long Persistent Phosphors Doped with Rare-Earth Elements

Andrea Silvestri, Maria Laura Ligabue, Gianluca Malavasi and Gigliola Lusvardi \*

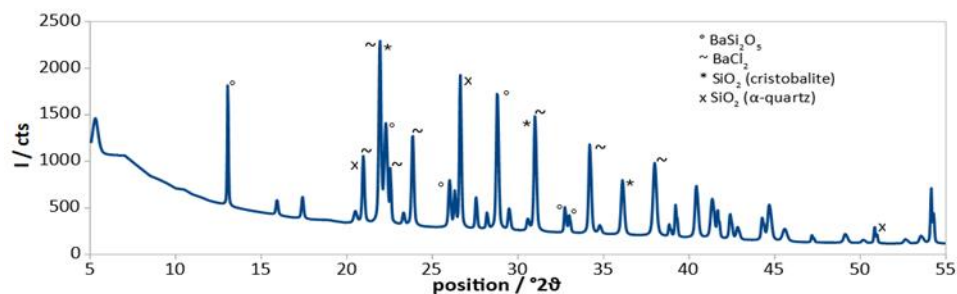
**Table S1.** Most important peaks of NaCl, BaCO<sub>3</sub> in the sample C before the heat treatment compared with the reference data [18].

	NaCl (theo)			NaCl (exp)		
<b>d (Å)</b>	2.81	1.99	3.24	2.81	1.99	3.23
<b>I (%)</b>	100	55	10	83	27	6
	BaCO <sub>3</sub> (theo)			BaCO <sub>3</sub> (exp)		
<b>d (Å)</b>	3.72	3.66	2.62	3.70	3.65	2.62
<b>I (%)</b>	100	50	30	100	34	27

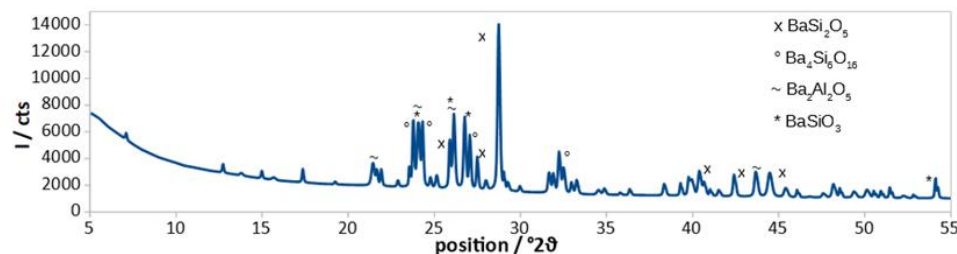
**Table S2.** Most important peaks of Ba<sub>5</sub>Si<sub>8</sub>O<sub>21</sub>, Ba<sub>4</sub>Si<sub>6</sub>O<sub>16</sub>, BaSi<sub>2</sub>O<sub>5</sub> compared with the reference data [18].

	A	B	C	D	E	F	G	H	
<b>Ba<sub>5</sub>Si<sub>8</sub>O<sub>21</sub></b>									
<b>d (Å)</b>	<b>3.80</b>	3.81	3.82	3.84	3.79	3.81	3.84	3.83	3.82
<b>I (%)</b>	<b>100</b>	37	100	33	51	98	82	100	99
<b>I(Counts)</b>	/	1134	1522	1295	2408	2530	1155	2344	3117
<b>d (Å)</b>	<b>3.27</b>	3.28	3.28	3.30	3.27	3.27	3.27	3.29	3.29
<b>I (%)</b>	<b>82</b>	64	69	26	66	100	65	58	47
<b>I(Counts)</b>	/	1953	1052	1020	3111	2573	919	1363	1491
<b>d (Å)</b>	<b>3.73</b>	3.75	3.75	3.75	3.73	3.73	3.76	3.76	3.74
<b>I (%)</b>	<b>74</b>	100	55	26	100	99	62	59	86
<b>I(Counts)</b>	/	3070	845	1036	4738	2539	867	1387	2730
<b>d (Å)</b>	<b>6.88</b>	6.85	6.85	6.88	6.88	6.89	6.88	6.86	6.85
<b>I (%)</b>	<b>13</b>	12	14	100	13	71	100	77	33
<b>I(Counts)</b>	/	380	447	3925	628	2010	1406	1810	1038
<b>Ba<sub>4</sub>Si<sub>6</sub>O<sub>16</sub></b>									
<b>d (Å)</b>	<b>3.74</b>	3.75	3.78	3.75	3.73	3.73	3.76	3.76	3.74
<b>I (%)</b>	<b>100</b>	100	84	26	100	99	62	59	86
<b>I(Counts)</b>	/	3070	1274	1036	4738	2539	867	1387	2730
<b>d (Å)</b>	<b>3.67</b>	3.68	/	/	/	/	/	/	/
<b>I (%)</b>	<b>51</b>	80	/	/	/	/	/	/	/
<b>I(Counts)</b>	/	2452	/	/	/	/	/	/	/
<b>d (Å)</b>	<b>3.25</b>	3.25	3.25	3.26	/	3.22	3.25	3.24	3.24
<b>I (%)</b>	<b>45</b>	52	55	24	/	68	72	43	59
<b>I(Counts)</b>	/	1601	1504	932	/	3065	1010	1012	1860
<b>d (Å)</b>	<b>3.29</b>	3.28	3.28	3.30	3.27	3.27	3.27	3.29	3.29
<b>I (%)</b>	<b>41</b>	64	69	26	66	100	65	58	47
<b>I(Counts)</b>	/	1953	1052	1020	3111	2573	919	1363	1491

BaSi <sub>2</sub> O <sub>5</sub>									
d (Å)	3.10	3.10	3.13	3.12	3.11	3.10	3.12	3.12	3.11
I (%)	100	43	59	21	21	43	53	47	100
I(Counts)	/	1318	900	811	995	1108	748	1094	3162
d (Å)	3.97	3.98	4.02	4.00	3.96	3.97	4.02	3.99	3.99
I (%)	85	58	53	30	9	63	28	13	48
I(Counts)	/	1779	807	1169	415	1628	388	297	1521
d (Å)	3.34	3.35	3.36	3.36	3.34	3.35	3.36	3.36	3.36
I (%)	70	48	31	14	9	38	34	30	23
I(Counts)	/	1470	479	538	434	988	478	703	718
d (Å)	3.42	3.43	3.44	3.41	3.42	3.43	3.41	3.44	3.44
I (%)	50	34	25	36	3	56	20	14	19
I(Counts)	/	1054	758	1416	157	2045	279	330	616



**Figure S1.** XRD of sample synthesised with SiO<sub>2</sub>, BaCl<sub>2</sub> as precursor with molar ratio Ba/Si = 0.625; H<sub>3</sub>BO<sub>3</sub> as flux agent; Eu<sub>2</sub>O<sub>3</sub>, Dy<sub>2</sub>O<sub>3</sub> as dopants with molar ratios Eu/Si = 2.8 × 10<sup>-3</sup> and Dy/Si = 3.6 × 10<sup>-3</sup>. Thermal treatment conditions are 1200 °C for 12 h. The crucible is in alumina.



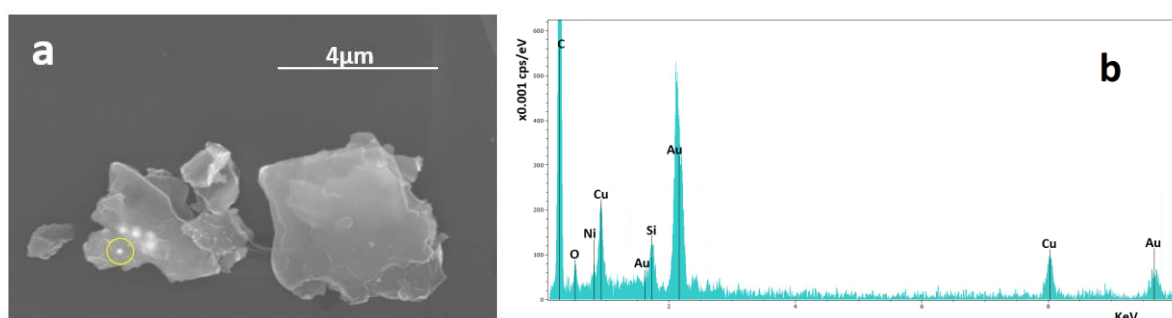
**Figure S2.** XRD of sample synthesised with Na<sub>2</sub>SiO<sub>3</sub>, BaCO<sub>3</sub> and NH<sub>4</sub>Cl as precursor with molar ratio Ba/Si = 0.7; Eu<sub>2</sub>O<sub>3</sub>, Dy<sub>2</sub>O<sub>3</sub> as dopants with molar ratios Eu/Si = 2.8 × 10<sup>-3</sup> and Dy/Si = 3.6 × 10<sup>-3</sup>. Thermal treatment conditions are 1100 °C for 12 h. The crucible is in alumina.

## **Appendix B**

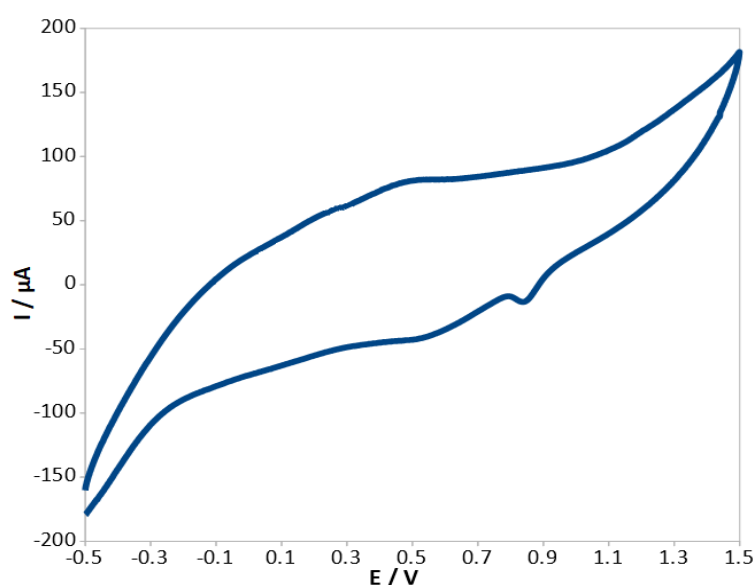
## Supporting Information

### ***One-pot sonocatalyzed synthesis of sol-gel graphite electrodes containing gold nanoparticles for application in amperometric sensing***

Maria Laura Ligabue, Fabio Terzi, Chiara Zanardi,\* Gigliola Lusvardi\*

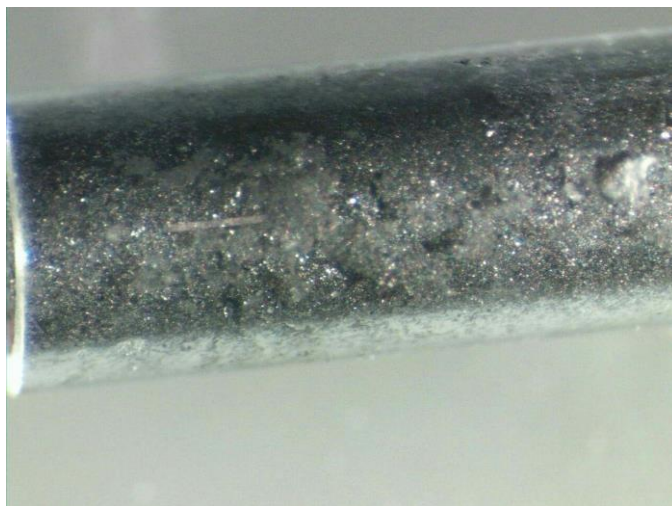


**Online Resource 1.** (a) SEM-FEG micrograph (secondary electron mode) and (b) relevant EDS analysis of the spot in the yellow circle of SG-Au<sub>TR</sub> electrode prepared with NaAuCl<sub>4</sub> with chemical reduction. Cu and Ni peaks are due to the sample holder. At variance with Fig. 2a,b and 3a,b, AuNPs appear as bright spots in secondary electron mode.

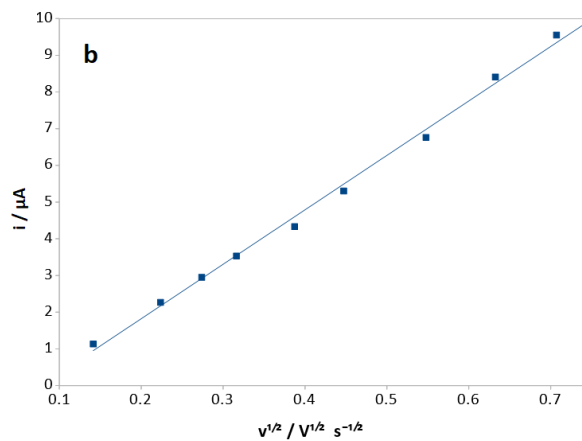
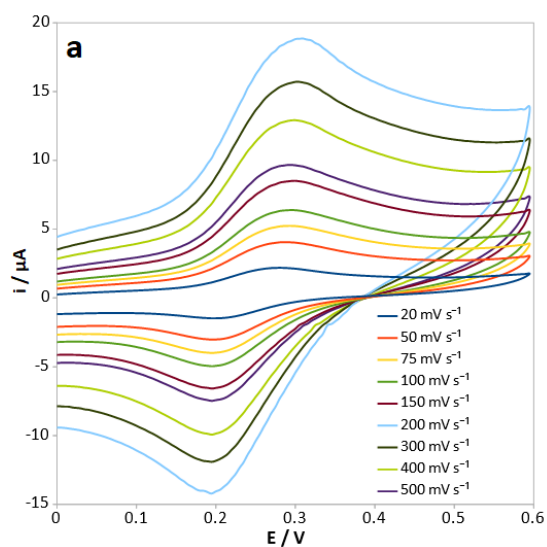


**Online Resource 2.** 50<sup>th</sup> CV trace of SG-Au<sub>CR</sub> electrode in 0.05 M H<sub>2</sub>SO<sub>4</sub>, 0.05 V s<sup>-1</sup> potential scan rate.

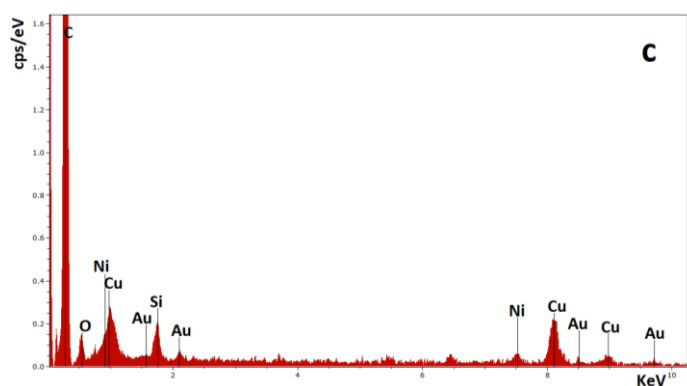
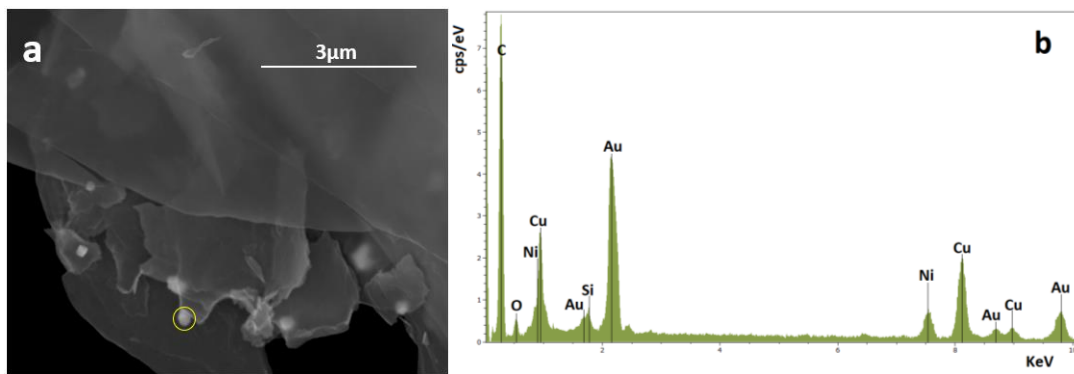




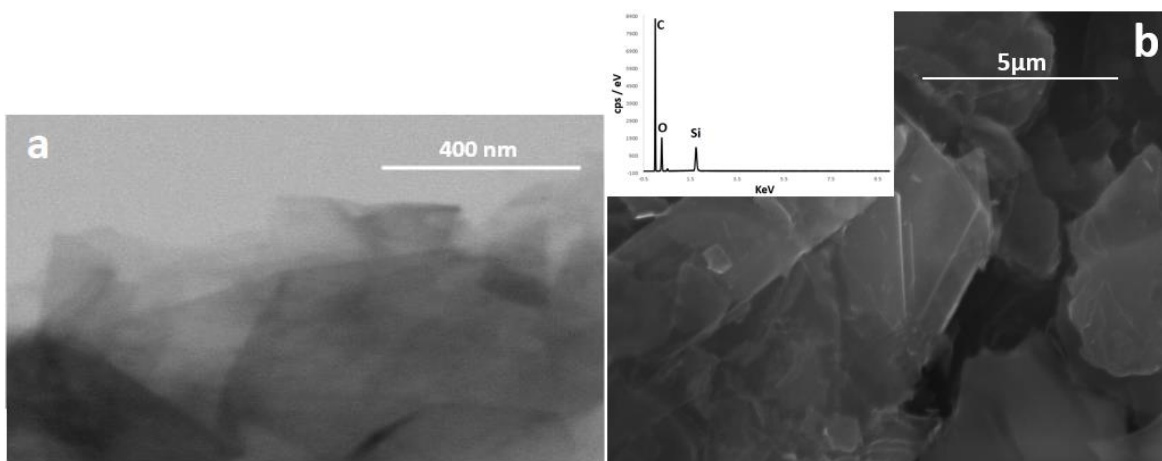
**Online Resource 3.** Image obtained with optical microscope for SG-Au<sub>TR</sub> (HAuCl<sub>4</sub> as precursor).



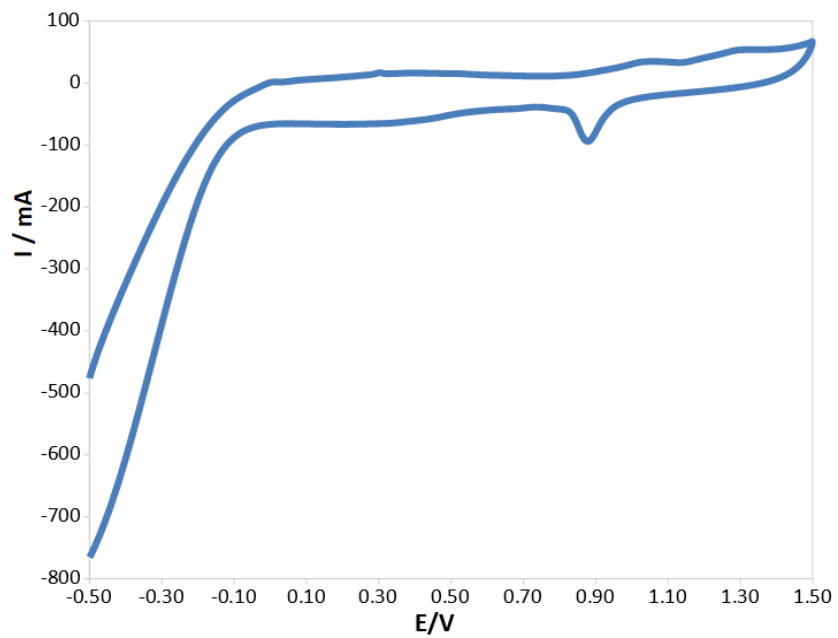
**Online Resource 4.** (A) CV traces registered at SG-Au<sub>TR</sub> electrode, obtained from NaAuCl<sub>4</sub> reduction (150°C, 24h), in 1 mM Fc-MeOH<sub>2</sub>, 0.1 M LiClO<sub>4</sub> at different scan rate. (B) Relevant plot reporting the height of the oxidation peaks vs. the square root of the scan rates.



**Online Resource 5.** (a) SEM-FEG micrograph (secondary electron mode) obtained for SG-Au<sub>TR</sub> electrode prepared with NaAuCl<sub>4</sub> with thermal reduction at 150°C for 24h associated to the relevant EDS analysis of (b) the spot in the yellow circle, (c) the entire matrix. Cu and Ni peaks are due to the sample holder.



**Online Resource 6.** SEM-FEG micrograph obtained for a SG<sub>TR</sub> electrode (150°C for 24h) in (a) STEM and (b) secondary electron mode; (b) also reports the relevant EDS analysis of the entire matrix in the inset.



**Online Resource 7.** CV traces registered at SG-Au<sub>TR</sub> electrode, prepared from NaAuCl<sub>4</sub> reduction (150°C, 24h), in 0.05M H<sub>2</sub>SO<sub>4</sub>, 0.05 V s<sup>-1</sup> potential scan rate.

## **Appendix C**

## Supporting Information

### ***Recycling of thermally treated cement-asbestos for the production of porcelain stoneware slabs***

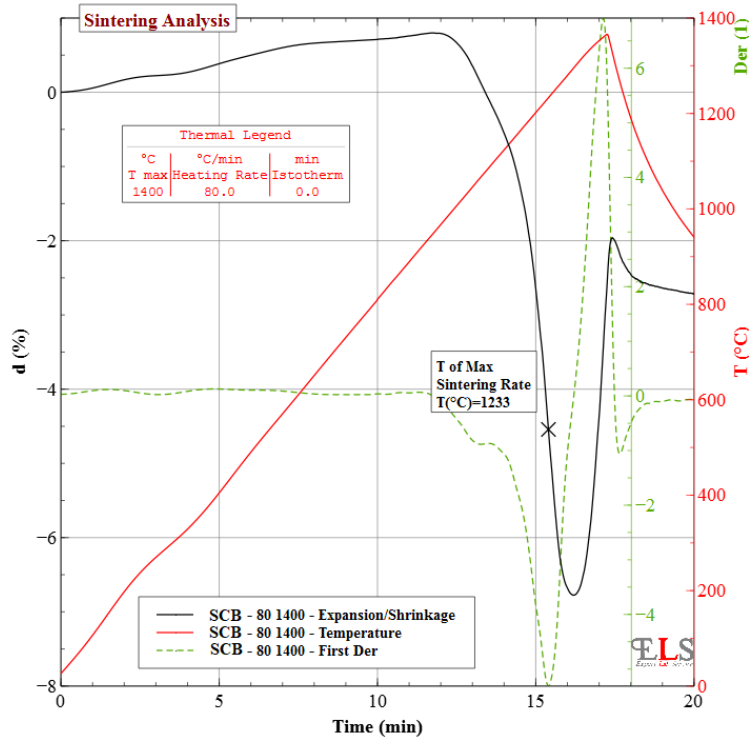
*Maria Laura Ligabue, Alessandro F. Gualtieri, Magdalena Lassinantti Gualtieri, Daniele Malferrari, Gigliola Lusvardi*

**Table 1 SI.** Results from full quantitative phase analyses (XRPD data and Rietveld-RIR) of fired bodies.

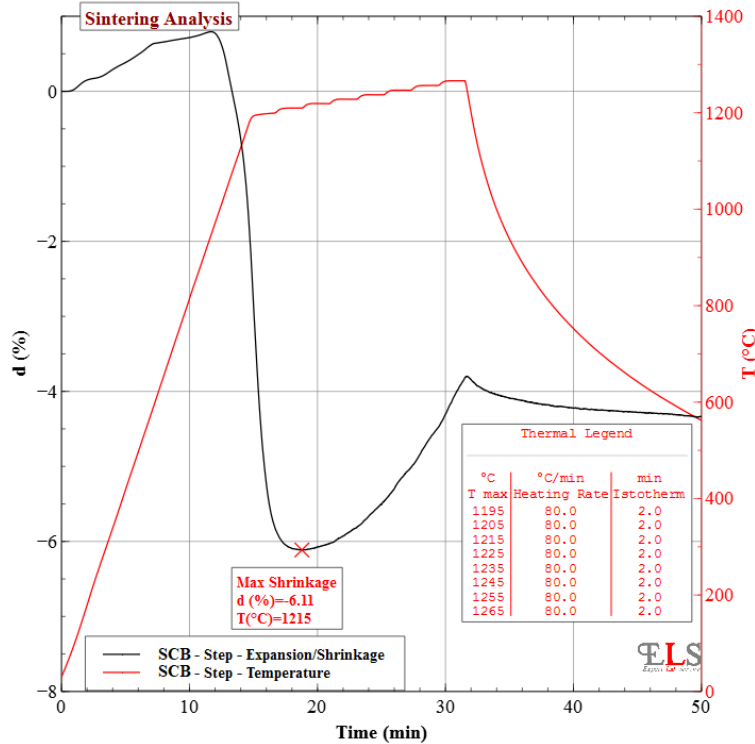
<b>Sample</b>	<b>Amorphous</b>	<b>Quartz</b>	<b>K-Feldspar</b>	<b>Mullite</b>	<b>Plagioclase</b>
<b>SCB</b>	68.1 (3)	17.2 (1)	1.0 (1)	11.9 (2)	1.9 (1)
<b>F<sub>ref_1</sub></b>	68.8 (3)	16.3 (1)	1.1 (1)	11.0 (2)	2.9 (1)
<b>F<sub>ref_3</sub></b>	69.7 (3)	15.6 (1)	1.1 (1)	10.6 (2)	3.0 (1)
<b>F<sub>ref_5</sub></b>	69.9 (3)	14.5 (1)	1.7 (1)	8.7 (2)	5.2 (1)
<b>F1_1</b>	70.5 (3)	15.6 (1)	0.9 (1)	10.6 (2)	2.4 (1)
<b>F1_3</b>	69.8 (3)	15.3 (1)	1.4 (1)	9.7 (2)	3.8 (1)
<b>F1_5</b>	71.1 (3)	12.9 (1)	1.5 (1)	8.3 (2)	6.2 (1)
<b>F2_1</b>	70.6 (3)	15.5 (1)	1.0 (1)	10.5 (2)	2.4 (1)
<b>F2_3</b>	71.5 (2)	14.2 (1)	1.1 (1)	8.5 (2)	4.7 (1)
<b>F2_5</b>	74.0 (2)	11.8 (1)	1.7 (1)	6.6 (2)	5.9 (1)

**Table 2 SI.** Chemical composition (mol%) of the amorphous fraction of each fired ceramic body, calculated by extracting the results from the quantitative phase analyses from the overall chemical composition (XRF). The shear viscosity ( $\eta$ ) at 1200 °C, calculated according to Giordano et al. (2008) is also shown.

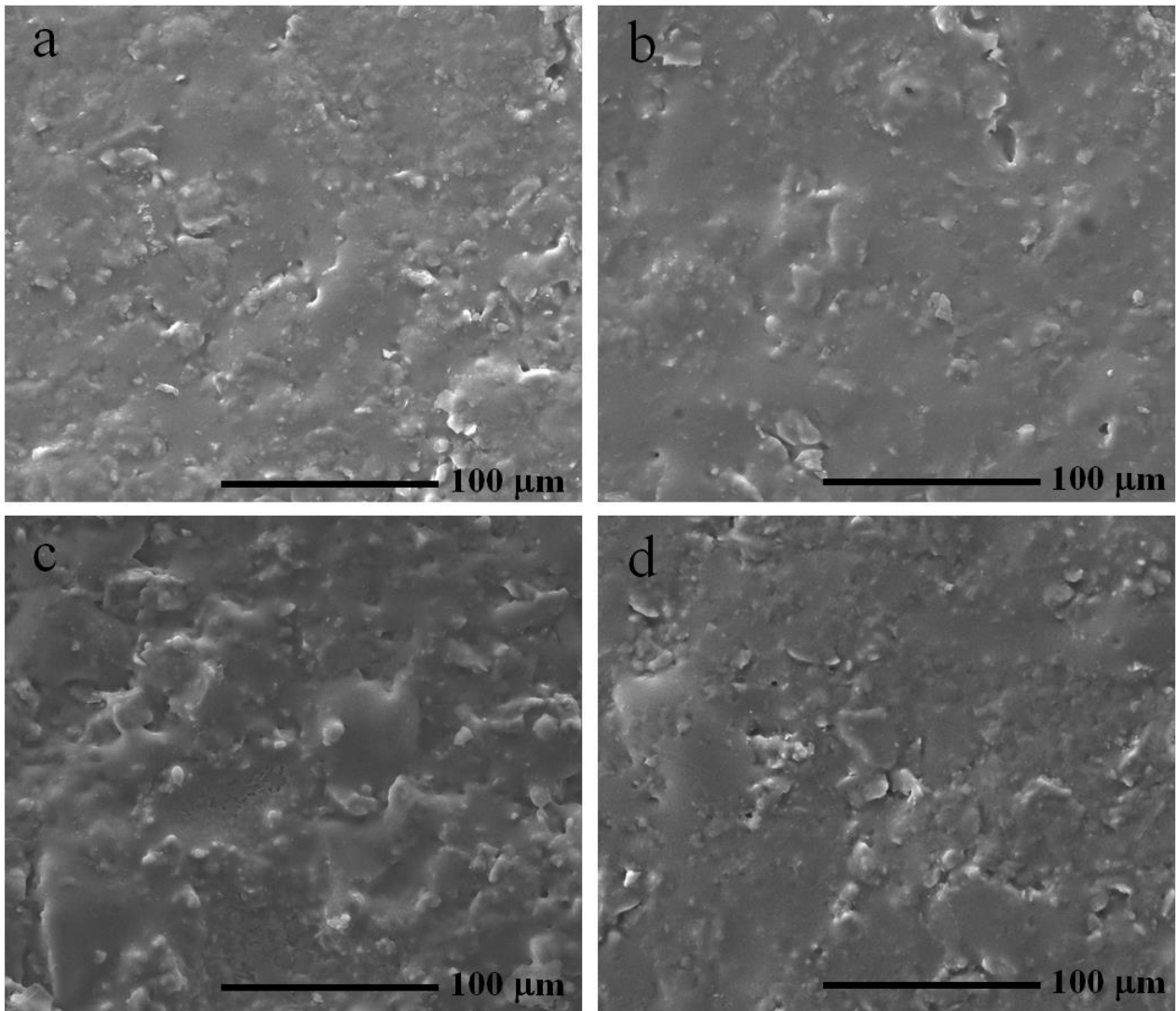
	$\eta$ (log <sub>10</sub> Pas)	Chemical composition (Mol. %)									
		SiO <sub>2</sub>	Al <sub>2</sub> O <sub>3</sub>	TiO <sub>2</sub>	Fe <sub>2</sub> O <sub>3</sub>	CaO	MgO	Na <sub>2</sub> O	K <sub>2</sub> O	Mn <sub>2</sub> O <sub>3</sub>	P <sub>2</sub> O <sub>5</sub>
<b>SCB</b>	4.89	74.9	14.1	0.7	0.3	0.4	1.4	6.2	1.8	<0.1	0.2
<b>F<sub>ref_1</sub></b>	4.87	74.8	14.1	0.6	0.3	0.4	1.6	6.2	1.8	<0.1	0.2
<b>F<sub>ref_3</sub></b>	4.79	74.2	14.0	0.6	0.3	1.0	2.1	5.9	1.7	<0.1	0.2
<b>F<sub>ref_5</sub></b>	4.73	73.8	14.2	0.6	0.3	0.9	2.5	5.8	1.6	<0.1	0.2
<b>F1_1</b>	4.90	74.8	14.2	0.6	0.3	0.6	1.5	6.0	1.8	<0.1	0.2
<b>F1_3</b>	4.84	74.4	14.1	0.6	0.3	0.9	1.7	6.0	1.7	<0.1	0.2
<b>F1_5</b>	4.87	75.0	13.8	0.6	0.3	0.7	1.8	5.8	1.7	<0.1	0.2
<b>F2_1</b>	4.89	74.8	14.1	0.6	0.3	0.7	1.5	6.0	1.7	<0.1	0.2
<b>F2_3</b>	4.84	74.6	14.0	0.6	0.3	0.8	1.7	6.0	1.7	<0.1	0.2
<b>F2_5</b>	4.81	74.5	13.9	0.6	0.3	1.3	1.9	5.9	1.5	<0.1	0.2



**Figure 1 SI.** Results from optical dilatometry measurements of a dry standard ceramic body (SCB). Expansion (%) as a function of time measured during heating (constant heating rate of 80 °C/min) of the dry standard ceramic body (SCB) up to ca. 1350 °C followed by fast cooling. The first derivative curve (green dashed line) shows a minimum at ca. 1200 °C (maximum sintering rate).



**Figure 2 SI.** Results from optical dilatometry measurements of a dry standard ceramic body (SCB). Expansion (%) as a function of time measured during constant heating up to 1195 °C followed by 10 °C stepwise heating followed by 2 min isotherms (see text for details). The applied heating rate was 80 °C/min.



**Figure 3 SI.** SEM micrographs of tile surfaces: SCB (a),  $F_{ref\_5}$  (b), F1\_5 (c) and F2\_5 (d).